

**UCLA**

**UCLA Electronic Theses and Dissertations**

**Title**

Optical Properties of Secondary Organic Aerosols

**Permalink**

<https://escholarship.org/uc/item/5c75f542>

**Author**

Kim, Hwajin

**Publication Date**

2012

Peer reviewed|Thesis/dissertation

UNIVERSITY OF CALIFORNIA

Los Angeles

Optical Properties of Secondary Organic Aerosols

A dissertation submitted in partial satisfaction of the  
requirements for the degree Doctor of Philosophy  
in Atmospheric and Oceanic Sciences

by

HWA JIN KIM

2012

© Copyright by

HWA JIN KIM

2012

## ABSTRACT OF THE DISSERTATION

### Optical Properties of Secondary Organic Aerosols

by

HWA JIN KIM

Doctor of Philosophy in Atmospheric and Oceanic Sciences

University of California, Los Angeles, 2012

Professor Suzanne E. Paulson, Chair

The refractive index is the fundamental property controlling aerosol optical properties. Secondary organic aerosols (SOA) constitute a large fraction of aerosols in the atmosphere, and yet the optical properties of this complex material are just beginning to be understood. They appear to be much more variable than expected. We explore the factors controlling the real refractive indices ( $m_r$ ) of SOA under conditions that are as close to atmospheric conditions as possible. SOA were generated from the  $\alpha$ -pinene,  $\beta$ -pinene, limonene and toluene using several oxidation chemistries including ozonolysis with and without scavenger and photooxidation at different HC/NO<sub>x</sub> ratios, different mass concentration and experimental temperatures.  $M_r$  were retrieved from polar nephelometer measurements using parallel and perpendicular polarized 532 or 670 nm light where there is no evidence of significant absorption by the particles investigated here. Retrievals were performed with a genetic algorithm method using Mie-Lorenz scattering theory and measured particle size distributions. Overall examination of the SOA data shows that SOA  $m_r$  ranges from 1.34 to 1.62, reflecting the factors to control the chemical composition;

decreases as the HC/NO<sub>x</sub> ratio increases, decrease at lower temperature (< 20 °C) and toluene SOA has higher m<sub>r,s</sub> than biogenic SOA. Aerosol mass spectrometer (AMS) measurement reveals that laboratory SOA is less oxidized than ambient aerosol and the increase in refractive index is most correlated with the H:C ratio, indicating that condensation of semivolatile species increases the refractive index, although all other combined factors relate to the m<sub>r,s</sub>. In an effort to measure more atmospheric relevant SOA, high volatile species are evaporated using thermodenuder (TD) at 65 - 110 °C temperature. Retrieved m<sub>r</sub> become narrower but still has range of 1.41-1.62 which has a significant impact on radiative transfer calculations of SOA direct effects. We showed that changing the m<sub>r,s</sub> from 1.4 to 1.5 can produce an increase in the radiative forcing by at least 12-19 % for non-absorbing particles. There is more work to be done before recommendations can be made for atmospheric applications, but this thesis clearly highlights a single value for SOA m<sub>r</sub> will not be sufficient to accurately model radiative transfer.

The dissertation of HWA JIN KIM is approved.

Qinbin Li

Kuo-Nan Liou

Arthur M. Winer

Suzanne E. Paulson, Committee Chair

University of California, Los Angeles

2012

# TABLE OF CONTENTS

<b>LIST OF FIGURES.....</b>	<b>x</b>
<b>LIST OF TABLES.....</b>	<b>xvii</b>
<b>ACKNOWLEDGEMENT.....</b>	<b>xviii</b>
<b>VITA.....</b>	<b>xx</b>
<b>CHAPTER 1 INTRODUCTION.....</b>	<b>1</b>
1.1 background.....	2
1.2 Motivation and Scientific Objectives.....	6
1.3 Organization of of thesis.....	8
1.4 References.....	14
Tables.....	19
<b>CHAPTER 2 APPROACH; EXPERIMENTAL AND ANAYLSIS.....</b>	<b>21</b>
2.1 Generation of Representative Aerosols.....	22
2.1.1 Aerosol Generation chamber.....	22
2.1.2 Model aerosols.....	24
2.1.3 Gas phase and particle phase analysis of chamber.....	27
2.2 Pholar nephelometer.....	27
2.3 Validation and calibration of instrument.....	29
2.4 Determination of the refractive index: Genetic algorithm.....	31
2.5 References.....	34

Tables and figures.....	36
-------------------------	----

**CHAPTER 3 Real refractive indices of  $\alpha$ - and  $\beta$ -pinene and Toluene Secondary Organic Aerosols generated from Ozonolysis and Photo-oxidation.....40**

3.1 Experimental.....	41
-----------------------	----

3.2 Results and Discussion.....	42
---------------------------------	----

3.2.1 Reaction profile of a photooxidation experiment.....	42
--	----

3.2.2 Aerosol formation yields.....	43
-------------------------------------	----

3.2.3 SOA refractive indices.....	44
-----------------------------------	----

3.2.3.1 Ozonolysis SOA.....	45
-----------------------------	----

3.2.3.2 Photochemically generated SOA.....	45
--	----

3.2.4 Effect of the refractive index on radiative transfer.....	48
---	----

3.3 Conclusions.....	49
----------------------	----

3.4 References.....	49
---------------------	----

Tables and figures.....	52
-------------------------	----

**CHAPTER 4 Real refractive indices and formation yields of secondary organic aerosol generated from photooxidation of limonene and  $\alpha$ -pinene: the effect of the HC/NO<sub>x</sub> ratio.....62**

4.1 Experimental .....	63
------------------------	----

4.2 Photochemical oxidation and partitioning calculations .....	64
---	----

4.3 Results and Discussion.....	65
---------------------------------	----

4.3.1 Reaction profile of a photooxidation experiment.....	66
--	----



4.3.2 Aerosol formation yields.....	67
4.3.3 Determination of refractive index.....	68
4.3.3.1 SOA refractive indices.....	68
4.3.3.2 Estimation of RO <sub>2</sub> reaction pathways.....	72
4.3.4 Quantitative structure property relationship (QSPR) approach for estimation of refractive indices of SOA.....	74
4.4 Summary and atmospheric implications.....	76
4.5 References.....	77
Tables and figures.....	80
<b>CHAPTER 5 Real refractive indices and volatility of secondary organic aerosol generated from photooxidation and ozonolysis of limonene, <math>\alpha</math>-pinene and toluene upon heating.....</b>	<b>94</b>
5.1 Experimental .....	95
5.1.1 Secondary organic aerosol generation.....	95
5.1.2 Thermodenuder.....	95
5.1.3 SOA characterization and experimental setup.....	96
5.1.4 Particle losses in the thermodenuder.....	97
5.2 Results and Discussion.....	98
5.2.1 Reaction profile of a photooxidation experiment.....	99
5.2.2 Volaitlity measurements.....	100
5.2.2.1 Volatility of SOA from photooxidation .....	100
5.2.2.2 Volatility of SOA from ozonolysis.....	101

5.2.3 SOA refractive indices.....	102
5.2.3.1 Photochemically generated SOA.....	103
5.2.3.2 Ozonolysis SOA.....	107
5.3 Atmospheric implications.....	109
5.4 References.....	110
Tables and Figures.....	114

**CHAPTER 6 Real refractive indices and elemental composition of secondary organic aerosol generated from ozonolysis and photooxidation of limonene and  $\alpha$ -pinene.....126**

6.1 Experimental .....	127
6.2 Results and Discussion.....	128
6.2.1 SOA refractive indices.....	128
6.2.2 Chemical composition of SOA.....	131
6.2.3 $m_r$ and chemical composition of SOA.....	133
6.2.3.1 $\alpha$ -pinene ozonolysis SOA .....	133
6.2.3.2 Photochemically generated $\alpha$ -pinene SOA.....	134
6.2.3.3 Photochemically generated limonene SOA.....	135
6.2.3.4 HC/NO <sub>x</sub> effect on photochemically generated limonene SOA.....	136
6.3 Summary and Atmospheric implications .....	138
6.4 References.....	139
Tables and figures.....	143

**CHAPTER 7 FINAL CONCLUSIONS AND ATMOSPHERIC IMPLICATION.....155**

7.1 Final conclusions and atmospheric implications.....	156
7.2 Future works.....	160
7.3 References.....	162
Figure.....	165
<b>Appendix A;</b> Optical properties of absorbing Secondary Organic Aerosols generated from photo-oxidation of toluene, phenol and limonene.....	166
<b>Appendix B;</b> Aerosol partitioning of condensing species.....	182
<b>Appendix C;</b> Tables of initial conditions, temperatures, relative humidities and results of the experiments not described in main chapters.....	187
<b>Appendix D;</b> Bi-modal size distribution of SOA generated from photooxidation of $\alpha$ -humulene/ $\text{NO}_x$ experiment ( $\text{HC}/\text{NO}_x = 8.3$ ) .....	192

## LIST OF FIGURES

- Figure 2.1.** (a) Incident 670 nm laser light polarized parallel (circles) and perpendicular (filled diamonds) scattered by 800 nm PSL particles measured by the polar nephelometer before calibration and expectations (lines) developed from Mie-Lorenz calculations. (b) Calibration constants (circles) determined from the 800 nm PSL measurement in (a) with parallel incident light, along with the same for PSL particles with a diameter of 596 nm. Error bars are based on the standard deviation of calibration constants derived from 40-50 PN measurements taken over a period of several minutes. Differences between these calibration constants are assumed to be from multiple internal reflections within the scattering volume.....38
- Figure 2.2.** (a) Selected scattering properties recorded with the PN as particles grow for the experiment performed on 21 October. (b) Scattering at 13:16 (after 46 min), when the particle had a median size of 291 nm. Also shown GA determined fit using Mie-Lorenz theory, with a  $m_r=1.48$ , and at fitness of 0.965.....39
- Figure 3.1.** Profile of an  $\alpha$ -pinene photooxidation experiment performed on Oct. 21, with initial concentrations of 500 ppb  $\alpha$ -pinene and 260 ppb  $\text{NO}_x$ . (a) Gas phase concentrations (hydrocarbon, NO,  $\text{NO}_x$ ,  $\text{O}_3$ ) and aerosol mass concentration (corrected for wall losses; see text). (b) Time evolution of the SOA particle number concentrations, mean diameter and integrated scattering ( $\beta_{\text{sca}}$ ). (c) The GA determined real refractive index, and associated fitness values for all viable polar nephelometer measurements.....54
- Figure 3.2.** (a) Selected scattering properties recorded with the PN as particles grow for the experiment performed on 21 October. (b) Scattering at 13:16 (after 46 min), when the

particle had a median size of 291 nm. Also shown GA determined fit using Mie-Lorenz theory, with a $m_r=1.48$ , and at fitness of 0.965.....	55
<b>Figure 3.3.</b> Retrieved refractive indices for SOA formed by $\alpha$ -pinene ozonolysis with and without scavenger. The experiment on Feb. 12 was performed at lower temperature than the others (Table 3.2) .....	56
<b>Figure 3.4.</b> Retrieved refractive indices for SOA formed by ozonolysis of (a) $\alpha$ - pinene (b) $\beta$ -pinene at different initial concentration. $\alpha$ -pinene data from June 29 and July 31 at low mass concentration are also shown in the insert in Figure 4a, and the low temperature data (Feb. 12) are omitted.....	57
<b>Figure 3.5.</b> Retrieved refractive indices for SOA generated from photooxidation of (a) $\alpha$ -pinene (b) $\beta$ -pinene and (c) toluene.....	58
<b>Figure 3.6.</b> Retrieved refractive indices for SOA formed by $\alpha$ -pinene ozonolysis with and without scavenger as a function of diameter.....	59
<b>Figure 3.7.</b> Retrieved refractive indices for SOA formed by ozonolysis of (a) $\alpha$ - pinene (b) $\beta$ -pinene at different initial concentration as a function of diameter.....	60
<b>Figure 3.8.</b> Retrieved refractive indices for SOA formed by photooxidation of (a) $\alpha$ -pinene (b) $\beta$ -pinene (c) toluene as a function of diameter.....	61
<b>Figure 4.1.</b> (a) Selected scattering properties recorded with the PN as particles grow for the experiment performed on 30 August. (b) Scattering at 12:38 (after 126 min), when the particle had a median size of 256 nm. Also shown GA determined fit using Mie-Lorenz theory, with a $m_r=1.456$ , and at fitness of 0.968.....	84
<b>Figure 4.2.</b> Profile of a limonene photooxidation experiment performed on Nov. 5, with initial concentrations of 72 ppb limonene and 115 ppb $\text{NO}_x$ . (a) Gas phase concentrations	

(hydrocarbon, NO, NO<sub>x</sub>, O<sub>3</sub>), aerosol mass concentration (corrected for wall losses; see text) and GA determined real refractive index. (symbol; experiment, line; simulation) (b) Time evolution of the SOA particle number concentrations, mean diameter and integrated scattering ( $\beta_{sca}$ ) .....85

**Figure 4.3.** SOA yield as a function of mass concentration from (a) limonene photooxidation and (b)  $\alpha$ -pinene photooxidation. All yields are normalized to a density of 1.25 and 1.2 g/cm<sup>3</sup> for limonene and  $\alpha$ -pinene, respectively to facilitate comparison. The Hoffman et al.<sup>19</sup> results are from experiments using with 300 ppb propene, a HC/NO<sub>x</sub> = 9 – 10.3 with initial limonene concentration of 89.2 – 95 ppb and HC/NO<sub>x</sub> = 6.9 – 15.1 with initial  $\alpha$ -pinene concentration of 19.5 – 144 ppb. The Griffin et al.<sup>20</sup> results are from the experiments using 250 ppb propene under HC/NO<sub>x</sub> = 2 – 4.6 with initial limonene concentration of 20.6 – 65.1 ppb.....86

**Figure 4.4.** Relationship between the HC/NO<sub>x</sub> ratio and the average refractive index for an experiment. Data are presented as means of  $m_r$ s retrieved over the growth of particles  $\pm$  SD. Black and red cross symbols indicate the  $m_r$ s of  $\alpha$ -pinene and limonene precursors .....87

**Figure 4.5.** Retrieved refractive indices for SOA formed by photooxidation of (a) limonene and (b)  $\alpha$ -pinene at different HC/NO<sub>x</sub> ratios as a function of particle diameter.....88

**Figure 4.6.** Retrieved refractive indices for SOA formed by photooxidation of (a) limonene and (b)  $\alpha$ -pinene at different HC/NO<sub>x</sub> ratios as a function of mass concentration in the chamber.....89

**Figure 4.7.** Maximum number concentration vs. Ozone/HC<sub>i</sub> ratio for limonene (black circle)  $\alpha$ -pinene (blue triangle). Maximum number concentrations appear shortly after the

particles start to nucleate. The ozone concentration corresponding to time at which the maximum number concentration was recorded is used.....90

**Figure 4.8.** Mode of particle as a function of pre-consumed HC concentration for limonene (black circle) and  $\alpha$ -pinene (blue triangle). Pre-consumed HC is the amount of HC consumed before ozone begins to build up and particles begin to nucleate.....91

**Figure 4.9.** Cumulative contribution of 5 different reaction types that generate condensable species at the simulation time corresponding to the end of the experiments from kinetic simulations using the initial  $\text{NO}_x$  and limonene concentrations listed in Table 4.1..... 92

**Figure 4.10.** Predicted refractive indices based on kinetics simulation and QSPR (equation 4.3, see text) for limonene SOA at different at different HC/ $\text{NO}_x$  ratios at 589 nm. The estimated values at 532nm should be somewhat higher, by 0.002 – 0.022; see text.....93

**Figure 5.1.** Temperature profile along the axis of the heating section at a flow rate of 1LPM for three set temperatures.....116

**Figure 5.2.** Schematic drawing of the experimental setup used for SOA volatility, angularscattering and size distribution.....117

**Figure 5.3.** Particle number loss as a function of size within the TD at five different temperatures, as due to diffusion, thermophoresis and sedimentation. NaCl particles were used for the study of number loss because of their non-volatility under all experimental temperatures.....118

**Figure 5.4.** Profile of the  $\alpha$ -pinene photooxidation experiment performed on Aug. 22. (initial  $\alpha$ -pinene, 152 ppb;  $\text{NO}_x$ , 110 ppb. (a) temperature profile of TD (b) Gas phase

concentrations (hydrocarbon, NO, NO<sub>x</sub>, O<sub>3</sub>), aerosol mass concentration and GA determined real refractive index of SOA from chamber and thermodenuder (c) Time evolution of the SOA particle number concentrations, mean diameter of SOA from chamber and thermodenuder and scattering coefficient ( $\beta_{sca}$ ) .....119

**Figure 5.5.** Mass fraction remaining after passing through TD as a function of TD temperature for SOA formed by photooxidation of (a)  $\alpha$ -pinene (b) limonene and (c) toluene at different HC/NO<sub>x</sub> ratios. All data corrected for experimentally determined TD losses (Figure 5.3) .....120

**Figure 5.6.** Mass fraction remaining after passing through TD as a function of TD temperature for SOA formed by ozonolysis of  $\alpha$ -pinene (circles) and limonene (triangles) without (filled symbol) and with (empty symbol) scavenger. All data shown here is corrected for experimentally determined losses in the TD (Figure 5.3) .....121

**Figure 5.7.** Retrieved refractive indices for thermodenuded (empty symbol) and non thermodenuded (filled symbol) SOA formed by photooxidation of toluene at different HC/NO<sub>x</sub> ratios. SOA were thermodenuded at different temperatures from 65 °C to 98 °C.....122

**Figure 5.8.** Retrieved refractive indices for thermodenuded (empty symbol) and non thermodenuded (filled symbol) SOA formed by photooxidation of limonene (upper panel; a-c) and  $\alpha$ -pinene (lower panels; d-f) at different HC/NO<sub>x</sub> ratios. SOA were thermodenuded at different temperatures from 65 °C to 90 °C.....123

**Figure 5.9.** Retrieved refractive indices for thermodenuded (empty symbol) and non thermodenuded (filled symbol) SOA formed by ozonolysis of (a)  $\alpha$ -pinene and (b)



limonene with and without scavenger. SOA were thermodenuded at different temperatures in from 64 °C to 98 °C.....	124
<b>Figure 5.10.</b> Comparisons of refractive indices of SOA formed by photooxidation of (a) limonene and (b) $\alpha$ -pinene from current study with <i>Kim et al.</i> , [2010] .....	125
<b>Figure 6.1.</b> Retrieved refractive indices for SOA formed by (a) photooxidation of limonene and $\alpha$ -pinene at different HC/NO <sub>x</sub> ratios and (b) ozonolysis of $\alpha$ -pinene with and without scavenger as a function of particle diameter.....	144
<b>Figure 6.2.</b> Triangle plot for photooxidation of (a) limonene at different HC/NO <sub>x</sub> ratios and (b) ozonolysis of $\alpha$ -pinene with and without scavenger. Outline of triangle shown in gray line indicate the space where ambient OOA components fall [ <i>Ng et al.</i> , 2010]. Arrows represent the time progression of experiments.....	145
<b>Figure 6.3.</b> Van Krevelen diagram for limonene SOA at different HC/NO <sub>x</sub> ratios and ozonolysis of $\alpha$ -pinene SOA with and without scavenger. Line with slopes with -1 and -2 are represented by black line.....	146
<b>Figure 6.4.</b> Change of $f_{44}$ as a function of organic loading in the chamber over the course of (a) ozonolysis of $\alpha$ -pinene with and without scavenger (b) photooxidation of $\alpha$ -pinene (c) photooxidation of limonene at different HC/NO <sub>x</sub> ratio.....	147
<b>Figure 6.5.</b> Retrieved refractive index of ozonolysis of $\alpha$ -pinene with and without scavenger and photooxidation of $\alpha$ -pinene and limonene at different HC/NO <sub>x</sub> ratio with the variation of (a) O:C (b) H:C (c) $f_{44}$ (d) $f_{43}$ .....	148
<b>Figure 6.6.</b> Retrieved refractive index of limonene at HC/NO <sub>x</sub> =14 with the variation of (a) oxygenated compounds and (b) non-oxygenated compounds.....	149

**Figure 6.7** Retrieved refractive index of limonene at  $HC/NO_x = 33$  with the variation of (a) oxygenated compounds and (b) non-oxygenated compounds.....150

**Figure 6.8.** Retrieved refractive index of limonene at  $HC/NO_x = 6.6$  with the variation of (a) oxygenated compounds and (b) non-oxygenated compounds.....151

**Figure 6.9.** O:C and H:C ratio with retrieved refractive indices for each separate experiments (a,b,c) photochemically generated limonene SOA at different  $HC/NO_x$  ratio, (d) photochemically generated  $\alpha$ -pinene SOA at high  $HC/NO_x$  ratio ( $=31$ ), (e) SOA generated from ozonolysis with scavenger and (f) without scavenger .....152

**Figure 7.1.** Refractive indices of various types of SOA studied in this thesis. Ranges of refractive index for each SOA result from changing chemical composition as the particles are growing or ageing. Dashed lines represent the values for SOA or organic aerosol that assumed by different current models. Black symbols represent literature values of SOA generated using same hydrocarbon and oxidation chemistries denoted in the figure.....165

## LIST OF TABLES

Table 1.1. Refractive index values of SOA.....	19
Table 1.2. Lists of refractive indices of SOA used in the model (Real part) .....	20
Table 2.1. Structure of SOA precursors presented in this thesis.....	36
Table 2.2. Support instrumentation for the chamber.....	37
Table 3.1. Initial conditions, temperatures, relative humidities and results of the photo oxidation experiments.....	52
Table 3.2. Initial conditions, temperatures, relative humidities and results of the ozonolysis experiments.....	53
Table 4.1. Initial conditions, temperatures, relative humidities and results of the experiments.....	80
Table 4.2. Calculated $m_p$ s and $V_p$ of representative compounds expected to condense on limonene SOA .....	81
Table 5.1. Initial conditions, temperatures, relative humidities and results of the ozonolysis experiment.....	114
Table 5.2. Initial conditions, temperatures, relative humidities and results of the photo oxidation experiments.....	115
Table 6.1. Initial conditions, temperatures, relative humidities and results of the experiments.....	143

## ACKNOWLEDGEMENTS

Looking back my past five years at UCLA, I feel blessed every moment along the way. It has been such a wonderful journey, not just because of all the great science in the roof lab, but also the many lessons that I have learned about life, truth and faith. There were sometimes quite tough moments but I could go through all with the supports of many people.

I would like to express my sincere gratitude to my advisors, Prof. Suzanne Paulson for her continuous trust, support, and guidance throughout the years. Her scientific insights are invaluable, and her enthusiasm about science is especially inspiring. I thank her for giving me the opportunity to join the lab. Despite her busy schedules, she was always there when I need guidance. I would also like to thank my thesis committee members, Prof. Kuo-Nan Liou, Prof. Qinbin Li and Prof. Arthur Winer for their valuable time and comments. Their enthusiasm, ideas, suggestions and supports have been encouraging and helpful for me to advance my research.

I would like to thank the past and present group members, Dr. Brian Barkey, Dr. Abert Chung, Leila Lackey, Dr. Ying Wang, Michelle Kuang, Dr. Wonsik Choi. They were always welcome to ask help and gave me useful comments for research and presentations. I am especially grateful to Dr. Brian Barkey for his patience in teaching me and helping me so many things, from development and operation of optical instruments to data analysis and develop several programs. And he was always being there to advise and help me even if he is in different city. I considered myself lucky to have the opportunity to work with him.

I also would like to thank my colleagues and friends in department, Peng, Lunjin, Carmen, Peggy, Catalina, Bokjin, Clare and Justine. They are a constant source of laughter and encouragement; with them even the most stressful periods in the graduate school seem more manageable. Especially I would like to thank Peng and Lunjin helping me to go through all

dynamics and space physics classes. Their patience in teaching me from very basic knowledge to upper level makes me possible to pass all core courses. Very special thanks go to Peng for being such a great friend for my life in UCLA.

I also thank all my friends that I met in church during my graduate school for their help, encouragement and praying for me. I am glad to have met so many spiritual friends outside the lab who made my time here enjoyable. Especially, I thank Pastor Kang and Byun for their spiritual advice.

And I thank my parents, my brother for their love and support. They filled my life with so much happiness, love and hope. I could not have finished this without the unceasing support and encouragement they have given me throughout my life.

## VITA

### Educations and experiences

2000-2004	B.A., Environmental Engineering, Yonsei Universtiy, S.Korea
2002-2003	Education Abroad Program Universtiy of California, Los Angeles
2004-2006	M.A., Environmental Engineering Pohang University of Science and Technology, S. Korea
2006-2007	Researcher Institute of Environment and Energy Technology, S. Korea
2007-present	Graduate Student Researcher Department of Atmospheric and Oceanic Sciences University of California, Los Angeles
2008-2011	Teaching Assistent Department of Atmospheric and Oceanic Sciences University of California, Los Angeles

### Publications

1. **H.Kim**, B.Barkey and S.E. Paulson, Real refractive indices of secondary organic aerosol generated from photooxidation of limonene and  $\alpha$ -pinene: the effect of HC/NO<sub>x</sub> ratio, *J. Phys. Chem. A*, 10.1021/jp301302z.
2. **H.Kim**, B.Barkey and S.E. Paulson, Real refractive indices of alpha-and beta-pinene and Toluene Secondary Organic Aerosols generated from Ozonolysis and Photo-oxidation, *J. Geophys. Res.* **115** (2010) D24212.
3. **H.Kim** and W.Choi, Effect of Surface Fluorination of TiO<sub>2</sub> on Photocatalytic Oxidation of Gaseous Acetaldehyde, *Appl.Catal.B*, **69** (2007) 127
4. Wang, Y. **Kim, H.**, Paulson, S. E. Hydrogen Peroxide Generation from  $\alpha$ -and  $\beta$ - pinene and Toluene Secondary Organic Aerosols. *Atmospheric Environment*, **45** (2011), 3149.
5. B.Barkey, **H.Kim** and S.E. Paulson, Genetic Algorithm Retrieval of Real Refractive Index from Aerosol Distributions that are not Lognormal, *Aerosol Science and Technology*, **44** (2010) 1089.

6. Paulson, S.E., C. Arellanes, Y. Wang, D. Curtis and **H. Kim**, *Particle Phase Peroxides: Concentrations, Sources, and Behavior*, California Air Resources Board Report No. 04-319. 92pp. (2009), <http://www.arb.ca.gov/research/apr/past/04-319.pdf>

#### Presentations

- Aug. 2008*     **H.Kim**, B.Barkey and S.E. Paulson “Measurements of aerosol refractive indices using a polar nephelometer”, **9<sup>th</sup> international conference on carbonaceous particles in atmosphere, Lawrence Berkeley Laboratory, Berkeley, California**
- Mar. 2009*     **H.Kim**, B.Barkey and S.E. Paulson “Optical properties of non-absorbing secondary organic aerosols from various precursor chemistries”, **26<sup>th</sup> informal symposium on Kinetic and Photochemical Processes in the Atmosphere, University of California, Riverside**
- Nov. 2010*     **H.Kim**, B.Barkey and S.E. Paulson “Refractive indices of  $\alpha$ - and  $\beta$ -pinene and Toluene Secondary Organic Aerosols grown from Ozonolysis and Photo-oxidation”, platform presentation, **2010 Air & Waste Management Association, Los Angeles, CA, Nov. 2-4**
- Mar. 2011*     **H.Kim**, B.Barkey and S.E. Paulson “The Effect of NO<sub>x</sub> level on the real Refractive indices of SOA generated from photooxidation of limonene”, **28<sup>th</sup> informal symposium on Kinetic and Photochemical Processes in the Atmosphere, University of California, Irvine**
- Oct. 2011*     **H.Kim**, B.Barkey and S.E. Paulson “The Effect of NO<sub>x</sub> level on the real refractive indices of SOA generated from photooxidation of limonene”, platform presentation, **30<sup>th</sup> American Association for Aerosol Research, Orlando, Florida, Oct. 3-7**
- Dec. 2011*     **H.Kim**, B.Barkey and S.E. Paulson “The Effect of HC/NO<sub>x</sub> ratio on the real refractive indices of SOA generated from photooxidation of  $\alpha$ -pinene limonene”, platform presentation, **30<sup>th</sup> American Geophysical Union Fall meeting, San Francisco, California, Dec. 5-9**
- Feb. 2012*     **H.Kim**, B.Barkey and S.E. Paulson “The Effect of HC/NO<sub>x</sub> ratio on the real refractive indices of SOA generated from photooxidation of  $\alpha$ -pinene limonene”, **29<sup>th</sup> informal symposium on Kinetic and Photochemical Processes in the Atmosphere, Cal State Univerty, Fullerton**

## **Chapter 1**

### **Introduction**



## 1.1 Background

Atmospheric aerosols play an important role in determining the direct radiative transfer by scattering and absorbing solar radiation [*Intergovernmental Panel on Climate Change, 2007*] but the magnitude as well as the sign of the forcing effect is highly uncertain. Wavelength dependent aerosol optical properties, which depend on the size distribution, chemical composition, mixing state and shape combine to determine the aerosol direct effect. Refractive indices are also necessary to determine the parameters relevant to radiative transfer, such as single scatter albedo, asymmetry factor and specific absorption using Mie-Lorenz theory. Sensitivity studies show that 10% decrease in asymmetry factor (the ratio of forward to backward scattered light) would result in a 12-19% reduction in the top of the atmospheric radiation forcing [*Marshall et al., 1995; Andrews et al., 2006*], underscoring the importance of well-constrained optical parameters. Additionally, reliable phase function and polarization information is essential for the interpretation of satellite and aircraft measurements to infer aerosol optical depth, size and single scatter albedo [*Mishchenko, 2007*].

Organic compounds constitute 20 – 70 % of aerosol mass in the lower troposphere depending on space and time [*Zhang et al., 2007; Hallquist et al., 2009*], of which roughly 70 – 90 % is contributed by secondary organic aerosols (SOA) [*Hallquist et al., 2009*]. Their contribution to the global radiation balance depends on their production and loss rates, their interactions with other radiatively important atmospheric constituents, (via the ‘indirect and semi-direct’ effects), and on their direct interactions with solar insolation and upwelling terrestrial infrared radiation. The radiative properties of these ubiquitous SOA particles are poorly understood [*Kanakidou et al., 2005*]. The detailed chemical composition of secondary organic aerosols is still largely unknown. The material is believed to contain hundreds of

different species and thus is not accurately mimicked by bulk materials. Also deriving optical properties from all aerosol (rather than bulk materials) presents a technical challenge that has been met only recently. This is due to the chemical and physical complexity of the organic aerosols as well as the limited number of measurements available.

Recently several methods to measure or estimate of optical properties of secondary organic aerosols (rather than bulk materials) have been developed for field [Zhao, 1999; Dick *et al.*, 2007; Hock *et al.*, 2008; Moffet *et al.*, 2008] and laboratory [Schneider *et al.*, 2005; Dinar *et al.*, 2008; Adler *et al.*, 2010; Barkey *et al.*, 2010; Kim *et al.*, 2010; Lang-Yona *et al.*, 2010; Nakayama *et al.*, 2010; Redmond and Thompson, 2011; Kim *et al.*, 2012] as summarized in Table 1.1

A few studies have attempted to derive refractive indices from ambient aerosols of which SOA is a major component. Dick *et al.*, [2007] measured the refractive indices of aerosols near Smokey Mountain National Park and found real refractive indices of 1.49 for dry and 1.42 for wet aerosol, respectively, with little dependence on size between 0.2 and 0.5  $\mu\text{m}$ . They modeled their observed angular scattering data (between 40° and 140°) using volumetric fractions of the different constituents measured on filters, and known or estimated refractive indices for the components. The best fit was obtained when the refractive index of the OC component was adjusted to 1.46. By inverting optical counter data, Hock *et al.* [2008] measured rural aerosol with a ratio of highly oxidized aerosol to hydrocarbon-like organic aerosol of 4:1 and found 1.40 - 1.45. Moffet *et al.* [2008] estimated optical properties of ambient aerosols from size-dependent scattering as a function of chemical composition using an aerosol time-of-flight mass spectrometer. Most of their results are for mixed aerosols, however they did report a value for  $m_r$

of  $1.53 \pm 0.04$  for a class of spherical particles from Mexico City classified as high mass organic carbon.

Most laboratory studies have addressed materials other than organics, but some have investigated organic materials similar to components in SOA. In the review of SOA related materials, *Kanakidou et al.*, [2005] found a range of refractive indices of about 1.37 – 1.63 for the real part at 430- 670 nm with minimal absorption at wavelengths above 400 nm.

A tiny handful of experimental investigations have begun to derive refractive indices from secondary organic aerosols in the laboratory. *Schnaiter et al.*, [2005] estimated a refractive index of roughly 1.5 for  $\alpha$ -pinene- $O_3$  SOA by fitting Mie-Lorenz calculations to scattering and absorption measurements at 3 wavelengths. Using a polar nephelometer, *Barkey et al.*, [2007] retrieved a refractive index of 1.42 for SOA formed by  $\alpha$ -pinene reacting in the presence of  $NO_x$ . *Lang-Yona et al.*, [2010] retrieved refractive indices of SOA generated from Holm Oak emissions (mostly terpenes), by measuring extinction coefficients as a function of particle size using cavity ring down at 532 nm. The biogenic hydrocarbons were oxidized in a chamber using  $O_3$  and OH at very low  $NO_x$  levels, and the resulting SOA had a  $m_r$  of  $1.53 \pm (0.06 - 0.08)$ . *Nakayama et al.*, [2010] estimated the wavelength-dependent real refractive indices of toluene and  $\alpha$ -pinene SOA in the presence of  $NO_x$  or  $O_3$  by fitting Mie-Lorenz calculations to scattering and absorption measured by cavity ring down at 355 and 532 nm, and found values ranging from 1.46 to 1.63 depending on the precursor and wavelength. Very recently, *Redmond and Thompson*, [2011] estimated the refractive indices of  $\alpha$ -pinene- $O_3$  and toluene SOA by fitting Mie-Lorenz calculations to scattering and extinction measured using an “albedometer” (an instrument that measures both extinction and scattering in the same volume using cavity ring down spectroscopy) at 532 nm and found values of 1.49 – 1.51 and 1.49 – 1.50, respectively.

They also predicted the  $m_{r,s}$  as 1.476 and 1.483 for  $\alpha$ -pinene and toluene SOA using a quantitative structure-property relationship (QSPR) model applied to primary reaction products expected to partition into the aerosol phase. *Kim et al.*, [2010] retrieved real refractive indices from 1.38 and 1.62 at 670 nm for SOA generated from  $\alpha$ -pinene,  $\beta$ -pinene and toluene under a wide range of conditions, including aerosol mass concentration, oxidation chemistry, temperature and aerosol aging.

These studies on optical properties of SOA have been performed on particles generated in environmental chambers or flow tube (see e.g. references in [*Hallquist et al.*, 2009; *Kim et al.*, 2012]), often at unrealistically high aerosol mass concentrations. We note that smaller particles (e.g.  $< \sim 200$  nm) do not scatter much light, which presents measurement challenges and in some cases requires high mass concentrations. Very recently, *Kim et al.*, [2012] showed that refractive index ranges from 1.34 to 1.56 for limonene and from 1.36 to 1.52 for  $\alpha$ -pinene at 532 nm within the atmospherically relevant aerosol mass concentration and temperature ranges as possible. And it was found that refractive index generally decreases as the HC/NO<sub>x</sub> ratio increases between 6.3-8.1 and 33 ppbC/ppb, combined by several other factors including temperature and initial HC concentration.

Absorption at wavelengths above 500 nm was measured to be very small, or zero for biogenic SOA [*Lang-Yona et al.*, 2010; *Redmond and Thompson*, 2011; *Zhong and Jang*, 2011; *Nakayama et al.*, 2010]. *Kim et al.*, [2012] also showed that there is no evidence of significant absorption at 532 and 670 nm for the particles generated from  $\alpha$ -pinene and limonene, showing GA retrievals (which can provide only a rough estimate of absorption) return imaginary components of order  $10^{-5}$ , and particles are colorless when collected on filters.

However, there have been several evidences of absorption of SOA at short wave length [Jacobson, 1999; Jaoui *et al.*, 2008; Bones *et al.*, 2010; Chang and Thompson, 2010; Laskin *et al.*, 2010]. Jacobson, [1999] investigated the possible importance of the near-UV light absorption by nitrated and aromatic aerosol components on reductions in downward solar irradiance in Los Angeles. Recently, some studies measured absorption coefficient at near-UV light. Zhong and Jang, [2011] reported a small absorption coefficient of  $0.038 \text{ m}^2/\text{g}$  at 350 nm for limonene SOA generated by photooxidation ( $\text{HC}/\text{NO}_x = 30$ ). Nakayama *et al.*, [2010] measured absorption coefficient of SOA generated from toluene SOA at 355nm as  $0.3 - 3 \text{ m}^2/\text{g}$  using cavity ring down method. These evidences showed that further studies on the measurement of absorption of secondary organic aerosols is necessary for better radiative transfer model and preliminary study on this is described in Appendix A.

## 1.2 Motivation and Scientific Objectives

Previously reported refractive index values are generally in good agreement within relatively large measurement uncertainties. Because the set of SOA measurements is small and indicates a reasonably wide range of refractive indices among SOA, it is not yet clear what values are most representative of ambient aerosols. This has implications for the understanding and representation of the optical properties of SOA derived from different sources (biogenic vs. anthropogenic, different oxidation chemistry) and evolution of these properties as organic particles age in the atmosphere. It is necessary to have a framework wherein the optical properties of organic aerosol can be explained depending on different sources and how they may be altered by in situ chemical processing. The variability in atmospheric organic aerosol sources and composition [Ng *et al.*, 2010] suggest that there may not be a single, well defined refractive

index that can be used to characterize SOA; nonetheless, this is the approach currently taken by most models as shown at Table 1.2 [Kinne *et al.*, 2003; Zaveri *et al.*, 2010; Pere *et al.*, 2011].

The sensitivity studies of refractive index and related asymmetry parameter [Kim *et al.*, 2010] indicate that a single value for SOA refractive index will not be sufficient to accurately estimate radiative transfer [Marshall *et al.*, 1995; Andrews *et al.*, 2006]. For instance, the asymmetry parameter  $\langle g \rangle$ , a key parameter in radiative transfer calculations, is defined as:

$$\langle g \rangle = \int_{\theta} P(\theta) \cos(\theta) \sin(\theta) d\theta \quad (1.1)$$

where the integration is over the scattering angle,  $\theta$ . The azimuthal component of the solid angle ( $\Omega$ ) integration is constant when random particle orientation is assumed [Van de Hulst, 1957]. The non-dimensional scattering phase function  $P(\Omega)$  describes the average light intensity scattering properties of the particle distribution and is normalized via:

$$1 = \frac{1}{4\pi} \int_{\Omega} P(\Omega) d\Omega = \frac{1}{2} \int_{\theta} P(\theta) \sin(\theta) d\theta. \quad (1.2)$$

$\langle g \rangle$  describes the amount of light scattered by the particles into the forward or reverse hemispheres.  $\langle g \rangle = 1$  for full forward scattering,  $-1$  for scattering into the reverse hemisphere and  $0$  for isotropic scattering. Generally,  $\langle g \rangle$  decreases as  $m_r$  increases for distributions associated with aerosols. Using the Mie-Lorenz scattering theory, wavelength = 670 nm and  $m_r = 1.4$ ,  $\langle g \rangle = 0.744$  for a lognormal distribution with  $E(x) = 200$  nm and a standard deviation of 200. Changing the  $m_r$  to 1.5 produces  $\langle g \rangle = 0.677$ . This change can produce an increase in the negative radiative forcing by at least 12% for non-absorbing particles [Marshall *et al.*, 1995].

The range and representative value of refractive indices for different types of SOA needs to be elucidated so that the research community can accurately include it into models to reduce uncertainties in the direct effects of aerosols. One of the important factors to control the

refractive indices of SOA is the chemical compositions of particles and in order to verify how different chemical compositions are reflected to the SOA refractive index, a large set of different types of SOA are generated controlling,

- Parent hydrocarbon
- Oxidation chemistry
- In-particle, heterogeneous reactions
- Temperature
- Mass concentration and size

to have different chemical composition of SOA [George and Abbatt, 2007; Kroll and Seinfeld, 2008; Shilling *et al.*, 2009; Warren *et al.*, 2009; Qi *et al.*, 2010; Salo *et al.*, 2012].

The aim of my PhD research is to estimate a large set of direct optical property for different types of SOA, controlling the chemical compositions under atmospheric relevant conditions as possible. This study will help understand controlling factors of variations of refractive index as well as reduce the uncertainties in the direct effects of SOA, providing improved data to research community for the calculation of direct forcing accurately.

### **1.3 Organization of thesis**

In Chapter 2, detailed experimental, instrumentation and data analysis methods are discussed. In order to study the properties of atmospheric aerosols, specifically their optical properties, an outdoor chamber was used to generate large quantities of controlled but realistic aerosols. In addition, a polar nephelometer (PN) has been developed for aerosol scattering measurements. The PN can measure the light scattered into a two dimensional plane by a stream of aerosols that intersect a 670 nm or 532 nm laser beam. Refractive indices of aerosols generated in the chamber can be retrieved from the resulting angular scattering data and measured particle size

distributions using a Genetic Algorithm (GA) method with Mie-Lorenz scattering theory. The PN measurement is arranged by a suite of other measurements of scattering and absorption coefficient, size distribution and chemical composition.

In Chapter 3, the refractive indices of SOA particles generated from  $\alpha$ - and  $\beta$ -pinene and toluene using several different oxidation chemistries is investigated, in an effort to probe the importance of several different oxidation chemistries and other different factors on SOA refractive indices. For dark ozone reactions of unsaturated hydrocarbons, reactions can be initiated either solely by  $O_3$  or by  $O_3$  together with OH. For VOC/ $NO_x$  photochemistry, at “high” VOC/ $NO_x$  ratios, organic peroxy radicals ( $RO_2$ ) react with  $RO_2$  or  $HO_2$  to produce lower volatility products than the  $RO_2 + NO$  reactions that dominate under “low” VOC/ $NO_x$  conditions [Presto *et al.*, 2005; Ng *et al.*, 2007]. Retrieved refractive indices for the SOA vary between 1.38 and 1.62, depending on several factors including aerosol mass concentration, oxidation chemistry, temperature and aerosol aging. For  $\alpha$ - and  $\beta$ -pinene ozonolysis, SOA  $m_r$ s ranges from 1.4 to 1.5, and within the resolution of our method and bounds of our experiments, are not affected by the addition of an OH scavenger, and are only slightly dependent on the aerosol mass concentration. For photochemically generated SOA,  $m_r$  generally increases as experiments progress, ranging from about 1.4 to 1.53 for  $\alpha$ -pinene, 1.38 to 1.53 for  $\beta$ -pinene, and 1.4 to 1.62 for toluene. The pinene SOA  $m_r$ s decrease somewhat toward the end of the experiments. Aspects of the data suggest aerosol mass concentration, oxidation chemistry, temperature and aerosol aging may all influence the refractive index. Chapter 3 provides the foundation for building up our understanding for the ranges SOA refractive indices in the subsequent chapters.

In Chapter 4, SOA generated at mass concentrations in the ambient range, 5 – 18 times lower mass concentration than the mass concentration used in Chapter 3 is investigated. Lower



mass concentration were made possible by upgrading the PN laser to a 1W 532 nm model. This provides data near the peak of the solar spectrum as well as greatly increasing sensitivity.

SOA was generated from limonene and  $\alpha$ -pinene with different HC/NO<sub>x</sub> ratios. For limonene SOA, the data suggests the most important factor controlling the refractive index is the HC/NO<sub>x</sub> ratio. However the refractive index is much less sensitive to the aerosol age or mass concentration than it appeared to be in the earlier study (Chapter 3). The refractive index ranges from about 1.34 to 1.56 for limonene and from 1.36 to 1.52 for  $\alpha$ -pinene, and generally decreasing as the HC/NO<sub>x</sub> ratio increased. Especially for limonene under summer condition, particle diameter is also inversely related to the HC/NO<sub>x</sub> ratio; the final size mode increases from 220 to 330 nm as the HC/NO<sub>x</sub> ratio decreases from 33 – 6. The results here are the first to explore the changing refractive index as particles grow, especially for mass concentrations that are relevant to the atmosphere, the first to report a refractive index for limonene SOA, and the first to investigate the influence of HC/NO<sub>x</sub> ratio on this important optical parameter. Further, in an effort to explore the ability of models from the literature to explain the observed refractive indices, a recent limonene oxidation mechanism was combined with SOA partitioning and a structure-property relationship for estimating refractive indices of condensing species. A detailed description of kinetic simulation model, gas-aerosol partitioning, estimation of vapor pressure and examples for characterization of dominant condensing species are provided at Appendix B. The resulting refractive indices fell in a much narrower range ( $1.475 \pm 0.02$ ) of  $m_r$ s than observed experimentally. We hypothesize the experimentally observed high  $m_r$  values are due to oligomerization and the low values to water uptake, small soluble molecules such as glyoxal and other factors, each of which is not included in the oxidation mechanism.

In the result discussed in Chapter 5, a thermodenuder (TD) was used to examine the relationship between SOA volatility and refractive index. Optical measurements in previous Chapter 3, 4 and currently available studies have been performed on particles generated in environmental chambers or flow tubes (see e.g. references in [Hallquist *et al.*, 2009]), often at unrealistically high aerosol mass concentrations. Recently, some experiments showed that SOA at low mass loading ( $< 20 \mu\text{g}/\text{m}^3$ ) tends to be less volatile and more oxygenated than high mass loading by the measurements of average oxygen to carbon (O:C), hydrogen to carbon (H:C) atomic ratios and the fraction of oxygenated organic materials ( $f_{44}$ ) using aerosol mass spectrometer [Bahreini *et al.*, 2005; Shilling *et al.*, 2009]. Very recently Gao *et al.*, [2010] investigated the detailed molecular information with a mass loading as low as  $3.5 \mu\text{g}/\text{m}^3$  using liquid chromatography mass spectrometry and high-resolution fourier transform ion cyclotron resonance mass spectrometry techniques employed with electrospray ionization (ESI). Common products with high mass loadings of chamber experiment were identified, but the relative intensities changed; a species with the oligomer formula  $\text{C}_{17}\text{H}_{26}\text{O}_8$  increased substantially in intensity relative to other products as the mass loading decreased. These discrepancies between different mass loadings are because partitioning to the particle phase depends on the mass loading where the compounds can condense. As the mass loading increases, compounds of higher vapor pressure that tend not to partition to the particle phase under low mass loadings do so at the higher mass loadings.

We note that smaller particles (e.g.  $< \sim 200 \text{ nm}$ ) do not scatter light efficiently, which presents measurement challenges for many measurements and in some cases requires high mass concentrations. Thus chamber generated SOA contain species with a wide range of volatilities, while low volatile species are dominant in ambient aerosols. Thus, laboratory generated SOA is

less relevant with the atmospheric SOA [Bahreini *et al.*, 2005; Zhang *et al.*, 2005; Alfarra *et al.*, 2006; Ng *et al.*, 2010; Chhabra *et al.*, 2011]. The thermodenuder (TD) is a tool that can be used to help unravel some aspects of volatility, and it has been applied in a number of recent laboratory and field studies. [Burtscher *et al.*, 2001; Wehner *et al.*, 2002; Johnson *et al.*, 2005; An *et al.*, 2007; Huffman *et al.*, 2009; Kostenidou *et al.*, 2009; Lee *et al.*, 2010; Cappa and Wilson, 2011; Lee *et al.*, 2011].

With an in-house developed thermodenuder using the design described by Lee *et al.*, [2011], we evaporate the high volatility components from the SOA generated in the smog chamber and retrieve the refractive indices of SOA. Also the temperature dependence of volatility is explored. Mostly two or three different temperature steps were carried out between 60 – 110 °C in which, almost all biogenic SOA volume is evaporated and somewhat similar chemical composition to ambient oxygenated organic aerosol was obtained [Kostenidou *et al.*, 2009; Lee *et al.*, 2011].

We investigated SOA generated from limonene,  $\alpha$ -pinene and toluene using the different oxidation chemistries described above. Toluene SOA was not affected by heating. Generally, as biogenic SOA are heated, particle diameters decrease and the  $m_{r,s}$  return to the values observed for the corresponding size particle observed earlier in the experiments before heating. However, there were a few exceptions; 1) for  $\alpha$ -pinene SOA from ozonolysis with OH radical scavenger, after heating,  $m_{r,s}$  increase from 1.48-1.5 (before heating) to 1.49-1.55 (after heating) 2) For photochemical SOA from  $\alpha$ -pinene and limonene under low  $\text{NO}_x$  conditions, after heating,  $m_{r,s}$  slightly decrease by about 0.08 for 300 nm particles and about 0.04 for 200nm particles. For limonene, heating 240-270 nm particles resulted in decrease  $m_r$  of about 0.07. After thermodenuding, biogenic SOA refractive indices still fall in a range between 1.39-1.55.

In Chapter 6, we present measurements that directly address the relationship between elemental composition and refractive index for SOA generated from limonene and  $\alpha$ -pinene using several different oxidation chemistries. Particle chemical composition was monitored with a high-resolution time-of-flight aerosol mass spectrometer (HR-ToF-AMS). AMS can quantify total organic aerosol (OA) as well as specific OA components such as  $m/z$  43 ( $C_2H_3O^+$ ,  $C_3H_7^+$ ),  $m/z$  44 ( $CO_2^+$ ), indicator of semi-volatile and low-volatile material, respectively. For photochemically generated SOA, the refractive index ranges from about 1.34 to 1.55 for limonene and from 1.44 to 1.47 for  $\alpha$ -pinene, generally increasing with diameter. Combining with chemical composition measurements, limonene SOA shows more variations in fraction of  $m/z$  43 to the total organic signal ( $f_{43}$ ) and H:C than  $\alpha$ -pinene SOA.  $\alpha$ -Pinene SOA generated from ozonolysis also shows a narrow range of  $m_p/s$  1.43-1.45 (19-22 °C) and 1.46-1.53 (23-29 °C) with small changes of  $f_{43}$  and H:C ratio. H:C ratio appears to be the best correlation with refractive index showing that  $m_p/s$  increase with H:C due to condensation of semivolatile species [Shilling *et al.*, 2009]. However, from some points, at high H:C, refractive index starts to decrease and that suggests H:C ratio is not the only factor to control the refractive index of SOA. These investigations provide results for the first time, the relationship between refractive index and chemical composition of SOA. Also, by presenting chemical composition data in the  $f_{43}$  vs.  $f_{44}$  space (triangle plot), where  $f_{43}$  and  $f_{44}$  are the ratios of the  $m/z$  43 ( $C_2H_3O^+$ ,  $C_3H_7^+$ ),  $m/z$  44 ( $CO_2^+$ ) to the total organic signal in AMS spectra, it showed that chamber generated particles are less oxidized than ambient aerosols but in narrower range of  $f_{44}$  (0.13-0.26) and  $f_{43}$  (0.13-0.26) than ambient aerosols in the Northern hemisphere falling into a triangle plot with a range of  $f_{44}$  (0.01- 0.3) and  $f_{43}$  (0.02 - 0.17). This suggests that there would possibly be more variations of  $m_p/s$  of ambient aerosols.

Finally, Chapter 7 summarizes the findings presented in the previous six chapters and highlights the atmospheric implications of this work. In addition, from the work demonstrated in Chapters 3–6, it is concluded that the value of refractive indices for SOA appear to be much more variable than expected as 1.34-1.62. There is more work to be done before recommendations can be made for atmospheric applications, however, in that current approach to estimate the radiative transfer depends on single value of refractive index, this thesis clearly highlights a single value for SOA refractive index will not be sufficient to accurately model radiative transfer.

#### 1.4 References

- Adler, G., A. A. Riziq, C. Erlick, and Y. Rudich (2010), Effect of intrinsic organic carbon on the optical properties of fresh diesel soot, *Proceedings of the National Academy of Sciences of the United States of America*, 107(15), 6699-6704.
- Alfarra, M. R., D. Paulsen, M. Gysel, A. A. Garforth, J. Dommen, A. S. H. Prevot, D. R. Worsnop, U. Baltensperger, and H. Coe (2006), A mass spectrometric study of secondary organic aerosols formed from the photooxidation of anthropogenic and biogenic precursors in a reaction chamber, *Atmospheric Chemistry and Physics*, 6, 5279-5293.
- An, W. J., R. K. Pathak, B. H. Lee, and S. N. Pandis (2007), Aerosol volatility measurement using an improved thermodenuder: Application to secondary organic aerosol, *Journal of Aerosol Science*, 38(3), 305-314.
- Andrews, E., P. J. Sheridan, M. Fiebig, A. McComiskey, J. A. Ogren, P. Arnott, D. Covert, R. Elleman, R. Gasparini, D. Collins, H. Jonsson, B. Schmid, and J. Wang (2006), `Comparison of methods for deriving aerosol asymmetry parameter, *Journal of Geophysical Research-Atmospheres*, 111(D5).
- Bahreini, R., M. D. Keywood, N. L. Ng, V. Varutbangkul, S. Gao, R. C. Flagan, J. H. Seinfeld, D. R. Worsnop, and J. L. Jimenez (2005), Measurements of secondary organic aerosol from oxidation of cycloalkenes, terpenes, and m-xylene using an Aerodyne aerosol mass spectrometer, *Environmental Science & Technology*, 39(15), 5674-5688.
- Barkey, B., S. E. Paulson, and A. Chung (2007), Genetic algorithm inversion of dual polarization polar nephelometer data to determine aerosol refractive index, *Aerosol Science and Technology*, 41(8), 751-760.
- Barkey, B., H. Kim, and S. E. Paulson (2010), Genetic Algorithm Retrieval of Real Refractive Index from Aerosol Distributions That Are Not Lognormal, *Aerosol Science and Technology*, 44(12 ), 1089–1095.
- Bones, D. L., D. K. Henricksen, S. A. Mang, M. Gonsior, A. P. Bateman, T. B. Nguyen, W. J. Cooper, and S. A. Nizkorodov (2010), Appearance of strong absorbers and fluorophores in limonene-O(3) secondary organic aerosol due to NH(4)(+)-mediated chemical aging over long time scales, *Journal of Geophysical Research-Atmospheres*, 115.

- Burtscher, H., U. Baltensperger, N. Bukowiecki, P. Cohn, C. Huglin, M. Mohr, U. Matter, S. Nyeki, V. Schmatloch, N. Streit, and E. Weingartner (2001), Separation of volatile and non-volatile aerosol fractions by thermodesorption: instrumental development and applications, *Journal of Aerosol Science*, 32(4), 427-442.
- Cappa, C. D., and K. R. Wilson (2011), Evolution of organic aerosol mass spectra upon heating: implications for OA phase and partitioning behavior, *Atmospheric Chemistry and Physics*, 11(5), 1895-1911.
- Chang, J. L., and J. E. Thompson (2010), Characterization of colored products formed during irradiation of aqueous solutions containing H<sub>2</sub>O<sub>2</sub> and phenolic compounds, *Atmospheric Environment*, 44(4), 541-551.
- Chhabra, P. S., N. L. Ng, M. R. Canagaratna, A. L. Corrigan, L. M. Russell, D. R. Worsnop, R. C. Flagan, and J. H. Seinfeld (2011), Elemental composition and oxidation of chamber organic aerosol, *Atmospheric Chemistry and Physics*, 11(17), 8827-8845.
- Dick, W. D., P. J. Ziemann, and P. H. McMurry (2007), Multiangle light-scattering measurements of refractive index of submicron atmospheric particles, *Aerosol Science and Technology*, 41(5), 549-569.
- Dinar, E., A. A. Riziq, C. Spindler, C. Erlick, G. Kiss, and Y. Rudich (2008), The complex refractive index of atmospheric and model humic-like substances (HULIS) retrieved by a cavity ring down aerosol spectrometer (CRD-AS), *Faraday Discussions*, 137, 279-295.
- Gao, Y. Q., W. A. Hall, and M. V. Johnston (2010), Molecular Composition of Monoterpene Secondary Organic Aerosol at Low Mass Loading, *Environmental Science & Technology*, 44(20), 7897-7902.
- George, I. J., and J. P. D. Abbatt (2007), Chemical evolution of secondary organic aerosol from OH-initiated heterogeneous oxidation, *Atmospheric Chemistry and Physics*, 10(12), 5551-5563.
- Hallquist, M., J. C. Wenger, U. Baltensperger, Y. Rudich, D. Simpson, M. Claeys, J. Dommen, N. M. Donahue, C. George, A. H. Goldstein, J. F. Hamilton, H. Herrmann, T. Hoffmann, Y. Iinuma, M. Jang, M. E. Jenkin, J. L. Jimenez, A. Kiendler-Scharr, W. Maenhaut, G. McFiggans, T. F. Mentel, A. Monod, A. S. H. Prevot, J. H. Seinfeld, J. D. Surratt, R. Szmigielski, and J. Wildt (2009), The formation, properties and impact of secondary organic aerosol: current and emerging issues, *Atmospheric Chemistry and Physics*, 9(14), 5155-5236.
- Hock, N., J. Schneider, S. Borrmann, A. Rompp, G. Moortgat, T. Franze, C. Schauer, U. Poschl, C. Plass-Dulmer, and H. Berresheim (2008), Rural continental aerosol properties and processes observed during the Hohenpeissenberg Aerosol Characterization Experiment (HAZE2002), *Atmospheric Chemistry and Physics*, 8(3), 603-623.
- Huffman, J. A., K. S. Docherty, C. Mohr, M. J. Cubison, I. M. Ulbrich, P. J. Ziemann, T. B. Onasch, and J. L. Jimenez (2009), Chemically-Resolved Volatility Measurements of Organic Aerosol from Different Sources, *Environmental Science & Technology*, 43(14), 5351-5357.
- Jacobson, M. Z. (1999), Isolating nitrated and aromatic aerosols and nitrated aromatic gases as sources of ultraviolet light absorption, *Journal of Geophysical Research-Atmospheres*, 104(D3), 3527-3542.
- Jaoui, M., E. O. Edney, T. E. Kleindienst, M. Lewandowski, J. H. Offenberg, J. D. Surratt, and J. H. Seinfeld (2008), Formation of secondary organic aerosol from irradiated alpha-pinene/toluene/NO(x) mixtures and the effect of isoprene and sulfur dioxide, *Journal of Geophysical Research-Atmospheres*, 113(D9).

- Johnson, D., M. E. Jenkin, K. Wirtz, and M. Martin-Reviejo (2005), Simulating the formation of secondary organic aerosol from the photooxidation of aromatic hydrocarbons, *Environmental Chemistry*, 2(1), 35-48.
- Kanakidou, M., J. H. Seinfeld, S. N. Pandis, I. Barnes, F. J. Dentener, M. C. Facchini, R. Van Dingenen, B. Ervens, A. Nenes, C. J. Nielsen, E. Swietlicki, J. P. Putaud, Y. Balkanski, S. Fuzzi, J. Horth, G. K. Moortgat, R. Winterhalter, C. E. L. Myhre, K. Tsigaridis, E. Vignati, E. G. Stephanou, and J. Wilson (2005), Organic aerosol and global climate modelling: a review, *Atmospheric Chemistry and Physics*, 5, 1053-1123.
- Kim, H., B. Barkey, and S. E. Paulson (2010), Real refractive indices of alpha- and beta-pinene and toluene secondary organic aerosols generated from ozonolysis and photo-oxidation, *Journal of Geophysical Research-Atmospheres*, 115, 10.
- Kim, H., B. Barkey, and S. E. Paulson (2012), Real refractive indices and formation yields of secondary organic aerosol generated from photooxidation of limonene and  $\alpha$ -pinene: the effect of the HC/NO<sub>x</sub> Ratio, *The Journal of Physical Chemistry A*, *accepted*.
- Kinne, S., U. Lohmann, J. Feichter, M. Schulz, C. Timmreck, S. Ghan, R. Easter, M. Chin, P. Ginoux, T. Takemura, I. Tegen, D. Koch, M. Herzog, J. Penner, G. Pitari, B. Holben, T. Eck, A. Smirnov, O. Dubovik, I. Slutsker, D. Tanre, O. Torres, M. Mishchenko, I. Geogdzhayev, D. A. Chu, and Y. Kaufman (2003), Monthly averages of aerosol properties: a global comparison among models, satellite data, and AERONET ground data, *Journal of Geophysical Research*, 108(D20).
- Kostenidou, E., B. H. Lee, G. J. Engelhart, J. R. Pierce, and S. N. Pandis (2009), Mass Spectra Deconvolution of Low, Medium, and High Volatility Biogenic Secondary Organic Aerosol, *Environmental Science & Technology*, 43(13), 4884-4889.
- Kroll, J. H., and J. H. Seinfeld (2008), Chemistry of secondary organic aerosol: Formation and evolution of low-volatility organics in the atmosphere, *Atmospheric Environment*, 42(16), 3593-3624.
- Lang-Yona, N., Y. Rudich, T. F. Mentel, A. Buchholz, A. Kiendler-Scharr, E. Kleist, C. Spindler, R. Tillmann, and J. Wildt (2010), The chemical and microphysical properties of secondary organic aerosols from Holm Oak emissions, *Atmos. Chem. Phys.*, 10(2), 4753-4788.
- Laskin, J., A. Laskin, P. J. Roach, G. W. Slysz, G. A. Anderson, S. A. Nizkorodov, D. L. Bones, and L. Q. Nguyen (2010), High-Resolution Desorption Electrospray Ionization Mass Spectrometry for Chemical Characterization of Organic Aerosols, *Analytical Chemistry*, 82(5), 2048-2058.
- Lee, B. H., E. Kostenidou, L. Hildebrandt, I. Riipinen, G. J. Engelhart, C. Mohr, P. F. DeCarlo, N. Mihalopoulos, A. S. H. Prevot, U. Baltensperger, and S. N. Pandis (2010), Measurement of the ambient organic aerosol volatility distribution: application during the Finokalia Aerosol Measurement Experiment (FAME-2008), *Atmospheric Chemistry and Physics*, 10(24), 12149-12160.
- Lee, B. H., J. R. Pierce, G. J. Engelhart, and S. N. Pandis (2011), Volatility of secondary organic aerosol from the ozonolysis of monoterpenes, *Atmospheric Environment*, 45(14), 2443-2452.
- Marshall, S. F., D. S. Covert, and R. J. Charlson (1995), Relationship between asymmetry parameter and hemispheric backscatter ratio - implications for climate forcing by aerosols, *Applied Optics*, 34(27), 6306-6311.
- Mishchenko, M. I., B. Cairns, G. Kopp, C.F. Schueler, B.A. Fafaul, J.E. Hansen, R.J. Hooker, T. Itchkawich, H.B. Maring, and L.D. Travis (2007), Accurate Monitoring of Terrestrial

- Aerosols and Total Solar Irradiance: Introducing the Glory Mission, *Bull. Amer. Meteor. Soc.*, 88, 677-691.
- Moffet, R. C., X. Y. Qin, T. Rebotier, H. Furutani, and K. A. Prather (2008), Chemically segregated optical and microphysical properties of ambient aerosols measured in a single-particle mass spectrometer, *Journal of Geophysical Research-Atmospheres*, 113(D12), 11.
- Nakayama, T., Y. Matsumi, K. Sato, T. Imamura, A. Yamazaki, and A. Uchiyama (2010), Laboratory studies on optical properties of secondary organic aerosols generated during the photooxidation of toluene and the ozonolysis of alpha-pinene, *Journal of Geophysical Research-Atmospheres*, 115, 11.
- Ng, N. L., J. H. Kroll, A. W. H. Chan, P. S. Chhabra, R. C. Flagan, and J. H. Seinfeld (2007), Secondary organic aerosol formation from m-xylene, toluene, and benzene, *Atmospheric Chemistry and Physics*, 7(14), 3909-3922.
- Ng, N. L., M. R. Canagaratna, Q. Zhang, J. L. Jimenez, J. Tian, I. M. Ulbrich, J. H. Kroll, K. S. Docherty, P. S. Chhabra, R. Bahreini, S. M. Murphy, J. H. Seinfeld, L. Hildebrandt, N. M. Donahue, P. F. DeCarlo, V. A. Lanz, A. S. H. Prevot, E. Dinar, Y. Rudich, and D. R. Worsnop (2010), Organic aerosol components observed in Northern Hemispheric datasets from Aerosol Mass Spectrometry, *Atmospheric Chemistry and Physics*, 10(10), 4625-4641.
- Pere, J. C., M. Mallet, V. Pont, and B. Bessagnet (2011), Impact of aerosol direct radiative forcing on the radiative budget, surface heat fluxes, and atmospheric dynamics during the heat wave of summer 2003 over western Europe: A modeling study, *Journal of Geophysical Research-Atmospheres*, 116.
- Presto, A. A., K. E. H. Hartz, and N. M. Donahue (2005), Secondary organic aerosol production from terpene ozonolysis. 2. Effect of NO<sub>x</sub> concentration, *Environmental Science & Technology*, 39(18), 7046-7054.
- Qi, L., S. Nakao, P. Tang, and D. R. Cocker (2010), Temperature effect on physical and chemical properties of secondary organic aerosol from m-xylene photooxidation, *Atmospheric Chemistry and Physics*, 10(8), 3847-3854.
- Redmond, H., and J. E. Thompson (2011), Evaluation of a quantitative structure-property relationship (QSPR) for predicting mid-visible refractive index of secondary organic aerosol (SOA), *Phys. Chem. Chem. Phys.*, 13(15), 6872-6882.
- Salo, K., M. Hallquist, A. M. Jonsson, H. Saathoff, K. H. Naumann, C. Spindler, R. Tillmann, H. Fuchs, B. Bohn, F. Rubach, T. F. Mentel, L. Muller, M. Reinnig, T. Hoffmann, and N. M. Donahue (2012), Volatility of secondary organic aerosol during OH radical induced ageing, *Atmospheric Chemistry and Physics*, 11(21), 11055-11067.
- Schnaiter, M., C. Linke, O. Mohler, K. H. Naumann, H. Saathoff, R. Wagner, U. Schurath, and B. Wehner (2005), Absorption amplification of black carbon internally mixed with secondary organic aerosol, *Journal of Geophysical Research-Atmospheres*, 110(D19), 11.
- Shilling, J. E., Q. Chen, S. M. King, T. Rosenoern, J. H. Kroll, D. R. Worsnop, P. F. DeCarlo, A. C. Aiken, D. Sueper, J. L. Jimenez, and S. T. Martin (2009), Loading-dependent elemental composition of alpha-pinene SOA particles, *Atmospheric Chemistry and Physics*, 9(3), 771-782.
- Van de Hulst, H. C. (1957), *Light Scattering by Small Particles*, Wiley.
- Warren, B., R. L. Austin, and D. R. Cocker (2009), Temperature dependence of secondary organic aerosol, *Atmospheric Environment*, 43(22-23), 3548-3555.



- Wehner, B., S. Philippin, and A. Wiedensohler (2002), Design and calibration of a thermodenuder with an improved heating unit to measure the size-dependent volatile fraction of aerosol particles, *Journal of Aerosol Science*, 33(7), 1087-1093.
- Zaveri, R. A., J. C. Barnard, R. C. Easter, N. Riemer, and M. West (2010), Particle-resolved simulation of aerosol size, composition, mixing state, and the associated optical and cloud condensation nuclei activation properties in an evolving urban plume, *Journal of Geophysical Research-Atmospheres*, 115.
- Zhang, Q., M. R. Alfarra, D. R. Worsnop, J. D. Allan, H. Coe, M. R. Canagaratna, and J. L. Jimenez (2005), Deconvolution and quantification of hydrocarbon-like and oxygenated organic aerosols based on aerosol mass spectrometry, *Environmental Science & Technology*, 39(13), 4938-4952.
- Zhang, Q., J. L. Jimenez, M. R. Canagaratna, J. D. Allan, H. Coe, I. Ulbrich, M. R. Alfarra, A. Takami, A. M. Middlebrook, Y. L. Sun, K. Dzepina, E. Dunlea, K. Docherty, P. F. DeCarlo, D. Salcedo, T. Onasch, J. T. Jayne, T. Miyoshi, A. Shimono, S. Hatakeyama, N. Takegawa, Y. Kondo, J. Schneider, F. Drewnick, S. Borrmann, S. Weimer, K. Demerjian, P. Williams, K. Bower, R. Bahreini, L. Cottrell, R. J. Griffin, J. Rautiainen, J. Y. Sun, Y. M. Zhang, and D. R. Worsnop (2007), Ubiquity and dominance of oxygenated species in organic aerosols in anthropogenically-influenced Northern Hemisphere midlatitudes, *Geophysical Research Letters*, 34(13), 6.
- Zhao, F. (1999), Determination of the complex index of refraction and size distribution of aerosols from polar nephelometer measurements, *Applied Optics*, 38(12), 2331-2336.
- Zhong, M., and M. Jang (2011), Light absorption coefficient measurement of SOA using a UV-Visible spectrometer connected with an integrating sphere, *Atmospheric Environment*, 45(25), 4263-4271.

Table 1.1. Refractive index values of SOA.

SOA	Refractive index	$\lambda$ (nm)	Reference
$\alpha$ -Pinene/ $\text{NO}_x$	$1.42 \pm 0.02$	670	[ <i>Barkey et al.</i> , 2007]
$\alpha,\beta$ -pinene, Toluene/ $\text{NO}_x$	1.4 -1.6	670	[ <i>Kim et al.</i> , 2010]
$\alpha$ -pinene, Limonene	1.34-1.56	532	[ <i>Kim et al.</i> , 2012]
$\alpha$ -Pinene/Ozone	1.5	450, 550 & 700	[ <i>Schnaiter et al.</i> , 2005]
Photooxidation of VOCs from Holm Oak	$1.53 \pm$ (0.06 – 0.08)	532	[ <i>Lang-Yona et al.</i> , 2010]
$\alpha$ -pinene, Toluene/ $\text{NO}_x$	1.458 – 1.632	355, 532	[ <i>Nakayama et al.</i> , 2010]
$\alpha$ -pinene, Toluene/Ozone	1.49-1.51	532	[ <i>Redmond and Thompson</i> , 2011]

Table 1.2. Lists of refractive indices of SOA used in the model (Real part)

Model	$M_r$ of component at 0.55 $\mu\text{m}$					References
	Dust	OC	BC	SS	sulfate	
<b>ECHAM4/ Max-planck-Inst.</b>	1.5	1.53	1.75	1.5	1.43	
<b>GOCART (Geogia tech., NASA Goddard)</b>	1.5	1.53	1.75	1.5	1.43	
<b>MIRAGE/PNNL</b>	1.5	1.55	1.9	1.5	1.53	
<b>GISS/NASA- GISS</b>	1.56	1.53	1.57	1.45	1.43	[Kinne <i>et al.</i> , 2003]
<b>CCSR/Japan</b>	1.53	1.53	1.75	1.38	1.43	
<b>Grantour/ (U. of Michigan)</b>	1.53	1.53	1.75	1.38	1.43	
<b>ULAQ/Italy</b>	1.56	1.6	2.07	1.5	1.45	
<b>PartMC- MOSAIC</b>			1.45/SOA			[Zaveri <i>et al.</i> , 2010]
<b>CHEMERE</b>			1.45/SOA			[Pere <i>et al.</i> , 2011]

## **Chapter 2**

### **APPROACH; EXPERIMENTAL AND ANALYSIS**

## 2.1 Generation of Representative Aerosols

### 2.1.1 Aerosol Generation chamber

Experiments were performed in a 24 m<sup>3</sup> Teflon chamber constructed on the roof of the Math Sciences Building at UCLA. Solar Teflon chambers provide the most effective platform in which to generate realistic secondary organic aerosols. Outdoor chambers are subject to more temperature variations than enclosed chambers, but they have the advantage of the most realistic light source. With its close proximity to the coast and Mediterranean climate, UCLA has exceptionally optimal weather for chamber work with modest summer daytime highs, combined with 6-7 months each year without any rain. The chamber is also useful for non-photochemical experiments because it provides a convenient method to contain homogeneous samples for multiple analysis methods. New chambers are constructed as needed.

The chamber build on UCLA roof top is described in detail in *Chung et al.*, [2008]. Air is supplied to the chamber by two 33 gallon oil-free portable air compressors (Craftsman) purified with a series of packed bed scrubbers filled with Purafil Triple Blend (Purafil Inc.), activated charcoal, and HEPA capsule filters (Gelman). The scrubbed air has typically < 5, but always < 20 particles cm<sup>-3</sup> and NO<sub>x</sub> (Thermo Electron model 14B/E), O<sub>3</sub> (Dasibi 1001-RS), and organics (GC, HP 5890-II) levels below the 1 ppb detection limits. Access to the inside of the chamber is provided by custom Teflon sampling ports. Teflon (gasses) and copper (particles) sampling lines extend 20 cm into the chamber and pull samples at 0.6 (NO<sub>x</sub>), 2 (O<sub>3</sub> and organics), and 1 (particles) LPM. Between experiments, a vent is opened and the chamber is flushed with clean air for 10 hours in full sun in preparation for the next experiment. Tables in each chapter as well as Tables in Appendix C show initial conditions and summary statistics for all performed experiments.

For photooxidation experiments, initially, the chamber, covered with a black tarpaulin (supported on a frame above the chamber), was half filled with purified air. At this point NO (Scott Specialty Gases) was added. Next, the SOA precursor hydrocarbon liquid was evaporated into the air stream filling the chamber. All hydrocarbons considered in this study are described in Table 2.1. The chamber contents were then allowed to mix for about 40 min. Once the gas chromatograph returned two SOA precursor hydrocarbon measurements within 2% of one another, the tarps were removed and photochemistry initiated. The overall oxidation time was from 4 – 4.5h to 6h depending on the HC/NO<sub>x</sub> ratio and precursors. Typically, high NO<sub>x</sub> conditions (low HC/NO<sub>x</sub> ratio) and aromatic compounds (toluene and phenol) take longer oxidation time.

For ozone experiments, the hydrocarbon of interest and an OH scavenger (cyclohexane) for selected experiments were injected. After the chamber contents were well mixed, excess, ozone was generated by flowing pure oxygen (0.5 L/min) through a mercury lamp O<sub>3</sub> generator (Jelight, model 600) and introduced into the chamber. In order to minimize inhomogeneities, the chamber mixed manually while ozone was injected. Some of experiments performed at 2009, ozone and OH scavenger (cyclohexane) was first injected and then the hydrocarbon of interest was injected mixing manually to minimize inhomogeneities.

SOA is lost to the walls of the chamber during the experiment. Because of wall losses, aerosol populations are not perfectly stable in the chamber; however the losses are modest relative to the sampling times of the instruments so that losses can be accounted for and introduce negligible errors [Cocker *et al.*, 2001]. They do, however preclude allowing particles to age realistically. Size dependent wall loss was determined in a separate experiment using (NH<sub>4</sub>)<sub>2</sub>SO<sub>4</sub> aerosol, generated by nebulizing (Collison spray nebulizer, BGI Inc.) 0.125 % weight

(NH<sub>4</sub>)<sub>2</sub>SO<sub>4</sub> solution. The size dependent first order wall loss rate was estimated from measuring aerosol decay in the chamber over time measured with the SMPS and ranged from 0.0012 min<sup>-1</sup> to 0.0081 min<sup>-1</sup>.

### 2.1.2 Model aerosols

The relative importance of precursors to SOA formation will depend on the precursor concentration in the atmosphere, the volatility of its products and its chemical reactivity. Most organic compounds do not form aerosol under atmospheric conditions due to the high vapor pressure of their products. All alkanes with up to six carbon atoms (from methane to hexane isomers), all alkenes with up to six carbon atoms (from ethane to hexene isomers), benzene and many low-molecular weight carbonyls, chlorinated compounds, and oxygenated solvents form little if any aerosol [Grosjean and Seinfeld, 1989]. It is well known that the atmospheric reactions of monoterpenes and aromatics have been associated with SOA formation and they are representative biogenic and anthropogenic organic compounds, respectively [Grosjean and Seinfeld, 1989; Kroll and Seinfeld, 2008].

Hydrocarbons investigated are summarized in Table 2.1. SOA particles generated from four monoterpenes ( $\alpha$ - and  $\beta$ -pinene limonene, myrcene), one sesquiterpene ( $\alpha$ -humulene) and two aromatic compounds (toluene and phenol.) as a representative biogenic and anthropogenic hydrocarbon using several different oxidation chemistries, in an effort to probe the importance of different oxidation chemistries and other different factors on SOA refractive indices.

- *Biogenic Secondary Organic Aerosol*

- **Isoprene (C<sub>5</sub>H<sub>8</sub>):** Isoprene accounts for about half of all natural VOC emissions [Kanakidou *et al.*, 2005], and appears to produce SOA with a very high degree of oxygenation which may affect its polarizability and thus its  $m_r$ . Isoprene SOA was investigated under a variety of relevant conditions, including at high and low NO<sub>x</sub> and with acid and neutral seeds. However the aerosol yield was not high enough to retrieve the refractive index, thus no  $m_r$  result with that. Experimental conditions that we performed are described in tables in Appendix. C
- **Monoterpenes (C<sub>10</sub>H<sub>16</sub>):**  $\alpha$ - and  $\beta$ -pinene and limonene are the most abundant monoterpenes in the atmosphere, accounting for approximately 25% and 16% of global monoterpene emissions, for  $\alpha$ -pinene and for both  $\beta$ -pinene and limonene, respectively [Kanakidou *et al.*, 2005]. Also limonene is doubly unsaturated so that it has much higher SOA yields as well as it was expected to generate SOA with different chemical and optical properties due to different chemical structures. With the same manner, myrcene (three double bonds) was tried, but its aerosol yield was not high enough to measure the optical properties. Experimental conditions are described in Tables in Appendix C
- **Sesquiterpene (C<sub>15</sub>H<sub>24</sub>):** Sesquiterpene is also abundant terpenes in the atmosphere [Kanakidou *et al.*, 2005].  $\alpha$ -humulene was used as a representative sesquiterpene. Because of the significantly different chemical structure and high aerosol yield due to high molecular weight than others, somewhat different optical properties were expected to be observed. However, bimodal size distribution of particles was generated and our current analysis method (mie theory assumes lognormal distribution) does not allow to retrieve the refractive index. The size distribution can be seen in the Figure in Appendix D.



- **Anthropogenic Secondary Organic Aerosol:** Toluene and phenol were used. Aromatic hydrocarbons comprise 20% of nonmethane hydrocarbons in the urban area and considered to be one of the major precursors to urban SOA [Calvert *et al.*, 2002], through multigenerational reactions [Ng *et al.*, 2007a; Sato *et al.*, 2007]. Phenolic compounds are one of the major first generation products of OH reaction with aromatic hydrocarbons [Calvert *et al.*, 2002] and toluene is typically the most abundant aerosol forming hydrocarbon in ambient air [Kanakidou *et al.*, 2005]. They react rather slowly, so a small non-aerosol forming molecule like propene can be added to speed up photochemistry.

Organic aerosols can be generated using any one of at least 4 oxidation chemistries. These are; O<sub>3</sub> alone and O<sub>3</sub> + OH, both in the dark, VOC/NO<sub>x</sub> photochemistry at “high” or “low” VOC/NO<sub>x</sub> ratios. VOC/NO<sub>x</sub> photochemistry best mimics the atmosphere. OH is the primary oxidant but O<sub>3</sub>, NO<sub>3</sub> and O(<sup>3</sup>P) also contribute. For VOC/NO<sub>x</sub> photochemistry, at “high” VOC/NO<sub>x</sub> ratios, organic peroxy radicals (RO<sub>2</sub>) react with RO<sub>2</sub> or HO<sub>2</sub> to produce lower volatility products than the RO<sub>2</sub> + NO reactions that dominate under “low” VOC/NO<sub>x</sub> conditions [Kroll and Seinfeld, 2008; Ng *et al.*, 2007b; Presto *et al.*, 2005]. The effect of products from RO<sub>2</sub> + NO vs. RO<sub>2</sub> + HO<sub>2</sub> and RO<sub>2</sub> + RO<sub>2</sub> on SOA refractive indices can be investigated. For dark ozone reactions of unsaturated hydrocarbons, reactions can be initiated either solely by O<sub>3</sub> or by O<sub>3</sub> together with OH. Because unsaturated hydrocarbon and ozone reaction yields OH radicals (e.g., the yield of OH radicals from the  $\alpha$ -pinene reaction with ozone is about 70% [Paulson *et al.*, 1998]), in the absence of scavenger, nearly half of the hydrocarbon will react with OH rather than ozone.

### **2.1.3 Gas phase and particle phase analysis of chamber**

A suite of instrumentations were used to provide characterization of the chamber and aerosols, shown in Table 2.2. This includes a gas chromatograph (GC, HP 5890-II) to monitor concentrations of organics, NO<sub>x</sub> (Thermo Electron) and O<sub>3</sub> analyzers (Dasibi, 1001-RS) for gas phase measurements. Aerosols were characterized with the polar nephelometer (described below), an integrating nephelometer (Ecotech M9003), a scanning mobility particle sizer (SMPS, TSI model 3080), aethalometer (OT21, MAGEE Scientific, Berkeley, California) and by gravimetric mass ( $\pm 1 \mu\text{g}$ , Sartorius). The integrating nephelometer measures scattering at 700 nm as well as relative humidity and temperature with one min. time resolution., Filter-based gravimetric samples provide check for SMPS measurement as well as are used for a absorption coefficient measurement with aethalometer. Filter samples for gravimetric analysis and were collected on pre-baked (24 h at 550 °C) 25 mm quartz fiber for 10 – 40 min depending on mass concentrations in chamber at 20 LPM toward the end of the experiments. Filters were allowed to equilibrate for 24 h in a temperature and humidity controlled room before weighting using a microbalance ( $\pm 1 \mu\text{g}$ , Sartorius).

### **2.2 Polar nephelometer**

The Polar nephelometer (PN) is used to measure the optical properties of SOA. Unlike with other optical instruments (e.g., cavity ring down), the polar nephelometer has a fast time response and thus can probe the refractive index as the particles grow and change during the experiments. Investigating of changing refractive index as particles grow is the first to be explored.

Polar nephelometers (PN) have been used to make angular scattering measurements with the goal of deriving various physical parameters of aerosol particles, including the complex refractive index. Several theoretical studies [*Shaw*, 1979; *Verhaege et al.*, 2008] have shown it is possible to determine both the real refractive index and some mono-modal size distribution parameters from PN measurements, if the particles are spherical and homogeneous. Experimentally, *Jones et al.*, [1994] used a 15 channel polar nephelometer with an 840 nm laser to determine the refractive index and size distribution of polystyrene latex (PSL) spheres. *Zhao*, [1999] estimated a retrieval error of a few percent in the real component and up to 50% in the imaginary for their goniometer type PN. *Lienert et al.*, [2003] determined aerosol size distributions using a 532 nm goniometer PN using the genetic algorithm (GA) method, Mie-Lorenz scattering and an assumed refractive index. *Barkey et al.*, [2007] measure angular scattering, including polarization, with a polar nephelometer designed at UCLA.

The Polar Nephelometer (PN) used in this study is an upgraded version (1<sup>st</sup> and 2<sup>nd</sup>) of the instrument described by *Barkey et al.*, [2007]. Upgrades include a machined aluminum casing that provides a hermetic seal for the scattering volume. The instrument dynamic range has been increased about a decade from improvements to the photo-diode detector/amplifier circuits. Finally, detector aperture diameters are now inversely proportional to the expected intensity levels to reduce the large range in detector signals that results from uniform aperture sizes. Every 16 seconds it measures light intensities scattered into 21 discrete angles by a stream of aerosols intersecting the beam of 350 milliwatt 670 nm diode laser (1<sup>st</sup> generation upgraded PN). For 2<sup>nd</sup> generation PN, light source was replaced with a 1W 532 nm laser (Intelite Inc.). With this 2<sup>nd</sup> generation of PN, in addition to providing data near the peak of the solar spectrum, this laser has greatly increased sensitivity so that we could obtain reliable retrievals at ambient mass

concentrations in the 10 – 140  $\mu\text{g}/\text{m}^3$  range, and in some cases below 10  $\mu\text{g}/\text{m}^3$ . Every 16 seconds, the PN measures light intensities scattered at 21 discrete angles by a stream of aerosols intersecting the beam of the laser. A  $\frac{1}{2}$  wave plate appropriate for 532 nm rotates the polarization plane of the incident light to be parallel or perpendicular to the measurement scattering plane. The 1 LPM aerosol sample flow, which intersects a 2 x 5 mm beam, is confined to the center of the scattering plane by a 10 LPM sheath flow. A  $\frac{1}{2}$  wave plate rotates the plane of incident light to be parallel or perpendicular to the measurement scattering plane. Sample phase functions and retrievals are shown in Figure 2.2.

Combining with polar nephelometer data using parallel and perpendicular polarized light (670 or 532 nm), refractive indices were obtained with measured size distributions, and retrievals were performed using a genetic algorithm and Mie-Lorenz scattering theory. The absolute error associated with the  $m_r$  retrieval is  $\pm 0.03$ , and reliable retrievals are possible for mass concentrations above 5 - 20  $\mu\text{g}/\text{m}^3$  depending on particle size.

### 2.3 Validation and calibration of instrument

PSL microspheres (Duke Scientific) with well characterized size distributions and a manufacturer specified  $m_r$  of 1.5854 at 670 nm and  $m_r$  of 1.5982 at 532 nm are used to calibrate the PN. The PSL particles were aerosolized in a Collison spray nebulizer (BGI Inc.) and then directed through sufficient desiccant tubes to dry them completely. Shown in Supplemental Figure 2.1a is a plot of the light scattered by 800 nm in diameter PSL spheres as measured by the uncalibrated PN along with Mie-Lorenz determined expectations. Calibration constants,  $k_i$ , are developed from these measurements via;

$$k_i = \frac{P_{p,thy}(\theta_i, m_r, \mu, \sigma)}{V_{p,meas}(\theta_i)} \quad (2.1)$$

where  $\mu$  and  $\sigma$  are the manufacturers specified geometric mean and standard deviation respectively,  $P_{p,thy}(\theta_i, m_r, \mu, \sigma)$  is the theoretically determined relative intensity for a discrete sensing angle ( $\theta_i$ ) and  $V_{p,meas}(\theta_i)$  is the measured detector voltage signal at  $\theta_i$ . The subscript ‘ $p$ ’ is either ‘ $l$ ’ for incident light polarized parallel to the scattering plane and ‘ $r$ ’ for perpendicular polarization. The theoretical results are adjusted to the PN instrument geometric intensity response characteristics as described in *Barkey et al.* [2007], and are fitted to the measurement using the method of least squares. Calibration constants are derived from relatively isotropic scattering measurements, i.e., the parallel incident light results of the 800 nm PSL particles shown in Figure 2.1a, rather than the highly variable scattering pattern for the perpendicular incident light for the same particle. The signal responses at angles with low intensities, such as the dips near 60° and 100° (Figure 2.1a), are more susceptible to noise and multiple internal reflections within the scattering volume.

The constants,  $k_i$ , are multiplicative corrections for the measured voltages and should be the same for any calibration particle size. Any differences in  $k_i$  developed using different size PSL particles are due to instrument noise or differences in the amount of unwanted signal from stray reflections. Shown in Figure 2.1b are the calibration constants that range from about 0.5 to 1.8, developed using measurements of the 800 nm PSL particles (Figure 2.1a) as well as for those developed using PSL particles with a mean diameter of 596 nm. Error bars based on the standard deviation of calibration constants developed from 40-50 separate PN measurements of the PSL particles average 2-3% and range from 0.7 to 5%. These error bars are less than the average difference (3.4%) between the calibration constants for the 596 and 800 nm PSL particles, which have a maximum difference of 9% at 18°. (The 800 and 600 nm PSL calibration constants match within 0.04 - 3 % with 532nm of light)The larger difference at 18° is caused by

laser beam directional drift. However, the values are still low, due to efforts to redirect unwanted scattering signals into light absorbers positioned above and below the scattering plane. Importantly, differences below 15% and produce  $m_r$  retrieval uncertainties below  $\pm 0.03$ , as discussed below (Section 2.4). PSL particles smaller than about 500 nm are not used for calibration as they have a tendency to clump into dimers which cannot be modeled with the single particle Mie-Lorenz solution. From time to time, we perform a validation using 45 – 70 nm ammonium sulfate particles at known relative humidity, as described in *Barkey et al.*, [2007] and are able to match the expected  $m_r$  (1.41 – 1.43 depending on humidity) within  $\pm 0.01$ .

## 2.4 Determination of the refractive index: Genetic algorithm

A detailed description of the genetic algorithm real refractive index retrieval scheme is provided in *Barkey et al.* [2007] thus here we provide a brief description of the method and focus on changes applied in this study. The GA is a directed search, or optimization method that mimics the way the best organisms are selected for their environment. For PN retrievals, a population of possible solutions consisting of real refractive indices and size distribution parameters is randomly selected from within predefined search limits. The population is examined numerically to see which member best describes the measured scattering,  $P_{l,meas}(\theta_j)$  via a fitness value defined by:

$$F_p = 1 - \frac{1}{N} \sum_{j=1}^N \left| \text{Log}(P_{p,theo}(\theta_j, m_r, \mu, \sigma)) - \text{Log}(P_{p,meas}(\theta_j)) \right| \quad (2.2)$$

where,  $P_{p,theo}(\theta_j, m_r, \mu, \sigma)$  is the theoretically determined intensity for each discrete sensing angle ( $\theta_j$ ) as described in eqn. 2.1 [*Lienert et al.*, 2003]. The fitness values for the two light polarization orientations are combined via  $F = F_r + F_l$ , where  $r$  indicates polarization parallel to the scattering plane and  $l$  indicates the perpendicular orientation.

The limits to the refractive index search space were set at 1.1 to 1.7. The search space for the lognormal distribution parameters are set at  $\pm 30\%$  of the SMPS measured mean and standard deviation. The accuracy of the size distributions returned by the SMPS (with a scan time of 180s) is  $\pm 10\%$ , [Russell *et al.*, 1995; Tokonami and Knutson, 2000]. However, the search space for the SMPS measured mean and standard deviation is set to  $\pm 30\%$  because of differences in the measured size distribution and the lognormal distribution assumed in the GA retrieval scheme, and to provide sufficient search space for the inherent error in SMPS distribution during the rapid growth phase (below). The difference between the measured distribution profile ( $PDF_{meas}(x)$ ) and the assumed lognormal profile ( $PDF_{calc}(x, \mu, \sigma)$ ) is defined by;

$$\Delta_{dist} = \int |PDF_{meas}(x) - PDF_{calc}(x, \mu, \sigma)| dx, \quad (2.3)$$

and are normalized such that

$$\int PDF_{meas}(x) dx = \int PDF_{calc}(x, \mu, \sigma) dx = 1.0 \quad (2.4)$$

where  $x$  is the particle diameter. The profiles of measured distributions with  $\Delta_{dist} < 0.07$  do not seem distorted at first glance, while  $\Delta_{dist}$  values  $> 0.2$  can have distinct dual mode features. In Barkey *et al.* [2010], it is shown theoretically and experimentally that the retrieved  $m_r$  is accurate to within  $\pm 0.014$  of the expected  $m_r$  when  $\Delta_{dist}$  is less than 0.585. The average  $\Delta_{dist}$  for the aerosols seen in these experiments is about 0.2, with a range of 0.04 to 0.4. Although increasing the size distribution search space always produces better fitness values, the GA retrieved mean is usually higher than the measured value and the GA determined standard deviation is lower than measured. The mean falls within  $\pm 10\%$  in 77% of cases. This is expected as the scattering from a non-lognormal distribution is not the same as that from a lognormal distribution as discussed in Barkey *et al.* [2010].

Figure 2.2b shows the PN measurement from 13:16 (i.e.,  $P_{p,meas}(\theta_j)$  of eqn. 2.2), and the GA determined best fit Mie-Lorenz theoretical expectation, (or  $P_{p,thy}(\theta_j, m_r, \mu, \sigma)$  of eqns. 2.1 and 2.2). Six separate GA searches were performed, each with an aggressive population of 300. Each search ran for 3 generations and had a mutation factor of 0.9. A population size of 50 is usually sufficient, however, the larger population ensures that the solution converges and that the highly complex solution space [Hodgson, 2000] is thoroughly searched. The retrieved  $m_r$  of each of these six searches varied less than 1% from the average GA-determined refractive index of 1.48. The small difference between each search indicates that the solution has converged to a single result and that the selected search spaces are reasonable, i.e., the spaces are not so large as to include two or more possible results. The average fitness value retrieved was 0.965. GA  $m_r$  retrievals of the scattering from ammonium sulfate and water drops and various sizes of PSL spheres with this instrument has shown that the GA  $m_r$  is accurate to  $\pm 0.03$  for detector noise levels of over 15% as long as the particles are spherical and homogeneous [Barkey *et al.*, 2007]. At the start of the experiment, the signal to noise ratio is low ( $\sim 1$  to 3) due to low particle concentrations and small particle sizes and produces the obviously noisy scattering patterns at 12:58 and 13:04 in Figure 2.2a. GA retrieved parameters from these scans are not reliable as the fitness values are less than 0.8. Normally, once the scattering coefficient has increased to about  $500 \text{ Mm}^{-1}$ , at which time the particles have grown to over 200 nm, the fitness values increase to above 0.94.

The PN measurement frequency (16 seconds) is higher than that of the SMPS (3 minutes). At later times the SMPS mean and standard deviation do not change significantly during the 3 minute SMPS sampling time. However, during the initial particle growth period (such as 13:00 – 13:20, Figure 3.1b), there is a systematic error in the SMPS measurement as the



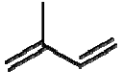
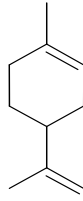
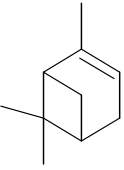
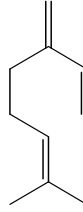
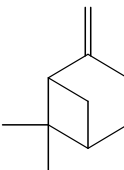
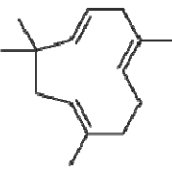
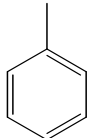
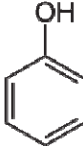
particle mean size changes significantly (~12 nm/minute) during the 3 minute scanning interval. The resulting inconsistencies are generally acceptable within the framework of the GA retrieval. This is first because the phase function itself is only slightly affected by the shifting size distribution as the mean size changes only by about 3 nm during the 16 second time period of the PN measurement, a small change compared to the particle size of 200 nm. Further, any difference between the actual size distribution at the measurement time and that produced from the SMPS measurement is encompassed by the large ( $\pm 30\%$ ) GA size parameter search space. GA searches converged on the size parameters and  $m_r$  for all retrievals in rapid growth regions, indicating solution viability.

## 2.5 References

- Barkey, B., S. E. Paulson, and A. Chung (2007), Genetic algorithm inversion of dual polarization polar nephelometer data to determine aerosol refractive index, *Aerosol Science and Technology*, 41(8), 751-760.
- Calvert, J. G., R. Atkinson, K. H. Becker, R. M. Kamens, J. H. Seinfeld, T. J. Wallington, and G. Yarwood (2002), The mechanism of atmospheric oxidation of aromatics hydrocarbons, *Oxford University Press*.
- Chung, A., A. A. Lall, and S. E. Paulson (2008), Particulate emissions by a small non-road diesel engine: Biodiesel and diesel characterization and mass measurements using the extended idealized aggregates theory, *Atmospheric Environment*, 42(9), 2129-2140.
- Cocker, D. R., R. C. Flagan, and J. H. Seinfeld (2001), State-of-the-art chamber facility for studying atmospheric aerosol chemistry, *Environmental Science & Technology*, 35(12), 2594-2601.
- Grosjean, D., and J. H. Seinfeld (1989), Parameterization of the formation potential of secondary organic aerosol, *Atmos. Environ.*, 23(8), 1733-1747.
- Hodgson, R. J. W. (2000), Genetic algorithm approach to particle identification by light scattering, *Journal of Colloid and Interface Science*, 229(2), 399-406.
- Jones, M. R., K. H. Leong, M. Q. Brewster, and B. P. Curry (1994), Inversion of light - scattering measurements for particle size and optical constants; experimental study, *Applied Optics*, 33(18), 4035-4041.
- Kanakidou, M., J. H. Seinfeld, S. N. Pandis, I. Barnes, F. J. Dentener, M. C. Facchini, R. Van Dingenen, B. Ervens, A. Nenes, C. J. Nielsen, E. Swietlicki, J. P. Putaud, Y. Balkanski, S. Fuzzi, J. Horth, G. K. Moortgat, R. Winterhalter, C. E. L. Myhre, K. Tsigaridis, E. Vignati, E. G. Stephanou, and J. Wilson (2005), Organic aerosol and global climate modelling: a review, *Atmospheric Chemistry and Physics*, 5, 1053-1123.

- Kroll, J. H., and J. H. Seinfeld (2008), Chemistry of secondary organic aerosol: Formation and evolution of low-volatility organics in the atmosphere, *Atmospheric Environment*, 42(16), 3593-3624.
- Lienert, B. R., J. N. Porter, and S. K. Sharma (2003), Aerosol size distributions from genetic inversion of polar nephelometer data, *Journal of Atmospheric and Oceanic Technology*, 20(10), 1403-1410.
- Ng, N. L., P. S. Chhabra, A. W. H. Chan, J. D. Surratt, J. H. Kroll, A. J. Kwan, D. C. McCabe, P. O. Wennberg, A. Sorooshian, S. M. Murphy, N. F. Dalleska, R. C. Flagan, and J. H. Seinfeld (2007a), Effect of NO<sub>x</sub> level on secondary organic aerosol (SOA) formation from the photooxidation of terpenes, *Atmospheric Chemistry and Physics*, 7(19), 5159-5174.
- Ng, N. L., J. H. Kroll, A. W. H. Chan, P. S. Chhabra, R. C. Flagan, and J. H. Seinfeld (2007b), Secondary organic aerosol formation from m-xylene, toluene, and benzene, *Atmospheric Chemistry and Physics*, 7(14), 3909-3922.
- Paulson, S. E., M. Chung, A. D. Sen, and G. Orzechowska (1998), Measurement of OH radical formation from the reaction of ozone with several biogenic alkenes, *Journal of Geophysical Research-Atmospheres*, 103(D19), 25533-25539.
- Presto, A. A., K. E. H. Hartz, and N. M. Donahue (2005), Secondary organic aerosol production from terpene ozonolysis. 2. Effect of NO<sub>x</sub> concentration, *Environmental Science & Technology*, 39(18), 7046-7054.
- Russell, L. M., R. C. Flagan, and J. H. Seinfeld (1995), Asymmetric instrument response resulting from mixing effects in accelerated DMA-CPC measurements, *Aerosol Science and Technology*, 23(4), 491-509.
- Sato, K., S. Hatakeyama, and T. Imamura (2007), Secondary organic aerosol formation during the photooxidation of toluene: NO<sub>x</sub> dependence of chemical composition, *Journal of Physical Chemistry A*, 111(39), 9796-9808.
- Shaw, G. E. (1979), Inversion of optical scattering and spectral extinction measurements to recover size spectra, *Applied Optics*, 18(7), 988-993.
- Tokonami, S., and E. O. Knutson (2000), The scan time effect on the particle size distribution measurement in the scanning mobility particle sizer system, *Aerosol Science and Technology*, 32(3), 249-252.
- Verhaege, C., V. Shcherbakov, and P. Personne (2008), Limitations on retrieval of complex refractive index of spherical particles from scattering measurements, *Journal of Quantitative Spectroscopy & Radiative Transfer*, 109(14), 2338-2348.
- Zhao, F. (1999), Determination of the complex index of refraction and size distribution of aerosols from polar nephelometer measurements, *Applied Optics*, 38(12), 2331-2336.

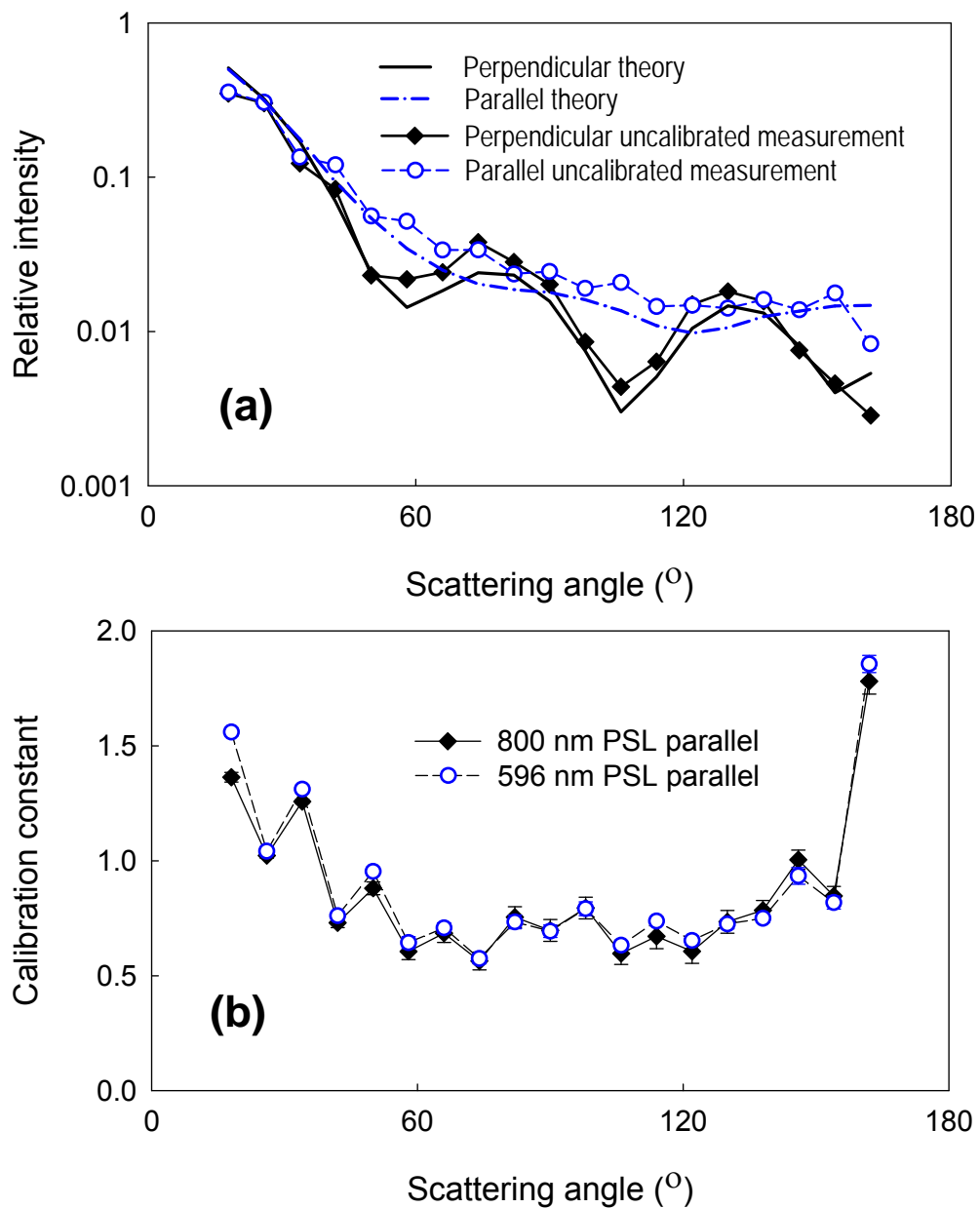
**Table 2.1. Structure of SOA precursors presented in this thesis.**

Parent Hydrocarbon	Structure	Formula (MW)	Parent Hydrocarbon	Structure	Formula (MW)
isoprene		C <sub>5</sub> H <sub>8</sub> (68)	limonene		C <sub>10</sub> H <sub>16</sub> (136)
α-pinene		C <sub>10</sub> H <sub>16</sub> (136)	myrcene		C <sub>10</sub> H <sub>16</sub> (136)
β-pinene		C <sub>10</sub> H <sub>16</sub> (136)	α-humulene		C <sub>15</sub> H <sub>24</sub> (204)
toluene		C <sub>7</sub> H <sub>8</sub> (92)	Phenol		C <sub>6</sub> H <sub>6</sub> O (94)

**Table 2.2. Support instrumentation for the chamber**

<b>Instrument</b>	<b>Model</b>	<b>Measurement</b>	<b>Detection Limit</b>
Gas Chromatograph/Flame Ionization Detector	HP 5890-II	Analysis of gas-phase organics	~50 ng/m <sup>3</sup>
Ozone Analyzer	Dasibi 1001-RS	Ozone	~1 µg/m <sup>3</sup>
NO, NO <sub>2</sub> , NO <sub>x</sub> and HNO <sub>3</sub>	Thermo Electron	Nitrogen oxides; nitric acid can be measured using a nylon filter	~1 µg/m <sup>3</sup>
Scanning Mobility Particle Sizer (SMPS)	TSI-3936L10	Particle size distributions, 10 nm-1 µm, 1 min. time resolution	N/A
Dual Polarization Polar Nephelometer	—	Angular dependent scattering at 670/532 nm	N/A
Transmissometer (Aethalometer)	Magee Scientific AE3	Filter-based absorption at seven wavelength channels (370 to 950 nm)	~1 ng BC
Microbalance	Sartorius	Gravimetric mass measurement	1 µg
Integrating Nephelometer	EcoTech M9008	Chamber Relative Humidity & Temperature (in addition to scattering)	N/A

**Figure 2.1.** (a) Incident 670 nm laser light polarized parallel (circles) and perpendicular (filled diamonds) scattered by 800 nm PSL particles measured by the polar nephelometer before calibration and expectations (lines) developed from Mie-Lorenz calculations. (b) Calibration constants (circles) determined from the 800 nm PSL measurement in (a) with parallel incident light, along with the same for PSL particles with a diameter of 596 nm. Error bars are based on the standard deviation of calibration constants derived from 40-50 PN measurements taken over a period of several minutes. Differences between these calibration constants are assumed to be from multiple internal reflections within the scattering volume.



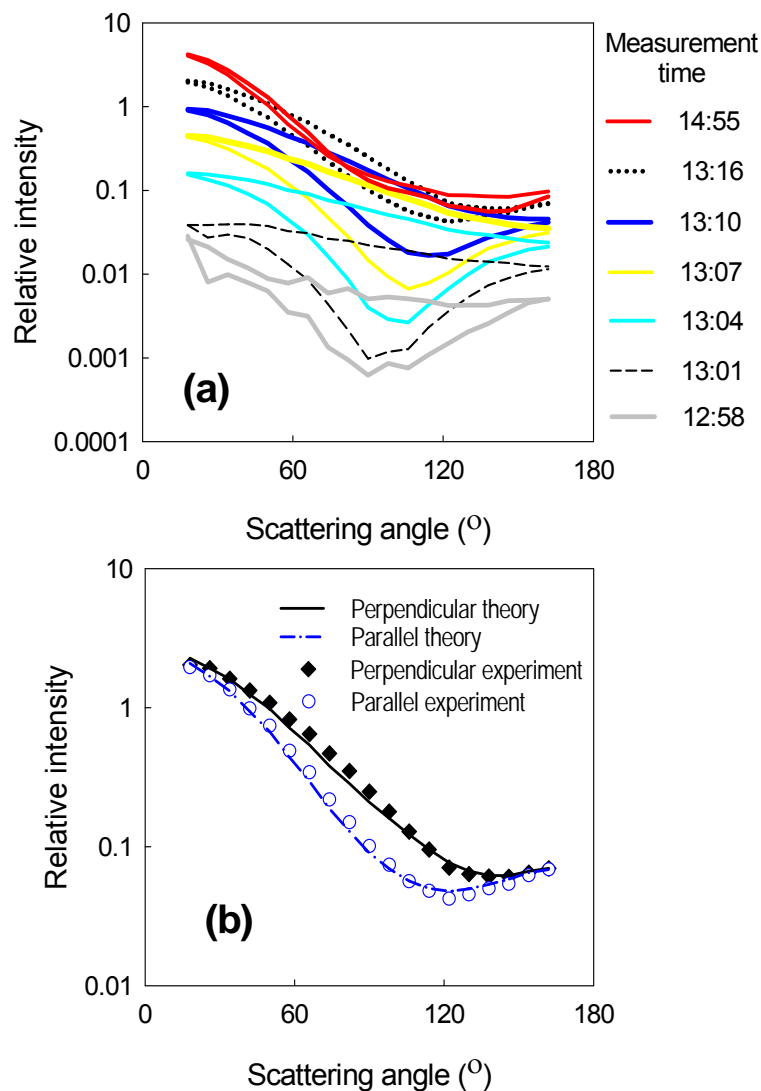


**Figure 2.2.** (a) Selected scattering properties recorded with the PN as particles grow for the experiment performed on 21 October. (b) Scattering at 13:16 (after 46 min), when the particle had a median size of 291 nm. Also shown GA determined fit using Mie-Lorenz theory, with a  $m_r=1.48$ , and at fitness of 0.965.

## **Chapter 3**

### **Real refractive indices of $\alpha$ - and $\beta$ -pinene and Toluene Secondary Organic Aerosols generated from Ozonolysis and Photo-oxidation**

### 3.1 Experimental

Experiments were performed in a 24 m<sup>3</sup> Teflon chamber constructed on the roof of the Math Sciences Building at UCLA. The chamber is described in detail in *Chung et al.* [2008]. Air is supplied to the chamber by two 33 gallon oil-free portable air compressors (Craftsman) after passing through a series of packed bed scrubbers filled with Purafil Triple Blend (Purafil Inc.), activated charcoal, and HEPA capsule filters (Gelman). The scrubbed air has < 50 particles cm<sup>-3</sup>, and NO<sub>x</sub> (Thermo Electron model 14B/E), O<sub>3</sub> (Dasibi 1001-RS), and organics (GC, HP 5890-II) levels below the 1 ppb detection limits. Between experiments, a vent is opened and the chamber is flushed with clean air for 10 hours in full sun in preparation for the next experiment.  $\alpha$ - And  $\beta$ -pinene (Fluka, 98.5 %) and toluene (Aldrich, 99.8 %) were used as received.

Tables 1 and 2 show initial conditions and summary statistics for 28 experiments. For photooxidation experiments, the chamber, covered with a black tarpaulin (supported on a frame above the chamber), was half filled with purified air. At this point, gas phase reagents such as NO (Scott Specialty Gasses) and propene (Aldrich, as a photochemical initiator for toluene) were added. Finally, the SOA precursor hydrocarbon liquid was evaporated into the air stream filling the chamber. The chamber contents were allowed to mix for about 40 min. Once the gas chromatograph returned two measurements within 2% of one another, the tarps were removed and photochemistry initiated. The overall oxidation times for each species were 2.5h, 4h and 4-6h, for  $\alpha$ - and  $\beta$ -pinene and toluene, respectively.

For ozone experiments, ozone was generated by flowing pure oxygen (0.5 L/min) through a mercury lamp O<sub>3</sub> generator (Jelight, model 600) into a covered chamber as it was being filled. For selected experiments, an OH scavenger (cyclohexane) was injected. When



ozone and/or scavenger were well mixed, the hydrocarbon of interest was injected and the chamber mixed manually to minimize inhomogeneities.

Aerosols were characterized with the polar nephelometer (described below), an integrating nephelometer (Ecotech M9003), a scanning mobility particle sizer (SMPS, TSI model 3080), and by gravimetric mass ( $\pm 1 \mu\text{g}$ , Sartorius). The integrating nephelometer measures scattering at 700 nm as well as relative humidity and temperature with one min. time resolution. The SMPS measures the 19 – 948 nm particle size distributions every 3 minutes. Filter samples for gravimetric analysis were collected on pre-weighed 47 mm Teflon filters (Pallflex) for 5 - 10 min at 30 LPM toward the end of the experiments.

## **3.2 Results and Discussion**

### **3.2.1 Reaction profile of a photooxidation experiment**

Figures 3.1 – 3.2 show chamber results from a typical photooxidation experiment (21 October). Figure 3.1a shows NO, NO<sub>x</sub>, O<sub>3</sub>,  $\alpha$ -pinene and wall-loss corrected aerosol mass concentration. The experiment had initial concentrations of 500 ppb  $\alpha$ -pinene and 260 ppb NO. SOA began to nucleate 33 minutes after the chamber was initially exposed to sunlight, and quickly grew to several hundred nanometers. Figure 3.1b shows the evolution of particle numbers, mean diameter, and integrated scattering ( $\beta_{\text{sca}}$ ). The particles continued to grow throughout, however particle number concentrations dropped slowly due to coagulation and wall loss after 13:10. Viable retrievals from the PN signal were first obtained when the particles had grown to about 200 nm at 13:12 (Figure 3.1c).  $\beta_{\text{sca}}$  continues to increase as particle numbers drop until 14:05, after which it declines slowly. At this point, the increases in scattering associated with growing particles is overtaken by the decreases due to decreasing numbers (Figure 3.1c).

Selected phase functions for the growing particles are shown in Figure 3.2a, including the first measurement at 12:58 to the final measurement at 14:55. As expected, as particle sizes increase, scattering intensities increase. Typically, particle growth is rapid initially, and then slows considerably, thus after about 13:20 there is little change in the angular scattering properties. There is more electronic noise in the earlier scans, which are at the lower limits of the instrument sensitivity. Initially the intensity minimum is at about  $90^\circ$ . Because larger particles scatter light predominantly in the forward direction, the minimum is reduced and moves towards  $130^\circ$  as time progresses.

### 3.2.2 Aerosol formation yields

Tables 3.1 and 3.2 show aerosol yields (aerosol mass/HC reacted, both in  $\mu\text{g}/\text{m}^3$ ), calculated from SMPS volumes. SOA are accepted to be reasonably spherical, as verified in *Barkey et al.* [2007]. Reports of  $\alpha$ - and  $\beta$ -pinene SOA densities are in the range  $1.19 - 1.65 \text{ g}/\text{cm}^3$  [*Malloy et al.*, 2009; *Saathoff et al.*, 2009; *Shilling et al.*, 2009], and  $1.24 - 1.48 \text{ g}/\text{cm}^3$  has been reported for toluene [*Ng, et al.*, 2007]. At small mass concentrations, SOA densities appear to decrease as the SOA mass concentration increases and/or as the aerosol grows (e.g., *Malloy et al.*, 2009; *Shilling et al.*, 2009). Because of the polar nephelometer detection limits, most of our experiments were performed with significantly higher initial hydrocarbon concentrations, and as a result higher SOA mass concentrations than those for which density measurements have been made, we used density values at the low end of the literature reports. SOA mass was calculated based on size distributions measured by the SMPS assuming spherical particles with a density of  $1.2 \text{ g}/\text{cm}^3$  for  $\alpha$ - and  $\beta$ -pinene and  $1.24 \text{ g}/\text{cm}^3$  for toluene. Measured particle number concentrations were corrected for size-dependent wall loss, using coefficients determined from separate wall loss experiments. The wall loss rates ranged from  $0.0012$  to  $0.0081 \text{ min}^{-1}$ . Gravimetric mass

measurements were used to check the SMPS masses, and averaged  $87 \pm 12$  % of SMPS mass measurements. The gravimetric filter samples are expected to underestimate particle mass due to evaporation of semivolatiles from collected particles (e.g., [Chung, *et al.*, 2008]).

Aerosol yields and chemical composition is controlled by the parent hydrocarbon, oxidation chemistry, temperature and aerosol mass concentration [Hallquist *et al.*, 2009 and references therein]. Our yield data bear out the expected trends; where we have pairs or sets of similar experiments, yields appear to be higher at lower temperatures, higher initial HC/NO<sub>x</sub> ratios, and higher aerosol mass in the chamber. Because of significantly higher initial hydrocarbon concentrations and resulting high aerosol mass concentrations, yields at or above the upper end of literature values [Griffin *et al.*, 1999; Ng *et al.*, 2007; Saathoff *et al.*, 2009] are expected for our experiments (Tables 3.1, 3.2). The only SOA for which a direct comparison is available is  $\alpha$ -pinene ozonolysis; Saathoff *et al.* [2009] report yields of  $\sim 30$  % for experiments carried out at similar temperature and aerosol masses of  $100 - 200 \mu\text{g}/\text{m}^3$  for this system. Our yields for aerosol masses between  $450 - 1000 \mu\text{g}/\text{m}^3$  are in good agreement at  $32 - 50\%$ , but very high aerosol masses appear to lead to qualitatively higher yields (55 and 97%, Table 3.1).

### 3.2.3 SOA refractive indices

Figures 3.3 – 3.5 show refractive indices retrieved as a function of particle mass concentration (in the chamber, not corrected for wall losses) from angular scattering data for groups of SOA generated in the chamber. Figures 3.6 – 3.8 shows the same data plotted as a function of diameter. Particle diameter is consistently the independent variable best correlated with refractive index data. All but four of the retrieved  $m_p$ s had fitness values of at least 0.94; the remaining 4 were between 0.92 and 0.94. Particle chemical composition is expected to depend

on the parent hydrocarbon, its oxidation chemistry, the particle mass concentration, the temperature, and under longer time scales, in-particle reactions and heterogeneous aging.

### 3.2.3.1 Ozonolysis SOA

Figure 3.3 shows results for SOA for  $\alpha$ -pinene ozonolysis performed with the same initial hydrocarbon concentration, with and without an OH scavenger. Because the yield of OH radicals from the  $\alpha$ -pinene reaction with ozone is about 70% [Paulson, *et al.*, 1998], in the absence of scavenger, nearly half of the  $\alpha$ -pinene molecules react with OH rather than ozone. Within the resolution of our method however the retrieved refractive indices are not distinguishable from one another (Figure 3.3), indicating the differences in SOA chemical composition for the two oxidation chemistries are not sufficient to affect the optical properties. In contrast, SOA particles that are generated at lower temperatures (Feb. 12,  $\sim 14$  °C instead of 26 °C, Table 3.2), appear to have significantly lower refractive indices (1.4 to 1.44). The retrieved refractive index of the  $26 \pm 4$  °C experiments increases slightly as the particle mass concentration increases from about 200 to about 1100  $\mu\text{g}/\text{cm}^3$  from about 1.45 to 1.5.

Figure 3.4 compares retrieved refractive indices for SOA formed by ozonolysis (without scavenger) of (a)  $\alpha$ - and (b)  $\beta$ -pinene at several initial concentrations.  $\beta$ -pinene required significantly higher precursor concentrations to produce similar mass concentration of SOA formed by ozonolysis of  $\alpha$ -pinene. The refractive indices of both types of SOA increase slowly as the aerosol mass concentration increases over a wide range (60 – 4000+  $\mu\text{g}/\text{m}^3$ ), from about 1.4 to 1.5 for  $\alpha$ -pinene and 1.43 to 1.48 for  $\beta$ -pinene. We note that the mass concentrations are generally well above ambient levels, and thus lower values seem to be implied for ambient aerosol mass concentrations.

### 3.2.3.2 Photochemically generated SOA

Figure 3.5 shows  $m_r$ s for photochemically generated aerosol from  $\alpha$ - and  $\beta$ -pinene and toluene. In each case, the photochemically derived SOA cover a wider range of  $m_r$  values than ozonolysis. As the experiments progress, several factors may influence particle chemical composition and refractive index; the aerosol mass concentration, the relative contribution of  $RO_2$  radical reactions with NO vs.  $HO_2$  or  $RO_2$ , the temperature and other factors such as water uptake and heterogeneous and in-particle reactions. The photochemical experiments were performed in a relatively narrow range of relative humidities (11 – 22%) in a region in which water uptake, or phase, is not expected to be changing rapidly (e.g., *Mikhailov et al.*, 2009). Temperatures span a moderate range (medians vary by 4 – 9°C depending on hydrocarbon, Table 3.1) and do not appear to explain the observed variability.

$\alpha$ - And  $\beta$ -pinene SOA indices (Figures 3.5a and b) increase from about 1.38 to a maximum of about 1.52, with somewhat different mass concentration dependences, and for both pinenes they drop off somewhat at the highest mass concentrations. For  $\alpha$ -pinene, there is some spread at lower mass concentrations, the source of which is not clear. We note that the higher refractive indices at mass concentrations between 0 and 1000 are associated with experiments in which NO dropped below our 1 ppb detection limit at an early point in the experiment (Table 3.1, last column). Some time after this point,  $RO_2$  and  $HO_2$  radicals may build up to sufficient levels to successfully compete with NO to be the predominant reaction partner for  $RO_2$ . This may hint at a higher  $m_r$  for the condensed products of  $RO_2$  reacting with  $RO_2/HO_2$  compared to NO. The  $\beta$ -pinene data are all in good agreement with one another (within the resolution of our method) and do not provide as much support for the notion that  $m_r$  increases as NO becomes depleted and the oxidation chemistry shifts through the experiment. The data do suggest that increasing aerosol mass causes species with higher  $m_r$ s to condense. The decrease of  $m_r$  at the

highest mass concentrations (and also at the end of the experiments) might be due to changes in particle composition brought about by heterogeneous or in-particle reactions (i.e., aging) or shifts in the composition of the condensing material. *Ng et al.* [2006]'s suggestion that parent hydrocarbons with one double bond such as  $\alpha$ - and  $\beta$ -pinene generate SOA from the first oxidation step, thus SOA chemical composition does not change appreciably as the hydrocarbon is consumed, does not support the notion that particle chemical composition is changing, leaving open the possibility that aging plays a role.

The shape of the  $m_r$  curve for toluene SOA (Figure 3.5c) is markedly different than that of the pinenes, and the range of values is larger (1.4-1.61). We note that the Aug 10 experiment is different in many respects from the other experiments. The only obvious difference is that this experiment had a lower initial hydrocarbon concentration, although it is unclear how this might influence results. In this data set, we see less support for the notion that mass concentration is a controlling variable; the data cluster in two distinct groups: high and low initial HC/NO<sub>x</sub> ratio (Fig. 3.5c). In general, the toluene SOA begin at low  $m_r$  values and increase dramatically as the particles grow, a phenomenon more consistent with  $m_r$  dependence on shifting chemical composition as the experiments progress.

As described in the introduction, there are three laboratory measurements of SOA to which we can compare our results. In our earlier study, we reported  $1.42 \pm 0.02$  for photochemically generated  $\alpha$ -pinene SOA, toward the end of an experiment similar to the July 15 and Sept. 23 experiments described here, which have final  $m_r$ s in the 1.45 – 1.5 range, reasonable agreement within the uncertainties. The current value is more reliable however; in earlier work, there was a mismatch between SMPS time stamps and clock time, and distribution distortion was not accounted for in the analysis. *Schnaiter et al.* [2005] derived a refractive index of 1.5 for  $\alpha$ -

pinene ozonolysis based on scattering and extinction measurements at 550 nm, for particles of unspecified size and mass concentration. *Lang-Yona et al.* [2010] report values of  $1.53 \pm (0.06 - 0.08)$  for mixed biogenic SOA oxidized with  $O_3$ , OH and low  $NO_x$ . Both the *Schnaiter et al.* [2005] and *Lang-Yona et al.* [2010] values are expected to be slightly higher than ours (by up to 0.02) because the measurements were made at shorter wavelengths. The values are in general agreement with our results.

### 3.2.4 Effect of the refractive index on radiative transfer

The value of the real refractive index affects the bulk radiative properties of aerosols. For instance the asymmetry parameter  $\langle g \rangle$ , a key parameter in radiative transfer calculations, is defined as:

$$\langle g \rangle = \int_{\theta} P(\theta) \cos(\theta) \sin(\theta) d\theta \quad (3.1)$$

where the integration is over the scattering angle,  $\theta$ . The azimuthal component of the solid angle ( $\Omega$ ) integration is constant when random particle orientation is assumed [*Van de Hulst, 1957*].

The non-dimensional scattering phase function  $P(\Omega)$  describes the average light intensity scattering properties of the particle distribution and is normalized via:

$$1 = \frac{1}{4\pi} \int_{\Omega} P(\Omega) d\Omega = \frac{1}{2} \int_{\theta} P(\theta) \sin(\theta) d\theta. \quad (3.2)$$

$\langle g \rangle$  describes the amount of light scattered by the particles into the forward or reverse hemispheres.  $\langle g \rangle = 1$  for full forward scattering,  $-1$  for scattering into the reverse hemisphere and  $0$  for isotropic scattering. Generally,  $\langle g \rangle$  decreases as  $m_r$  increases for distributions associated with aerosols. Using the Mie-Lorenz scattering theory, wavelength = 670 nm and  $m_r = 1.4$ ,  $\langle g \rangle = 0.744$  for a lognormal distribution with  $E(x) = 200$  nm and a standard deviation of

200. Changing the  $m_r$  to 1.5 produces  $\langle g \rangle = 0.677$ . This change can produce an increase in the radiative forcing by at least 12% for non-absorbing particles [Marshall, *et al.*, 1995].

### 3.3 Conclusions

This work is the first study to investigate SOA refractive indices with sufficient resolution to begin to assess variability of SOA  $m_r$  with precursor hydrocarbon, oxidation chemistry, aerosol mass concentration and possibly other factors such as temperature and aerosol aging. Aerosol  $m_r$ s for SOA studied here varies from about 1.38 to 1.61, a range that is likely to have a significant impact on radiative transfer calculations. Because of the polar nephelometer constraints, the experiments were performed at higher aerosol masses than generally observed in the atmosphere, which limits their direct applicability to radiative transfer calculations. Ongoing updates to the polar nephelometer will lower detection limits to a range more relevant to atmospheric conditions. More work is also needed to determine how  $m_r$  for SOA changes with hydrocarbon precursor, oxidation chemistry, mass concentration, temperature and other factors.

### 3.4 References

- Adler, G., A. A. Riziq, C. Erlick, and Y. Rudich (2010), Effect of intrinsic organic carbon on the optical properties of fresh diesel soot, *Proc. Natl. Acad. Sci. U. S. A.*, 107(15), 6699-6704.
- Barkey, B., S. E. Paulson, and A. Chung (2007), Genetic algorithm inversion of dual polarization polar nephelometer data to determine aerosol refractive index, *Aerosol Sci. Technol.*, 41(8), 751-760.
- Barkey, B., S.E. Paulson, and H. Kim (In press, 2010), Genetic algorithm retrieval of real refractive index from aerosol distributions that are not lognormal, *Aerosol Sci. Technol.*
- Chung, A., A. A. Lall, and S. E. Paulson (2008), Particulate emissions by a small non-road diesel engine: Biodiesel and diesel characterization and mass measurements using the extended idealized aggregates theory, *Atmos. Environ.*, 42(9), 2129-2140.
- Dick, W. D., P. J. Ziemann, and P. H. McMurry (2007), Multiangle light-scattering measurements of refractive index of submicron atmospheric particles, *Aerosol Sci. Technol.* 41(5), 549-569.



- Dinar, E., A. A. Riziq, C. Spindler, C. Erlick, G. Kiss, and Y. Rudich (2008), The complex refractive index of atmospheric and model humic-like substances (HULIS) retrieved by a cavity ring down aerosol spectrometer (CRD-AS), *Faraday Discuss.*, 137, 279-295.
- Griffin, R. J., D. R. Cocker, R. C. Flagan, and J. H. Seinfeld (1999), Organic aerosol formation from the oxidation of biogenic hydrocarbons, *J. Geophys. Res.-Atmos.*, 104(D3), 3555-3567.
- Hallquist, M., J. C. Wenger, U. Baltensperger, Y. Rudich, D. Simpson, M. Claeys, J. Dommen, N. M. Donahue, C. George, A. H. Goldstein, J. F. Hamilton, H. Herrmann, T. Hoffmann, Y. Iinuma, M. Jang, M. E. Jenkin, J. L. Jimenez, A. Kiendler-Scharr, W. Maenhaut, G. McFiggans, T. F. Mentel, A. Monod, A. S. H. Prevot, J. H. Seinfeld, J. D. Surratt, R. Szmigielski, and J. Wildt (2009), The formation, properties and impact of secondary organic aerosol: current and emerging issues, *Atmos. Chem. Phys.*, 9(14), 5155-5236.
- Hock, N., J. Schneider, S. Borrmann, A. Rompp, G. Moortgat, T. Franze, C. Schauer, U. Poschl, C. Plass-Dulmer, and H. Berresheim (2008), Rural continental aerosol properties and processes observed during the Hohenpeissenberg Aerosol Characterization Experiment (HAZE2002), *Atmos. Chem. Phys.*, 8(3), 603-623.
- Hodgson, R. J. W. (2000), Genetic algorithm approach to particle identification by light scattering, *J. Colloid Interface Sci.*, 229(2), 399-406.
- Jones, M. R., K. H. Leong, M. Q. Brewster, and B. P. Curry (1994), Inversion of light - scattering measurements for particle size and optical constants; experimental study, *Appl. Optics*, 33(18), 4035-4041.
- Kanakidou, M., J. H. Seinfeld, S. N. Pandis, I. Barnes, F. J. Dentener, M. C. Facchini, R. Van Dingenen, B. Ervens, A. Nenes, C. J. Nielsen, E. Swietlicki, J. P. Putaud, Y. Balkanski, S. Fuzzi, J. Horth, G. K. Moortgat, R. Winterhalter, C. E. L. Myhre, K. Tsigaridis, E. Vignati, E. G. Stephanou, and J. Wilson (2005), Organic aerosol and global climate modelling: a review, *Atmos. Chem. Phys.*, 5, 1053-1123.
- N. Lang-Yona, Y. Rudich, Th. F. Mentel, A. Bohne, A. Buchholz, A. Kiendler-Scharr, E. Kleist, C. Spindler, R. Tillmann, and J. Wildt (2010), The chemical and microphysical properties of secondary organic aerosols from Holm Oak emissions, *Atmos. Chem. Phys.*, 10, 7253-7265..
- Lienert, B. R., J. N. Porter, and S. K. Sharma (2003), Aerosol size distributions from genetic inversion of polar nephelometer data, *J. Atmos. Oceanic Technol.*, 20(10), 1403-1410.
- Malloy, Q. G. J., S. Nakao, L. Qi, R. Austin, C. Stothers, H. Hagino, and D. R. Cocker (2009), Real-Time Aerosol Density Determination Utilizing a Modified Scanning Mobility Particle Sizer Aerosol Particle Mass Analyzer System, *Aerosol Sci. Technol.*, 43(7), 673-678.
- Marshall, S. F., D. S. Covert, and R. J. Charlson (1995), Relationship between asymmetry parameter and hemispheric backscatter ratio - implications for climate forcing by aerosols, *Appl. Optics*, 34(27), 6306-6311.
- Mikhailov, E., S. Vlasenko, S. T. Martin, T. Koop, and U. Poschl (2009), Amorphous and crystalline aerosol particles interacting with water vapor: conceptual framework and experimental evidence for restructuring, phase transitions and kinetic limitations, *Atmos. Chem. Phys.*, 9(24), 9491-9522.
- Mishchenko, M. I., B. Cairns, G. Kopp, C.F. Schueler, B.A. Fafaul, J.E. Hansen, R.J. Hooker, T. Itchkawich, H.B. Maring, and L.D. Travis (2007), Accurate Monitoring of Terrestrial

- Aerosols and Total Solar Irradiance: Introducing the Glory Mission, *Bull. Amer. Meteor. Soc.*, 88, 677-691.
- Moffet, R. C., X. Y. Qin, T. Rebotier, H. Furutani, and K. A. Prather (2008), Chemically segregated optical and microphysical properties of ambient aerosols measured in a single-particle mass spectrometer, *J. Geophys Res.-Atmos.* 113(D12), 11.
- Ng, N. L., J. H. Kroll, A. W. H. Chan, P. S. Chhabra, R. C. Flagan, and J. H. Seinfeld (2007), Secondary organic aerosol formation from m-xylene, toluene, and benzene, *Atmos. Chem. Phys.*, 7(14), 3909-3922.
- Paulson, S. E., M. Chung, A. D. Sen, and G. Orzechowska (1998), Measurement of OH radical formation from the reaction of ozone with several biogenic alkenes, *J. Geophys Res.-Atmos.* 103(D19), 25533-25539.
- Presto, A. A., K. E. H. Hartz, and N. M. Donahue (2005), Secondary organic aerosol production from terpene ozonolysis. 2. Effect of NO<sub>x</sub> concentration, *Environ. Sci. Technol.*, 39(18), 7046-7054.
- Pye, H. O. T., and J. H. Seinfeld (2010), A global perspective on aerosol from low-volatility organic compounds, *Atmos. Chem. Phys.*, 10(9), 4079-4141.
- Russell, L. M., R. C. Flagan, and J. H. Seinfeld (1995), Asymmetric instrument response resulting from mixing effects in accelerated DMA-CPC measurements, *Aerosol Sci. Technol.* 23(4), 491-509.
- Saathoff, H., K. H. Naumann, O. Mohler, A. M. Jonsson, M. Hallquist, A. Kiendler-Scharr, T. F. Mentel, R. Tillmann, and U. Schurath (2009), Temperature dependence of yields of secondary organic aerosols from the ozonolysis of alpha-pinene and limonene, *Atmos. Chem. Phys.*, 9(5), 1551-1577.
- Schnaiter, M., C. Linke, O. Mohler, K. H. Naumann, H. Saathoff, R. Wagner, U. Schurath, and B. Wehner (2005), Absorption amplification of black carbon internally mixed with secondary organic aerosol, *J. Geophys Res.-Atmos.*, 110(D19), 11.
- Shaw, G. E. (1979), Inversion of optical scattering and spectral extinction measurements to recover size spectra, *Appl. Optics*, 18(7), 988-993.
- Shilling, J. E., Q. Chen, S. M. King, T. Rosenoern, J. H. Kroll, D. R. Worsnop, P. F. DeCarlo, A. C. Aiken, D. Sueper, J. L. Jimenez, and S. T. Martin (2009), Loading-dependent elemental composition of alpha-pinene SOA particles, *Atmos. Chem. Phys.*, 9(3), 771-782.
- Tokonami, S., and E. O. Knutson (2000), The scan time effect on the particle size distribution measurement in the scanning mobility particle sizer system, *Aerosol Sci. Technol.*, 32(3), 249-252.
- Van de Hulst, H. C. (1957), *Light Scattering by Small Particles*, Wiley.
- Verhaege, C., V. Shcherbakov, and P. Personne (2008), Limitations on retrieval of complex refractive index of spherical particles from scattering measurements, *J. Quant. Spectrosc. & Rad. Trans.* 109(14), 2338-2348.
- Zhao, F. (1999), Determination of the complex index of refraction and size distribution of aerosols from polar nephelometer measurements, *Appl. Optics*, 38(12), 2331-2336.

**Table 3.1. Initial conditions, temperatures, relative humidities and results of the photo oxidation experiments**

Expt.	Initial Conditions						Results					
	Hydrocarbon	HC (ppb)	NO <sub>x</sub> (ppb)	HC/NO <sub>x</sub> (ppbC/ppb)	Temp (°C) <sup>1</sup>	RH (%) <sup>1</sup>	ΔHC (ppb)	# density (#/cm <sup>3</sup> ) <sup>2</sup>	Size mode (nm) <sup>2</sup>	Mass <sup>3</sup> (μg/m <sup>3</sup> )	NO < 1 ppb Mass <sup>4</sup> (μg/m <sup>3</sup> )	Yield <sup>5</sup> (%)
<b>15-Jul</b>	α-pinene	845	780	11	37-39	14-13	840	18100	573	190-2100	420	47
<b>23-Sep</b>	α-pinene	540	480	11	43-48	17-14	540	9250	514	530-830	530	34
<b>13-Jul</b>	α-pinene	470	270	17	39-42	17-15	460	27800	359	340-970	420	42
<b>21-Sep</b>	α-pinene	550	240	23	40-37	15-17	547	31100	429	530-1500	950	62
<b>21-Oct</b>	α-pinene	500	260	19	38-36	14-16	485	21800	478	440-1600	910	68
<b>27-Jul</b>	β-pinene	610	240	25	39-35	14-17	459	6640	496	97-550	150	25
<b>25-Sep</b>	β-pinene	640	230	28	46-37	12-17	528	9140	533	150-900	550	37
<b>3-Aug</b>	β-pinene	405	370	11	39-33	19-25	328	9210	400	93-430	120	26
<b>10-Aug</b>	Toluene	1710	820	15	38-37	15-17	617	19000	289	190-310	86	15
<b>12-Aug</b>	Toluene	3670	940	29	36-39	18-16	914	18500	372	580-560	190	23
<b>7-Oct</b>	Toluene	3240	820	29	32-28	15-17	761	19000	385	200-680	200	29
<b>14-Aug</b>	Toluene	3750	3100	8.6	38-34	17-22	1160	10400	414	150-490	N/A	12
<b>9-Oct</b>	Toluene	3400	2800	8.9	33-25	13-19	663	12400	322	160-240	N/A	11
<b>23-Oct</b>	Toluene	3200	3100	7.5	42-30	11-19	974	9300	414	150-410	410	14

<sup>1</sup>Initial and final temperature and relative humidity

<sup>2</sup>Final aerosol number concentration and size mode. These values have not been adjusted for wall losses.

<sup>3</sup>Mass concentration in the chamber was determined from the SMPS measured size distribution in the chamber over the period for which meaningful PN measurements were made. Particle density was assumed as 1.2 g/cm<sup>3</sup> for α and β-pinene and 1.24 g/cm<sup>3</sup> for toluene.

<sup>4</sup>Mass concentration when [NO] went below the 1ppb detection limit of the NO<sub>x</sub> instrument. [NO] did not reach this level on 14-Aug and 9-Oct.

<sup>5</sup>Calculated from peak measured aerosol mass corrected for wall losses and the corresponding quantity of reacted hydrocarbon. Because of the uncertainties in the measurement from GC (± 3 %) and measurement of SMPS (± 10 %) yields are uncertain to ± 10 %.

**Table 3.2. Initial conditions, temperatures, relative humidities and results of the ozonolysis experiment**

Run	Hydrocarbon	Initial conditions				Results				
		HC <sup>1</sup> (ppb)	Ozone (ppb)	Temp (°C)	RH (%)	$\Delta$ HC (ppb)	# density <sup>2</sup> (#/cm <sup>3</sup> )	Size mode <sup>2</sup> (nm)	Mass <sup>3</sup> ( $\mu$ g/m <sup>3</sup> )	Yield <sup>4</sup> (%)
29-Jun	$\alpha$ -pinene	100	50	25-22	32-38	N/A	5440	269	57-78	N/A
31-Jul	$\alpha$ -pinene	100	50	26-29	33-29	N/A	4990	279	59-87	N/A
7-Nov	$\alpha$ -pinene	500	300	29-30	20-19	N/A	9410	478	420-650	N/A
12-Feb	$\alpha$ -pinene	500	240	12-16	28-22	456	78100	260	760-960	50
17-Jul	$\alpha$ -pinene	500	240	26-29	33-29	443	25300	346	750-790	44
1-Jul	$\alpha$ -pinene <sup>5</sup>	500	250	24-26	38-35	464	24300	334	440-700	32
3-Jul	$\alpha$ -pinene <sup>5</sup>	500	250	24-23	29-31	463	18900	372	720-740	37
29-Jul	$\alpha$ -pinene	1000	500	28-29	26-25	905	34900	429	2000-2300	55
19-Oct	$\alpha$ -pinene	1000	500	22-23	31-25	743	84900	334	2500-2700	97
19-Jun	$\beta$ -pinene	500	238	25-26	43-38	399	19800	300	160-350	21
13-Apr	$\beta$ -pinene	1000	485	26-24	33-38	660	88800	241	790-1200	46
17-Jun	$\beta$ -pinene	1000	485	24-23	39-42	695	89800	300	1100-1300	41
2-Nov	$\beta$ -pinene	2000	1003	27-28	26-24	1222	69400	359	1200-2900	65
4-Nov	$\beta$ -pinene	3000	1300	22-26	28-23	1404	42700	478	2600-3700	61

<sup>1</sup>Because hydrocarbons react immediately with O<sub>3</sub>, hydrocarbon initial concentrations are estimated based on injected liquid and are accurate to within  $\pm 20\%$ .

<sup>2</sup>Final aerosol number concentration and size mode. These values have not been adjusted for wall losses.

<sup>3</sup>Mass was determined from the SMPS measured size distribution in the chamber over the period for which meaningful pn measurements were made. Particle density was assumed as 1.2 g/cm<sup>3</sup> for  $\alpha$  and  $\beta$ -pinene and 1.24 g/cm<sup>3</sup> for toluene. Measured particle number concentrations were corrected.

<sup>4</sup>Calculated from peak measured aerosol mass corrected for wall losses and the corresponding quantity of reacted hydrocarbon. Because of the uncertainty in the initial concentrations ( $\pm 20\%$ ), measurement of GC ( $\pm 3\%$ ) and measurement of SMPS ( $\pm 10\%$ ) yields are uncertain to  $\pm 25\%$ .

<sup>5</sup>Cyclohexane was added in 50 fold excess compared to the hydrocarbon to suppress OH formation.

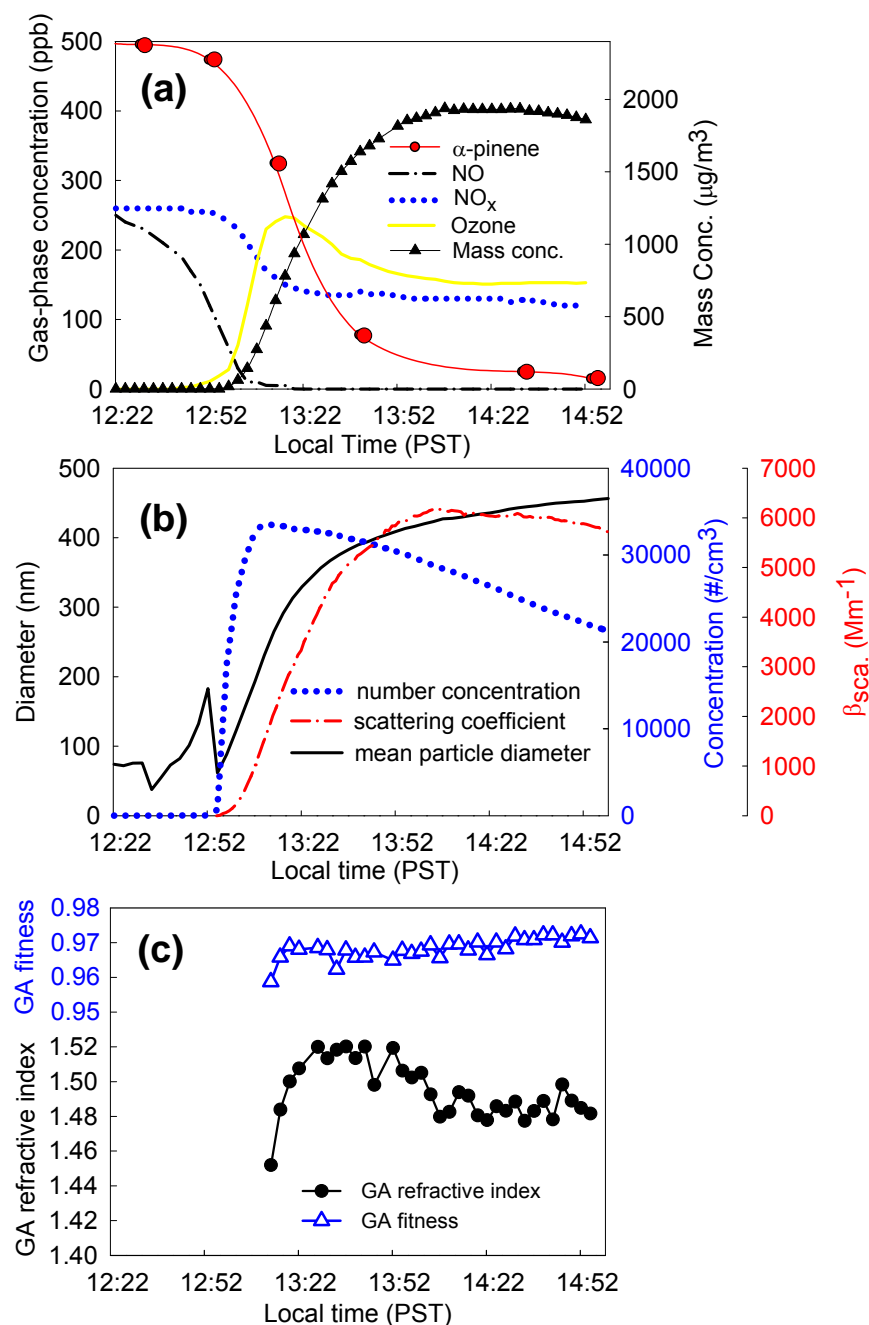


**Figure 3.1.** Profile of an  $\alpha$ -pinene photooxidation experiment performed on Oct. 21, with initial concentrations of 500 ppb  $\alpha$ -pinene and 260 ppb  $\text{NO}_x$ . (a) Gas phase concentrations (hydrocarbon, NO,  $\text{NO}_x$ ,  $\text{O}_3$ ) and aerosol mass concentration (corrected for wall losses; see text). (b) Time evolution of the SOA particle number concentrations, mean diameter and integrated scattering ( $\beta_{\text{sca}}$ ). (c) The GA determined real refractive index, and associated fitness values for all viable polar nephelometer measurements.

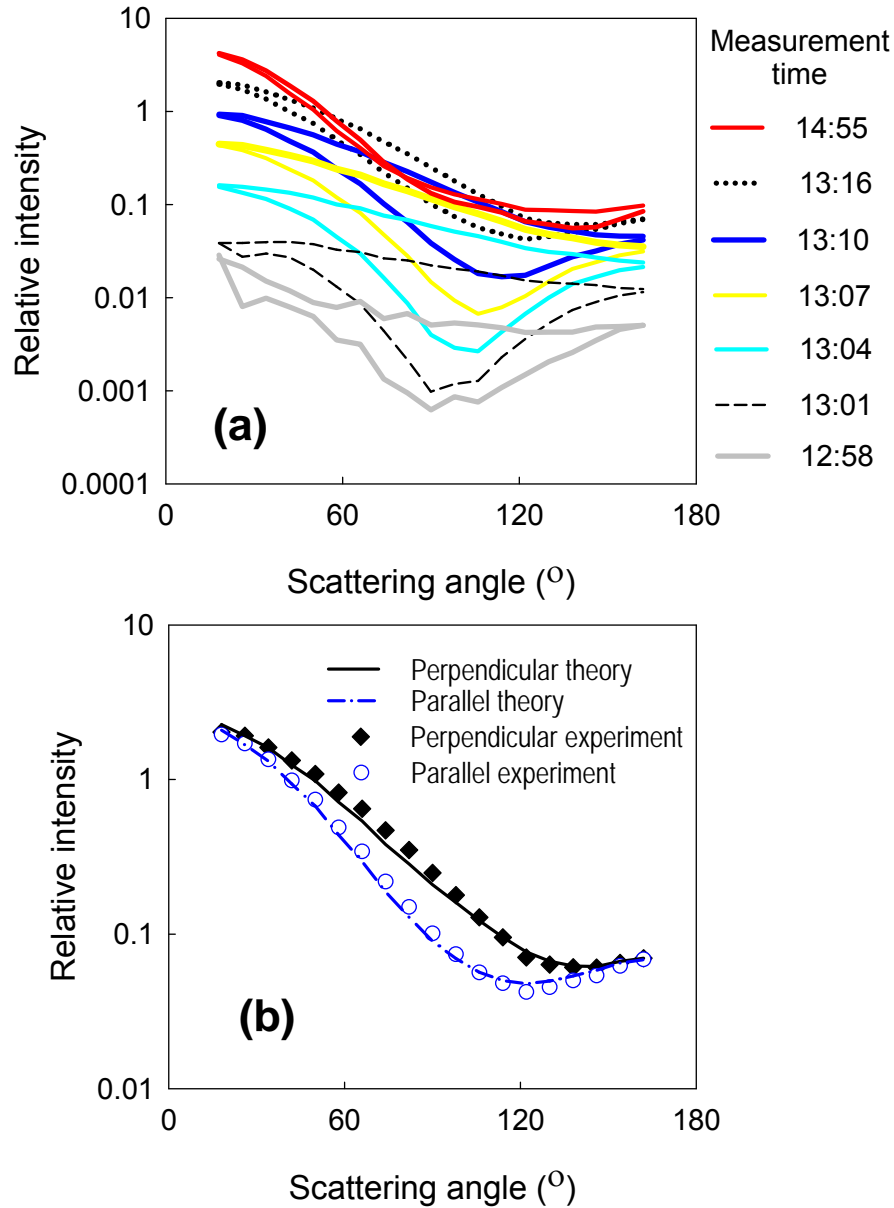


**Figure 3.2.** (a) Selected scattering properties recorded with the PN as particles grow for the experiment performed on 21 October. (b) Scattering at 13:16 (after 46 min), when the particle had a median size of 291 nm. Also shown GA determined fit using Mie-Lorenz theory, with a  $m_r=1.48$ , and at fitness of 0.965.

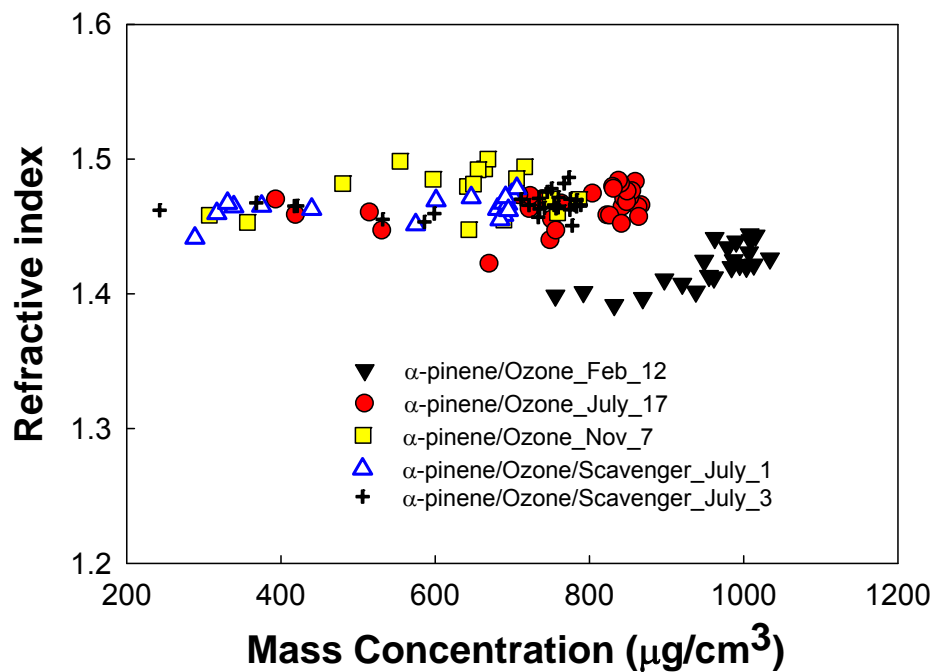


**Figure 3.3.** Retrieved refractive indices for SOA formed by  $\alpha$ -pinene ozonolysis with and without scavenger. The experiment on Feb. 12 was performed at lower temperature than the others (Table 3.2).

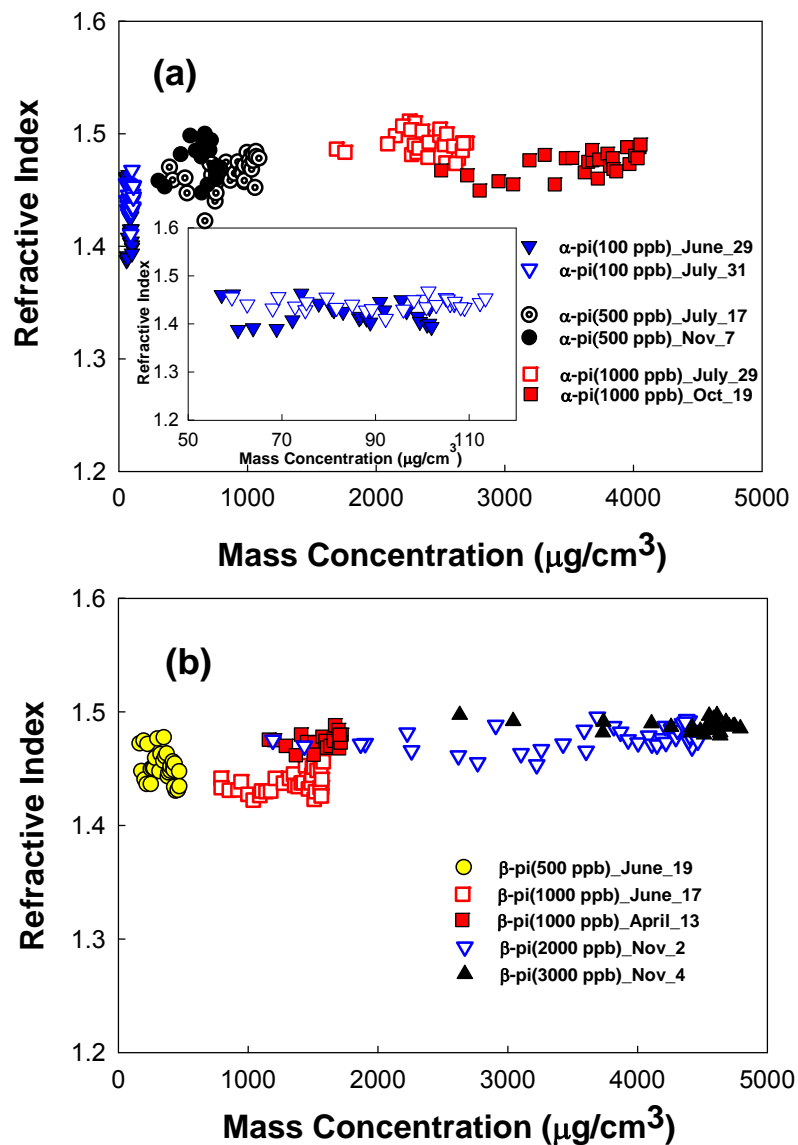


**Figure 3.4.** Retrieved refractive indices for SOA formed by ozonolysis of (a)  $\alpha$ - pinene (b)  $\beta$ - pinene at different initial concentration.  $\alpha$ -pinene data from June 29 and July 31 at low mass concentration are also shown in the insert in Figure 4a, and the low temperature data (Feb. 12) are omitted.



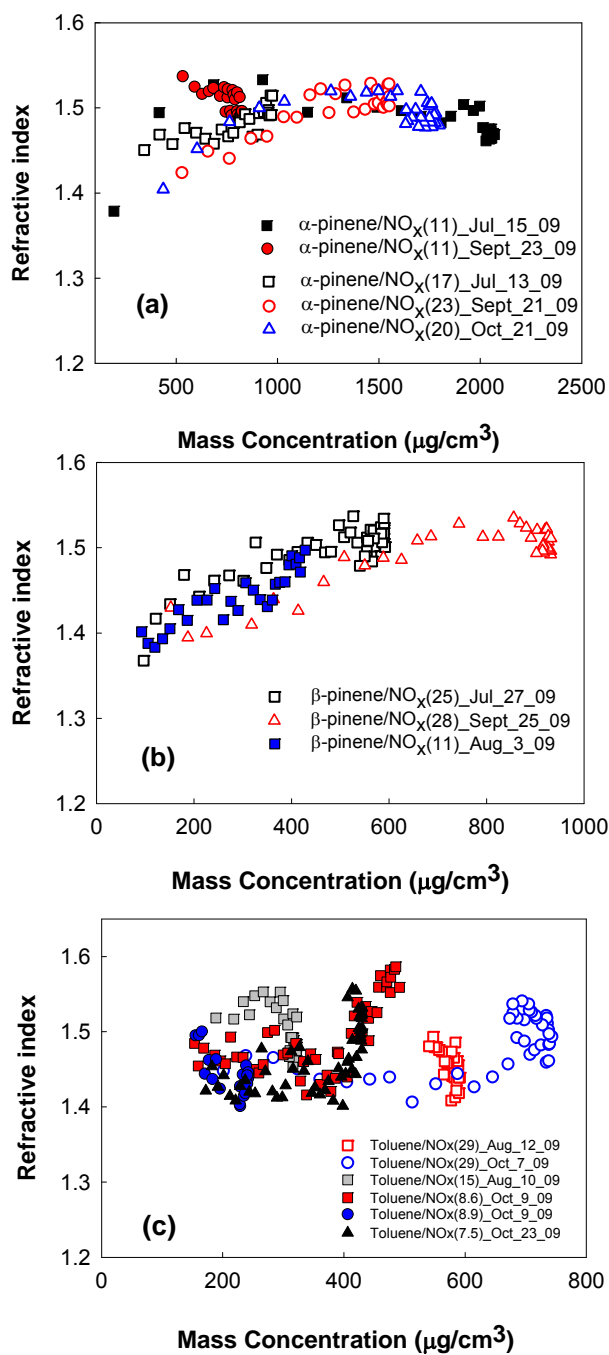


**Figure 3.5.** Retrieved refractive indices for SOA generated from photooxidation of (a)  $\alpha$ -pinene (b)  $\beta$ -pinene, and (c) toluene.

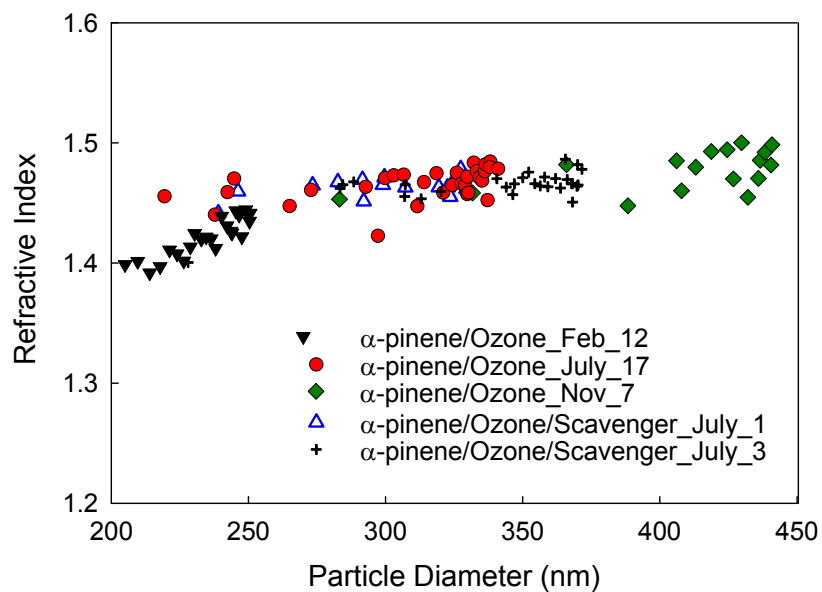


**Figure 3.6.** Retrieved refractive indices for SOA formed by  $\alpha$ -pinene ozonolysis with and without scavenger as a function of diameter.

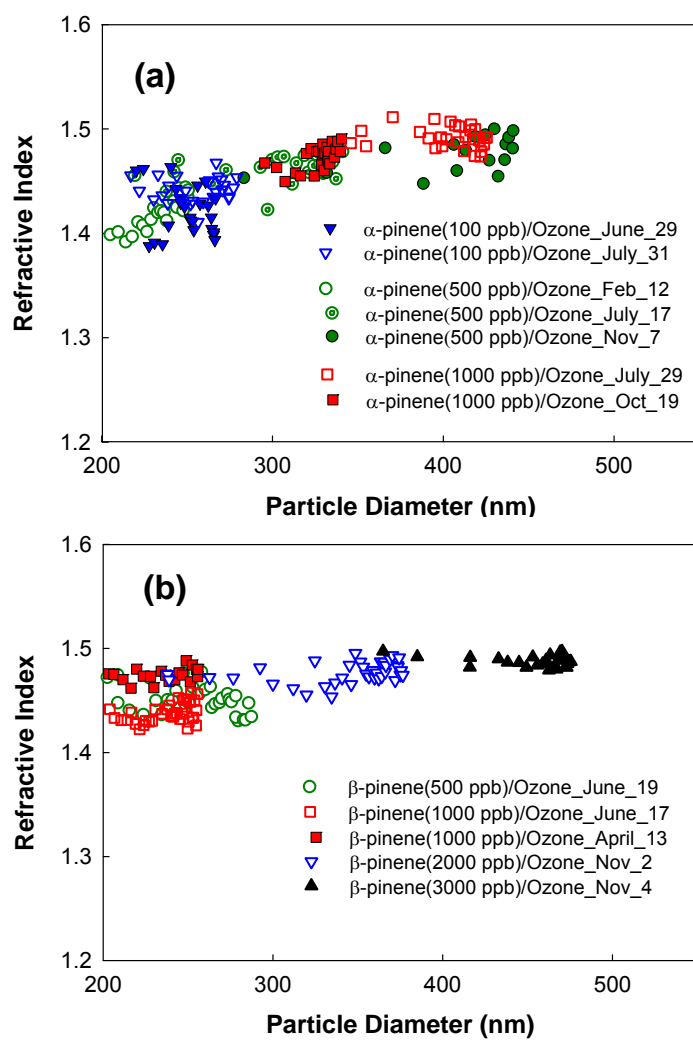


**Figure 3.7.** Retrieved refractive indices for SOA formed by ozonolysis of (a)  $\alpha$ - pinene (b)  $\beta$ - pinene at different initial concentration as a function of diameter.

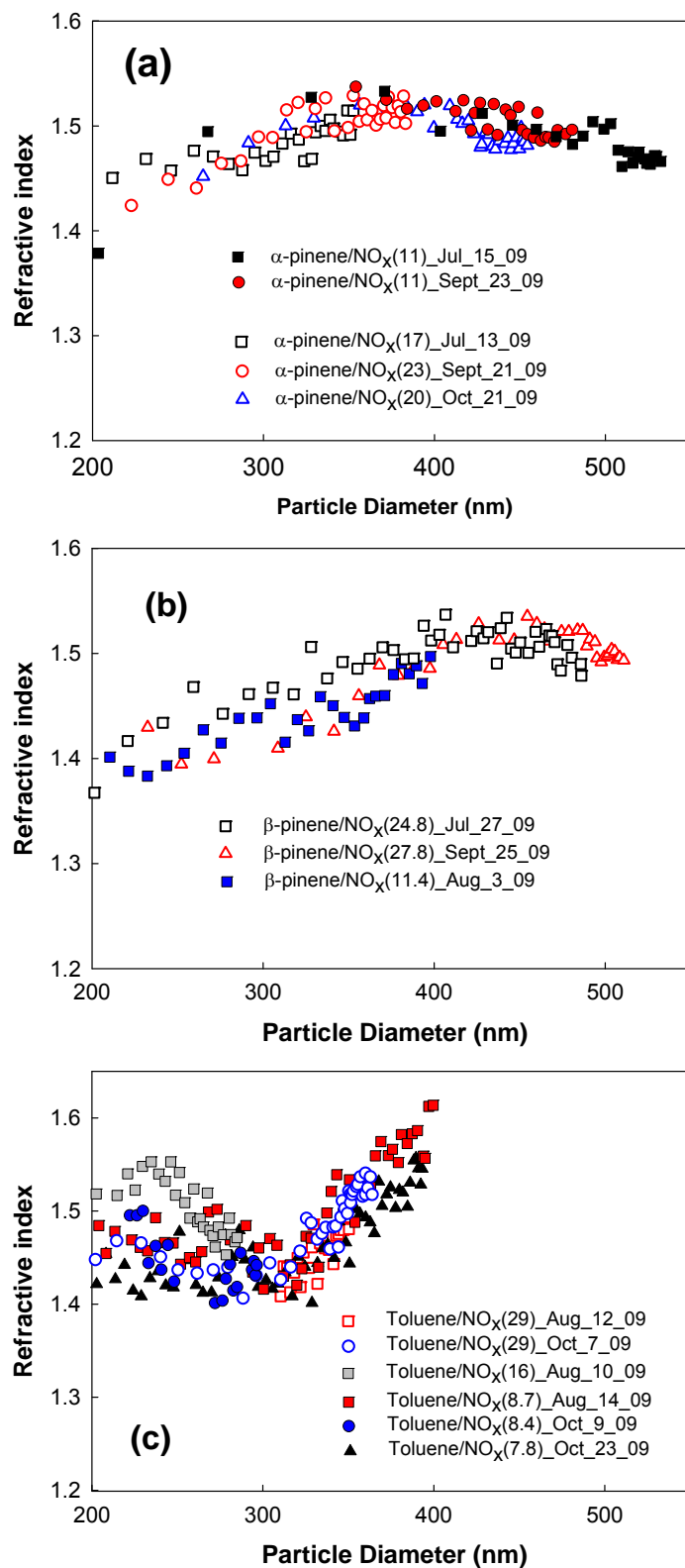


**Figure 3.8.** Retrieved refractive indices for SOA formed by photooxidation of (a)  $\alpha$ -pinene (b)  $\beta$ -pinene (c) toluene as a function of diameter

## **Chapter 4**

**Real refractive indices and formation yields of secondary organic aerosol generated from photooxidation of limonene and  $\alpha$ -pinene: the effect of the HC/NO<sub>x</sub> ratio**

## 4.1 Experimental

Table 4.1 shows initial conditions and summary statistics for 11 experiments. Initially, the chamber, covered with a black tarpaulin (supported on a frame above the chamber), was half filled with purified air. At this point NO (Scott Specialty Gases) was added. Next, the SOA precursor hydrocarbon liquid was evaporated into the air stream filling the chamber. Limonene (Aldrich, 99.8 %) and  $\alpha$ -pinene (Fluka, 98.5 %) were used as received. The chamber contents were then allowed to mix for about 40 min. Once the gas chromatograph returned two SOA precursor hydrocarbon measurements within 2% of one another, the tarps were removed and photochemistry initiated. The overall oxidation time for limonene and  $\alpha$ -pinene was 4 – 6 h and 4 – 4.5 h, respectively depending on the HC/NO<sub>x</sub> ratio.

Aerosols were characterized with the polar nephelometer (described below), an integrating nephelometer (Ecotech M9003), a scanning mobility particle sizer (SMPS, TSI model 3080), and by gravimetric mass ( $\pm 1 \mu\text{g}$ , Sartorius). The primary purpose of the integrating nephelometer and gravimetric measurement is to provide checks for the SMPS and PN; the integrating nephelometer also provides temperature and relative humidity in the chamber, and some of the filter-based gravimetric samples are used for a separate project investigating reactive oxygen species in particles (e.g. Wang et al.<sup>12</sup>). Filter samples for gravimetric analysis and were collected on pre-baked (24 h at 550 °C) 25 mm quartz fiber for 20 – 40 min at 20 LPM toward the end of the experiments. Filters were allowed to equilibrate for 24 h in a temperature and humidity controlled room before weighting using a microbalance ( $\pm 1 \mu\text{g}$ , Sartorius).

SOA is lost to the walls of the chamber during the experiment. Size dependent wall loss was determined in a separate experiment described in Kim et al.<sup>7</sup> The first order loss coefficients vary between  $0.0012 \text{ min}^{-1}$  and  $0.0081 \text{ min}^{-1}$ , depending on particle size.

The upgraded polar nephelometer used in this study and its calibrations are described in detail in Kim et al.<sup>7</sup> For this study, however, we have replaced the laser with a 1W 532 nm laser (Intelite Inc.). In addition to providing data near the peak of the solar spectrum, this laser has greatly increased sensitivity so that we can now obtain reliable retrievals at ambient mass concentrations in the 10 – 140  $\mu\text{g}/\text{m}^3$  range, and in some cases below 10  $\mu\text{g}/\text{m}^3$ . Every 16 seconds, the PN measures light intensities scattered at 21 discrete angles by a stream of aerosols intersecting the beam of the laser. A  $\frac{1}{2}$  wave plate appropriate for 532 nm rotates the polarization plane of the incident light to be parallel or perpendicular to the measurement scattering plane. The 1 LPM aerosol sample flow, which intersects a 2 x 5 mm beam, is confined to the center of the scattering plane by a 10 LPM sheath flow. Sample phase functions and retrievals are shown in Figure 4.1. The SMPS measures 19 – 948 nm particle size distributions every 3 minutes, and these are used to interpret the PN data as well as determine aerosol formation yields. A multiple charging correction supplied by the manufacturer was applied to all SMPS scans.

#### **4.2 Photochemical oxidation and partitioning calculations**

We explore limonene oxidation in more detail with two aims: first to assess how well current literature understanding is able to reproduce observed  $m_p/s$ , and second to explore the influence of the different reaction pathways on the aerosol refractive index. The majority of limonene reaction rates and chemical mechanisms in our model are taken from Leungsakul et al.<sup>14</sup> Initial oxidation reactions with OH, O<sub>3</sub>, NO<sub>3</sub> and O(<sup>3</sup>P) with the terminal and internal double bonds of limonene lead to first generation products. These products can undergo further reactions in which their remaining double bond is also oxidized, leading to second generation products. Second generation products can undergo further oxidative steps leading to third generation

products. Where mechanistic information for third generation products (i.e., C<5) was available in the Master Chemical Mechanisms (MCM v 3.2), those pathways were added to the chemical kinetic model. Alkyl peroxy radicals (RO<sub>2</sub>) formed by reactions of limonene with OH, NO<sub>3</sub> and O(<sup>3</sup>P) play a central role in the production of lower volatility products. Using the approach of Leungsakul et al.,<sup>14</sup> here we lumped all RO<sub>2</sub> species together to make the reaction scheme tractable. Criegee intermediates are treated separately. We note that a significant shortcoming of the model is that it does not include oligomerization reactions or any processes that incorporate smaller more volatile species into the particle phase. The dominant condensing species produced by the oxidation mechanism are shown in Table 4.2.

We calculated the gas-aerosol partitioning of the limonene oxidation products using the equilibrium absorptive partitioning equation<sup>15</sup> described in the Appendix B. Vapor pressures of most limonene products have not been measured, so these were estimated based on structure-activity relationships developed by Myrdal and Yakowsky<sup>16</sup> and modified by Camredon et al.<sup>17</sup>, as described in the supplementary material.

### 4.3 Results and Discussion

Eleven experiments were performed with two different precursors (limonene and  $\alpha$ -pinene) under three different conditions; low NO<sub>x</sub> (initial HC/NO<sub>x</sub> = 19 – 33 ppbC/ppb), intermediate NO<sub>x</sub> (HC/NO<sub>x</sub> = 13 ppbC/ppb) and high NO<sub>x</sub> (HC/NO<sub>x</sub> = 6.3 – 9.6 ppbC/ppb). Detailed experimental conditions are shown in Table 4.1; precursor concentrations ranged from 60 – 77 ppb for limonene, 65 – 120 ppb for  $\alpha$ -pinene and 20 – 125 ppb for NO.  $\alpha$ -Pinene required higher precursor concentrations to produce similar SOA mass concentrations compared



to limonene. With the exception of one  $\alpha$ -pinene experiment, temperatures ranged from 31°C – 39°C and relative humidity (RH) ranged from 10 % – 26 %.

#### 4.3.1 Reaction profile of a photooxidation experiment

The observed and simulated evolution of NO, NO<sub>x</sub>, O<sub>3</sub>, limonene and wall-loss corrected aerosol mass concentration in a typical photooxidation limonene experiment (Nov. 5) is shown in Figure 4.2. The experiment had initial concentrations of 72 ppb limonene and 115 ppb NO. SOA began to nucleate 2h after the chamber was initially exposed to sunlight, and quickly grew to several hundred nanometers. The time evolution of experimental (symbols) gaseous compounds (limonene, O<sub>3</sub>, NO<sub>x</sub>) are mostly well represented by the model (lines). Much of the difference between the NO<sub>x</sub> concentration of the experiment and simulation is likely due to detection of species such as nitric acid by the NO<sub>x</sub> instrument. Limonene reacts somewhat faster in the model than the experiments. This has the result of overestimating the importance of RO<sub>2</sub> + NO reaction relative to the chemistry in the experiment because most of the limonene is consumed while the model NO is still several ppb. This issue is discussed further below (section 4.5.3.2).

Figure 4.2b shows the evolution of particle number, mean diameter, and integrated scattering ( $\beta_{\text{sca}}$ ). The particles continued to grow throughout, however particle number concentrations dropped slowly due to coagulation and wall loss after 13:10.  $\beta_{\text{sca}}$  continues to increase as particle numbers drop until 15:17, after which it declines slowly. At this point, the decreases in scattering associated decreasing numbers overtake the increases due to growing particles (Figure 4.2b). Viable retrievals from the PN signal were first obtained when the particles had grown to about 247 nm at 14:08 (Figure 4.2a).

### 4.3.2 Aerosol formation yields

Table 4.1 shows aerosol yields (aerosol mass/HC reacted, both in  $\mu\text{g}/\text{m}^3$ ), calculated from SMPS volumes. SOA are accepted to be reasonably spherical, as verified in Barkey et al.<sup>8</sup> SOA mass was calculated based on size distributions measured by the SMPS assuming spherical particles with a density of  $1.25 \text{ g}/\text{cm}^3$  for limonene and  $1.2 \text{ g}/\text{cm}^3$  for  $\alpha$ -pinene.<sup>1,18</sup> Measured particle number concentrations were corrected for size-dependent wall loss (Section 4.3). Gravimetric mass measurements were used to check the SMPS masses, and averaged  $17 \pm 7 \%$  higher than that of SMPS mass measurements. The gravimetric filter samples are expected to overestimate particle mass somewhat due to adsorption of gases during sampling.<sup>11</sup>

Aerosol yields are controlled by the parent hydrocarbon, oxidation chemistry, temperature and aerosol mass concentration, suggesting that yields should be higher at lower temperatures, higher initial HC/NO<sub>x</sub> ratios, and higher aerosol mass in the chamber (e.g., Hallquist et al.<sup>1</sup>). All of these effects on aerosol yield are observed in our experiments. As shown in Figure 4.3, yield is a strong function of mass concentration, particularly at low masses. Our results are in excellent agreement with literature yields for both  $\alpha$ -pinene and limonene.<sup>19,20</sup> Note that literature data shown in Figure 4.3 was normalized using the same density assumptions (above) to allow comparison. As expected, aerosol yields from limonene are significantly higher than for  $\alpha$ -pinene (e.g., 25 – 33% vs 14 -18% at  $100 \mu\text{g}/\text{m}^3$  respectively).

The influence of HC/NO<sub>x</sub> ratio on aerosol yield can be seen in Figure 4.3; higher HC/NO<sub>x</sub> ratios, which produce more RO<sub>2</sub> + HO<sub>2</sub> and RO<sub>2</sub> + RO<sub>2</sub> chemistry, produce somewhat higher aerosol yields. This effect is more pronounced for  $\alpha$ -pinene than for limonene. Averaging similar temperature experiments (Aug. 26 & Sept 17 vs. Sept. 15 & Nov. 5 for limonene and Sept. 3 & 10 vs. Sept. 13 & 20 for  $\alpha$ -pinene) and fitting each resulting curve with a 2<sup>nd</sup> order

polynomial ( $R^2 > 0.98$ ), results in yields that are higher under low  $\text{NO}_x$  conditions by 33 to 17% for limonene and 30 to 50% for  $\alpha$ -pinene as the aerosol mass concentration increases from 1 to  $100 \mu\text{g}/\text{m}^3$ . Given instrumental uncertainties and temperature and other differences between the experiments, these values carry  $\sim \pm 30\%$  uncertainties.

Most of our experiments were performed at moderate temperatures (31 – 39 °C). Experiments performed at cooler temperatures (Sept. 17 limonene and Sept. 3  $\alpha$ - pinene), have slightly higher yields than experiments performed at  $\sim 5$  °C higher temperatures but with similar mass concentrations and  $\text{HC}/\text{NO}_x$  ratios (Aug. 26 limonene and Sept. 24  $\alpha$ - pinene; Table 4.1 and Figure 4.3).

### **4.3.3 Determination of refractive index**

#### **4.3.3.1 SOA refractive indices**

Figure 4.4 shows the average  $m_r$  for each experiment, plotted as a function of  $\text{HC}/\text{NO}_x$  ratio. There is a clear inverse relationship between  $m_r$  and the  $\text{HC}/\text{NO}_x$  ratio for limonene at lower values:  $m_r$  begins at 1.54 at  $\text{HC}/\text{NO}_x = 6.3$ , decreases to 1.41 at  $\text{HC}/\text{NO}_x = 19$ , and remains at this low value at higher  $\text{HC}/\text{NO}_x$  ratios. The trend for  $\alpha$ -pinene is similar but less clear. The  $\text{HC}/\text{NO}_x$  ratio also strongly influences particle diameters (discussed below), and Figure 4.5 shows retrieved refractive indices as a function of particle diameter. Figure 4.6 shows the same data plotted as a function of mass concentration (in the chamber, not corrected for wall losses). Particle diameter is consistently the independent variable best correlated with refractive index data; this was also the case for the experiments presented by Kim et al.,<sup>7</sup> although the data were not plotted with respect to particle diameter in that paper. We observe that  $m_r$ s can increase or decrease with particle size, depending on the size range, parent HC, oxidation chemistry and

other factors. We note that there is no evidence of significant absorption at 532 nm by the particles investigated here. GA retrievals (which can provide only a rough estimate of absorption) return imaginary components of order  $10^{-5}$ , and particles are colorless when collected on filters. Zhong et al.<sup>10</sup> report a small absorption coefficient of  $0.038 \text{ m}^2/\text{g}$  at 350 nm for limonene SOA generated by photooxidation ( $\text{HC}/\text{NO}_x = 30$ ), and negligible absorption above 500 nm. In addition to  $\text{HC}/\text{NO}_x$  ratio, particle chemical composition is expected to depend on the particle mass concentration, temperature, water uptake and over longer time scales, particle phase reactions and heterogeneous aging. Our experiments were performed in a narrow range of relative humidities (14 % – 25 %) and vary by 1 – 3% in any individual experiment, so that water uptake, or phase, is not expected to change much due to changes in RH (e.g., Mikhailov et al.<sup>21</sup>). The amount of water uptake may change considerably, however as the particles grow.<sup>22,23</sup> Fresher/smaller particles may contain a higher fraction of hygroscopic highly oxidized polar compounds with low volatility, while older/larger particles may contain less hygroscopic, higher volatility condensing species and/or oligomers.<sup>22,24,25</sup> Temperatures span a moderate range (in most cases  $31^\circ\text{C} - 39^\circ\text{C}$ , Table 4.1) and the experiments that deviate outside this range have reasonably consistent refractive indices with the other data (Figures 4.5 and 4.6). The refractive index appears to increase only slightly (Figure 4.6) with mass concentration. Mass concentration appeared to be one of the controlling variables of  $m_p$ s of  $\alpha$ - and  $\beta$ -pinene SOA described by Kim et al.,<sup>7</sup> however, that study explored mass concentrations that were factors of 5 – 18 higher than the mass concentrations in the current study.

For both precursors,  $\text{HC}/\text{NO}_x$  ratios have a strong influence on particle size distributions. Table 4.1 includes the maximum number concentration and size mode for each experiment. Generally high  $\text{NO}_x$  conditions generate small numbers of large particles, whereas low  $\text{NO}_x$

conditions generate high numbers of small particles. In our experiments, as is typical for biogenic photooxidation experiments,<sup>7,14</sup> particle nucleation consistently occurs after ozone starts to build up. The maximum particle number concentration has a positive correlation with the ratio of the ozone concentration at the time particles start nucleating to the initial HC concentration ( $O_3/HC_i$ ; Table 4.1, Figure 4.7), a relationship suggested by Gao et al.<sup>25</sup> Prior to the initiation of nucleation, a significant fraction of the HC (38% - 58% for limonene and 34% - 42 % for  $\alpha$ -pinene) had already reacted (with OH and to a lesser degree,  $O(^3P)$ ). Once nucleation began, the particles grew rapidly due to the buildup of products with sufficiently low volatility to condense but not nucleate. It follows that if a larger fraction of the HC is consumed prior to nucleation, larger concentrations of condensing species will be available to make particles grow larger. Figure 4.8 shows a good correlation between the particle size and the quantity of HC consumed before measurable ozone forms for both limonene and  $\alpha$ -pinene. Generally we observe that less HC is consumed under low  $NO_x$  (high  $HC/NO_x$ ) conditions due to early ozone generation compared to high  $NO_x$ , explaining the formation of more abundant smaller particles (and higher mass yields) under low  $NO_x$  conditions.

Complicating the hypothesis put forth above is the potential influence of growth stage and other factors such as temperature, which for a given particle size may vary considerably between experiments. Growth stage depends on factors such as initial HC, but also changes in insolation and temperature, which are not completely controllable in our outdoor chamber. For example, the 235 nm  $\alpha$ -pinene particles generated on Sept. 10, 20 and 13 were at the end, middle and beginning of growth, respectively.

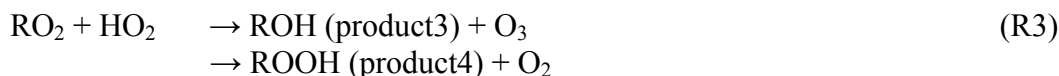
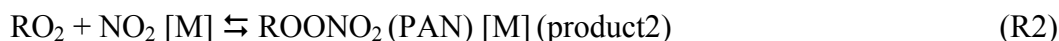
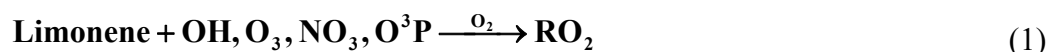
For limonene especially, we consistently observe that the smallest, newest particles have a significantly lower refractive indices than slightly older, larger particles (Figs 4.5 and 4.6); after

the particles grow to approximately 90 % of their maximum size, their  $m_r$ s level out. The HC/NO<sub>x</sub> ratio-dependent differences in condensing species and their relative contribution appear to determine size distribution as well as the  $m_r$ s. The trend for  $\alpha$ -pinene is similar to limonene, except that for this system  $m_r$ s are reasonably flat, even slightly decreasing at the smallest sizes/youngest particles, before increasing at sizes above 180 nm. The explanation for the low values may lie in a high fraction of water ( $m_r = 1.334$ ) uptake by the fresh particles. The smaller/newer particles are expected to contain a higher fraction of low volatility, highly oxidized material compared to larger particles, which have grown via condensation of more volatile, less oxidized material<sup>22,24</sup>. Consistent with this, Varutbankul et al.<sup>22</sup> reported remarkably high water fractions of up to 45% for newer particles in chamber experiments similar to ours. These measurements were performed at somewhat higher relative humidities, ~50%, and for different biogenic precursors, including  $\alpha$ -pinene. However, a high water fraction for limonene SOA might be expected based on other measurements indicating limonene SOA is more hygroscopic than several other types of SOA, including  $\alpha$ -pinene<sup>23</sup>. We also note that the organic hydroperoxides which should dominate under low NO<sub>x</sub> conditions, are more hygroscopic than species such as organic nitrates associated with high NO<sub>x</sub> conditions, consistent with the observation that the lowest  $m_r$ s are associated with low NO<sub>x</sub> conditions. Additionally, a high water fraction may result in increased uptake of water soluble species such as glyoxal and acetic acid (= 1.39, 1.36 respectively)<sup>26-29</sup>, which would further lower the refractive index. Small, low  $m_r$  species may also result from particle phase reactions such as carbocation rearrangements and retroaldol reactions.<sup>1,30</sup> The trend for increasing  $m_r$  as the experiments progress is consistent between experiments; generally these younger particles follow the same  $m_r$  trend as particles of similar size in other experiments. The observation that the low NO<sub>x</sub> experiments reach lower

final refractive indices (compared to the high NO<sub>x</sub> experiments) is consistent with the low refractive index of the smaller, younger particles, as both contain more low volatility material.

#### 4.3.3.2 Estimation of RO<sub>2</sub> reaction pathways

No refractive indices for limonene SOA are available in the literature. To further probe the effect of the HC/NO<sub>x</sub> ratio on m<sub>r,s</sub> and attempt to assess the ability of the current literature to predict refractive indices, we explore the predictions of combined photochemical oxidation/SOA partitioning/refractive index estimation models available in the literature, described above and in the supplementary material. Several of the RO<sub>2</sub> reaction pathways produce condensable products (labeled products 1-4) in the kinetics model:



Products 1, 2 and 4 contain organic nitrate, peroxyxynitrate and hydro-peroxide (ROOH) moieties, respectively. Product 3 usually contains at least one carbonyl and one hydroxy functional group. This suggests that organic peroxides from RO<sub>2</sub> + HO<sub>2</sub> should be more important in SOA with low m<sub>r,s</sub> (from low NO<sub>x</sub>, high HC/NO<sub>x</sub> experiments) and organic nitrates or other products from RO<sub>2</sub> + NO are more important in SOA with high m<sub>r,s</sub> from low HC/NO<sub>x</sub> experiments.

Several recent studies have shown that  $\text{NO}_x$  levels and the  $\text{HC}/\text{NO}_x$  ratio govern SOA formation and speciation (e.g., see summary by Kroll and Seinfeld<sup>30</sup>). In the kinetics model (Section 4.4), between 24 and 49 condensing species make up 99% of the observed aerosol mass, depending on the experiment. Figure 4.9 shows the percent contribution of  $\text{RO}_2$  reacting with  $\text{NO}$ ,  $\text{NO}_2$ ,  $\text{HO}_2$  or  $\text{RO}_2$  for these reactions. As mentioned in section 4.5.1, the  $\text{NO}$  concentration is over-predicted by the model early in the experiments. For example, even when the measured  $\text{NO}$  concentration had reached the 1 ppb detection limit, model simulations showed 45-56 %  $\text{NO}$  concentration remaining for low  $\text{NO}_x$  simulations ( $\text{HC}/\text{NO}_x = 19\text{-}33$  ppbC/ppb), 24 % for the intermediate  $\text{NO}_x$  simulation ( $\text{HC}/\text{NO}_x = 13$  ppbC/ppb) and 13-18 % for high  $\text{NO}_x$  simulations ( $\text{HC}/\text{NO}_x = 6.3\text{-}9.4$  ppbC/ppb). To assess the contribution of the  $\text{RO}_2 + \text{NO}$  vs.  $\text{RO}_2 + \text{RO}_2$  reaction pathways under conditions closer to the chamber experiments, the model was tuned as follows. A “reaction” converting  $\text{NO}$  to  $\text{NO}_2$  was added, and to keep  $\text{O}_3$  in good agreement with the measurements, a “wall loss” term for  $\text{O}_3$  was added. The magnitude of the tuning reaction necessary to match the experiment was much higher for the low  $\text{NO}_x$  experiments than the high  $\text{NO}_x$  experiments, and in turn tuning had a negligible effect on the  $\text{RO}_2$  branching ratio for the high  $\text{NO}_x$  experiments (shown in Figure 4.9). With the  $\text{NO}$  matched to observations this way, kinetic simulations (Figure 4.9) show that the contribution of  $\text{RO}_2 + \text{HO}_2$  increases from 0.16 % to 68 % as the  $\text{HC}/\text{NO}_x$  ratio increases, and conversely  $\text{RO}_2 + \text{NO}$  contributions are most dominant at low  $\text{HC}/\text{NO}_x$  ratios. The contribution from  $\text{RO}_2 + \text{RO}_2$  is small for all conditions. This result suggests that the hydroperoxide groups may make a larger contribution to low  $m_r$ s and organic nitrates and other products from  $\text{RO}_2 + \text{NO}$  may have higher average  $m_r$ s.



#### 4.3.4 Quantitative structure property relationship (QSPR) approach for estimation of refractive indices of SOA.

To quantitatively compare the measured refractive indices with the composition calculated from the kinetics model and partitioning coefficients (above and supplementary material), we calculate refractive indices for SOA components with a quantitative structure property relationship (QSPR) approach developed by Redmond and Thompson.<sup>5</sup> We assume that the SOA are homogeneous mixtures, and that the refractive index can be calculated on a volume weighted basis (e.g., Liu and Daum<sup>31</sup>). The effective refractive index ( $n_e$ ) is calculated as:

$$n_e = \sum f_i n_i \quad (4.1)$$

where  $n_i$  is the refractive index of the  $i^{\text{th}}$  component,  $f_i$  is the volume fraction of that component. 282 condensable semivolatile species from RO<sub>2</sub> reactions produced by the kinetic simulation model were considered. Redmond and Thompson<sup>5</sup> derived an expression using a multiple regression approach relating the refractive index to several bulk physical properties of molecules:

$$\text{R.I.}_{\text{predicted}} = 0.031717(\mu) + 0.0006087(\alpha) - 3.0227\left(\frac{\rho_m}{M}\right) + 1.38709 \quad (4.2)$$

where  $\alpha$  is the mean polarizability,  $\rho_m$  is the mass density (g/cm<sup>3</sup>),  $M$  is the molecular weight (g/mol) and  $\mu$  is the degree of unsaturation. From the molecular formula of each component, each of these parameters can be estimated.<sup>32,33</sup>

We note that equation 4.2 was built with 589 nm data while our measurements were made at 532 nm. Refractive indices of single bulk organic materials typically have only very slight dependence on wavelength in the mid-visible, changing by less than about 0.002 - 0.005 between 589 and 532 (e.g., Moreels et al.<sup>34</sup>); always decreasing with increasing wavelength. However, Yu et al.<sup>35</sup> derived values of 1.56, 1.51, and 1.46 for  $\alpha$ -pinene/NO<sub>x</sub> SOA at 450, 550, and 700 nm, respectively, suggesting that SOA optical properties might deviate from predictions

based on single component bulk  $m_r$ s. This slope implies a correction factor of about +0.02 might be added to the QSPR values to compare our experimental results. Adjustment in the opposite direction may be needed however because Equation 4.2 was presumably built on data collected at 15 -25 °C (this was not specified in the QSPR development<sup>5</sup>), while our limonene experiments were performed at 28 – 39 °C. This correction is probably of similar order as the wavelength correction, (-0.005 – 0.02), but it is not well known. The QSPR approach assumes that mixtures contained in SOA can be represented by applying the volume mixing rule to refractive indices derived for the bulk single component species. Features such as supramolecular interactions have been suggested that may make estimates based on pure materials less accurate for complex mixtures.<sup>5,36</sup> Taken together, the uncertain adjustments needed for supramolecular interactions, and the wavelength and temperature differences between experiment and model, the uncertainty on each of these values when comparing them to our chamber data is  $\sim \pm 0.03$ ).

Using the volume mixing rule with the partitioning coefficient of each species, we can estimate the refractive indices for SOA for each experiment every three minutes as shown in Figure 4.10. The QSPR approach combined with the simulation results predicted refractive indices in a range from 1.455–1.495. The trend, an inverse relationship between  $m_r$  and HC/NO<sub>x</sub> ratio, agrees with the experimental trend. However, because it spans a much narrower range than observed (1.34–1.56), it is not clear if the direction of the trends have the same origin. The QSPR values are in good agreement with the results from experiments performed at HC/NO<sub>x</sub> ratios of ~9-13. We note that errors associated with predicting the detailed product spectrum and SOA partitioning cannot explain the disagreement, because almost all of the condensable species calculated by the kinetics model have predicted  $m_r$  values of 1.45 – 1.51 (Table 4.2).

Further explanation is needed to explain much the observed deviation between measurement and model, and may lie in species in the particles that are not produced by the kinetics model. Refractive indices of oligomeric compounds are expected to be higher, in the range of 1.55 – 1.60 because of their higher polarizability.<sup>5</sup> The presence of oligomeric species is well documented, especially as particles grow and as oxidation progresses.<sup>25,37,38</sup>

The deviations at the low end may be due to several factors, particularly water content in the small/fresher particles. Beginning from the  $m_r$ s estimated with the model for the fresher low HC/NO<sub>x</sub> ratio particles (1.425 – 1.485 including uncertainties in wavelength and temperature correction, and other uncertainties), assuming a volumetric water content of 50%, expected measured  $m_r$ s would be ~1.38 – 1.41. Additional contributions from small water soluble molecules and particle phase reaction products<sup>1,30</sup>, such as glyoxal and acetic acid, can further lower the expected refractive index, into reasonable agreement with the low end of observed refractive indices, within mutual uncertainties.

Our results suggest the chemical speciation of particles formed under high and low NO<sub>x</sub> conditions are different; oligomerization may possibly be favored under high NO<sub>x</sub> conditions whereas perhaps the uptake water and/or formation/uptake of small molecular weight components play a larger role under low NO<sub>x</sub> conditions. Combining measurement of  $m_r$ s with detailed chemical analysis of the particle phase may shed more light on the causes of the variation in the observed refractive indices.

#### **4.4 Summary and atmospheric implications**

Our laboratory chamber results show that limonene and  $\alpha$ -pinene SOA refractive indices are closely related to the particle size, which are in turn influenced by the HC/NO<sub>x</sub> ratio and several

other factors including temperature and initial HC concentration. Within the atmospherically relevant aerosol mass concentration and temperature ranges and short time periods addressed in our study, refractive indices are less sensitive to the aerosol mass concentration or aerosol aging. The refractive index ranges from 1.34 to 1.56 for limonene and from 1.36 to 1.52 for  $\alpha$ -pinene, and generally decreases as the HC/NO<sub>x</sub> ratio increases between 6.3- 8.1 and 33 ppbC/ppb.

Ranges of  $m_{rs}$  for SOA studied here are likely to have a significant impact on radiative transfer calculations of SOA direct effects. In Kim et al.,<sup>7</sup> we showed that changing the  $m_{rs}$  from 1.4 to 1.5 can produce an increase in the radiative forcing by at least 12% for non-absorbing particles. There is more work to be done before recommendations can be made for atmospheric applications, but our  $m_r$  variations on HC/NO<sub>x</sub> ratio indicate that a single value for SOA refractive index will not be sufficient to accurately model radiative transfer.

#### 4.5 References

- (1) Hallquist, M.; Wenger, J. C.; Baltensperger, U.; Rudich, Y.; Simpson, D.; Claeys, M.; Dommen, J.; Donahue, N. M.; George, C.; Goldstein, A. H. et al. *Atmos. Chem. Phys.* **2009**, *9*, 5155-5236.
- (2) Kanakidou, M.; Seinfeld, J. H.; Pandis, S. N.; Barnes, I.; Dentener, F. J.; Facchini, M. C.; Van Dingenen, R.; Ervens, B.; Nenes, A.; Nielsen, C. J. et al. *Atmos. Chem. Phys.* **2005**, *5*, 1053-1123.
- (3) Mishchenko, M. I., B. Cairns, G. Kopp, C.F. Schueler, B.A. Fafaul, J.E. Hansen, R.J. Hooker, T. Itchkawich, H.B. Maring, and L.D. Travis. *Bull. Amer. Meteor. Soc.* **2007**, *88*, 677-691.
- (4) Nakayama, T.; Matsumi, Y.; Sato, K.; Imamura, T.; Yamazaki, A.; Uchiyama, A. *J. Geophys. Res.,-Atmos.* **2010**, *115*, D24204, doi: 10.1029/2010jd014387.
- (5) Redmond, H.; Thompson, J. E. *Phys. Chem. Chem. Phys.* **2011**, *13*, 6872-6882.
- (6) Schnaiter, M.; Linke, C.; Mohler, O.; Naumann, K. H.; Saathoff, H.; Wagner, R.; Schurath, U.; Wehner, B. *J. Geophys. Res.,-Atmos.* **2005**, *110*, D19204, doi: 1029/2005jd006046.
- (7) Kim, H.; Barkey, B.; Paulson, S. E. *J. Geophys. Res.,-Atmos.* **2010**, *115*, D24212, doi: 10.1029/2010jd014549.
- (8) Barkey, B.; Paulson, S. E.; Chung, A. *Aerosol Sci. Technol.* **2007**, *41*, 751-760.
- (9) Lang-Yona, N.; Rudich, Y.; Mentel, T. F.; Buchholz, A.; Kiendler-Scharr, A.; Kleist, E.; Spindler, C.; Tillmann, R.; Wildt, J. *Atmos. Chem. Phys.* **2010**, *10*, 4753-4788.
- (10) Zhong, M.; Jang, M. *Atmos. Environ.* **2011**, *45*, 4263-4271.

- (11) Chung, A.; Lall, A. A.; Paulson, S. E. *Atmos. Environ.* **2008**, *42*, 2129-2140.
- (12) Wang, Y.; Kim, H.; Paulson, S. E. *Atmos. Environ.* **2011**, *45*, 3149-3156.
- (13) Lienert, B. R.; Porter, J. N.; Sharma, S. K. *Journal of Atmospheric and Oceanic Technology* **2003**, *20*, 1403-1410.
- (14) Leungsakul, S.; Jeffries, H. E.; Kamens, R. M. *Atmos. Environ.* **2005**, *39*, 7063-7082.
- (15) Pankow, J. F. *Atmos. Environ.* **1994**, *28*, 189-193.
- (16) Myrdal, P. B.; Yalkowsky, S. H. *Ind. Eng. Chem. Res.* **1997**, *36*, 2494-2499.
- (17) Camredon, M.; Aumont, B.; Lee-Taylor, J.; Madronich, S. *Atmos. Chem. Phys.* **2007**, *7*, 5599-5610.
- (18) Ng, N. L.; Kroll, J. H.; Keywood, M. D.; Bahreini, R.; Varutbangkul, V.; Flagan, R. C.; Seinfeld, J. H.; Lee, A.; Goldstein, A. H. *Environ. Sci. Technol.* **2006**, *40*, 2283-2297.
- (19) Hoffmann, T.; Odum, J. R.; Bowman, F.; Collins, D.; Klockow, D.; Flagan, R. C.; Seinfeld, J. H. *Journal of Atmospheric Chemistry* **1997**, *26*, 189-193.
- (20) Griffin, R. J.; Cocker, D. R.; Flagan, R. C.; Seinfeld, J. H. *J. Geophys. Res.,-Atmos.* **1999**, *104*, 3555-3567.
- (21) Mikhailov, E.; Vlasenko, S.; Martin, S. T.; Koop, T.; Poschl, U. *Atmos. Chem. Phys.* **2009**, *9*, 9491-9522.
- (22) Varutbangkul, V.; Brechtel, F. J.; Bahreini, R.; Ng, N. L.; Keywood, M. D.; Kroll, J. H.; Flagan, R. C.; Seinfeld, J. H.; Lee, A.; Goldstein, A. H. *Atmos. Chem. Phys.* **2006**, *6*, 2367-2388.
- (23) VanReken, T. M.; Ng, N. L.; Flagan, R. C.; Seinfeld, J. H. *J. Geophys. Res.,-Atmos.* **2005**, *110*, D07206, doi: 10.1029/2004jd005465.
- (24) Chhabra, P. S.; Ng, N. L.; Canagaratna, M. R.; Corrigan, A. L.; Russell, L. M.; Worsnop, D. R.; Flagan, R. C.; Seinfeld, J. H. *Atmos. Chem. Phys.* **2011**, *11*, 8827-8845.
- (25) Gao, Y. Q.; Hall, W. A.; Johnston, M. V. *Environ. Sci. Technol.* **2010**, *44*, 7897-7902.
- (26) Camredon, M.; Hamilton, J. F.; Alam, M. S.; Wyche, K. P.; Carr, T.; White, I. R.; Monks, P. S.; Rickard, A. R.; Bloss, W. J. *Atmos. Chem. Phys.* **2010**, *10*, 2893-2917.
- (27) Galloway, M. M.; Loza, C. L.; Chhabra, P. S.; Chan, A. W. H.; Yee, L. D.; Seinfeld, J. H.; Keutsch, F. N. *Geophys. Res. Lett.* **2011**, *38*, L17811, doi: 10.1029/2011gl048514
- (28) Kroll, J. H.; Ng, N. L.; Murphy, S. M.; Flagan, R. C.; Seinfeld, J. H. *Environ. Sci. Technol.* **2006**, *40*, 1869-1877.
- (29) Kroll, J. H.; Ng, N. L.; Murphy, S. M.; Varutbangkul, V.; Flagan, R. C.; Seinfeld, J. H. *J. Geophys. Res.,-Atmos.* **2005**, *110*, D23207, doi: 10.1029/2005jd006004.
- (30) Kroll, J. H.; Seinfeld, J. H. *Atmos. Environ.* **2008**, *42*, 3593-3624.
- (31) Liu, Y. G.; Daum, P. H. *J. Aerosol Sci* **2008**, *39*, 974-986.
- (32) Bosque, R.; Sales, J. *J. Chem. Inf. Comput. Sci.* **2002**, *42*, 1154-1163.
- (33) Girolami, G. S. *J. Chem. Educ.* **1994**, *71*, 962-964.
- (34) Moreels, E.; Degreef, C.; Finsy, R. *Appl. Opt.* **1984**, *23*, 3010-3013.
- (35) Yu, Y.; Ezell, M. J.; Zelenyuk, A.; Imre, D.; Alexander, L.; Ortega, J.; D'Anna, B.; Harmon, C. W.; Johnson, S. N.; Finlayson-Pitts, B. J. *Atmos. Environ.* **2008**, *42*, 5044-5060.
- (36) Rincon, A. G.; Guzman, M. I.; Hoffmann, M. R.; Colussi, A. J. *J. Phys. Chem. A* **2009**, *113*, 10512-10520.

(37) Surratt, J. D.; Murphy, S. M.; Kroll, J. H.; Ng, N. L.; Hildebrandt, L.; Sorooshian, A.; Szmigielski, R.; Vermeylen, R.; Maenhaut, W.; Claeys, M.; Flagan, R. C.; Seinfeld, J. H. *J. Phys. Chem. A* **2006**, *110*, 9665-9690.

(38) Heaton, K. J.; Sleighter, R. L.; Hatcher, P. G.; Hall, W. A.; Johnston, M. V. *Environ. Sci. Technol.* **2009**, *43*, 7797-7802.

**Table 4.1. Initial conditions, temperatures, relative humidities and results of the experiments**

Expt.	Initial Conditions				Results								
	HC	HC (ppb)	NO <sub>x</sub> (ppb)	HC/NO <sub>x</sub> (ppbC/ppb)	Temp (°C) <sup>a</sup>	RH (%) <sup>a</sup>	ΔHC <sup>b</sup> (ppb)	O <sub>3</sub> /HC <sub>i</sub> <sup>c</sup>	# density (#/cm <sup>3</sup> )		Size mode <sup>d,e</sup> (nm)	Mass <sup>f</sup> (μg/m <sup>3</sup> )	Yield <sup>g</sup> (%)
								Max <sup>d</sup>	Final <sup>e</sup>				
<b>26-Aug-10</b>	Limonene	60	20	30	37-39-35	18-16-20	24	0.60	11702	3720	217	20.8-79.2	27
<b>17-Sep-10</b>	Limonene	65	20	33	31-34-33	17-15-16	25	0.62	19949	5640	217	41.7-109	38
<b>8-Oct-10</b>	Limonene	77	40	19	35-31	19-25	36	0.53	17604	7250	217	44.8-117	33
<b>30-Aug-10</b>	Limonene	75	56	13	31-32-28	21-20-25	37	0.51	11016	4560	260	54.2-136	40
<b>15-Sep-10</b>	Limonene	73	78	9.4	39-36	14-16	41	0.44	4865	2070	334	27.1-103	30
<b>5-Nov-10</b>	Limonene	72	115	6.3	39-35	14-17	42	0.42	7410	3530	334	79-110	35
<b>24-Sep-10</b>	α-pinene	69	22	31	42-43-39	14-13-15	26	0.62	5510	1400	225	6.3-25	8.1
<b>3-Sep-10</b>	α-pinene	65	22	30	37-36-37	15-16	23	0.65	6988	1960	209	19.4-26	8.6
<b>10-Sep-10</b>	α-pinene	106	32	33	33-35-30	16-15-19	36	0.66	18202	5900	241	58-102	24
<b>20-Sep-10</b>	α-pinene	78	96	8.1	35-30	17-23	33	0.58	2033	1180	260	14-18	5.3
<b>13-Sep-10</b>	α-pinene	120	125	9.6	37-31	15-19	45	0.63	6641	2720	300	35-77	13.5

<sup>a</sup>Initial, peak and final temperature and relative humidity.

<sup>b</sup>Quantity of HC that reacted before nucleation started.

<sup>c</sup>Ratio of the ozone concentration corresponding to the maximum particle number density to the initial HC concentration.

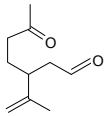
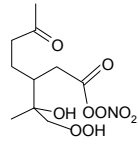
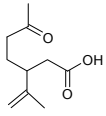
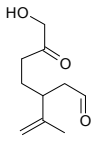
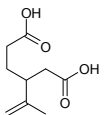
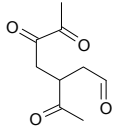
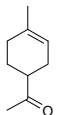
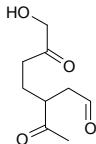
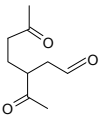
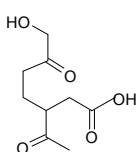
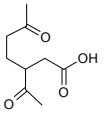
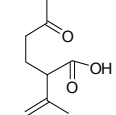
<sup>d</sup>Maximum aerosol number concentration and size mode. These values have not been adjusted for wall losses.

<sup>e</sup>Final aerosol number concentration and size mode (also maximum size mode). These values have not been adjusted for wall losses.

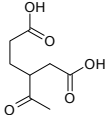
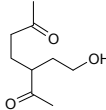
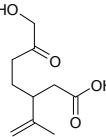
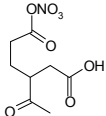
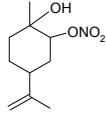
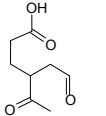
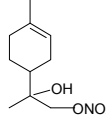
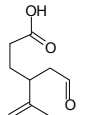
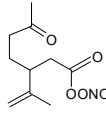
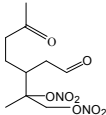
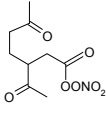
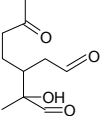
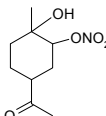
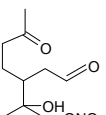
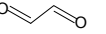
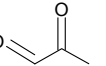
<sup>f</sup>Mass concentration in the chamber over the period for which meaningful PN measurements were made was determined from the SMPS measured size distribution. Particle density was assumed to be 1.2 and 1.25 g/cm<sup>3</sup> for α-pinene and limonene, respectively.

<sup>g</sup>Calculated from peak measured aerosol mass corrected for wall losses and the corresponding quantity of reacted hydrocarbon. Because of the uncertainties in the measurement from GC (± 3 %) and measurement of SMPS (± 10 %) yields are uncertain to ± 10 %.

Table 4.2. Calculated  $m_r$ s and  $V_p$  of representative compounds expected to condense on limonene SOA

Compound	Structure	Formula (MW)	$m_r^a$	$V_p^b$ (atm)	Compound	Structure	Formula (MW)	$m_r^a$	$V_p^b$ (atm)
LCHO		C <sub>10</sub> H <sub>16</sub> O <sub>2</sub> (168)	1.479	1.14E-04	POHLCNO5		C <sub>10</sub> H <sub>17</sub> O <sub>9</sub> N <sub>1</sub> (295)	1.484	8.74E-09
LNNICA		C <sub>10</sub> H <sub>16</sub> O <sub>3</sub> (184)	1.478	2.28E-06	7OHL		C <sub>10</sub> H <sub>16</sub> O <sub>3</sub> (184)	1.448	1.77E-06
LNICA		C <sub>9</sub> H <sub>14</sub> O <sub>4</sub> (186)	1.445	2.28E-06	OXYL		C <sub>9</sub> H <sub>12</sub> O <sub>3</sub> (168)	1.508	2.07E-05
KL		C <sub>9</sub> H <sub>14</sub> O <sub>1</sub> (138)	1.473	1.15E-03	7OHKL		C <sub>9</sub> H <sub>14</sub> O <sub>4</sub> (186)	1.477	6.14E-07
KLCHO		C <sub>9</sub> H <sub>14</sub> O <sub>3</sub> (170)	1.477	3.50E-05	7OHKLCO2H		C <sub>9</sub> H <sub>14</sub> O <sub>5</sub> (202)	1.477	3.48E-08
KLNNICA		C <sub>9</sub> H <sub>14</sub> O <sub>4</sub> (186)	1.477	7.92E-07	NLNNICA		C <sub>9</sub> H <sub>14</sub> O <sub>3</sub> (170)	1.476	5.62E-06



<b>KLNICA</b>		C <sub>8</sub> H <sub>12</sub> O <sub>5</sub> (188)	1.475	5.49E-08	<b>OXOACID</b>		C <sub>9</sub> H <sub>16</sub> O <sub>3</sub> (172)	1.445	5.18E-06
<b>OH7LCO2H</b>		C <sub>10</sub> H <sub>16</sub> O <sub>4</sub> (200)	1.479	8.52E-08	<b>KLNICACNO 5</b>		C <sub>8</sub> H <sub>11</sub> O <sub>8</sub> N <sub>1</sub> (249)	1.510	1.28E-07
<b>LOHINO3</b>		C <sub>10</sub> H <sub>17</sub> O <sub>4</sub> N <sub>1</sub> (215)	1.480	5.05E-06	<b>KLLICA</b>		C <sub>8</sub> H <sub>12</sub> O <sub>4</sub> (172)	1.474	1.03E-06
<b>LOHXNO3</b>		C <sub>10</sub> H <sub>17</sub> O <sub>4</sub> N <sub>1</sub> (215)	1.481	2.85E-06	<b>LLICA</b>		C <sub>9</sub> H <sub>14</sub> O <sub>3</sub> (170)	1.476	3.06E-06
<b>LCNO5</b>		C <sub>10</sub> H <sub>15</sub> O <sub>6</sub> N <sub>1</sub> (245)	1.515	6.06E-06	<b>LXNO3NO3</b>		C <sub>10</sub> H <sub>16</sub> O <sub>8</sub> N <sub>2</sub> (292)	1.518	6.94E-08
<b>KLCNO5</b>		C <sub>9</sub> H <sub>13</sub> O <sub>7</sub> N <sub>1</sub> (247)	1.514	8.69E-07	<b>LXOOH</b>		C <sub>10</sub> H <sub>16</sub> O <sub>4</sub> (200)	1.480	7.69E-07
<b>KLOHINO3</b>		C <sub>9</sub> H <sub>15</sub> O <sub>5</sub> N <sub>1</sub> (217)	1.479	1.78E-06	<b>LXOHNO3</b>		C <sub>10</sub> H <sub>17</sub> O <sub>6</sub> N <sub>1</sub> (247)	1.483	1.37E-07
<b>GLYOXAL<sup>c</sup></b>		C <sub>2</sub> H <sub>2</sub> O <sub>2</sub> (58)	1.393	7.68E-02	<b>MGLYOXAL<sup>c</sup></b>		C <sub>3</sub> H <sub>4</sub> O <sub>2</sub> (72)	1.411	5.09E-02

<sup>a</sup> $m_r$  is calculated with eqn. (3)<sup>15</sup> where  $\alpha$  is mean polarizability defined by  $\alpha = 1.51(\#C) + 0.17(\#H) + 0.57(\#O) + 1.05(\#N) + 2.99(\#S) + 2.48(\#P) + 0.22(\#F) + 2.16(\#Cl) + 3.29(\#Br) + 5.45(\#I) + 0.32$ ,  $\mu$  is degree of unsaturation defined by  $\mu = (\#C + 1) - 0.5(\#H - \#N)$  and  $\rho_m/M$  is the ratio of mass density to molecular weight. From the molecular formula of each component, each of these parameters can be estimated.<sup>32,33</sup>

<sup>b</sup> $V_p$  shown is calculated by the method of Myrdal and Yalkowsky<sup>16</sup> modified by Camredon et al.<sup>17</sup>

<sup>c</sup>Possible condensable species on SOA.

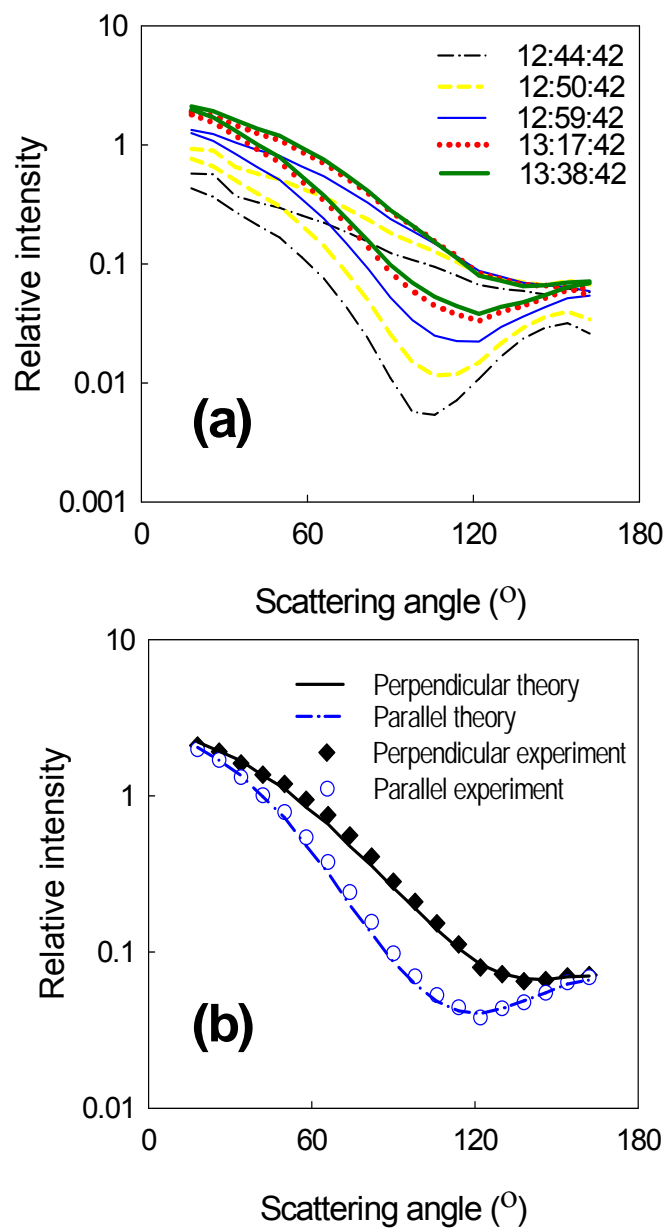


**Figure 4.1.** (a) Selected scattering properties recorded with the PN as particles grow for the experiment performed on 30 August. (b) Scattering at 12:38 (after 126 min), when the particle had a median size of 256 nm. Also shown GA determined fit using Mie-Lorenz theory, with a  $m_r=1.456$ , and at fitness of 0.968.

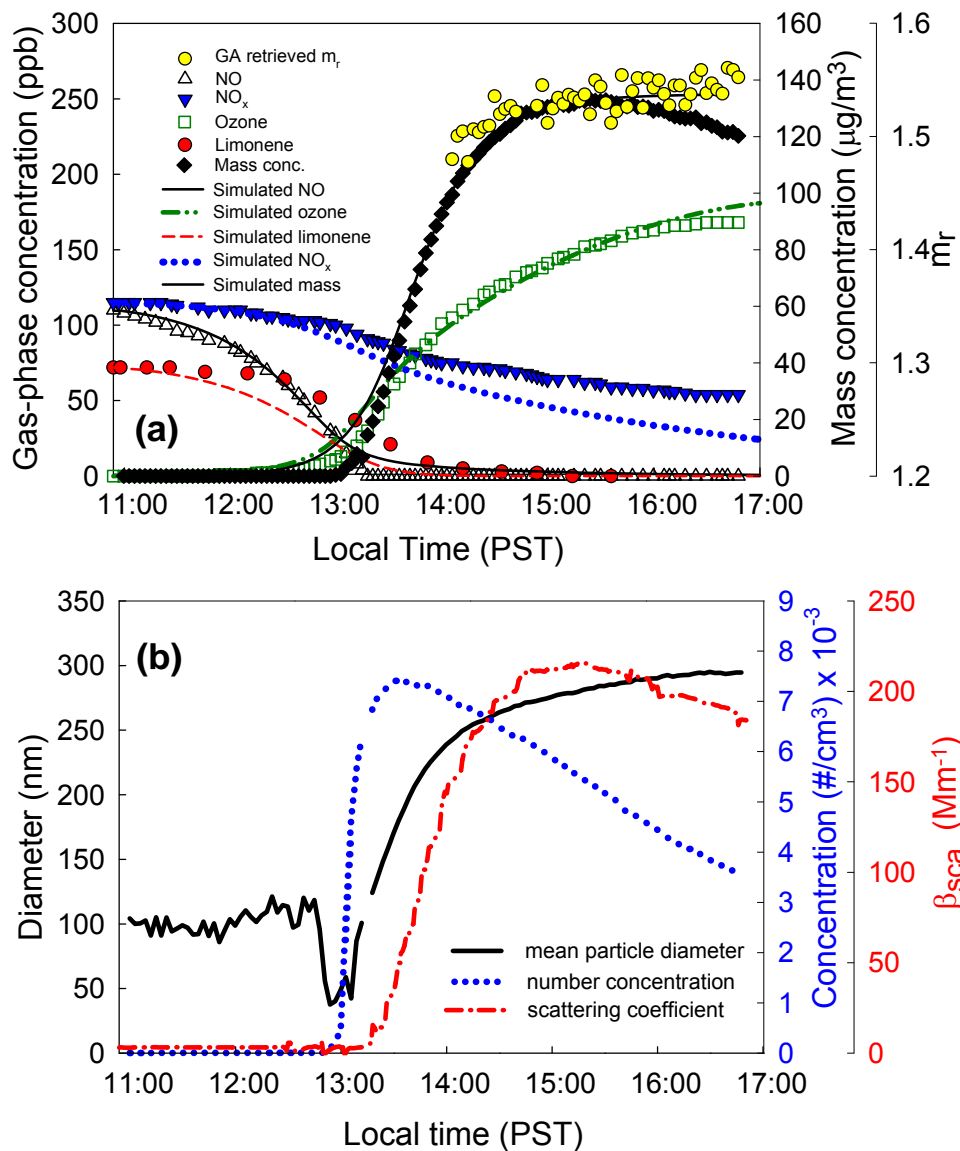


**Figure 4.2.** Profile of a limonene photooxidation experiment performed on Nov. 5, with initial concentrations of 72 ppb limonene and 115 ppb  $\text{NO}_x$ . (a) Gas phase concentrations (hydrocarbon, NO,  $\text{NO}_x$ ,  $\text{O}_3$ ), aerosol mass concentration (corrected for wall losses; see text) and GA determined real refractive index. (symbol; experiment, line; simulation) (b) Time evolution of the SOA particle number concentrations, mean diameter and integrated scattering ( $\beta_{\text{sca}}$ ).

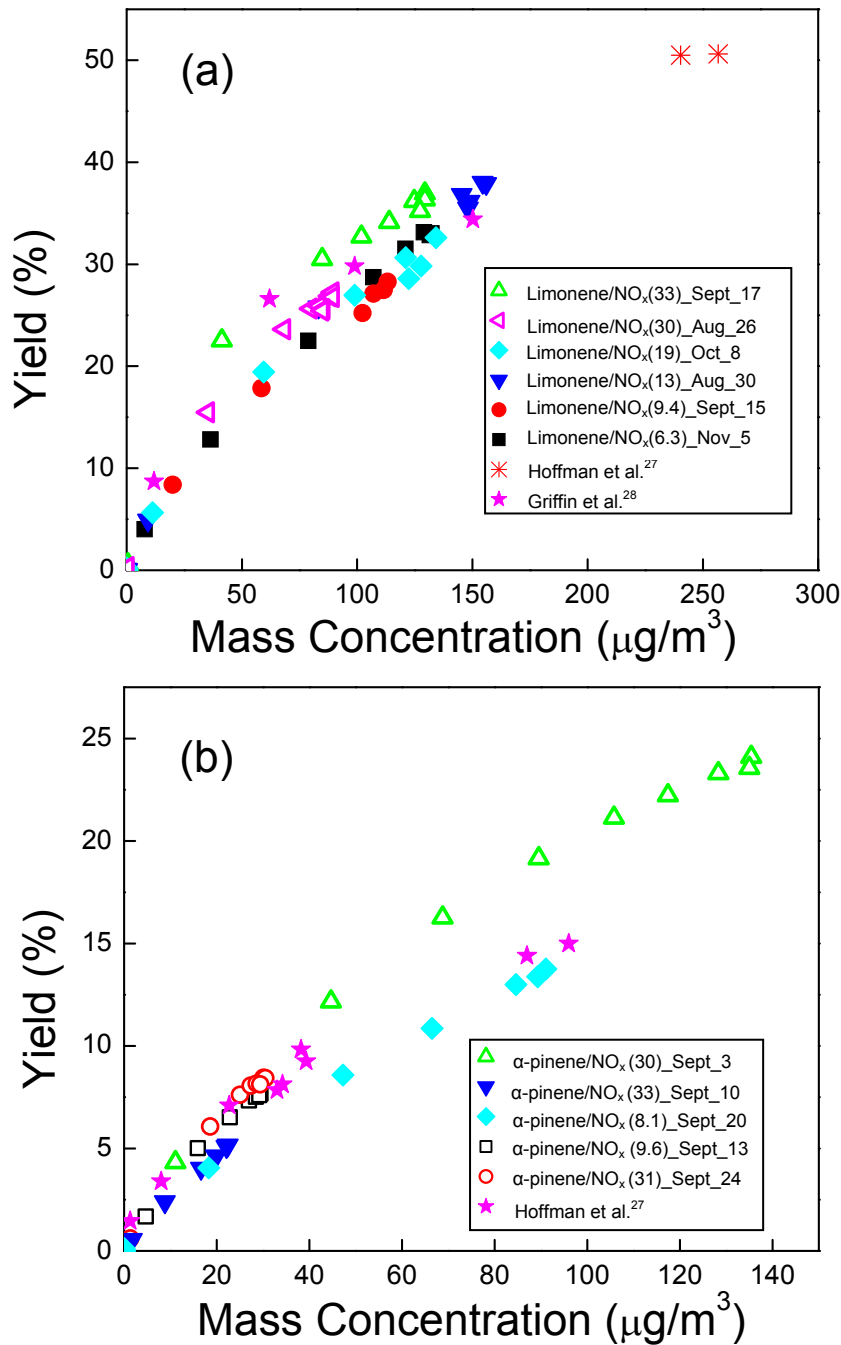


**Figure 4.3.** SOA yield as a function of mass concentration from (a) limonene photooxidation and (b)  $\alpha$ -pinene photooxidation. All yields are normalized to a density of 1.25 and 1.2  $\text{g}/\text{cm}^3$  for limonene and  $\alpha$ -pinene, respectively to facilitate comparison. The Hoffman et al.<sup>19</sup> results are from experiments using with 300 ppb propene, a HC/NO<sub>x</sub> = 9 –10.3 with initial limonene concentration of 89.2 – 95 ppb and HC/NO<sub>x</sub> = 6.9 – 15.1 with initial  $\alpha$ -pinene concentration of 19.5 – 144 ppb. The Griffin et al.<sup>20</sup> results are from the experiments using 250 ppb propene under HC/NO<sub>x</sub> = 2 – 4.6 with initial limonene concentration of 20.6 – 65.1 ppb.

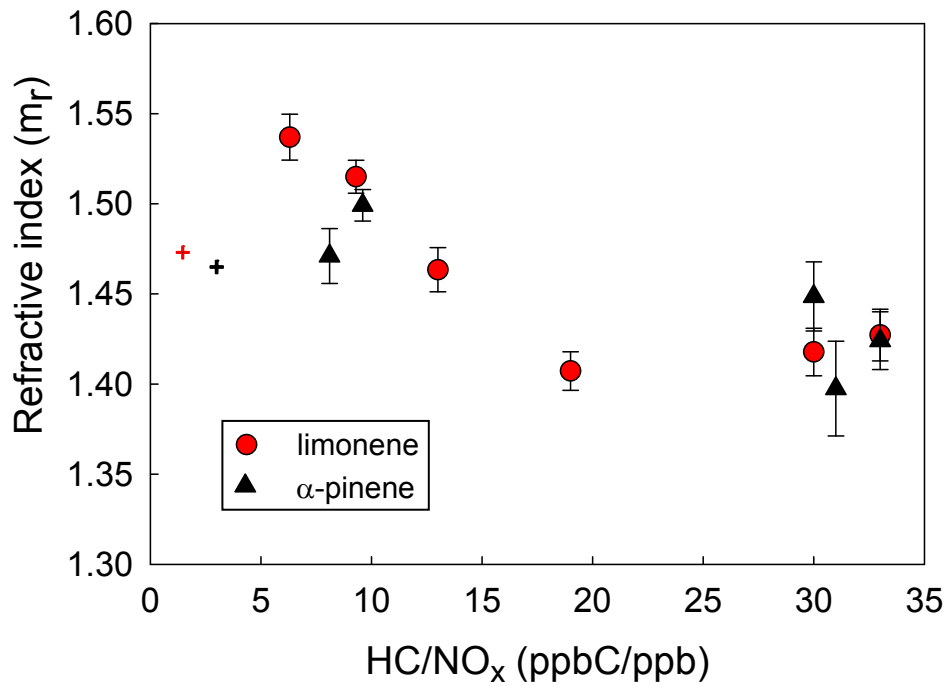


**Figure 4.4.** Relationship between the HC/NO<sub>x</sub> ratio and the average refractive index for an experiment. Data are presented as means of m<sub>r</sub>s retrieved over the growth of particles ± SD. Black and red cross symbols indicate the m<sub>r</sub>s of a-pinene and limonene precursors .

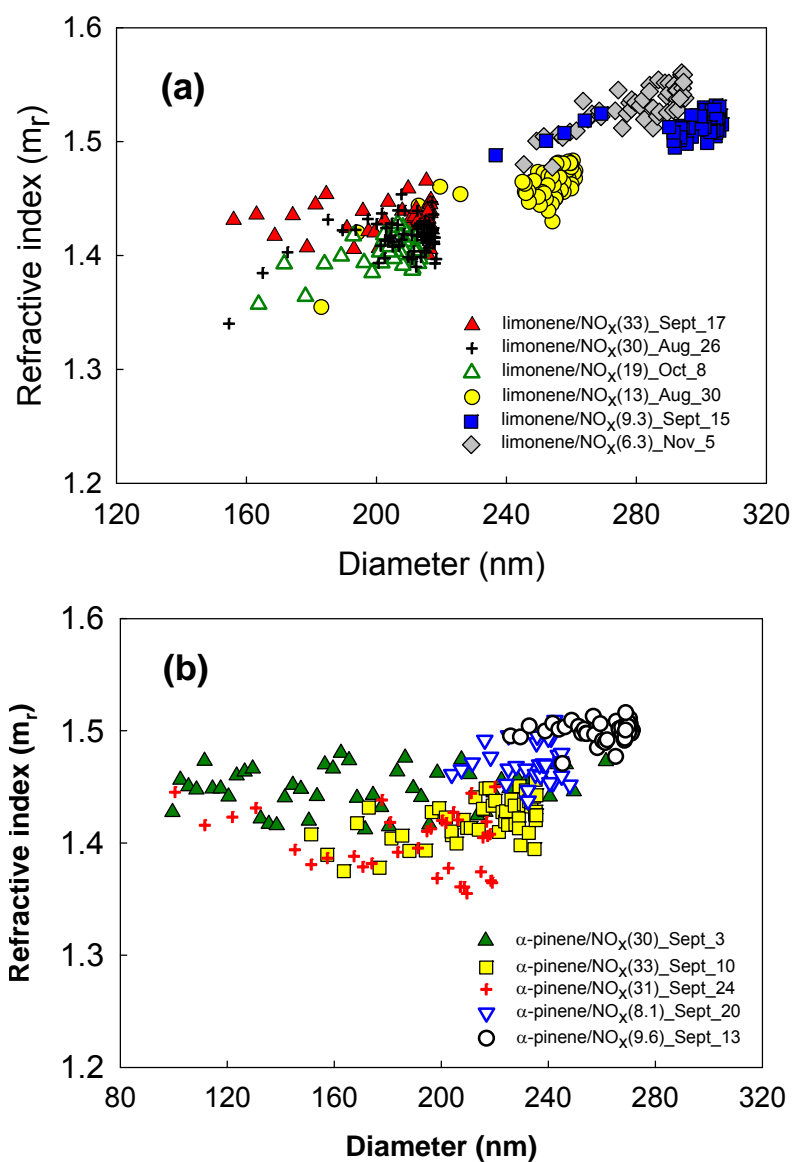


**Figure 4.5.** Retrieved refractive indices for SOA formed by photooxidation of (a) limonene and (b)  $\alpha$ -pinene at different HC/ $\text{NO}_x$  ratios as a function of particle diameter.

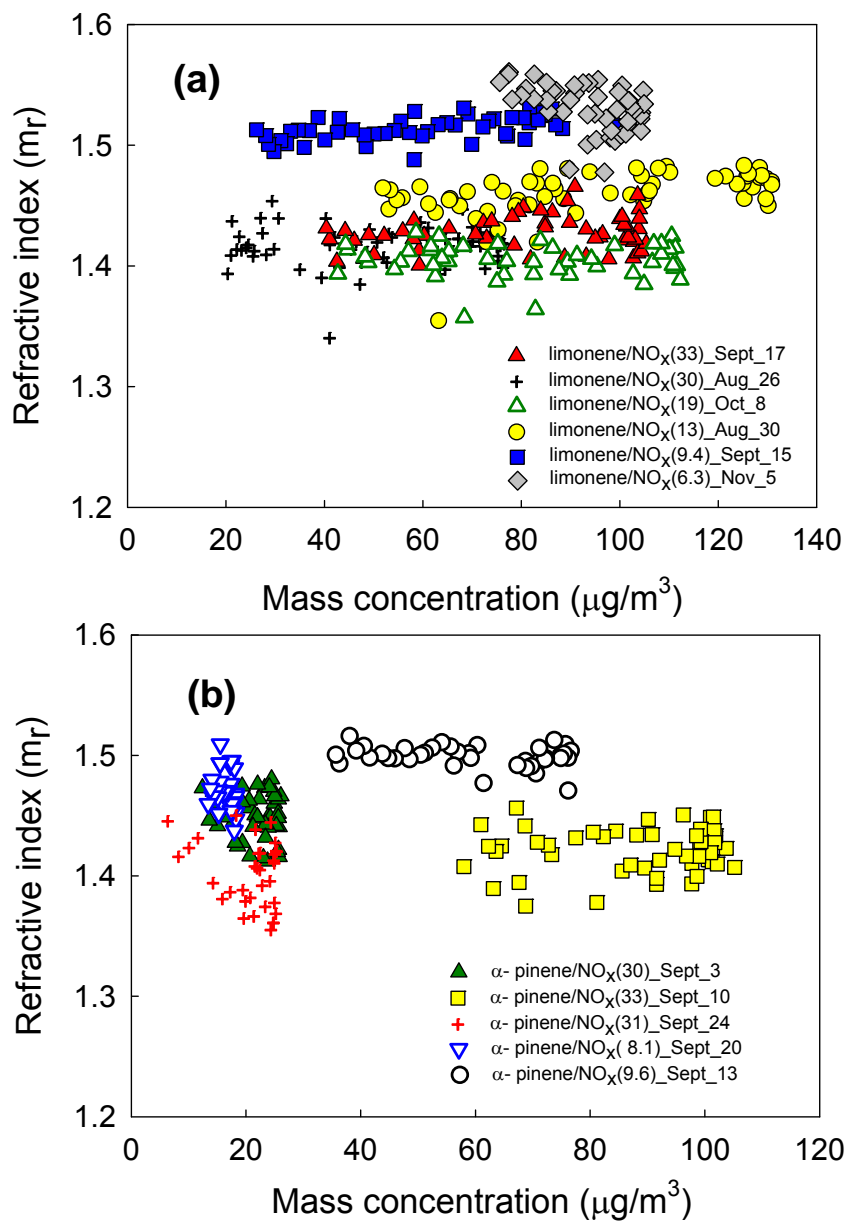


**Figure 4.6.** Retrieved refractive indices for SOA formed by photooxidation of (a) limonene and (b)  $\alpha$ -pinene at different HC/ $\text{NO}_x$  ratios as a function of mass concentration in the chamber.



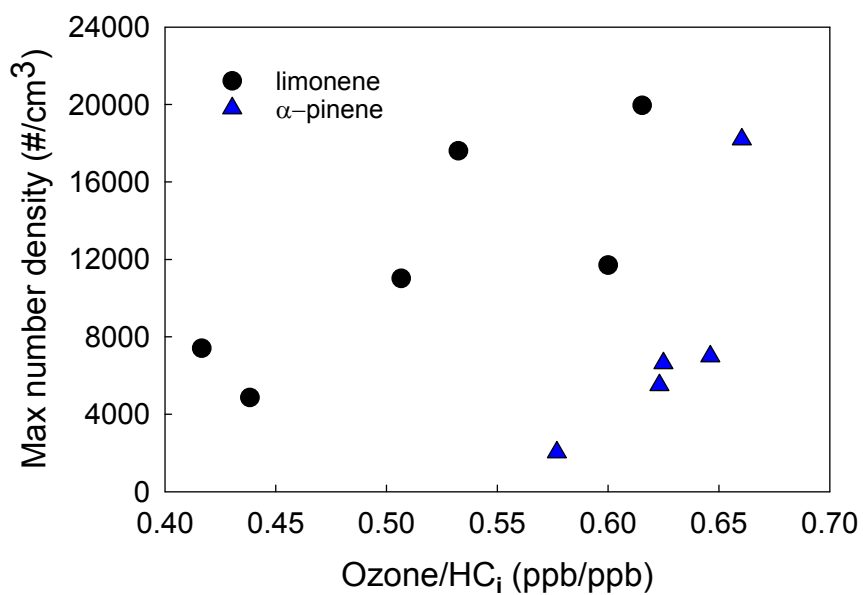


**Figure 4.7.** Maximum number concentration vs. Ozone/HC<sub>i</sub> ratio for limonene (black circle) α-pinene (blue triangle). Maximum number concentrations appear shortly after the particles start to nucleate. The ozone concentration corresponding to time at which the maximum number concentration was recorded is used.

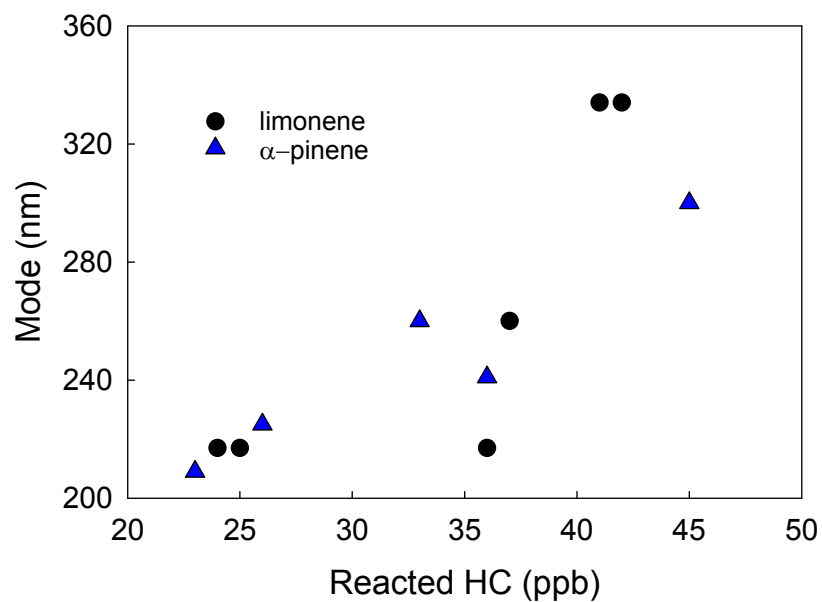


**Figure 4.8.** Mode of particle as a function of pre-consumed HC concentration for limonene (black circle) and  $\alpha$ -pinene (blue triangle). Pre-consumed HC is the amount of HC consumed before ozone begins to build up and particles begin to nucleate.

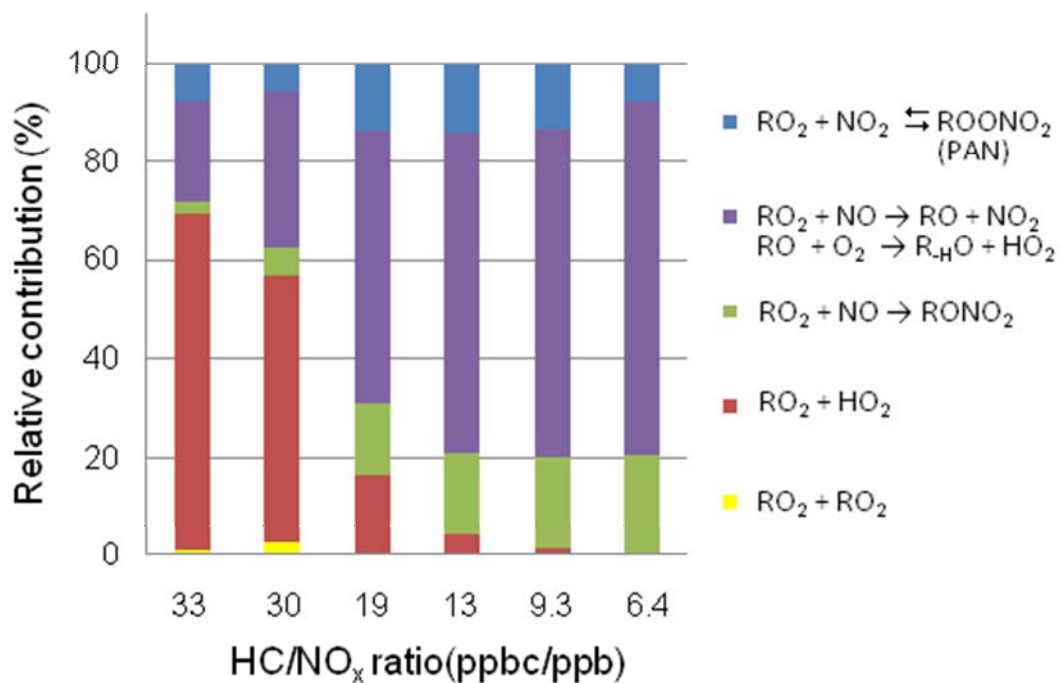


**Figure 4.9.** Cumulative contribution of 5 different reaction types that generate condensable species at the simulation time corresponding to the end of the experiments from kinetic simulations using the initial NO<sub>x</sub> and limonene concentrations listed in Table 4.1.

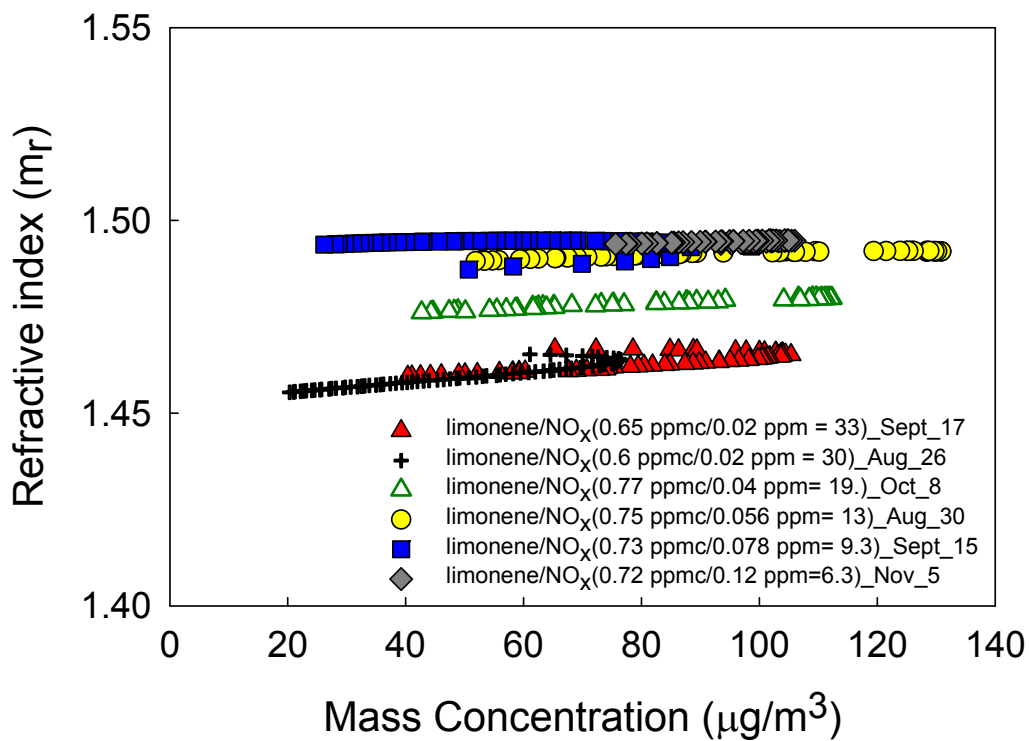


**Figure 4.10.** Predicted refractive indices based on kinetics simulation and QSPR (equation 4.2, see text) for limonene SOA at different at different HC/ $\text{NO}_x$  ratios at 589 nm. The estimated values at 532nm should be somewhat higher, by 0.002 – 0.022; see text.

## **Chapter 5**

**Real refractive indices and volatility of secondary organic aerosol generated from photooxidation and ozonolysis of limonene,  $\alpha$ -pinene and toluene upon heating**

## 5.1 Experimental

### 5.1.1 Secondary organic aerosol generation

Secondary organic aerosol generation in the chamber is described in detail in Chapter 2. Tables 5.1 and 5.2 show initial conditions and summary statistics for 20 experiments. Aerosols were characterized with the polar nephelometer, an integrating nephelometer (Ecotech M9003) and a scanning mobility particle sizer (SMPS, TSI model 3080). These instruments are described in detail in Chapter 2. Particularly, in the study, thermodenuder (TD) was used to measure volatility dependent refractive index of SOA.

### 5.1.2 Thermodenuder

The thermodenuder (TD) was constructed in-house using the design described by *Lee et al.*, [2011]. The TD consisted of a variable temperature heated section (L = 55 cm, inner tube D = 3.5 cm, outer tube D = 6 cm) followed by an activated carbon denuder section (L= 45 cm, inner mesh D = 3.5 cm, outer tube D = 6 cm). The space in between inner tube/mesh and outer tube was filled with sand (heating section) and activated carbon (denuding section), respectively. The flow rate through the TD was 1 LPM, corresponding to a centerline residence time of 16s. Measurements of volatility were made with the temperature of the heated section ranging from ambient temperature up to 98 °C. Temperature was controlled with heating tape wrapped on outer tube of heating sections. The temperature profile was measured with a 60 cm long thermocouple (OMEGA CLAD, KQXL-18E) positioned in the center of the heating tube. Temperatures were measured under the same flow conditions as used during experiments (1 LPM air flow). As shown on Figure 5.1, the temperature increase from the entrance of the heating tube and reached the maximum temperature at 27 cm from the entrance. For the mid-

section, the temperature varied within  $\pm 3$  °C of the maximum value before beginning to decrease near the exit, 45 cm from the entrance, at all temperatures (63 – 85 °C) . All the temperatures for each measurement and reported in this paper are the maximum temperature, measured at 35 cm from the entrance.

The TD measurements were carried out after mass concentration reached to the maximum to minimize complications by the rapid growth of particles with one exception; photooxidation of toluene. Because of the late particle nucleation and slow particle growth, the reaction was not completed within the range of our experimental scale (up to 6 h). So TD measurement of toluene SOA started when rapid particle growth stopped and particle growth rate become less than 2nm/min. SOA growth is sufficiently slow that the changing size distribution introduces minimal errors to refractive index retrievals and other calculations. Mostly three different temperatures steps (some cases, two steps when there are not enough particles left in the chamber) between 60 – 110 °C, were carried out. Within this temperature range, almost all SOA volume is evaporated and somewhat similar chemical composition to ambient oxygenated organic aerosol was obtained (for  $\alpha$ - and  $\beta$ -pinene SOA) [Kostenidou *et al.*, 2009; Lee *et al.*, 2011]. It took 6-9 minutes to change another state of temperatures showing the gradient of temperature changes (below, Figure 5.4a). While one state of temperature is held, thermodenuded and non thermodenuded particles were sampled every 3minutes by PN and SMPS, alternatively for about 30 minutes and once enough measurement is done, temperature of TD was changed to next higher step.

### **5.1.3 SOA characterization and experimental setup**

Figure 5.2 shows a schematic of SOA generation and measurements. Aerosols were characterized with the polar nephelometer (PN, described below), an integrating nephelometer

(Ecotech M9003), a scanning mobility particle sizer (SMPS, TSI model 3080), and by gravimetric mass ( $\pm 1 \mu\text{g}$ , Sartorius). The polar nephelometer and a scanning mobility particle sizer were placed downstream of both the thermodenuder and the bypass line. The aerosol flow direction was controlled by a four way valves (swagelock) in such a way that the bypass line (chamber particles) is sampled by the PN while the SMPS samples the thermodenuder line (denuded chamber particles) or vice-versa. The valve was switched every three minutes so that the PN and SMPS sampled original or thermodenuded particles alternately each for three minutes of every six minutes.

#### **5.1.4 Particle losses in the thermodenuder**

Number losses of SOA within the TD due to a combination of sedimentation, diffusion and the thermophoresis were determined in a separate experiment using NaCl (99%, sigma aldrich) aerosol, generated by nebulizing a 0.005 M NaCl solution (Collison spray nebulizer, BGI Inc.). NaCl particles were chosen because they do not volatilize at the temperature of interest [Huffman *et al.*, 2008]. The nebulized aerosol was dried through two silicagel driers in series and injected into the chamber. Relative humidity (RH) of the chamber was 28-32 % during the measurements in all cases reported here. Since sedimentation, diffusion and thermophoresis processes are size and temperature dependent, the total mass losses may be size and temperature dependent. Therefore we explored these dependencies by plotting the losses as a function of the particle size and also as a function of temperature (Figure 5.3). The curves at each of the 5 temperatures were obtained by taking the ratio of the output size distribution to the input distribution, averaging 8-10 scans. Error bars indicate the standard deviation for each of the data points. The particles losses increase for smaller sizes and are approximately constant above 80 nm, consistent with the result of Huffman *et al.*, [2008]. For small particles (< 50 nm), as the TD



temperature increases the particle losses increase from 5% at 65 °C to approximately 20% at 95 °C due to additional thermophoretic forces [Burtcher *et al.*, 2001]. Above 50 nm, the particles losses are independent of temperature and above 80 nm, they also cease to be size dependent. The averaged losses for each experimental curve are used to correct experimental data for mass losses as a function of temperature and size.

## 5.2 Results and Discussion

20 experiments with three different precursors (limonene,  $\alpha$ -pinene and toluene) under five different conditions were performed: photooxidation at low NO<sub>x</sub> (initial HC/NO<sub>x</sub> = 32 – 33), intermediate NO<sub>x</sub> (HC/NO<sub>x</sub> = 13-14) and high NO<sub>x</sub> (HC/NO<sub>x</sub> = 6.5 – 6.9) and ozonolysis with and without OH scavenger. Detailed experimental conditions are shown in Tables 5.1 and 5.2; precursor concentrations ranged from 130 – 258 ppb for limonene, 126 – 170 ppb for  $\alpha$ -pinene and 2760 – 2770 ppb for toluene. Toluene required higher precursor concentrations to produce sufficient SOA masses. Tables 5.1 and 5.2 show aerosol yields (aerosol mass/HC reacted, both in  $\mu\text{g}/\text{m}^3$ ). SOA are accepted to be reasonably spherical, as verified in Barkey *et al.* [2007]. SOA mass was calculated based on SMPS size distributions assuming spherical particles with a density of 1.25, 1.2 and 1.24  $\text{g}/\text{cm}^3$  for limonene,  $\alpha$ -pinene and toluene, respectively [Hallquist *et al.*, 2009; Ng *et al.*, 2006; Ng *et al.*, 2007b]. Measured particle number concentrations were corrected for size-dependent wall loss (above). Gravimetric mass measurements were used to check the SMPS masses, and averaged  $18 \pm 8$  % higher than that of SMPS mass measurements. The gravimetric filter samples are expected to overestimate particle mass somewhat due to adsorption of gases during sampling. Our yield data follow the expected trends; yields appear to be higher at lower temperatures, higher initial HC/NO<sub>x</sub> ratios, and higher aerosol mass in the

chamber [Hallquist *et al.*, 2009; Kim *et al.*, 2012]. Among precursors, as expected, aerosol yields from limonene are significantly higher than for  $\alpha$ -pinene for both ozonolysis and photooxidation (Tables 5.1 and 5.2). Because of higher initial hydrocarbon concentrations and resulting high aerosol mass concentrations, yields at the upper end of literature values [Kim *et al.*, 2012; Griffin *et al.*, 1999; Ng *et al.*, 2007b; Saathoff *et al.*, 2009] are expected for our experiments (Tables 5.1 and 5.2).

### 5.2.1 Reaction profile of a photooxidation experiment

Figure 5.4 shows chamber and thermodenuded results for a typical photooxidation experiment (22 August). The experiment had initial concentrations of 152 ppb limonene and 110 ppb NO. SOA began to nucleate 84 minutes after the chamber was initially exposed to sunlight, and quickly grew to several hundred nanometers (Figures 5.4b and 5.4c). The thermodenuder temperature was increased in three steps from 64-84 °C, beginning after the mass concentration had reached its maximum (Figures 5.4a and 5.4b). Figure 5.4b shows NO, NO<sub>x</sub>, O<sub>3</sub>,  $\alpha$ -pinene and aerosol mass concentration (not corrected for wall and thermodenuder-losses). Figure 5.4c shows the evolution of particle number, mean diameter, and integrated scattering ( $\beta_{\text{sca}}$ ). The particles continued to grow throughout, however particle number concentrations dropped due to coagulation and wall loss after 12:40.  $\beta_{\text{sca}}$  is measured from particles from chamber (not thermodenuded) and continues to increase as particle numbers drop until 14:18, after which it declines slowly. At this point, the decreases in scattering associated decreasing numbers overtake the increases due to growing particles (Figure 5.4c). Viable retrievals from the PN signal were first obtained when the particles had grown to about 344 nm at 13:07. Mr in this case increased from about 1.48-1.5 to 1.51-1.54 after the TD. In chamber experiments, we consistently observe

that the refractive index changes only slowly after the initial growth phase has ended and aerosol mass concentration has reached its peak values [Barkey *et al.*, 2007; Kim *et al.*, 2010; 2012], suggesting that the chemical composition of the SOA changes only slowly later in the experiment. The particle diameter and number concentration show the cycling of the thermodenuder every 3 minutes later in the experiments. The particle numbers are reduced to 74-78 % and diameter to 73-82 % of the original values, decreasing with increased TD temperature (discussed below).

## **5.2.2 Volatility measurements**

### **5.2.2.1 Volatility of SOA from photooxidation**

SOA mass fraction remaining (MFR) correlated for particles losses in the TD as a function of TD temperature are shown at Figure 5.5 for all photooxidation experiment. Overall, as thermodenuder temperature was increased (from 66 – 99 °C), mass fraction remaining decreased for both  $\alpha$ -pinene and limonene but not for toluene, which exhibited virtually no evaporation over the range investigated. There are no investigations available in the literature to compare the volatility of toluene SOA, however, AMS measurements of its chemical composition shows that SOA from aromatic HCs including toluene has consistently higher values of  $f_{44}$  compared to SOA from biogenic HCs, suggesting that the products formed from aromatic compounds are generally less volatile [Chhabra *et al.*, 2011; Ng *et al.*, 2010].

The volatility of both  $\alpha$ -pinene and limonene are higher than toluene SOA; mass fraction remaining (MFR) of  $\alpha$ -pinene SOA is 42–61% for the TD temperature range 64 – 86 °C, and the MFR of limonene SOA is 31–65% for the TD temperature of 58 – 113 °C. For both  $\alpha$ -pinene and limonene, there is no evidence of an impact of HC/NO<sub>x</sub> ratio on the volatility of the resulting

SOA for TD temperatures between 60 and 85 °C. This is surprising because it was reported that at low NO<sub>x</sub> conditions, a significant fraction of the SOA consist of hydroperoxide groups from RO<sub>2</sub> + HO<sub>2</sub> that are less volatile than the species (organic nitrate and other products) produced RO<sub>2</sub> + NO under low NO<sub>x</sub> conditions [Presto *et al.*, 2005; Ng *et al.*, 2007a]. Previously, Lee *et al.*, [2011] reported that the HC/NO<sub>x</sub> ratio can impact on the volatility of α-pinene SOA between NO<sub>x</sub> free and HC/NO<sub>x</sub> = 6, and TD temperature range 25 - 100 °C. The most significant NO<sub>x</sub> concentration effect was shown at 45- 60 °C below the temperatures examined here and at higher temperature, there are not significant differences of volatility between different NO<sub>x</sub> concentrations. This suggests that the TD temperature ranges in our experiments are high to investigate the difference of volatility of species from RO<sub>2</sub> + HO<sub>2</sub> and RO<sub>2</sub> + NO. For limonene SOA, Lee *et al.*, [2011] however, showed no NO<sub>x</sub> concentration impacts on the volatility between 25 - 100 °C, consistent with our result. Lee *et al.*, [2011] also reported that higher temperatures were required to almost completely evaporate limonene than α-pinene SOA suggest that limonene SOA is less volatile. This is consistent with our result above showing slightly higher MFR for limonene than α-pinene for the TD range 60 – 85 °C. The limonene experiment performed on Nov.16 is somewhat high volatile (by ~13-15 %) than other experiments. This experiment had significantly higher RH (by 10-19 %), implying RH might effects SOA volatility. Jonsson *et al.*, [2007] and Lee *et al.*, [2011] also observed moderate increases in volatility with increasing RH, consistent with our result.

#### **5.2.2.2 Volatility of SOA from ozonolysis**

Figure 5.6 shows volatility results for SOA produced from ozonolysis of α-pinene and limonene with and without scavenger. For both limonene and α-pinene, it appears that overall trends are similar to those for photooxidation SOA; as TD temperatures increase, MFRs decrease. When

the thermodenuder temperature was increased to 65 °C, it resulted in roughly 50 % and 70 % mass fraction remaining for  $\alpha$ -pinene and limonene, respectively. This indicates that the volatility of limonene SOA is lower than  $\alpha$ -pinene which is more distinct difference than photochemically generated  $\alpha$ -pinene and limonene SOA. The result that limonene SOA is less volatile than  $\alpha$ -pinene SOA is consistent with the investigation of *Lee et al.*, [2011].

For  $\alpha$ -pinene SOA, addition of an OH scavenger had no discernable effect on the volatility of SOA (60 - 88 °C), in agreement with *Jonsson et al.*, [2007] who reported no difference in volatility with and without scavenger at the moderate temperatures used here, although they did find that particles generated without OH scavenger are less volatile than with OH scavenger when SOA was heated above 150 °C. SOA generated in the Nov.10 experiment is somewhat less volatile (by ~10%) than SOA from other  $\alpha$ -pinene/ozone without scavenger experiments (Nov.18 and Sept. 29; Table 5.1). This experiment had significantly lower RH (24-25 % vs 30-43 %), implying RH might affect SOA volatility, the same trend found from photochemically generated SOA; high RH increases the volatility of SOA (Table 5.1).

To investigate the effect of OH scavenger on the volatility of limonene SOA, we increased the TD to higher temperatures (90-105 °C) than for  $\alpha$ -pinene because of its less volatility. Within this range (66 - 105 °C), no discernable effect of OH scavenger on the volatility of SOA was found.

### **5.2.3 SOA refractive indices**

SOA cover a wide range of  $m_r$  values indicating significant variability in chemical composition capable of altering optical properties. Aerosol chemical composition is expected to depend on the parent hydrocarbon, its oxidation chemistry, the particle mass concentration, size,

the temperature, and under longer time scales, in-particle reactions and heterogeneous aging [Kim *et al.*, 2012]. Since thermodenuded and chamber particles are sampled alternately by the SMPS or PN, before and after size distribution means and standard deviations for the same type of SOA (non-thermodeuded or thermodeuded) were averaged to use in retrievals of the refractive index for each point. As measurements were made, later in the experiment, after rapid growth had stopped, the phase functions and size distributions changes were little from one cycle to the next. Additionally, any differences between the actual size distributions for the phase function are encompassed by the large ( $\pm 30\%$ ) genetic algorithm size parameter search space.

### 5.2.3.1 Photochemically generated SOA

The photochemical experiments were performed over a range of relative humidities (15 – 24%) in which water uptake, or phase, is still not expected to be changing rapidly (e.g., [Mikhailov *et al.*, 2009; Varutbangkul *et al.*, 2006]). The amount of water uptake may change considerably, however as the particles grow rather than RH changes [VanReken *et al.*, 2005; Varutbangkul *et al.*, 2006]. Fresher/smaller particles may contain a higher fraction of hygroscopic highly oxidized polar compounds with low volatility, while older/larger particles may contain less hygroscopic, higher volatility condensing species and/or oligomers [Varutbangkul *et al.*, 2006; Gao *et al.*, 2010; Chhabra *et al.*, 2011] Temperatures span a moderate range (33 – 39 °C) except two experiments (Aug 26, Aug 2) and do not appear to affect  $m_r$ s showing reasonably consistent refractive indices with the other data.

Figure 5.7 shows  $m_r$ s of both from the chamber (filled symbols) and thermodenuder (open symbols) as a function of particle diameter for photochemically generated toluene SOA under different HC/NO<sub>x</sub> ratios. Before heating, the value of the  $m_r$  for toluene SOA is in the range of 1.35 - 1.62, consistent with previous studies. [Kim *et al.*, 2010; Nakayama *et al.*, 2010].

We note that there is no evidence of significant absorption at 532 nm by toluene SOA. GA retrievals (which can provide only a rough estimate of absorption) return imaginary components of order  $10^{-5}$ , *Nakayama et al.*, [2010] also report a negligible absorption ( $m_i = 0.037$ ) at 532 nm for toluene SOA. In general, the freshest toluene SOA has low  $m_r$  values and the value increase as the particles grow, ending at a very high value of 1.62. This is significantly higher than any  $m_r$ s observed for SOA generated from biogenic HC,  $\alpha$ -pinene,  $\beta$ -pinene and limonene [*Kim et al.*, 2010].

As discussed in sections 5.4.2.1, toluene SOA exhibited virtually no evaporation upon heating up to  $\sim 98$  °C, thus no significant changes in size of particles are observed. Figure 5.7 show open symbols for the thermodenuded particles are paired with close by the solid symbols indicating the non-thermodenuded particles. The numbers denote the TD temperature for the particles  $m_r$ s retrieved. As shown in Figure 5.7,  $m_r$ s also do not change significantly upon heating, consistent with a lack of significant changes with SOA properties.

Figure 5.8 shows  $m_r$ s of photochemically generated limonene and  $\alpha$ -pinene SOA under different HC/NO<sub>x</sub> ratios both from the chamber (filled symbols) and thermodenuder (open symbols) as a function of particle diameter. Overall, for SOA that has not been thermodenuded (solid symbols),  $m_r$ s generally increase as the particle diameters increase (from 200 - 320 nm for limonene and from 180- 380 nm for  $\alpha$ -pinene). This is consistent with the investigation of *Kim et al.*, [2012]. And as discussed in *Kim et al.*, [2012], HC/NO<sub>x</sub> ratio is one of the factors controlling the size of particles; HC/NO<sub>x</sub> ratios decrease (e.g. the middle and right panels in Figure 5.8), size ranges of the particles increase for both limonene and  $\alpha$ -pinene. Figure 5.10 compares directly the  $m_r$  data for limonene and  $\alpha$ -pinene with *Kim et al.*, [2012]; the two data sets are in good agreement. However, later in the experiments and at larger particles, the  $m_r$ s level out and start to

decrease. This has not been previously observed for limonene, but it has been observed for  $\alpha$ -pinene. For example, limonene SOA (Figure 5.8a-c), solid symbol (from non thermodenuded particle) shows that refractive indices increase from 1.47 to 1.55 as the diameter of particles increase up to  $\sim 320$  nm (figures 5.8a,b,c). They drop off somewhat as the particles continue to grow for  $\text{HC}/\text{NO}_x = 6.9-13$  (Figures 5.8b and c). Aug. 16 ( $\text{HC}/\text{NO}_x = 33$ , Figure 5.8a) data shows that the particle size grow up more than other experiments even though the  $\text{HC}/\text{NO}_x$  ratio is high. Although initial experimental conditions are similar with others (e.g., temperature, RH and initial HC and  $\text{NO}_x$  concentration), there are uncontrollable factors such as solar intensity due to the outdoor chambers and that will results different particle growth dynamics suggesting that  $\text{HC}/\text{NO}_x$  ratio is not the only factor controlling the size of particles.

$\alpha$ -Pinene (Figures 5.8d-f, solid symbols from non thermodenuded particles) shows the same  $m_r$  trend with diameter; refractive indices increase from 1.43 to 1.54 as the diameter of particles increase when the  $\text{HC}/\text{NO}_x$  ratio was 28-33 (Figure 5.8d). For the lower  $\text{HC}/\text{NO}_x$  ratio experiments,  $m_r$ s dropping off somewhat as particles grow above 370 nm (figures 5.8e and 5.8f). The decrease of  $m_r$  at the large particles (and also at the end of the experiments) might be due to shifts in the composition of the condensing material as particles are growing or possibly changes in particle composition caused by heterogeneous or in-particle reactions (i.e., aging).

For both limonene and  $\alpha$ -pinene SOA, applying the TD changes their  $m_r$  (Figure 5.8, shown with large ovals and arrows). For limonene SOA generated at medium and high  $\text{NO}_x$  (Figures 5.8b and c), as the TD temperature increases, the size of particles decrease, and the  $m_r$ s change to roughly the same value for corresponding to the unheated particles of the same size. For example, for intermediate  $\text{HC}/\text{NO}_x=14$  (Figures 5.8b and c), after heating, particle size was reduced from 370 nm to 290-320 nm while  $m_r$ s increased from 1.48-1.5 to 1.5-1.54. For  $\text{HC}/\text{NO}_x$



= 13, as the size was reduced from 320 nm to 220-240 nm, the  $m_{r,s}$  decreased from 1.51-1.53 to 1.4-1.48, matching the values for this size of SOA before heating. Low HC/NO<sub>x</sub> (= 6.9) (Figure 5.8c) also shows the same trend; as the size was reduced from 360-400 nm to 300-320 nm the  $m_{r,s}$  increased from 1.47-1.49 to 1.52-1.55, mirroring the undenuded particles.

$\alpha$ -Pinene SOA (Figure 5.8d,e,f) behaves similarly to limonene SOA. For low and intermediate HC/NO<sub>x</sub> ratio (Figures 5.8e and f), when particles are heated, their size is reduced from 550 nm to 340-400 nm, while  $m_{r,s}$  increase from 1.47-1.48 to 1.49-1.54, the same or above the values for the same size particles prior to evaporation.

For a simple inert particles, these  $m_r$  change trend upon heating for both limonene and  $\alpha$ -pinene SOA under intermediate and high NO<sub>x</sub> conditions implies that the most volatile materials is deposited last in the experiments and then this material is easily re-volatilized upon heating. Evaporation of high volatility compounds will remain the lower volatility species which was there before the condensation of high volatility compounds on it. This way let  $m_r$  retrieval be made with same composition particle before growth due to condensation and essentially same  $m_{r,s}$  are retrieved for the same size of particles. This explanation is more plausible under the assumption of minimal mixing, slow diffusion during the growth of particles which are the properties of glass, wax or amorphous organic aerosol. Some recent studies indicate the potential of glassy/wax/amorphous organic aerosol. [Murray *et al.*, 2010; Virtanen *et al.*, 2010; Vaden *et al.*, 2011]

However, for both limonene and  $\alpha$ -pinene at low NO<sub>x</sub> (HC/NO<sub>x</sub> = 33), thermodenuding particles produces a different trend in  $m_{r,s}$ . The size of particles is also reduced, but the resulting particles do not have the same  $m_{r,s}$  as the same size of particles before heating; rather, they are lower. For instance, under HC/NO<sub>x</sub> = 32-33 (Figure 5.8a), after the heating of particles, the size

of limonene SOA was reduced from 290 to 240-260 nm (Aug 2) and from 340-350 to 240-270 nm (Aug 16), with concomitant changes in the  $m_{r,s}$  to  $\sim 1.38-1.48$ , substantially lower than the value of particles with the same size before heating as 1.48-1.52. Similarly,  $m_{r,s}$  of  $\alpha$ -pinene SOA under  $HC/NO_x = 28-33$  (Figure 5.8d) decreased 1.52-1.54 to 1.42-1.47 with decreasing diameter from 360-380 nm to 260-300 nm (Aug. 26) and from 1.45-1.49 to 1.39 -1.45 with decreasing diameter from 270 nm to 200-215 nm (Spet. 21) after heating, each of which is lower than the  $m_{r,s}$  for these size undenuded particles. These results suggest that the chemical composition of SOA formed under low  $NO_x$  conditions is different than high  $NO_x$ . *Lee et al.*, [2011] suggested, while particles are heated, oligomers which is probably more favored under high  $NO_x$  conditions [*Kim et al.*, 2012] are breaking down to the monomers. If this is the case, particles under high  $NO_x$  will have monomers after heating and go back to the previous chemical composition and related  $m_{r,s}$  of particles before having oligomers whereas particles under low  $NO_x$  where oligomerization is not favored, heating will evaporate the surface layer remaining inner layer which has different chemical composition showing lower value of  $m_{r,s}$ . All of these explanations are highly speculative but suggest that heating will change the chemical composition of particles and related  $m_{r,s}$  in a different manner for particles generated high and low  $NO_x$ .

### 5.2.3.2 Ozonolysis SOA

Figure 5.9 shows refractive indices retrieved as a function of particle diameter from angular scattering data of undenuded and thermodenuded SOA generated from  $\alpha$ -pinene and limonene ozonolysis with and without an OH scavenger, increasing from about 1.39 to 1.52 for SOA from smog chamber (filled symbols). In a previous study, *Kim et al.*[2010] showed that the effect of OH scavenger on  $m_{r,s}$  were not distinguishable for SOA for  $\alpha$ -pinene ozonolysis with the mass concentration range of 420 - 960  $\mu\text{g}/\text{m}^3$ , indicating the differences in SOA chemical composition

for the two oxidation chemistries are not sufficient to affect the optical properties. Here we generated again slightly lower mass concentrations (250-400  $\mu\text{g}/\text{m}^3$  for  $\alpha$ -pinene) and there is no evidence for an OH scavenger effect on  $m_{r,s}$ . Undenuded limonene SOA does not exhibit a significant effect from an OH scavenger on  $m_r$  and increases from about 1.42 to 1.52 (filled symbols). The Nov 18 data exhibits lower refractive indices (1.39-1.45), a phenomenon we have observed before [Kim *et al.*, 2010] for particles generated at lower temperatures (18-20 °C). The difference of temperature is smaller than in Kim *et al.*, [2010], however Salo *et al.*, [2012] show observations suggesting  $\sim 20$  °C is an important transition temperature for the chemical composition of  $\alpha$ -pinene SOA.

Undenuded ozonolysis SOA (filled symbols) are compared with SOA thermodenuded (open symbols) at various TD temperatures (Figure 5.9). Generally the retrieved  $m_{r,s}$  for the thermodenuded particles with reduced size have the same value as the same sized particles before heating. However, for  $\alpha$ -pinene SOA with OH scavenger (Figure 5.9b),  $m_{r,s}$  of thermodenuded SOA (TD temperature of 65 - 85 °C) show different trend. For this oxidation chemistry, denuded particles have slightly higher  $m_{r,s}$  (1.49-1.55 compared to 1.48-1.5) than the undenuded particles. This suggests that although the MFR is independent of the experimental conditions (section 5.4.2.2 and Figure 5.6), the chemical composition of these particles after evaporations is different. As discussed by Smith *et al.*, [2009], the presence of OH radicals could lead to heterogeneous reactions that could modify the particle composition differently, resulting different evaporation effect on chemical composition of particles. The different behavior of  $m_{r,s}$  changes upon heating between with and without OH scavenger is consistent with the previous studies (e.g., [Huffman *et al.*, 2009; Kostenidou *et al.*, 2009; Cappa and Wilson, 2011]). In Cappa and Wilson, [2011] and Huffman *et al.*, [2009]'s investigation, within the temperature

range of 23-170 °C, mass spectra of SOA generated from  $\alpha$ -pinene/ozone does not change even though there were significant mass loss due to evaporation. However, *Kostenidou et al.*, [2009] showed that for SOA generated from  $\alpha$ -pinene/ozone/scavenger, the fraction of  $\text{CO}_2^+$  ( $m/z$  44) of SOA increased by 37.5% as increasing the evaporation temperature up to 60-70°C. However given different particles generation conditions (e.g., tube vs. chamber, oxidation time), residence time for heating and other possible sources can results other explanations for the differences other than OH scavenger.

In contrast, limonene SOA did not exhibit any difference with or without scavenger (Figure 5.9a). Limonene SOA  $m_r$ s were nearly independent of oxidation chemistry, with and without scavenger within the same temperature ranges of  $\alpha$ -pinene. It is possible that the TD temperature range was not sufficient to evaporate the organic compounds to shows the difference since the volatility of limonene SOA is lower than the case of  $\alpha$ -pinene as discussed in section 5.4.2.1. Or perhaps, even after the evaporation of enough organic compounds, the chemical composition is not different in a way that significantly influences the refractive index.

### 5.3 Atmospheric implications

In an effort to retrieve the  $m_r$ s of SOA which closely resemble ambient aerosol, this work explores the effect of parent hydrocarbon ( $\alpha$ -pinene, limonene and toluene) and oxidation chemistry (with and without OH scavenger for ozonolysis, different HC/NO<sub>x</sub> ratios for photooxidation) on the volatility and related refractive indices of SOA, accomplished by removing high volatility components using thermodenuder. All above factors as well as some minor contribution of RH and temperature appear contribute to the volatility and related  $m_r$ s of the SOA. For thermodenuded SOA, we obtain  $m_r$ s of 1.41-1.5 for  $\alpha$ -pinene/ozone in the absence of OH scavenger and 1.49-1.56 of  $m_r$ s with OH scavenger. For limonene/ozone, 1.42-1.45 of  $m_r$ s

were retrieved for both with and without OH scavenger. For thermodenuded photooxidized SOA,  $m_r$ s still span wider ranges from 1.39 to 1.54 and 1.38 to 1.54 for  $\alpha$ -pinene and limoene, respectively depending on the HC/NO<sub>x</sub> ratio. Toluene SOA show very low vapor pressure resulting no measurable components was removed up to 98°C having  $m_r$ s range from 1.35-1.62 quite different from the two biogenic HCs.

Overall, after thermodenuding SOA, the ranges of  $m_r$ s still span a wide range. As described in the introduction, the refractive index is the fundamental property controlling aerosol optical properties. In a previous study, we showed that changing the refractive index from 1.4 to 1.5 decreases asymmetry factor by 0.067, which in turn changes radiative forcing by at least 12-19% for non-absorbing particles [Kim *et al.*, 2010; Andrews *et al.*, 2006; Marshall *et al.*, 1995]. There is more work to be done before recommendations can be made for atmospheric applications, but our  $m_r$  variations on oxidation chemistry and HC precursor indicate that a single value for SOA refractive index will not be sufficient to accurately model radiative transfer.

## 5.4 References

- Alfarra, M. R., D. Paulsen, M. Gysel, A. A. Garforth, J. Dommen, A. S. H. Prevot, D. R. Worsnop, U. Baltensperger, and H. Coe (2006), A mass spectrometric study of secondary organic aerosols formed from the photooxidation of anthropogenic and biogenic precursors in a reaction chamber, *Atmospheric Chemistry and Physics*, 6, 5279-5293.
- An, W. J., R. K. Pathak, B. H. Lee, and S. N. Pandis (2007), Aerosol volatility measurement using an improved thermodenuder: Application to secondary organic aerosol, *Journal of Aerosol Science*, 38(3), 305-314.
- Andrews, E., P. J. Sheridan, M. Fiebig, A. McComiskey, J. A. Ogren, P. Arnott, D. Covert, R. Elleman, R. Gasparini, D. Collins, H. Jonsson, B. Schmid, and J. Wang (2006), `Comparison of methods for deriving aerosol asymmetry parameter, *Journal of Geophysical Research-Atmospheres*, 111(D5).
- Bahreini, R., M. D. Keywood, N. L. Ng, V. Varutbangkul, S. Gao, R. C. Flagan, J. H. Seinfeld, D. R. Worsnop, and J. L. Jimenez (2005), Measurements of secondary organic aerosol from oxidation of cycloalkenes, terpenes, and m-xylene using an Aerodyne aerosol mass spectrometer, *Environmental Science & Technology*, 39(15), 5674-5688.

- Barkey, B., S. E. Paulson, and A. Chung (2007), Genetic algorithm inversion of dual polarization polar nephelometer data to determine aerosol refractive index, *Aerosol Science and Technology*, 41(8), 751-760.
- Burtscher, H., U. Baltensperger, N. Bukowiecki, P. Cohn, C. Huglin, M. Mohr, U. Matter, S. Nyeki, V. Schmatloch, N. Streit, and E. Weingartner (2001), Separation of volatile and non-volatile aerosol fractions by thermodesorption: instrumental development and applications, *Journal of Aerosol Science*, 32(4), 427-442.
- Cappa, C. D., and K. R. Wilson (2011), Evolution of organic aerosol mass spectra upon heating: implications for OA phase and partitioning behavior, *Atmospheric Chemistry and Physics*, 11(5), 1895-1911.
- Chhabra, P. S., N. L. Ng, M. R. Canagaratna, A. L. Corrigan, L. M. Russell, D. R. Worsnop, R. C. Flagan, and J. H. Seinfeld (2011), Elemental composition and oxidation of chamber organic aerosol, *Atmospheric Chemistry and Physics*, 11(17), 8827-8845.
- Chung, A., A. A. Lall, and S. E. Paulson (2008), Particulate emissions by a small non-road diesel engine: Biodiesel and diesel characterization and mass measurements using the extended idealized aggregates theory, *Atmospheric Environment*, 42(9), 2129-2140.
- Griffin, R. J., D. R. Cocker, R. C. Flagan, and J. H. Seinfeld (1999), Organic aerosol formation from the oxidation of biogenic hydrocarbons, *Journal of Geophysical Research-Atmospheres*, 104(D3), 3555-3567.
- Hallquist, M., J. C. Wenger, U. Baltensperger, Y. Rudich, D. Simpson, M. Claeys, J. Dommen, N. M. Donahue, C. George, A. H. Goldstein, J. F. Hamilton, H. Herrmann, T. Hoffmann, Y. Iinuma, M. Jang, M. E. Jenkin, J. L. Jimenez, A. Kiendler-Scharr, W. Maenhaut, G. McFiggans, T. F. Mentel, A. Monod, A. S. H. Prevot, J. H. Seinfeld, J. D. Surratt, R. Szmigielski, and J. Wildt (2009), The formation, properties and impact of secondary organic aerosol: current and emerging issues, *Atmospheric Chemistry and Physics*, 9(14), 5155-5236.
- Huffman, J. A., P. J. Ziemann, J. T. Jayne, D. R. Worsnop, and J. L. Jimenez (2008), Development and characterization of a fast-stepping/scanning thermodesorber for chemically-resolved aerosol volatility measurements, *Aerosol Science and Technology*, 42(5), 395-407.
- Huffman, J. A., K. S. Docherty, C. Mohr, M. J. Cubison, I. M. Ulbrich, P. J. Ziemann, T. B. Onasch, and J. L. Jimenez (2009), Chemically-Resolved Volatility Measurements of Organic Aerosol from Different Sources, *Environmental Science & Technology*, 43(14), 5351-5357.
- Johnson, D., M. E. Jenkin, K. Wirtz, and M. Martin-Reviejo (2005), Simulating the formation of secondary organic aerosol from the photooxidation of aromatic hydrocarbons, *Environmental Chemistry*, 2(1), 35-48.
- Jonsson, A. M., M. Hallquist, and H. Saathoff (2007), Volatility of secondary organic aerosols from the ozone initiated oxidation of alpha-pinene and limonene, *Journal of Aerosol Science*, 38(8), 843-852.
- Kanakidou, M., J. H. Seinfeld, S. N. Pandis, I. Barnes, F. J. Dentener, M. C. Facchini, R. Van Dingenen, B. Ervens, A. Nenes, C. J. Nielsen, E. Swietlicki, J. P. Putaud, Y. Balkanski, S. Fuzzi, J. Horth, G. K. Moortgat, R. Winterhalter, C. E. L. Myhre, K. Tsigaridis, E. Vignati, E. G. Stephanou, and J. Wilson (2005), Organic aerosol and global climate modelling: a review, *Atmospheric Chemistry and Physics*, 5, 1053-1123.
- Kim, H., B. Barkey, and S. E. Paulson Real refractive indices and formation yields of secondary organic aerosol generated from photooxidation of limonene and  $\alpha$ -pinene: the effect of the HC/NO<sub>x</sub> Ratio, *Journal of Physical Chemistry A*, submitted.

- Kim, H., B. Barkey, and S. E. Paulson (2010), Real refractive indices of alpha- and beta-pinene and toluene secondary organic aerosols generated from ozonolysis and photo-oxidation, *Journal of Geophysical Research-Atmospheres*, *115*, 10.
- Kim, H., B. Barkey, and S. E. Paulson (2012), Real refractive indices and formation yields of secondary organic aerosol generated from photooxidation of limonene and  $\alpha$ -pinene: the effect of the HC/NO<sub>x</sub> Ratio, *The Journal of Physical Chemistry A*, *accepted*.
- Kostenidou, E., B. H. Lee, G. J. Engelhart, J. R. Pierce, and S. N. Pandis (2009), Mass Spectra Deconvolution of Low, Medium, and High Volatility Biogenic Secondary Organic Aerosol, *Environmental Science & Technology*, *43*(13), 4884-4889.
- Lee, B. H., E. Kostenidou, L. Hildebrandt, I. Riipinen, G. J. Engelhart, C. Mohr, P. F. DeCarlo, N. Mihalopoulos, A. S. H. Prevot, U. Baltensperger, and S. N. Pandis (2010), Measurement of the ambient organic aerosol volatility distribution: application during the Finokalia Aerosol Measurement Experiment (FAME-2008), *Atmospheric Chemistry and Physics*, *10*(24), 12149-12160.
- Lee, B. H., J. R. Pierce, G. J. Engelhart, and S. N. Pandis (2011), Volatility of secondary organic aerosol from the ozonolysis of monoterpenes, *Atmospheric Environment*, *45*(14), 2443-2452.
- Marshall, S. F., D. S. Covert, and R. J. Charlson (1995), Relationship between asymmetry parameter and hemispheric backscatter ratio - implications for climate forcing by aerosols, *Applied Optics*, *34*(27), 6306-6311.
- Mikhailov, E., S. Vlasenko, S. T. Martin, T. Koop, and U. Poschl (2009), Amorphous and crystalline aerosol particles interacting with water vapor: conceptual framework and experimental evidence for restructuring, phase transitions and kinetic limitations, *Atmospheric Chemistry and Physics*, *9*(24), 9491-9522.
- Murray, B. J., T. W. Wilson, S. Dobbie, Z. Q. Cui, S. Al-Jumur, O. Mohler, M. Schnaiter, R. Wagner, S. Benz, M. Niemand, H. Saathoff, V. Ebert, S. Wagner, and B. Karcher (2010), Heterogeneous nucleation of ice particles on glassy aerosols under cirrus conditions, *Nature Geoscience*, *3*(4), 233-237.
- Nakayama, T., Y. Matsumi, K. Sato, T. Imamura, A. Yamazaki, and A. Uchiyama (2010), Laboratory studies on optical properties of secondary organic aerosols generated during the photooxidation of toluene and the ozonolysis of alpha-pinene, *Journal of Geophysical Research-Atmospheres*, *115*, 11.
- Ng, N. L., J. H. Kroll, M. D. Keywood, R. Bahreini, V. Varutbangkul, R. C. Flagan, J. H. Seinfeld, A. Lee, and A. H. Goldstein (2006), Contribution of first- versus second-generation products to secondary organic aerosols formed in the oxidation of biogenic hydrocarbons, *Environmental Science & Technology*, *40*(7), 2283-2297.
- Ng, N. L., P. S. Chhabra, A. W. H. Chan, J. D. Surratt, J. H. Kroll, A. J. Kwan, D. C. McCabe, P. O. Wennberg, A. Sorooshian, S. M. Murphy, N. F. Dalleska, R. C. Flagan, and J. H. Seinfeld (2007a), Effect of NO<sub>x</sub> level on secondary organic aerosol (SOA) formation from the photooxidation of terpenes, *Atmospheric Chemistry and Physics*, *7*(19), 5159-5174.
- Ng, N. L., J. H. Kroll, A. W. H. Chan, P. S. Chhabra, R. C. Flagan, and J. H. Seinfeld (2007b), Secondary organic aerosol formation from m-xylene, toluene, and benzene, *Atmospheric Chemistry and Physics*, *7*(14), 3909-3922.
- Ng, N. L., M. R. Canagaratna, Q. Zhang, J. L. Jimenez, J. Tian, I. M. Ulbrich, J. H. Kroll, K. S. Docherty, P. S. Chhabra, R. Bahreini, S. M. Murphy, J. H. Seinfeld, L. Hildebrandt, N. M. Donahue, P. F. DeCarlo, V. A. Lanz, A. S. H. Prevot, E. Dinar, Y. Rudich, and D. R.

- Worsnop (2010), Organic aerosol components observed in Northern Hemispheric datasets from Aerosol Mass Spectrometry, *Atmospheric Chemistry and Physics*, 10(10), 4625-4641.
- Paulson, S. E., M. Chung, A. D. Sen, and G. Orzechowska (1998), Measurement of OH radical formation from the reaction of ozone with several biogenic alkenes, *Journal of Geophysical Research-Atmospheres*, 103(D19), 25533-25539.
- Presto, A. A., K. E. H. Hartz, and N. M. Donahue (2005), Secondary organic aerosol production from terpene ozonolysis. 2. Effect of NO<sub>x</sub> concentration, *Environmental Science & Technology*, 39(18), 7046-7054.
- Saathoff, H., K. H. Naumann, O. Mohler, A. M. Jonsson, M. Hallquist, A. Kiendler-Scharr, T. F. Mentel, R. Tillmann, and U. Schurath (2009), Temperature dependence of yields of secondary organic aerosols from the ozonolysis of alpha-pinene and limonene, *Atmospheric Chemistry and Physics*, 9(5), 1551-1577.
- Salo, K., M. Hallquist, A. M. Jonsson, H. Saathoff, K. H. Naumann, C. Spindler, R. Tillmann, H. Fuchs, B. Bohn, F. Rubach, T. F. Mentel, L. Muller, M. Reinnig, T. Hoffmann, and N. M. Donahue (2012), Volatility of secondary organic aerosol during OH radical induced ageing, *Atmospheric Chemistry and Physics*, 11(21), 11055-11067.
- Smith, J. D., J. H. Kroll, C. D. Cappa, D. L. Che, C. L. Liu, M. Ahmed, S. R. Leone, D. R. Worsnop, and K. R. Wilson (2009), The heterogeneous reaction of hydroxyl radicals with sub-micron squalane particles: a model system for understanding the oxidative aging of ambient aerosols, *Atmos. Chem. Phys.*, 9(9), 3209-3222.
- Vaden, T. D., D. Imre, J. Beranek, M. Shrivastava, and A. Zelenyuk (2011), Evaporation kinetics and phase of laboratory and ambient secondary organic aerosol, *Proceedings of the National Academy of Sciences of the United States of America*, 108(6), 2190-2195.
- Virtanen, A., J. Joutsensaari, T. Koop, J. Kannosto, P. Yli-Pirila, J. Leskinen, J. M. Makela, J. K. Holopainen, U. Poschl, M. Kulmala, D. R. Worsnop, and A. Laaksonen (2010), An amorphous solid state of biogenic secondary organic aerosol particles, *Nature*, 467(7317), 824-827.
- Wehner, B., S. Philippin, and A. Wiedensohler (2002), Design and calibration of a thermodenuder with an improved heating unit to measure the size-dependent volatile fraction of aerosol particles, *Journal of Aerosol Science*, 33(7), 1087-1093.
- Zhang, Q., M. R. Alfarra, D. R. Worsnop, J. D. Allan, H. Coe, M. R. Canagaratna, and J. L. Jimenez (2005), Deconvolution and quantification of hydrocarbon-like and oxygenated organic aerosols based on aerosol mass spectrometry, *Environmental Science & Technology*, 39(13), 4938-4952.



**Table 5.1. Initial conditions, temperatures, relative humidities and results of the ozonolysis experiment**

Run	Hydrocarbon	Initial conditions				Results				
		HC (ppb)	Ozone (ppb)	Temp (°C)	RH (%)	$\Delta$ HC (ppb)	# density <sup>1</sup> (#/cm <sup>3</sup> )	Size mode <sup>1</sup> (nm)	Mass <sup>2</sup> ( $\mu$ g/m <sup>3</sup> )	Yield <sup>3</sup> (%)
<b>20-Aug</b>	$\alpha$ -pinene <sup>4</sup>	143	500	26-27	33-31	107	1080	478	28-230	46
<b>18-Oct</b>	$\alpha$ -pinene <sup>4</sup>	150	500	23-26	34-36	130	2780	414	39-271	44
<b>29-Sep</b>	$\alpha$ -pinene	170	500	23-28	38-30	156	5820	322	37-271	40
<b>10-Nov</b>	$\alpha$ -pinene	160	500	23-22	24-25	160	25600	217	71-349	45
<b>18-Nov</b>	$\alpha$ -pinene	126	500	18-20	43-39	118	17400	233	34-215	39
<b>31-Aug</b>	limonene <sup>4</sup>	167	500	25-27	38-35	167	1280	300	98-579	78
<b>23-Nov</b>	limonene	198	500	20-22	41-35	198	33000	209	83-614	72
<b>24-Oct</b>	limonene	150	500	21-23	42-40	150	18800	250	96-454	72

<sup>1</sup> Final aerosol number concentration and size mode. These values have not been adjusted for wall losses.

<sup>2</sup> Mass concentrations in the chamber were determined from the SMPS measured size distribution in the chamber over the period for which meaningful PN measurements were made. Particle density was assumed as 1.2 g/cm<sup>3</sup> for  $\alpha$ -pinene and 1.25 g/cm<sup>3</sup> for limonene.

<sup>3</sup> Calculated from peak measured aerosol mass corrected for wall losses and the corresponding quantity of reacted hydrocarbon. Because of the uncertainty in measurement of GC ( $\pm$  3 %) and measurement of SMPS ( $\pm$  10 %) yields are uncertain to  $\pm$  10 %.

<sup>4</sup> Cyclohexane was added in 50 fold excess compared to the hydrocarbon to suppress OH formation.

**Table 5.2. Initial conditions, temperatures, relative humidities and results of the photo oxidation experiments**

Expt.	Initial Conditions						Results				
	Hydrocarbon	HC (ppb)	NO <sub>x</sub> (ppb)	HC/NO <sub>x</sub> (ppbC/ppb)	Temp (°C) <sup>1</sup>	RH (%) <sup>1</sup>	ΔHC (ppb)	# density (#/cm <sup>3</sup> ) <sup>2</sup>	Size mode (nm) <sup>2</sup>	Mass <sup>3</sup> (μg/m <sup>3</sup> )	Yield <sup>4</sup> (%)
<b>18-Aug</b>	α-pinene	150	230	6.5	39-33	17-23	150	255	573	9-44	5.9
<b>22-Aug</b>	α-pinene	152	110	14	37-39-33	20-17-24	148	599	514	19-103	14
<b>21-Sep</b>	α-pinene	142	50	28	33-36	28-25	138	3740	359	18-107	16
<b>26-Aug</b>	α-pinene	153	47	33	39-46-42	18-13-15	130	1540	429	22-118	17
<b>8-Aug</b>	limonene	208	300	6.9	37-32	16-20	206	3692	429	96-287	35
<b>4-Aug</b>	limonene	140	98	14	36-40	15-18	138	1833	400	34-195	35
<b>16-Nov</b>	limonene	157	120	13	24-26	38-34	144	3523	359	32-214	37
<b>2-Aug</b>	limonene	130	41	32	38-42	15-18	128	2470	300	11-219	43
<b>16-Aug</b>	limonene	130	39	33	35-39-34	22-18-24	130	2795	372	14-275	47
<b>29-Aug</b>	Toluene	2760	1350	15	42-35	18-26	990	5460	445	74-365	4.0
<b>24-Aug</b>	Toluene	2770	620	32	39-35	20-24	820	3090	429	100-320	11

<sup>1</sup>Initial and final temperature and relative humidity

<sup>2</sup>Final aerosol number concentration and size mode. These values have not been adjusted for wall losses.

<sup>3</sup>Mass concentration in the chamber was determined from the SMPS measured size distribution in the chamber over the period for which meaningful PN measurements were made. Particle density was assumed as 1.2 g/cm<sup>3</sup> for α-pinene, 1.25 g/cm<sup>3</sup> for limonene and 1.24 g/cm<sup>3</sup> for toluene.

<sup>4</sup>Calculated from peak measured aerosol mass corrected for wall losses and the corresponding quantity of reacted hydrocarbon. Because of the uncertainties in the measurement from GC (± 3 %) and measurement of SMPS (± 10 %) yields are uncertain to ± 10 %.

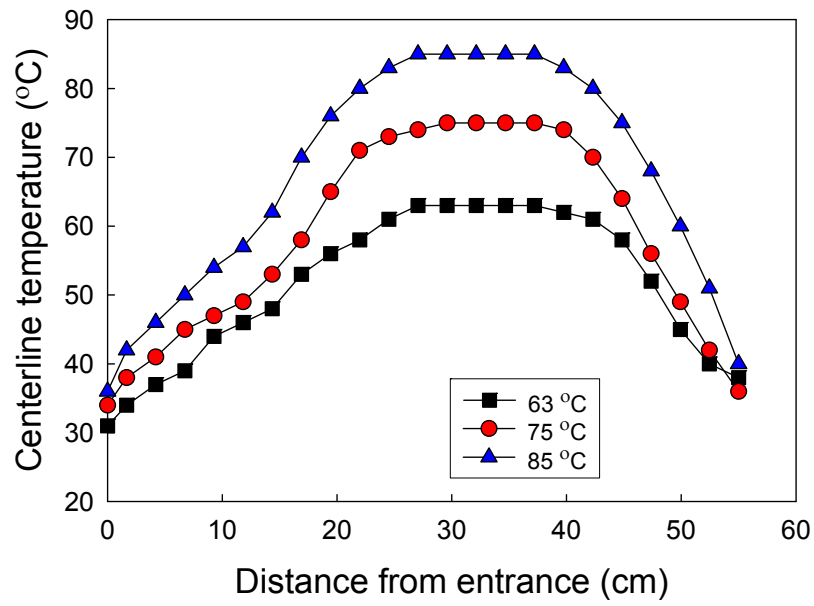


**Figure 5.1.** Temperature profile along the axis of the heating section at a flow rate of 1LPM for three set temperatures.

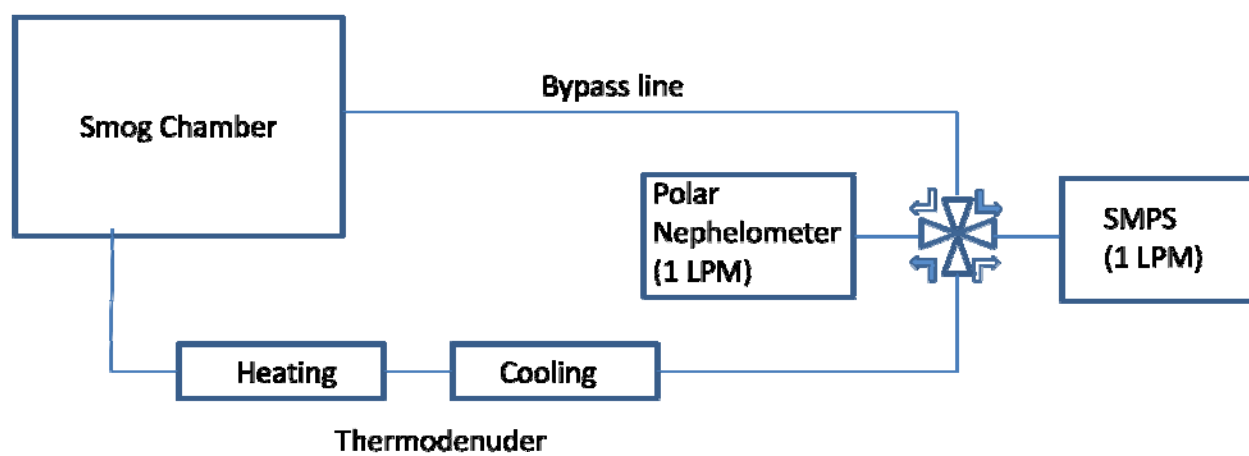


**Figure 5.2.** Schematic drawing of the experimental setup used for SOA volatility, angular scattering and size distribution

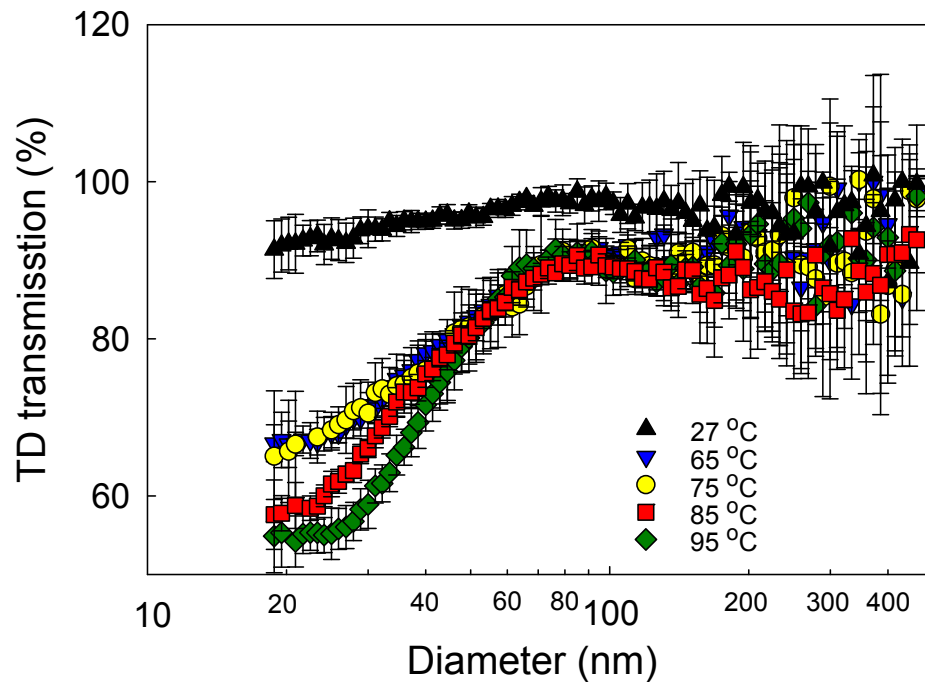


**Figure 5.3.** Particle number loss as a function of size within the TD at five different temperatures, as due to diffusion, thermophoresis and sedimentation. NaCl particles were used for the study of number loss because of their non-volatility under all experimental temperatures.

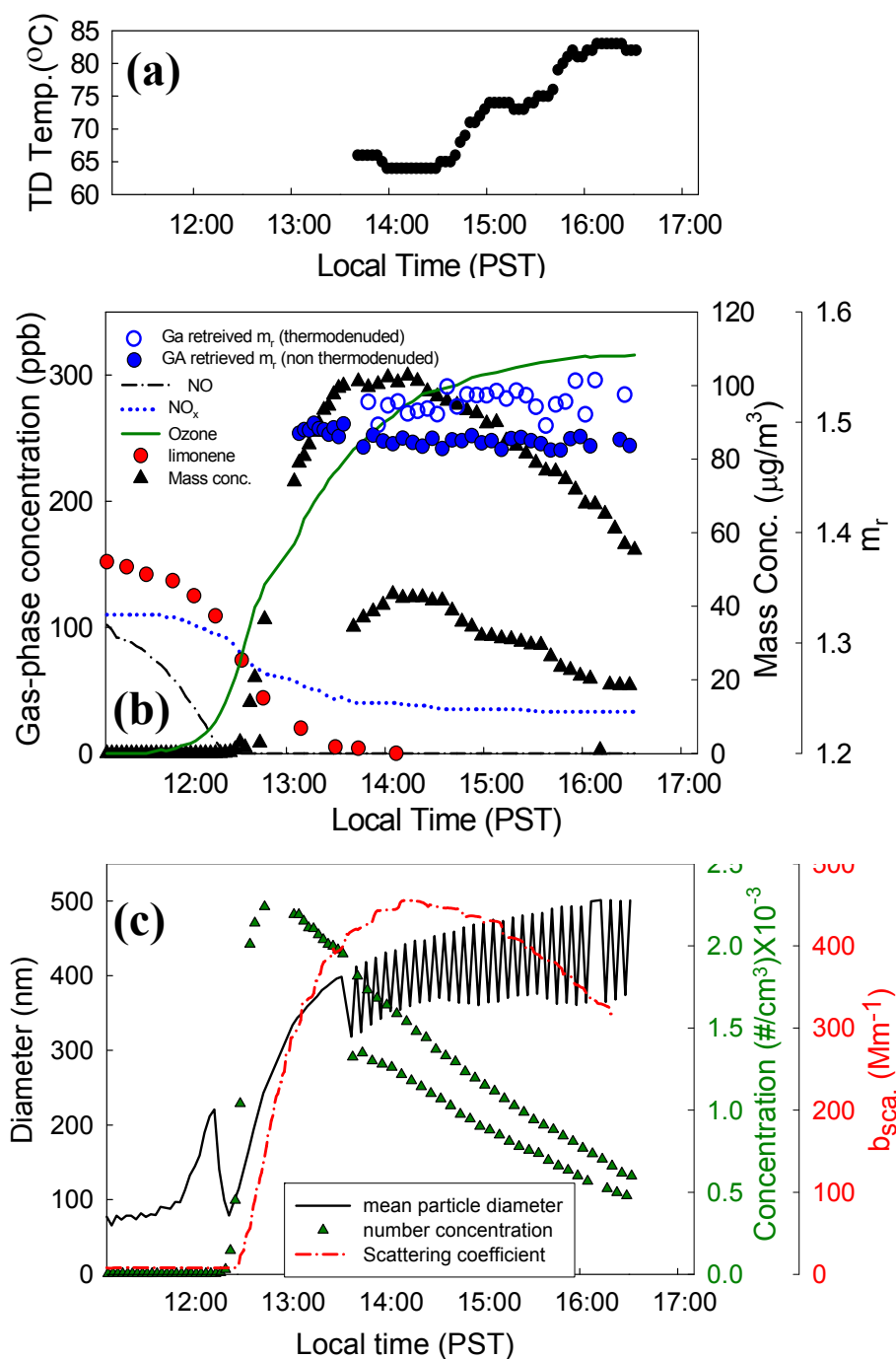


**Figure 5.4.** Profile of the  $\alpha$ -pinene photooxidation experiment performed on Aug. 22. (initial  $\alpha$ -pinene, 152 ppb; NO<sub>x</sub>, 110 ppb. (a) temperature profile of TD (b) Gas phase concentrations (hydrocarbon, NO, NO<sub>x</sub>, O<sub>3</sub>), aerosol mass concentration and GA determined real refractive index of SOA from chamber and thermodenuder (c) Time evolution of the SOA particle number concentrations, mean diameter of SOA from chamber and thermodenuder and scattering coefficient ( $\beta_{sca}$ ).

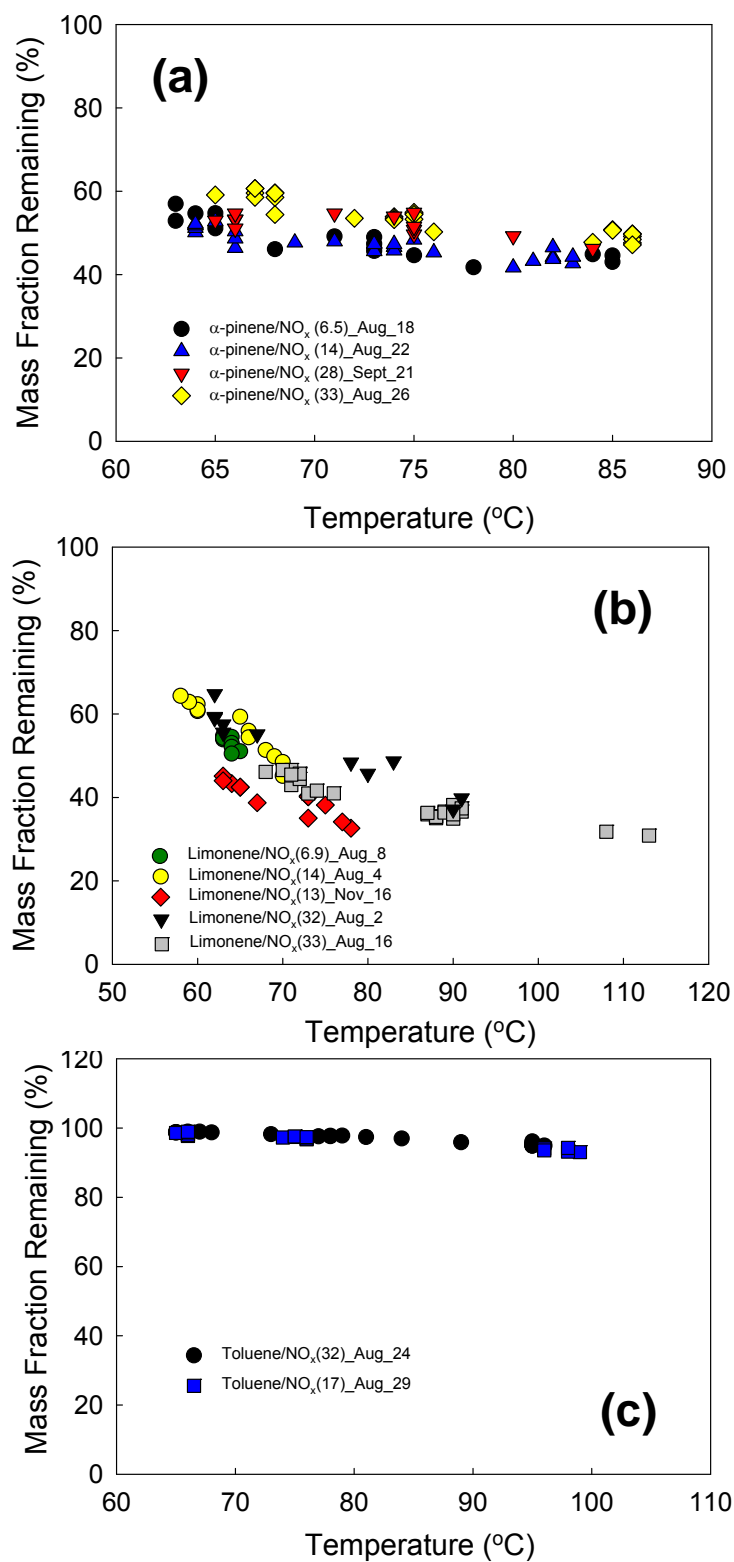


**Figure 5.5.** Mass fraction remaining after passing through TD as a function of TD temperature for SOA formed by photooxidation of (a)  $\alpha$ -pinene (b) limonene and (c) toluene at different HC/NO<sub>x</sub> ratios. All data corrected for experimentally determined TD losses ( Figure 5.3).

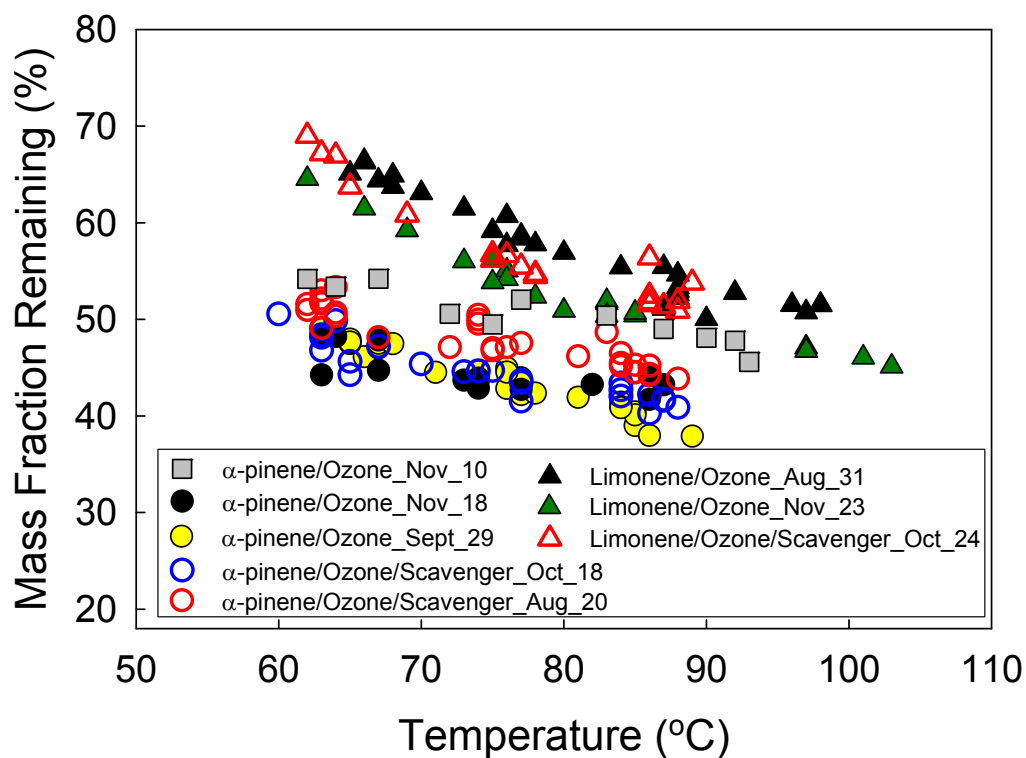


**Figure 5.6.** Mass fraction remaining after passing through TD as a function of TD temperature for SOA formed by ozonolysis of  $\alpha$ -pinene (circles) and limonene (triangles) without (filled symbols) and with (empty symbols) scavenger. All data shown here is corrected for experimentally determined losses in the TD (Figure 5.3).



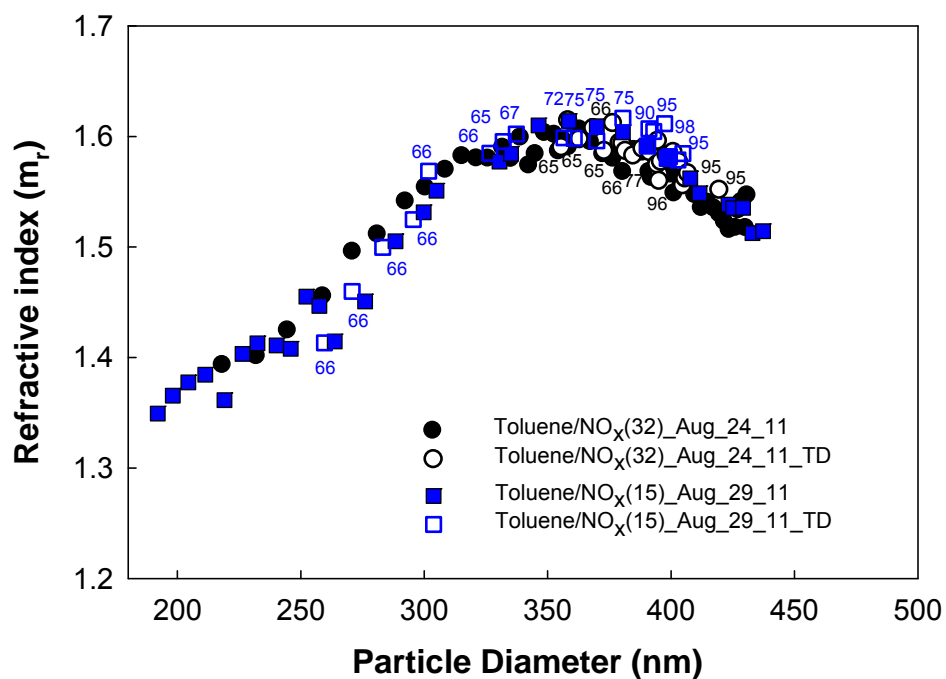


**Figure 5.7.** Retrieved refractive indices for thermodenuded (empty symbols) and non thermodenuded (filled symbols) SOA formed by photooxidation of toluene at different HC/NO<sub>x</sub> ratios. SOA were thermodenuded at different temperatures from 65 °C to 98 °C

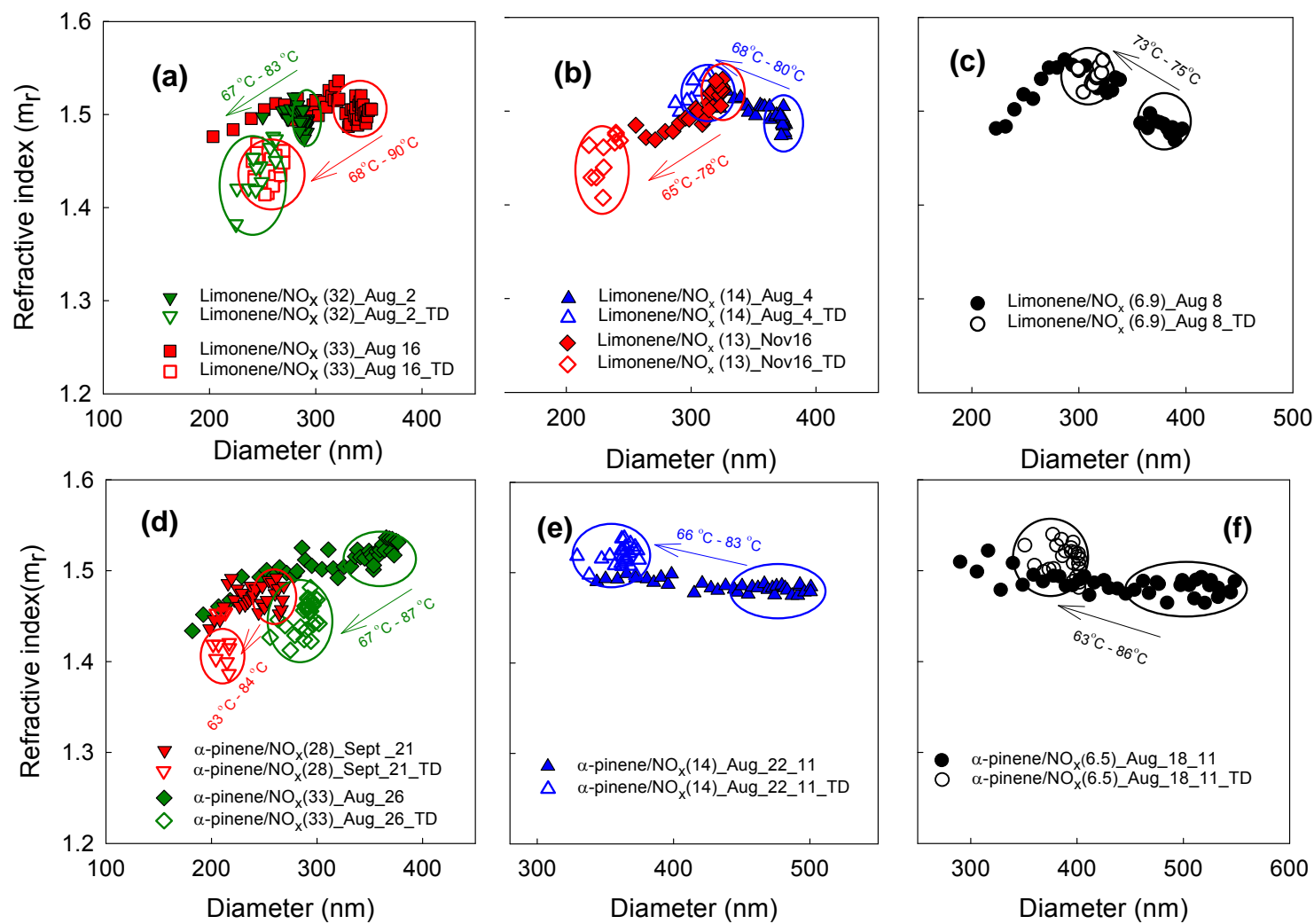


**Figure 5.8.** Retrieved refractive indices for thermodenuded (empty symbols) and non thermodenuded (filled symbols) SOA formed by photooxidation of limonene (upper panel; a-c) and  $\alpha$ -pinene (lower panels; d-f) at different HC/NO<sub>x</sub> ratios. SOA were thermodenuded at different temperatures from 65 °C to 90 °C

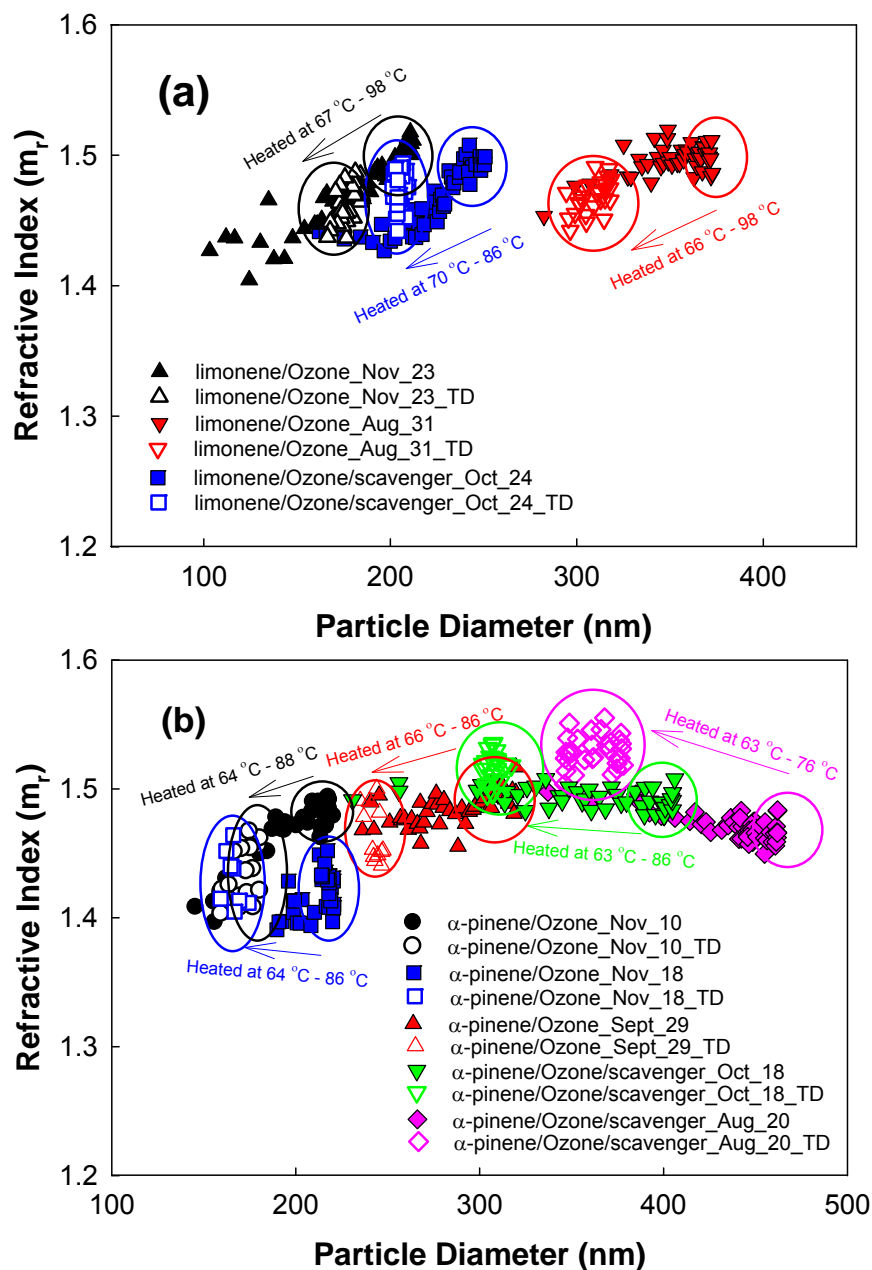


**Figure 5.9.** Retrieved refractive indices for thermodenuded (empty symbol) and non thermodenuded (filled symbol) SOA formed by ozonolysis of (a)  $\alpha$ -pinene and (b) limonene with and without scavenger. SOA were thermodenuded at different temperatures in from 64 °C to 98 °C

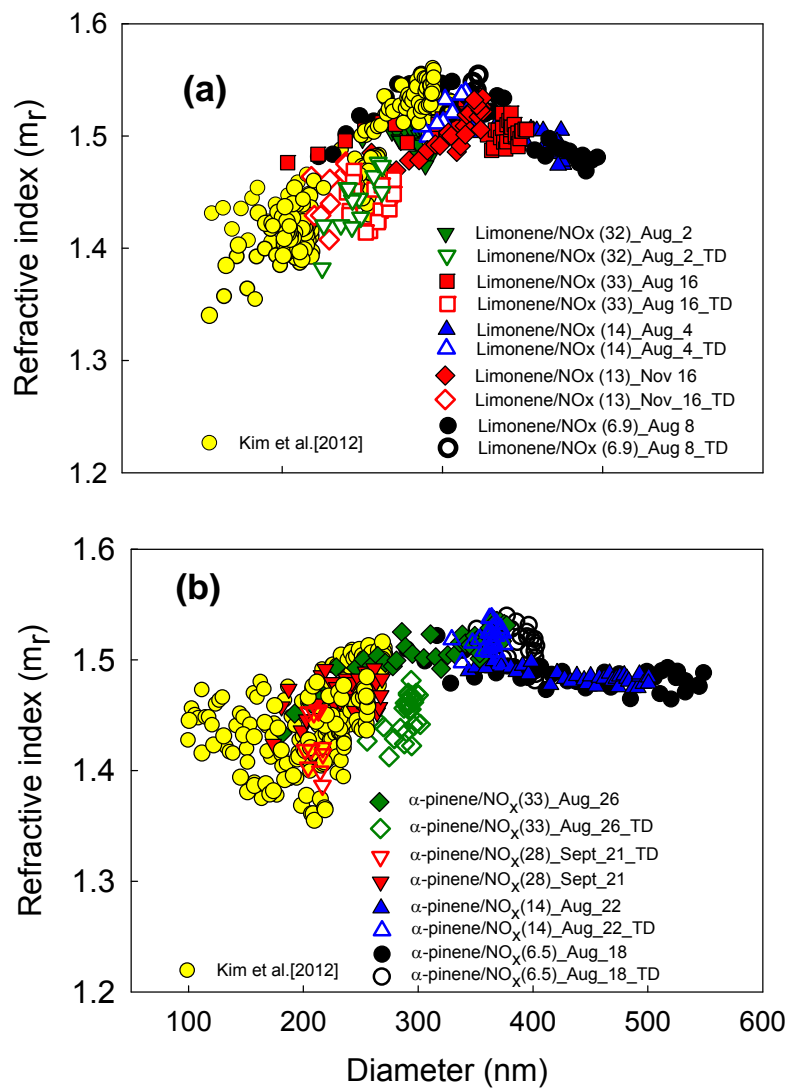


**Figure 5.10.** Comparisons of refractive indices of SOA formed by photooxidation of (a) limonene and (b)  $\alpha$ -pinene from current study with *Kim et al.*, [2010].

## **Chapter 6**

**Real refractive indices and elemental composition of secondary organic aerosol generated from ozonolysis and photooxidation of limonene and  $\alpha$ -pinene**

## 6.1 Experimental

Secondary organic aerosol generation in the chamber is described in detail in Chapter 2. Table 6.1 shows initial conditions and summary statistics for 6 experiments. Aerosols were characterized with the polar nephelometer, an integrating nephelometer (Ecotech M9003) and a scanning mobility particle sizer (SMPS, TSI model 3080). These instruments are described in detail in Chapter 2. Particularly, in the study, high-resolution time-of-flight aerosol mass spectrometer was used for the measurement of chemical composition.

An Aerodyne high-resolution time-of-flight aerosol mass spectrometer (HR-ToF-AMS; Aerodyne, Billerica, MA) was used to measure chemical composition and mass size distribution of SOA components. The HR-ToF-AMS is detailed in *DeCarlo et al.*, [2006]. Briefly, the instrument consists five major components: aerosol sampling inlet (aerodynamic lens), particle time-of-flight chamber, particle vaporization and ionization chamber, and a high-resolution time-of-flight mass spectrometer. Particles entering the instruments are focused by the aerodynamic lens, forming a highly collimated particle beam. The particles impact a heated surface (600°C) and the nonrefractory components are flash vaporized. The vapors are ionized by electron impact and simultaneously fragmented, followed by quantification with a time-of-flight mass spectrometer. Particle vacuum aerodynamic diameter (dva) is determined by particle time-of-flight (PTOF) between a mechanical rotating chopper (at the front of the particle time-of-flight chamber) and the vaporizer using a calibration curve, which is derived from PTOF of polystyrene latex particles of known sizes. During the measurements, the mass spectrometer (MS) mode (including the high S/N V mode and the high mass-resolution W mode) and the PTOF mode alternated with ~5 min time resolution. Chemical composition of ensemble

particles, including organic mass (OM), nitrate, and oxygen-to-carbon ratio (O/C) and hydrogen-to-carbon ratio (H/C) are derived from the V mode measurements.

## 6.2 Results and Discussion

Six experiments were performed with two different precursors (limonene and  $\alpha$ -pinene) using photooxidation and ozonolysis. For photooxidation, three different conditions of experiments are performed; low  $\text{NO}_x$  (initial  $\text{HC}/\text{NO}_x = 31 - 33$  ppbC/ppb), intermediate  $\text{NO}_x$  ( $\text{HC}/\text{NO}_x = 14$  ppbC/ppb) and high  $\text{NO}_x$  ( $\text{HC}/\text{NO}_x = 6.6$  ppbC/ppb). For ozonolysis, two different conditions of experiments are performed; with scavenger and without scavenger [Paulson *et al.*, 1998]. Detailed experimental conditions are shown in Table 6.1; precursor concentrations ranged from 170 – 200 ppb for limonene, 134 – 149 ppb for  $\alpha$ -pinene and 52 – 290 ppb for NO. With the exception of the  $\alpha$ -pinene photooxidation experiment (Jan 29, 33-37 °C), temperatures ranged from 16°C – 29°C and relative humidity (RH) ranged from 13 % – 29 %. The temperature range here is lower than summer experiments described in Kim *et al.*, [2012] (31°C – 39°C).

### 6.2.1 SOA refractive indices

Figure 6.1 shows  $m_p$ s of SOA generated under different conditions. SOA from photooxidation of limonene and  $\alpha$ -pinene under different  $\text{HC}/\text{NO}_x$  ratios (Figure 6.1a) and SOA from ozonolysis of  $\alpha$ -pinene performed with and without an OH scavenger (Figure 6.1b) are shown as a function of particle diameter. Particle diameter is consistently the independent variable best correlated with refractive index data [Kim *et al.*, 2012].

For photochemically generated SOA, limonene SOA  $m_r$ s increase from 1.34 to 1.55 with diameter (166 - 331 nm).  $\alpha$ -Pinene SOA  $m_r$ s are also appears to slightly increase from 1.44 to 1.47 as particles grow from 148 to 256 nm. Both the ranges and values are consistent with previous studies [Kim *et al.*, 2012] although the dependence on HC/NO<sub>x</sub> for limonene is different than observations by [Kim *et al.*, 2012]. Here  $m_r$ s of limonene SOA generated at different HC/NO<sub>x</sub> are compared to investigate the contribution of RO<sub>2</sub> + NO vs. RO<sub>2</sub> + HO<sub>2</sub> and RO<sub>2</sub> + RO<sub>2</sub> to both chemical composition and optical properties of particles. Previous studies showed that HC/NO<sub>x</sub> ratio is one of the factors to control the size of particles in such a way that as decreasing HC/NO<sub>x</sub> ratio, maximum size of particles increased and  $m_r$ s increased for both limonene and  $\alpha$ -pinene but more strong influence of HC/NO<sub>x</sub> ratio was observed with limonene SOA, so we are investigating limonene SOA here. The result shown at Figure 6.1a still shows the size dependent trend of  $m_r$ s but HC/NO<sub>x</sub> ratio effect on the size is less clear than previous [Kim *et al.*, 2012]. This seems because current experiments are performed during winter season when light intensity and temperature are low so that chemical reactions and growth of particles are slow, whereas the data of Kim *et al.*, [2012] performed during summer when there are strong light intensity and high temperature, chemical reactions and particle growth are fast reaching to the maximum size soon. Leungsakul *et al.*, [2005] investigated that ozone formation is most sensitive to the changes of light intensity; with the decreasing of actinic flux (photon cm<sup>2</sup> s<sup>-1</sup>) by 30% (from September to winter solstice) [Finlayson-Pitts and Pitts, 1999], ozone concentration decrease by 13% which is related with lower number of nucleated particles reaching the bigger particles later [Kim *et al.*, 2012]. In this study, although it is weak dependence, slight increasing trend of maximum size with decreasing HC/NO<sub>x</sub> is still found (Table 6.1) and also overall range and trend of  $m_r$ s are consistent with previous studies; smallest, newest particles have a



significantly lower refractive indices than slightly older, larger particles, after the particles grow to approximately 90 % of their maximum size, their  $m_r$ s level out and from certain size (~331nm)  $m_r$  start to decrease [Kim *et al.* 2012].  $\alpha$ -Pinene  $m_r$  starts with higher value as 1.44 than limonene SOA at similar particle size and this trend also was observed in Kim *et al.*, [2012]. This seems because  $m_r$  is retrieved for the different stage of particles;  $\alpha$ -pinene SOA is not younger particles comparing with limonene SOA, rather oxidized enough when  $m_r$  is retrieved, which will be discussed with chemical composition of SOA later in section 6.4.3. The limonene photochemical experiments were performed in a range of relative humidities (13 – 39%) in which water uptake, or phase, is still not expected to be changing rapidly (e.g., [Mikhailov *et al.*, 2009]) and temperatures span a moderate range (16 – 27 °C).  $\alpha$ -Pinene photochemical experiment was performed under somewhat different conditions; lower humidity (6-7%) and higher temperature (33 - 37°C) than limonene experiment but water uptake or phase is still not expected to change within this range of RH [Mikhailov *et al.*, 2009].

Figure 6.1b shows refractive indices of SOA generated from  $\alpha$ -pinene ozonolysis performed with and without an OH scavenger as a function of particle diameter. The two experiments have significantly different ranges; 1.46 to 1.52 and 1.43 to 1.45 for with and without scavenger, respectively. In previous studies, Kim *et al.*, [2010] showed that the addition of an OH scavenger did not have a discernable effect on  $m_r$ s of  $\alpha$ -pinene ozonolysis SOA, indicating the differences in SOA chemical composition for the two oxidation chemistries are not sufficient to affect to the optical properties within the resolution of our method. However, the same study showed that significantly lower oxidation temperatures (~14 °C instead of 26 °C from Kim *et al.*, [2010]) had a substantial effect on the refractive index. Several studies showed the evidence that temperature can affect to the chemical composition of SOA; Warren *et al.*,

[2009] found evidence for a non-reversible difference in the chemical composition of  $\alpha$ -pinene aerosol formed at  $\sim 5$  °C vs. at 28 °C and *Salo et al.*, [2012] showed that  $\sim 20$  °C seems to be the transition temperature to change the chemical composition of SOA.

The ranges of  $m_r$ s retrieved here (1.43-1.45 at 19-22 °C and 1.46-1.52 at 23-29 °C) are consistent with previous retrieved result (1.4-1.44 at  $\sim 14$  °C and 1.44-1.48 at 26 °C, [*Kim et al.*, 2010]) being higher by  $\sim 0.02$ - $0.03$  which is due to shorter wavelength of laser used here (532 nm) than the light used previous retrieval (670nm) [*Yu et al.*, 2008].

### 6.2.2 Chemical composition of SOA

The most intense peaks measured with the AMS occur at  $m/z$  27 ( $C_2H_3^+$ ),  $m/z$  29 ( $CHO^+$ ),  $m/z$  41 ( $C_3H_5^+$ ),  $m/z$  43 ( $C_2H_3O^+$ ,  $C_3H_7^+$ ),  $m/z$  44 ( $CO_2^+$ ),  $m/z$  55 ( $C_3H_3O^+$ ,  $C_4H_7^+$ ) and  $m/z$  57 ( $C_3H_5O^+$ ,  $C_4H_9^+$ ). Of these,  $m/z$  43 and 44 are the largest. The contributions by the different  $m/z$  signals vary with organic loadings. Figure 6.2 shows a triangle plot of  $f_{44}$  vs.  $f_{43}$  (e.g., 43/org) for SOA formed by the ozonolysis or photooxidation of  $\alpha$ -pinene and limonene during the experiment. The portion of the experiments that had retrievable  $m_r$ s are shown as filled symbols. The two dotted lines in these figures outline the space into which ambient data typically fall [*Ng et al.*, 2010]. The direction of the trend with time in each experiment is indicated with arrows in the Figure. Limonene SOA (Figure 6.2a) reside in a higher  $f_{44}$  and lower  $f_{43}$  (open symbol) when particles start to be nucleated and as particles are growing,  $f_{43}$  increases and  $f_{44}$  decreases.  $\alpha$ -Pinene (Figure 6.2b) shows little different trend;  $f_{44}$  slightly decrease and increase again (arrow) and  $f_{43}$  also change directions in the middle of the reactions. The trend of reaction directions are discussed in detail below. All of our  $m_r$  retrieved laboratory data fall outside of the ambient range, residing at low  $f_{44}$  and high  $f_{43}$ .

For  $m_r$  retrieved particles, the chamber SOA all fall in a fairly narrow range of  $f_{44}$  and  $f_{43}$ , although SOA from photooxidation and ozonolysis of  $\alpha$ -pinene (Figure 6.2b) has a relatively higher  $f_{44}$  and lower  $f_{43}$  than limonene (Figure 6.2a). Residing outside of the dotted lines indicates that the laboratory SOA is less oxidized as ambient aerosol. Possible reasons for laboratory SOA being less oxidized than ambient aerosols are; higher loadings employed in laboratory experiments that favor partitioning of less oxidized species (which should remain in the gas phase under atmospheric conditions) [Duplissy *et al.*, 2008; Shilling *et al.*, 2009] and the limited residence time (5-6h) in chambers, much shorter than the atmospheric lifetime (~4-5 days) of ambient aerosol [Rudich *et al.*, 2007].

Van Krevelen diagrams are shown in Figure 6.3. For limonene SOA, the earliest aerosol formed has an O:C ratio of 0.4. This decreases as the experiment progresses, reaching a final value of approximately 0.3. At the same time the H:C ratio increases from about 1.4 to 1.5. This behavior has been explained by increased partitioning of less oxidized semivolatile compounds as the mass concentration increases [Shilling *et al.*, 2009; Chan *et al.*, 2010]. In contrast, photochemically generated  $\alpha$ -pinene SOA, O:C starts at 0.4 and then increases to 0.42 while H:C changes little throughout the experiment (1.45-1.5). This is similar to  $\alpha$ -pinene SOA generated by ozonolysis, although this SOA had a slightly lower O:C ratio of 0.34-0.38. Although the trend and range of O:C and H:C ratio range is slightly different depending on the type of SOA, the overall range is in agreement with results for biogenic SOA in previous studies [Aiken *et al.*, 2008; Heaton *et al.*, 2009; Shilling *et al.*, 2009; Chhabra *et al.*, 2011].

The dependence of  $f_{44}$  on aerosol mass concentration (in the chamber) is shown at Figure 6.4.  $F_{44}(\text{CO}_2^+)$  is believed to be related to the contribution of low volatility material [Shilling *et al.*, 2009]. Particles for which refractive index data were retrieved are shown with filled symbols,

others with open symbols. Missing data for Jan 30 is due to an instrument problem at that time. In all cases,  $f_{44}$  decreases rapidly initially, and then begins to level out as particle growth slows. In some cases, late in the experiments,  $f_{44}$  trends upward again. This is consistent with the notion that initial nucleation and growth is due to the most highly oxygenated and least volatile species, which produce a higher  $f_{44}$ . These highly oxygenated species are later diluted in the particle phase by the partitioning of less oxygenated semivolatile species with lower  $f_{44}$ . Such behavior has been observed in several previous studies [Bahreini *et al.*, 2005; Kostenidou *et al.*, 2007; Shilling *et al.*, 2009].

### 6.2.3 $m_r$ and chemical composition of SOA

In an effort to relate SOA optical properties with chemical composition, the retrieved refractive indices of SOA are plotted with parameters explaining chemical compositions such as  $f_{44}$ ,  $f_{43}$  as well as O:C and H:C ratio (Figure 6.5).

#### 6.2.3.1 $\alpha$ -pinene ozonolysis SOA

Chemical composition and refractive index data for  $\alpha$ -pinene ozonolysis are shown in Figures 6.4a and 6.5. For both  $\alpha$ -pinene ozonolysis with and without scavenger,  $f_{44}$  is very similar. As shown at Figure 6.2 and 6.4a, at the beginning of  $m_r$  retrieval,  $f_{44}$  decreases ( $f_{43}$  increases from Figure 6.2) slightly from 0.13 to 0.1, a result of increased partitioning of less oxidized semivolatile compounds, which cause SOA growth. Later,  $f_{44}$  increase and  $f_{43}$  decrease possibly due to oxidation process overtaking partitioning of semivolatile species leading to an increase in the oxidation state of SOA [Chhabra *et al.*, 2011]. The increase in  $f_{44}$  is not obvious in Figure 6.4 because after SOA mass peaks when the organic loadings start to decrease owing to wall loss, the amount of  $f_{44}$  increased is not distinctive to be recognized but can be recognized at

Figure 6.2b with the direction of arrows. The slight increases in  $f_{44}$  coincide with small increases in refractive indices, which rise from 1.43 to 1.45 and 1.46 to 1.52 for Jan. 30 and Jan. 27, respectively, during the growth of particles (also see Figure 6.5c). The data in Figure 6.5c suggest that  $f_{44}$  by itself is not enough to explain the difference in  $m_r$  values between the two experiments performed on Jan 27 and 30 (for the part of the experiments with viable  $m_r$ , Figure 6.4). Jan 30 shows lower O:C and  $f_{44}$  and higher H:C and  $f_{43}$  than the Jan 27 experiment, indicating that SOA from Jan 30 may contain more high volatility species than Jan 27. This might be expected due to the difference in temperature of the two experiments; more condensation of higher volatility, high H:C and  $f_{43}$  material at lower temperature (Jan. 30).

#### 6.2.3.2 Photochemically generated $\alpha$ -pinene SOA

Chemical composition and refractive index data for photochemically generated  $\alpha$ -pinene SOA are shown in Figures 6.4b and 6.5. Figure 6.4b illustrates the mass loading effect on  $f_{44}$  for  $\alpha$ -pinene SOA generated by photochemical reaction. For particles (filled symbols) with sufficient scattering for  $m_r$  retrievals,  $f_{44}$  stay constant indicating that there is little change in higher volatility partitioning or level of oxidation. The portion of the experiments with constant  $f_{44}$  in the lower middle of Figure 6.4b is coincide with a period where  $\alpha$ -pinene SOA  $m_r$  is flat (Figure 6.1). Toward the end of the experiment,  $f_{44}$  increase (Figure 6.4b) and  $f_{43}$  decreases (Figure 6.2b with direction of arrow) slightly, indicating further changes in SOA composition, in the direction of increasing oxidation state. There is little associated change in refractive index, suggesting relatively little optical sensitivity to this shift. Including  $f_{44}$ , other parameters,  $f_{43}$ , H:C, and O:C change less than limonene SOA (Figure 6.5), consistent with the small variations of  $m_r$ s observed for  $\alpha$ -pinene compared to limonene SOA (discussed below).

### 6.2.3.3 Photochemically generated limonene SOA

Chemical composition and refractive index data for photochemically generated limonene SOA are shown in Figures 6.4c, 6.5 and 6.6. In contrast to  $\alpha$ -pinene SOA, both  $m_r$  and  $f_{44}$  continuously change throughout the experiments for photochemically generated limonene SOA (Figure 6.4c). The decreases in  $f_{44}$  suggest continuing condensation of less oxygenated species throughout the experiments, accompanied by continuous increases in the refractive index. This relationship is also exhibited in Figure 6.5c; decreases in  $f_{44}$  are associated with increases in  $m_r$ s. Also several other factors indicating the condensation of semivolatile species including H:C and  $f_{43}$  (Figures 6.5b and d) [Shilling *et al.*, 2009; Chan *et al.*, 2010; Chhabra *et al.*, 2010] also corroborate this trend; as increasing H:C (1.4-1.48),  $f_{43}$  (0.2-0.26) and decreasing O:C (0.33-0.39) (Figure 6.4),  $m_r$ s increase from 1.34 to 1.55. However low  $\text{NO}_x$  ( $\text{HC}/\text{NO}_x = 33$ ) experiments show different direction of changing of O:C than the intermediate and high  $\text{HC}/\text{NO}_x$  ratio experiments (discussed below). In contrast to  $\alpha$ -pinene, limonene is expected to produce products with a higher range of volatility due to its two double bonds [Ng *et al.*, 2010], and as a result limonene has wider range of  $f_{43}$  (0.2-0.26),  $f_{44}$  (0.065-0.093), H:C (1.4-1.48) and O:C (0.34-0.38), as well as  $m_r$ s (1.34-1.55). This comparison adds further credence to the notion that shifting chemical composition due to condensation of species with different volatility is responsible for the shifting refractive indices.

One might possibly think that it is perhaps because high mass loading produced from limonene experiments than the experiments of  $\alpha$ -pinene (60 vs 350  $\mu\text{g}/\text{m}^3$  at Figure 6.3b and c); with increasing SOA mass concentration, even the less oxidized and more volatility species will partition into the aerosol phase, resulting in a lower  $f_{44}$ . But most significant changes of chemical composition with mass loading were observed 0-20  $\mu\text{g}/\text{m}^3$  and level off at  $> 100 \mu\text{g}/\text{m}^3$  [Ng *et*

*al.*, 2010 and references therein], indicating within the observed range here (60 vs 350  $\mu\text{g}/\text{m}^3$ ), mass concentration may not affect to the chemical composition. .

From Jan 18, intermediate HC/NO<sub>x</sub> experiment (HC/NO<sub>x</sub> = 14), slight decreasing trend of  $m_r$  is observed from particles larger than 330 nm. This trend was being keep observed for limonene SOA larger than ~320 nm [Kim *et al.*, 2012]. Detail examinations of fraction of each component give more insights for changing  $m_r$ s (Figure 6.6). Figure 6.6 are grouped by components correlated with decreasing trend  $m_r$ s (Figure 6.6a) and non-correlated (Figure 6.6b) at the portion  $m_r$ s are decreasing. Figures 6.7 and 6.8 show the results from all other experimental conditions (Jan 17, Jan 18). Generally, non-oxygenated components (C<sub>2</sub>H<sub>3</sub>, C<sub>3</sub>H<sub>5</sub>, C<sub>3</sub>H<sub>7</sub>, C<sub>4</sub>H<sub>7</sub>, C<sub>4</sub>H<sub>9</sub>) are correlated with  $m_r$ s; fraction of C<sub>4</sub>H<sub>7</sub> and C<sub>3</sub>H<sub>5</sub> shows perfect linear relationship with  $m_r$ s and C<sub>4</sub>H<sub>9</sub>, C<sub>3</sub>H<sub>7</sub> and C<sub>2</sub>H<sub>3</sub> shows linear relationship initially but later stay at the same  $m_r$ s. However, oxygenated components are not; those fractions are keep increasing although  $m_r$ s start to decrease. Those different changes seem to result different chemical composition relating with decreasing  $m_r$ s. As shown at Figure 6.9b (Jan 18, limonene/NO<sub>x</sub> =14), at that time when  $m_r$  start to decrease, O:C ratio start to be increase. Since H:C ratio is keep increasing, there seems still continued partitioning of semivolatile species but more oxidized species than before from the result of higher O:C ratio. Also one thing different of Jan 18 data with others (Jan 17 & Jan 19) is the correlation of C<sub>2</sub>H<sub>3</sub> with  $m_r$ s. Only Jan 18 shows the increasing trend as  $m_r$ s are increasing. These all together seem to affect to decreasing trend of  $m_r$ s.

#### **6.2.3.4 HC/NO<sub>x</sub> effect on photochemically generated limonene SOA**

Three limonene photooxidation experiments were performed at low, intermediate and high HC/NO<sub>x</sub> ratios, respectively. As shown in Figure 6.3c, the ranges of  $f_{44}$  for different

HC/NO<sub>x</sub> are similar, decreasing from 0.09 to 0.06 with organic loading. For this metric, there are no significant differences between the experiments, a pattern also observed for the refractive indices (Figure 6.1). Chemical characterizations of SOA typically find significant concentrations of peroxides from RO<sub>2</sub> + HO<sub>2</sub> under low NO<sub>x</sub> conditions. At high HC/NO<sub>x</sub> ratios, organic nitrates and other non-peroxide products from RO<sub>2</sub> + NO<sub>2</sub> and RO<sub>2</sub> + RO<sub>2</sub> reactions dominate [Presto *et al.*, 2005; Kroll and Seinfeld, 2008]. It is possible that AMS is not enough to detect particular dominant reaction pathways between different HC/NO<sub>x</sub>; RO<sub>2</sub> + NO vs. RO<sub>2</sub> + HO<sub>2</sub> and RO<sub>2</sub> + RO<sub>2</sub>. Difficulty in measurements of different chemical composition between high and low NO<sub>x</sub> with AMS has been discussed in many previous studies [Chhabra *et al.*, 2010; Farmer *et al.*, 2010; Rollins *et al.*, 2010]; AMS cannot detect oxygen that is lost in fragmented organic nitrate and peroxide functionality from nitrogen bonded oxygen in the ONO<sub>2</sub> group and OH fragmentation from ROOH, respectively. Our previous study describing chamber experiments performed with higher insolation and temperatures showed that those different reaction contributions seem to control the size of particles and related m<sub>r,s</sub> [Kim *et al.*, 2012]. However, as discussed in above, these winter experiments do not show strong dependency of size on HC/NO<sub>x</sub>. It is likely that these different contribution of reaction pathways does not affect to substantial differences in ranges of f<sub>44</sub> as well as f<sub>43</sub> and elemental compositions of H:C and O:C (Figure 6.4) as the underlying species of SOA remains unchanged and eventually the m<sub>r,s</sub> exist within similar ranges for different HC/NO<sub>x</sub> ratio.

Although the range of all parameters (f<sub>43</sub>, f<sub>44</sub> H:C and O:C) are similar for similar range of m<sub>r,s</sub> for all three HC/NO<sub>x</sub> ratios, between O:C and m<sub>r</sub> trends in the opposite direction for from the lower HC/NO<sub>x</sub> ratios; m<sub>r,s</sub> increase with O:C increase at low HC/NO<sub>x</sub> ratio whereas others are opposite. Since low NO<sub>x</sub> conditions result particle nucleation faster and also limonene allows



multiple oxidation pathways, condensing more oxidized semivolatile species or heterogeneous reactions can increase O:C ratio. *Cappa et al.*, [2011] showed in a previous study that heterogeneous OH oxidation of the squalene and azelaic acid increase refractive index with addition of oxygen (increasing O:C). However, our other cases ( $\text{HC/NO}_x = 6.6, 14$ ) showing opposite relationship suggest that O:C ratio is not the only factor controlling the refractive index.

Overall Figure 6.5 shows that the best correlation is between  $m_r$  and H:C ratio. There is a clear relationship between  $m_r$  and the H:C ratio; as increasing H:C ratio,  $m_r$  increase till H:C ratio is about 1.47. Increasing H:C ratio has been explained by increased partitioning of less oxidized semivolatile compounds as the mass of partitioning medium grows in previous studies [*Shilling et al.*, 2009; *Chan et al.*, 2010; *Chhabra et al.*, 2010]. This indicates that the addition of semivolatile species leads to the growth particles and increase in the real refractive indices. After H:C ratio reached to the 1.47,  $m_r$  starts to decrease which indicate that there are some other factors in particle influencing to the  $m_r$ s. Therefore, all combining chemical factors rather than one factor seems influence to the value of  $m_r$ s.

### **6.3 Summary and Atmospheric implications**

The refractive index and chemical composition of different types of SOA generated under different oxidation chemistries and precursors are investigated in an effort to connect optical properties to the chemical compositions. The refractive indices vary fairly widely from 1.34-1.55. The strongest correlation between HR-ToF-AMS measurements and the refractive index are with the H:C ratio, indicating that condensation of semivolatile species increases the refractive index. However, there are some cases H:C cannot explain the variations of  $m_r$ s, suggesting that there are additional factors to controlling the  $m_r$ s, such as O:C ratio.

Ng *et al.*, [2010] showed that ambient aerosols in the Northern hemisphere fall into a triangle plot with a range of  $f_{44}$  (0.01- 0.3) and  $f_{43}$  (0.02 - 0.17). Although more studies linking between optical properties and chemical composition with atmospherically relevant aerosol need to be done, the variations of refractive index (1.34 - 1.55) with narrower ranges of  $f_{44}$  (0.13-0.26) and  $f_{43}$  (0.13-0.26) suggest that there would be more variations of  $m_s$  of ambient aerosols, and single value for SOA refractive index will not be sufficient to accurately model radiative transfer.

## 6.4 References

- Aiken, A. C., P. F. Decarlo, J. H. Kroll, D. R. Worsnop, J. A. Huffman, K. S. Docherty, I. M. Ulbrich, C. Mohr, J. R. Kimmel, D. Sueper, Y. Sun, Q. Zhang, A. Trimborn, M. Northway, P. J. Ziemann, M. R. Canagaratna, T. B. Onasch, M. R. Alfarra, A. S. H. Prevot, J. Dommen, J. Duplissy, A. Metzger, U. Baltensperger, and J. L. Jimenez (2008), O/C and OM/OC ratios of primary, secondary, and ambient organic aerosols with high-resolution time-of-flight aerosol mass spectrometry, *Environmental Science & Technology*, 42(12), 4478-4485.
- Bahreini, R., M. D. Keywood, N. L. Ng, V. Varutbangkul, S. Gao, R. C. Flagan, J. H. Seinfeld, D. R. Worsnop, and J. L. Jimenez (2005), Measurements of secondary organic aerosol from oxidation of cycloalkenes, terpenes, and m-xylene using an Aerodyne aerosol mass spectrometer, *Environmental Science & Technology*, 39(15), 5674-5688.
- Barkey, B., S. E. Paulson, and A. Chung (2007), Genetic algorithm inversion of dual polarization polar nephelometer data to determine aerosol refractive index, *Aerosol Science and Technology*, 41(8), 751-760.
- Cappa, C. D., D. L. Che, S. H. Kessler, J. H. Kroll, and K. R. Wilson (2011), Variations in organic aerosol optical and hygroscopic properties upon heterogeneous OH oxidation, *Journal of Geophysical Research*, 116, 12.
- Chan, A. W. H., M. N. Chan, J. D. Surratt, P. S. Chhabra, C. L. Loza, J. D. Crouse, L. D. Yee, R. C. Flagan, P. O. Wennberg, and J. H. Seinfeld (2010), Role of aldehyde chemistry and NO<sub>x</sub> concentrations in secondary organic aerosol formation, *Atmospheric Chemistry and Physics*, 10(15), 7169-7188.
- Chhabra, P. S., R. C. Flagan, and J. H. Seinfeld (2010), Elemental analysis of chamber organic aerosol using an aerodyne high-resolution aerosol mass spectrometer, *Atmospheric Chemistry and Physics*, 10(9), 4111-4131.
- Chhabra, P. S., N. L. Ng, M. R. Canagaratna, A. L. Corrigan, L. M. Russell, D. R. Worsnop, R. C. Flagan, and J. H. Seinfeld (2011), Elemental composition and oxidation of chamber organic aerosol, *Atmospheric Chemistry and Physics*, 11(17), 8827-8845.

- Chung, A., A. A. Lall, and S. E. Paulson (2008), Particulate emissions by a small non-road diesel engine: Biodiesel and diesel characterization and mass measurements using the extended idealized aggregates theory, *Atmospheric Environment*, 42(9), 2129-2140.
- DeCarlo, P. F., J. R. Kimmel, A. Trimborn, M. J. Northway, J. T. Jayne, A. C. Aiken, M. Gonin, K. Fuhrer, T. Horvath, K. S. Docherty, D. R. Worsnop, and J. L. Jimenez (2006), Field-deployable, high-resolution, time-of-flight aerosol mass spectrometer, *Analytical Chemistry*, 78(24), 8281-8289.
- Duplissy, J., M. Gysel, M. R. Alfarra, J. Dommen, A. Metzger, A. S. H. Prevot, E. Weingartner, A. Laaksonen, T. Raatikainen, N. Good, S. F. Turner, G. McFiggans, and U. Baltensperger (2008), Cloud forming potential of secondary organic aerosol under near atmospheric conditions, *Geophysical Research Letters*, 35(3).
- Farmer, D. K., A. Matsunaga, K. S. Docherty, J. D. Surratt, J. H. Seinfeld, P. J. Ziemann, and J. L. Jimenez (2010), Response of an aerosol mass spectrometer to organonitrates and organosulfates and implications for atmospheric chemistry, *Proceedings of the National Academy of Sciences of the United States of America*, 107(15), 6670-6675.
- Finlayson-Pitts, B. J., and J. N. Pitts (1999), Chemistry of the Upper and Lower Atmosphere; Theory, Experiments, and Applications, *Academic Press, San Diego*, 1040.
- Hallquist, M., J. C. Wenger, U. Baltensperger, Y. Rudich, D. Simpson, M. Claeys, J. Dommen, N. M. Donahue, C. George, A. H. Goldstein, J. F. Hamilton, H. Herrmann, T. Hoffmann, Y. Iinuma, M. Jang, M. E. Jenkin, J. L. Jimenez, A. Kiendler-Scharr, W. Maenhaut, G. McFiggans, T. F. Mentel, A. Monod, A. S. H. Prevot, J. H. Seinfeld, J. D. Surratt, R. Szmigielski, and J. Wildt (2009), The formation, properties and impact of secondary organic aerosol: current and emerging issues, *Atmospheric Chemistry and Physics*, 9(14), 5155-5236.
- Heaton, K. J., R. L. Slighter, P. G. Hatcher, W. A. Hall, and M. V. Johnston (2009), Composition Domains in Monoterpene Secondary Organic Aerosol, *Environmental Science & Technology*, 43(20), 7797-7802.
- Kanakidou, M., J. H. Seinfeld, S. N. Pandis, I. Barnes, F. J. Dentener, M. C. Facchini, R. Van Dingenen, B. Ervens, A. Nenes, C. J. Nielsen, E. Swietlicki, J. P. Putaud, Y. Balkanski, S. Fuzzi, J. Horth, G. K. Moortgat, R. Winterhalter, C. E. L. Myhre, K. Tsigaridis, E. Vignati, E. G. Stephanou, and J. Wilson (2005), Organic aerosol and global climate modelling: a review, *Atmospheric Chemistry and Physics*, 5, 1053-1123.
- Kim, H., B. Barkey, and S. E. Paulson (2010), Real refractive indices of alpha- and beta-pinene and toluene secondary organic aerosols generated from ozonolysis and photo-oxidation, *Journal of Geophysical Research-Atmospheres*, 115, 10.
- Kim, H., B. Barkey, and S. E. Paulson (2012), Real refractive indices and formation yields of secondary organic aerosol generated from photooxidation of limonene and  $\alpha$ -pinene: the effect of the HC/NO<sub>x</sub> Ratio, *The Journal of Physical Chemistry A*, *accepted*.
- Kinne, S., U. Lohmann, J. Feichter, M. Schulz, C. Timmreck, S. Ghan, R. Easter, M. Chin, P. Ginoux, T. Takemura, I. Tegen, D. Koch, M. Herzog, J. Penner, G. Pitari, B. Holben, T. Eck, A. Smirnov, O. Dubovik, I. Slutsker, D. Tanre, O. Torres, M. Mishchenko, I. Geogdzhayev, D. A. Chu, and Y. Kaufman (2003), Monthly averages of aerosol properties: a global comparison among models, satellite data, and AERONET ground data, *Journal of Geophysical Research*, 108(D20).
- Kostenidou, E., R. K. Pathak, and S. N. Pandis (2007), An algorithm for the calculation of secondary organic aerosol density combining AMS and SMPS data, *Aerosol Science and Technology*, 41(11), 1002-1010.

- Kroll, J. H., and J. H. Seinfeld (2008), Chemistry of secondary organic aerosol: Formation and evolution of low-volatility organics in the atmosphere, *Atmospheric Environment*, 42(16), 3593-3624.
- Leungsakul, S., H. E. Jeffries, and R. M. Kamens (2005), A kinetic mechanism for predicting secondary aerosol formation from the reactions of d-limonene in the presence of oxides of nitrogen and natural sunlight, *Atmospheric Environment*, 39(37), 7063-7082.
- Lienert, B. R., J. N. Porter, and S. K. Sharma (2003), Aerosol size distributions from genetic inversion of polar nephelometer data, *Journal of Atmospheric and Oceanic Technology*, 20(10), 1403-1410.
- Mikhailov, E., S. Vlasenko, S. T. Martin, T. Koop, and U. Poschl (2009), Amorphous and crystalline aerosol particles interacting with water vapor: conceptual framework and experimental evidence for restructuring, phase transitions and kinetic limitations, *Atmospheric Chemistry and Physics*, 9(24), 9491-9522.
- Mishchenko, M. I., B. Cairns, G. Kopp, C.F. Schueler, B.A. Fafaul, J.E. Hansen, R.J. Hooker, T. Itchkawich, H.B. Maring, and L.D. Travis (2007), Accurate Monitoring of Terrestrial Aerosols and Total Solar Irradiance: Introducing the Glory Mission, *Bull. Amer. Meteor. Soc.*, 88, 677-691.
- Ng, N. L., M. R. Canagaratna, Q. Zhang, J. L. Jimenez, J. Tian, I. M. Ulbrich, J. H. Kroll, K. S. Docherty, P. S. Chhabra, R. Bahreini, S. M. Murphy, J. H. Seinfeld, L. Hildebrandt, N. M. Donahue, P. F. DeCarlo, V. A. Lanz, A. S. H. Prevot, E. Dinar, Y. Rudich, and D. R. Worsnop (2010), Organic aerosol components observed in Northern Hemispheric datasets from Aerosol Mass Spectrometry, *Atmospheric Chemistry and Physics*, 10(10), 4625-4641.
- Paulson, S. E., M. Chung, A. D. Sen, and G. Orzechowska (1998), Measurement of OH radical formation from the reaction of ozone with several biogenic alkenes, *Journal of Geophysical Research-Atmospheres*, 103(D19), 25533-25539.
- Presto, A. A., K. E. H. Hartz, and N. M. Donahue (2005), Secondary organic aerosol production from terpene ozonolysis. 2. Effect of NO<sub>x</sub> concentration, *Environmental Science & Technology*, 39(18), 7046-7054.
- Rollins, A. W., J. D. Smith, K. R. Wilson, and R. C. Cohen (2010), Real Time In Situ Detection of Organic Nitrates in Atmospheric Aerosols, *Environmental Science & Technology*, 44(14), 5540-5545.
- Rudich, Y., N. M. Donahue, and T. F. Mentel (2007), Aging of organic aerosol: bridging the gap between laboratory and field studies, *Annu. Rev. Phys. Chem.*, 58.
- Salo, K., M. Hallquist, A. M. Jonsson, H. Saathoff, K. H. Naumann, C. Spindler, R. Tillmann, H. Fuchs, B. Bohn, F. Rubach, T. F. Mentel, L. Muller, M. Reinnig, T. Hoffmann, and N. M. Donahue (2012), Volatility of secondary organic aerosol during OH radical induced ageing, *Atmospheric Chemistry and Physics*, 11(21), 11055-11067.
- Shilling, J. E., Q. Chen, S. M. King, T. Rosenoern, J. H. Kroll, D. R. Worsnop, P. F. DeCarlo, A. C. Aiken, D. Sueper, J. L. Jimenez, and S. T. Martin (2009), Loading-dependent elemental composition of alpha-pinene SOA particles, *Atmospheric Chemistry and Physics*, 9(3), 771-782.
- Warren, B., R. L. Austin, and D. R. Cocker (2009), Temperature dependence of secondary organic aerosol, *Atmospheric Environment*, 43(22-23), 3548-3555.
- Yu, Y., M. J. Ezell, A. Zelenyuk, D. Imre, L. Alexander, J. Ortega, B. D'Anna, C. W. Harmon, S. N. Johnson, and B. J. Finlayson-Pitts (2008), Photooxidation of alpha-pinene at high relative

humidity in the presence of increasing concentrations of NO(x), *Atmospheric Environment*, 42(20), 5044-5060.

Zhang, Q., J. L. Jimenez, M. R. Canagaratna, J. D. Allan, H. Coe, I. Ulbrich, M. R. Alfarra, A. Takami, A. M. Middlebrook, Y. L. Sun, K. Dzepina, E. Dunlea, K. Docherty, P. F. DeCarlo, D. Salcedo, T. Onasch, J. T. Jayne, T. Miyoshi, A. Shimono, S. Hatakeyama, N. Takegawa, Y. Kondo, J. Schneider, F. Drewnick, S. Borrmann, S. Weimer, K. Demerjian, P. Williams, K. Bower, R. Bahreini, L. Cottrell, R. J. Griffin, J. Rautiainen, J. Y. Sun, Y. M. Zhang, and D. R. Worsnop (2007), Ubiquity and dominance of oxygenated species in organic aerosols in anthropogenically-influenced Northern Hemisphere midlatitudes, *Geophysical Research Letters*, 34(13), 6.

**Table 6.1: Initial conditions, temperatures, relative humidities and results of the experiments**

Expt.	Initial Conditions					Results						
	HC	HC (ppb)	NO <sub>x</sub> (ppb)	HC/NO <sub>x</sub> (ppbC/ppb)	Ozone (ppb)	Temp (°C) <sup>a</sup>	RH (%) <sup>a</sup>	ΔHC (ppb)	# density <sup>b</sup> (#/cm <sup>3</sup> )	Size mode <sup>b</sup> (nm)	Mass <sup>c</sup> (μg/m <sup>3</sup> )	Yield <sup>d</sup> (%)
<b>17-Jan-12</b>	Limonene	170	52	33	N/A	24-16	13-18	170	8680	311	121-324	38
<b>18-Jan-12</b>	Limonene	200	145	14	N/A	24-20	26-34	200	4820	385	54-315	29
<b>19-Jan-12</b>	Limonene	190	290	6.6	N/A	27-18	24-39	174	3120	359	38-98	10
<b>29-Jan-12</b>	α-pinene	138	44	31	N/A	33-37-34	6	138	3480	250	20-49	7
<b>27-Jan-12</b>	α-pinene	134	N/A	N/A	500	23-29	29-22	134	4170	322	14-168	31
<b>30-Jan-12</b>	α-pinene <sup>e</sup>	149	N/A	N/A	500	19-22	17-14	145	13300	242	53-255	28

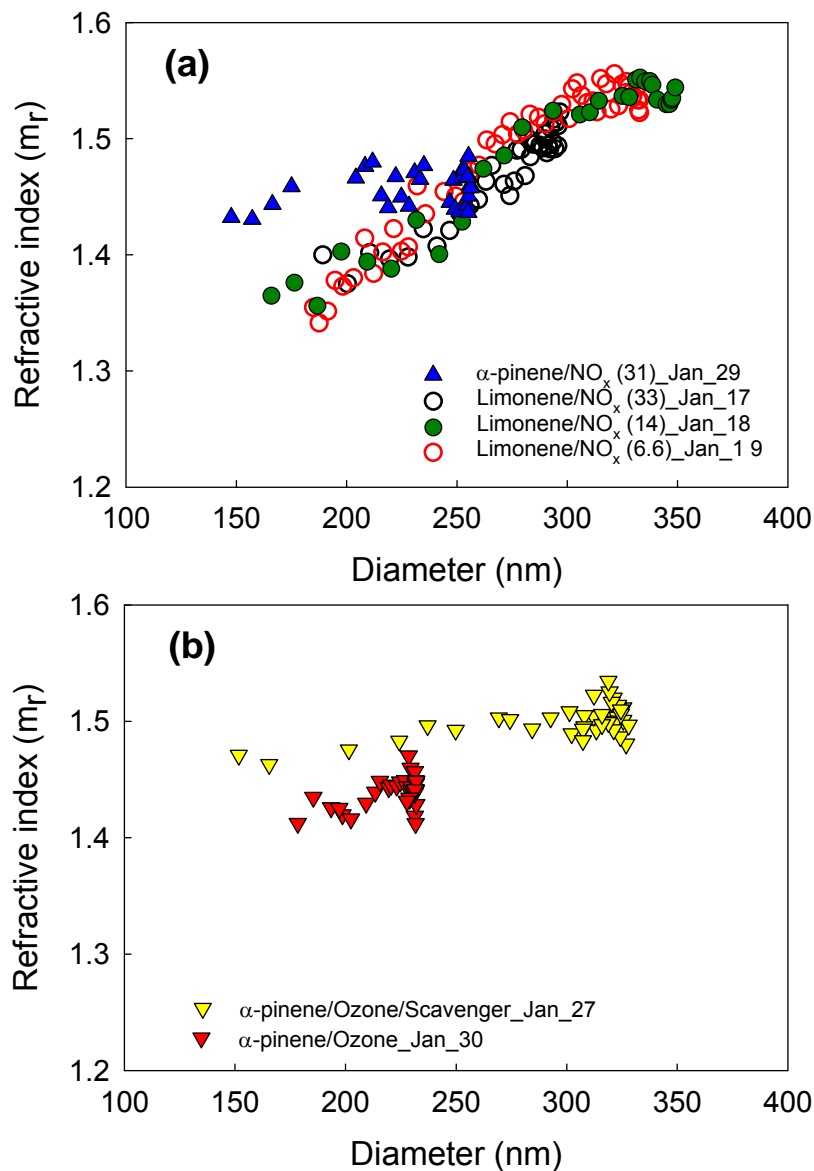
<sup>a</sup>Initial, peak and final temperature and relative humidity.

<sup>b</sup>Final aerosol number concentration and size mode (also maximum size mode). These values have not been adjusted for wall losses.

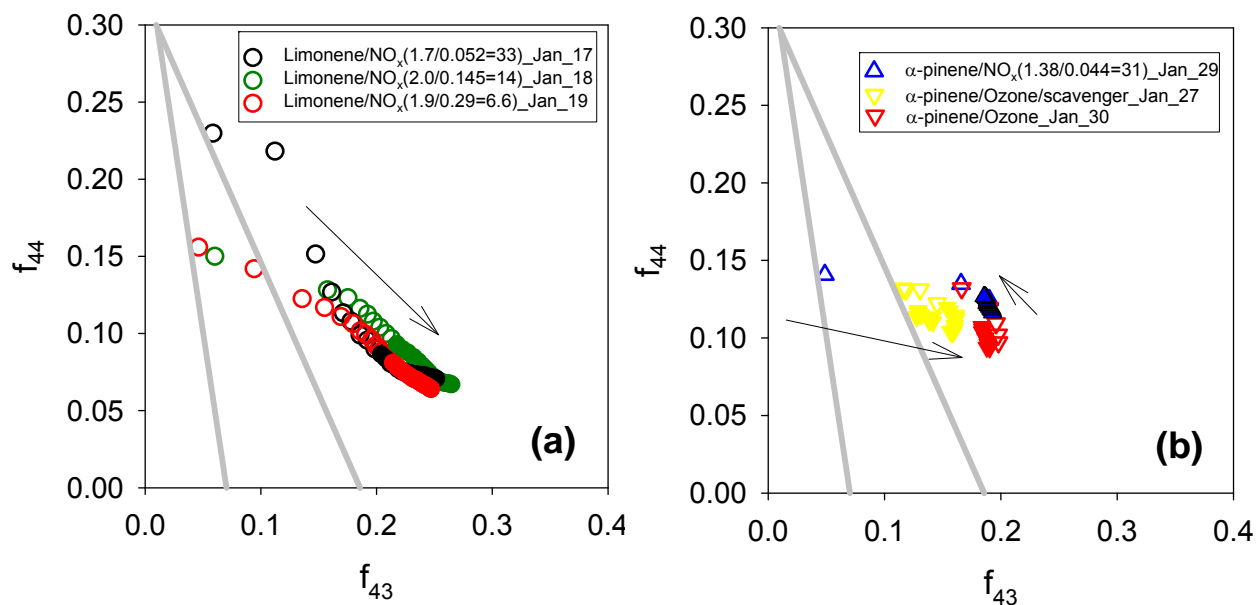
<sup>c</sup>Mass concentration in the chamber over the period for which meaningful PN measurements were made was determined from the SMPS measured size distribution. Particle density was assumed to be 1.2 and 1.25 g/cm<sup>3</sup> for α-pinene and limonene, respectively

<sup>d</sup>Calculated from peak measured aerosol mass corrected for wall losses and the corresponding quantity of reacted hydrocarbon. Because of the uncertainties in the measurement from GC (± 3 %) and measurement of SMPS (± 10 %) yields are uncertain to ± 10 %.

<sup>e</sup>Cyclohexane was added in 50 fold excess compared to the hydrocarbon to suppress OH formation.

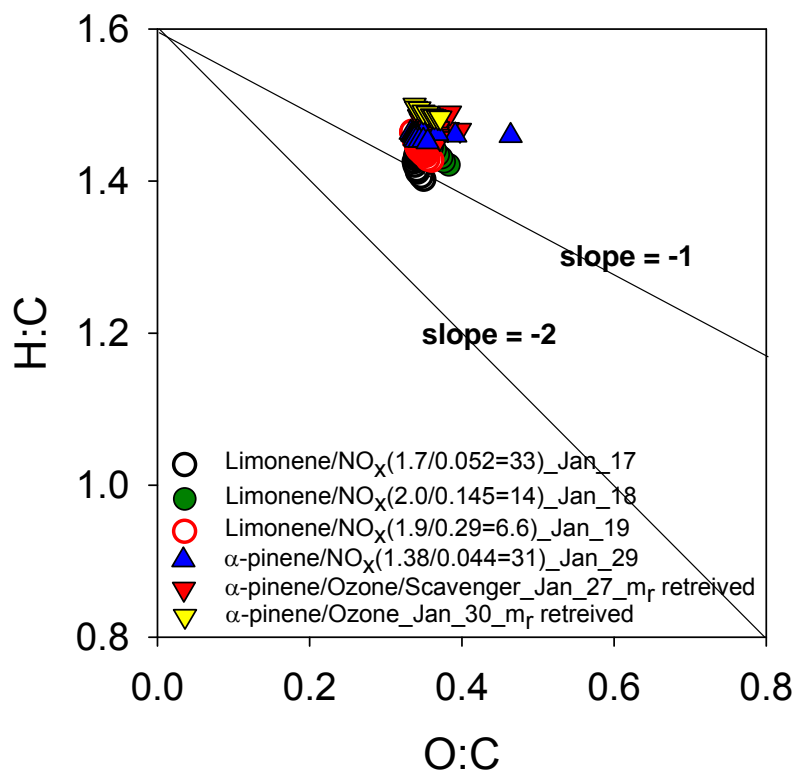


**Figure 6.1.** Retrieved refractive indices for SOA formed by (a) photooxidation of limonene and  $\alpha$ -pinene at different HC/ $\text{NO}_x$  ratios and (b) ozonolysis of  $\alpha$ -pinene with and without scavenger as a function of particle diameter

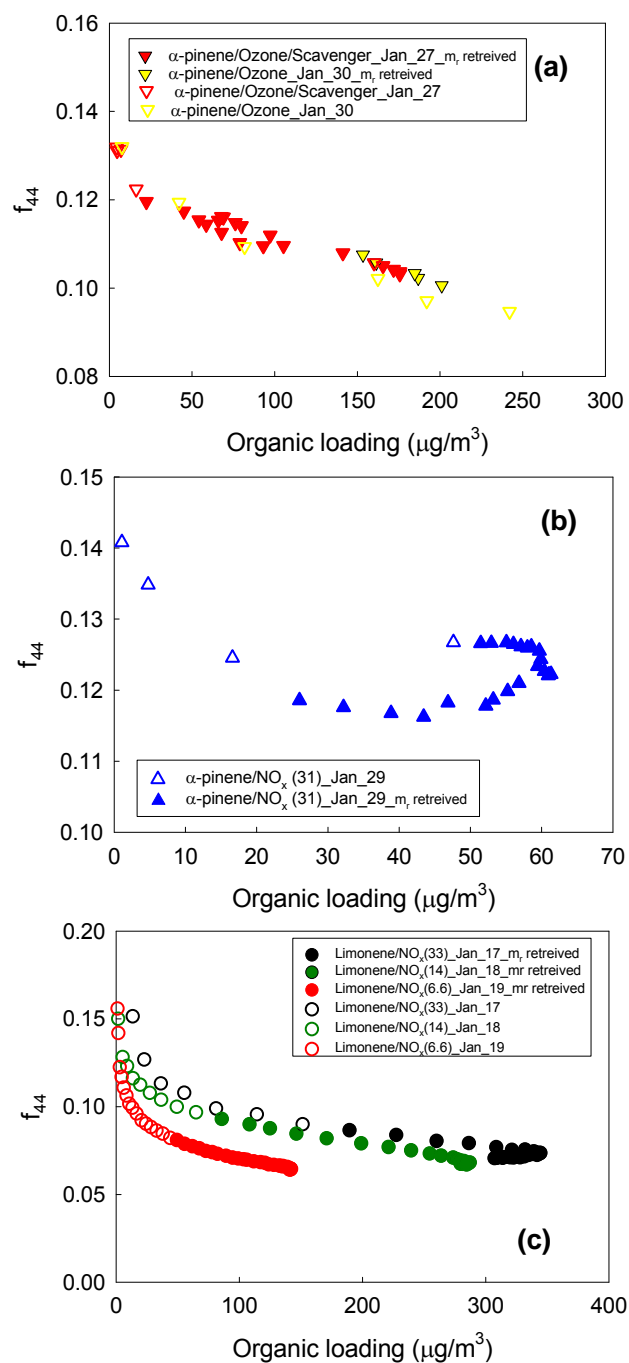


**Figure 6.2.** Triangle plot for photooxidation of (a) limonene at different HC/NO<sub>x</sub> ratios and (b) ozonolysis of  $\alpha$ -pinene with and without scavenger. Outline of triangle shown in gray line indicate the space where ambient OOA components fall [Ng *et al.*, 2010]. Arrows represent the time progression of experiments.

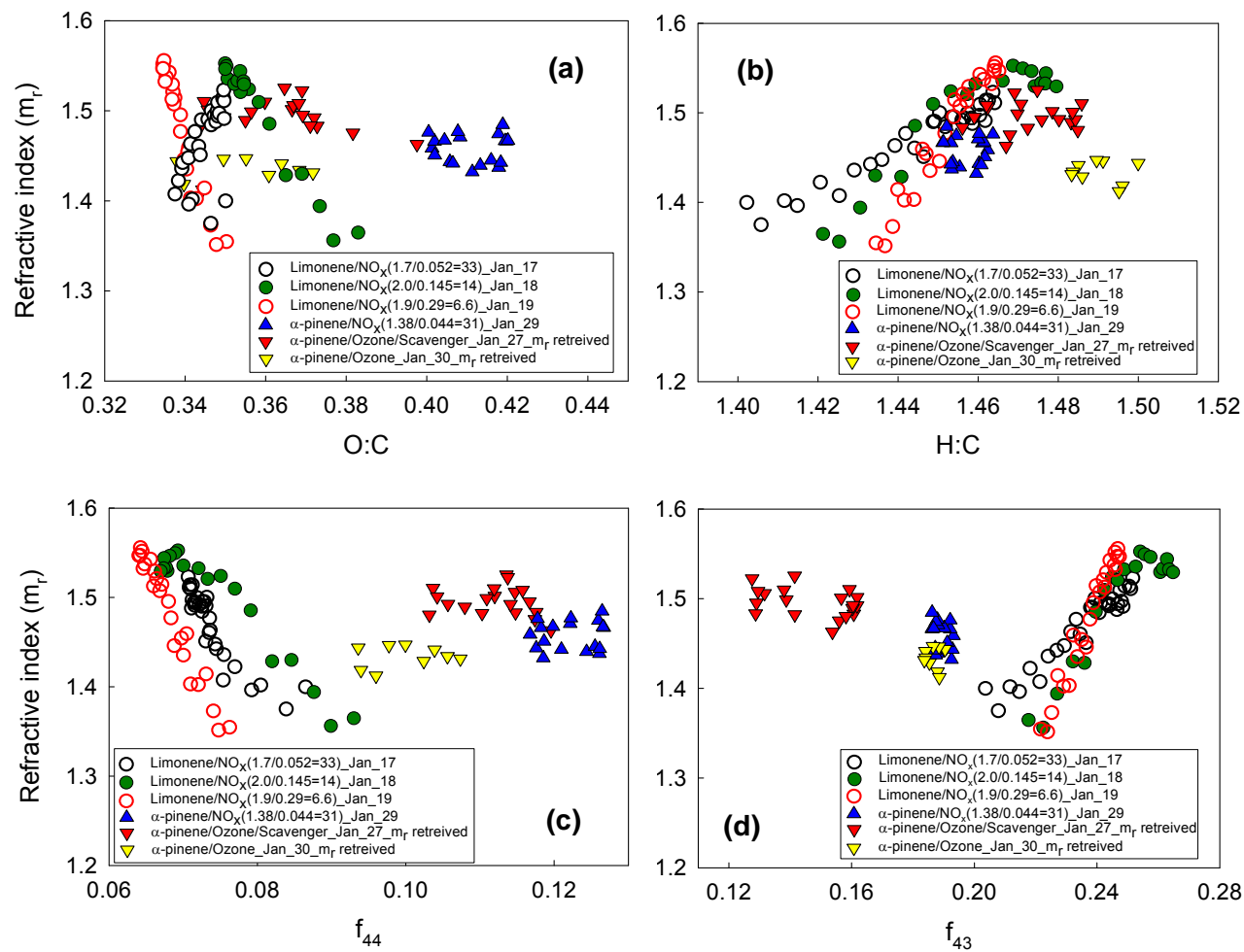




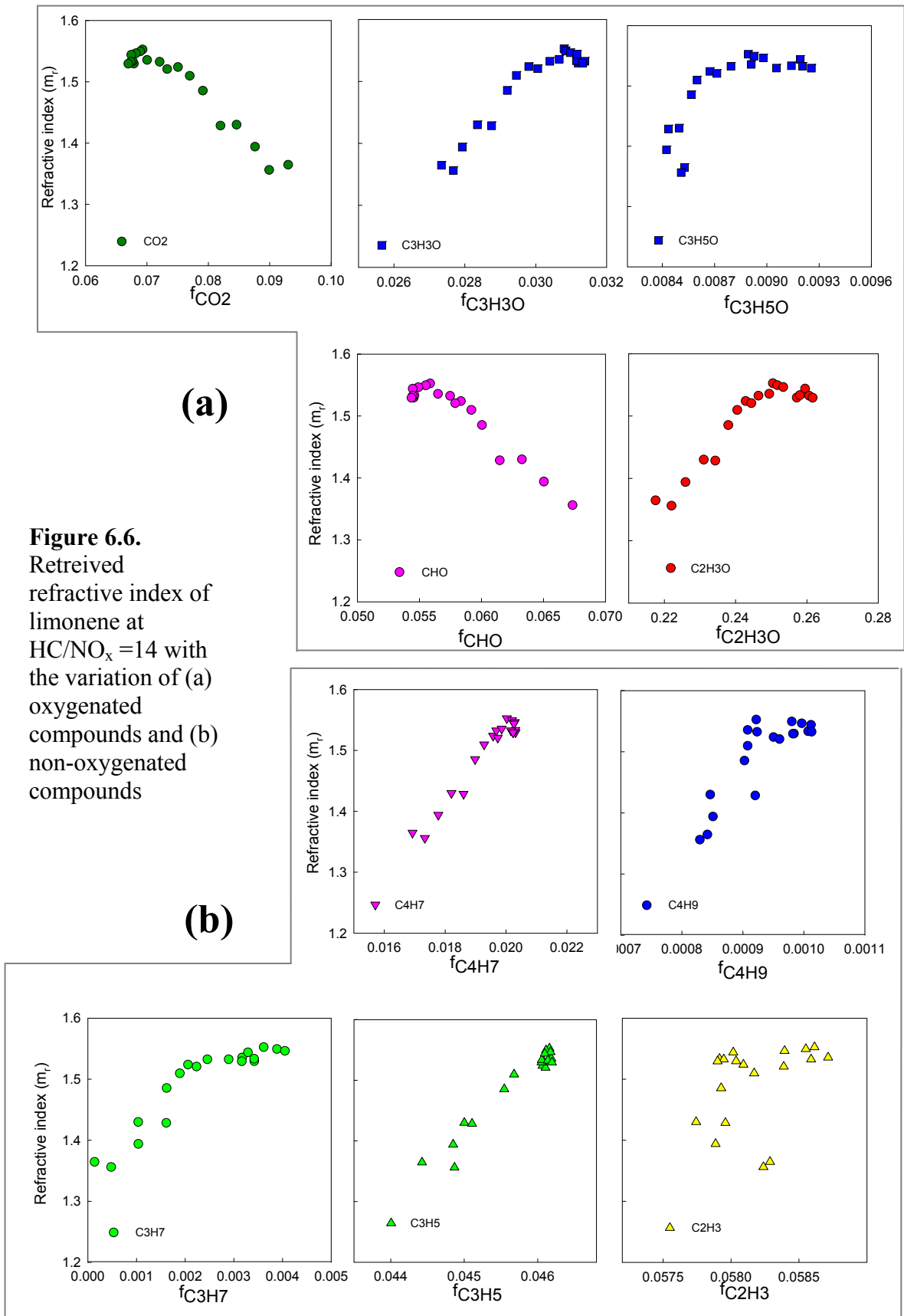
**Figure 6.3.** Van Krevelen diagram for limonene SOA at different HC/NO<sub>x</sub> ratios and ozonolysis of α-pinene SOA with and without scavenger. Line with slopes with -1 and -2 are represented by black line.

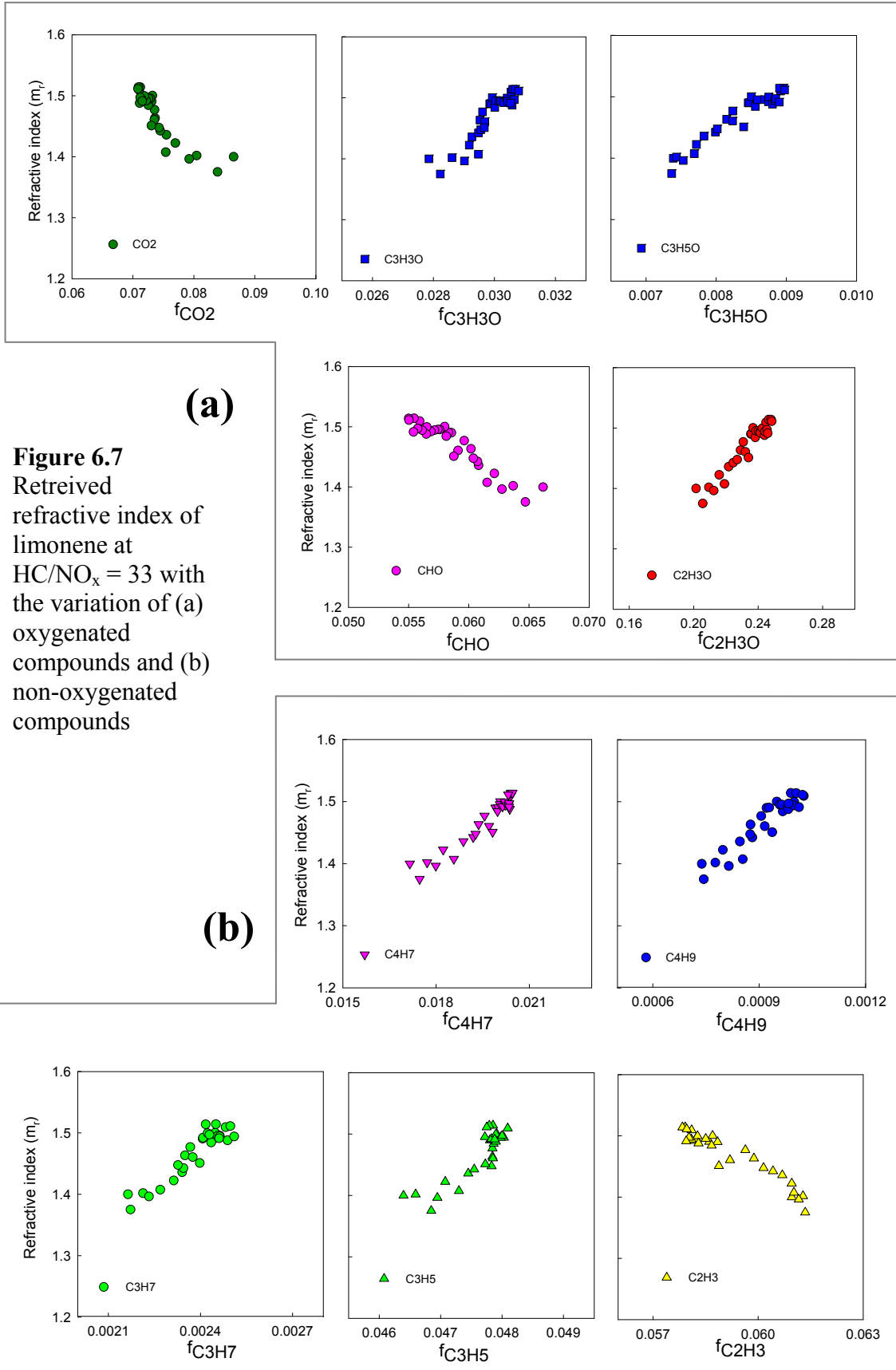


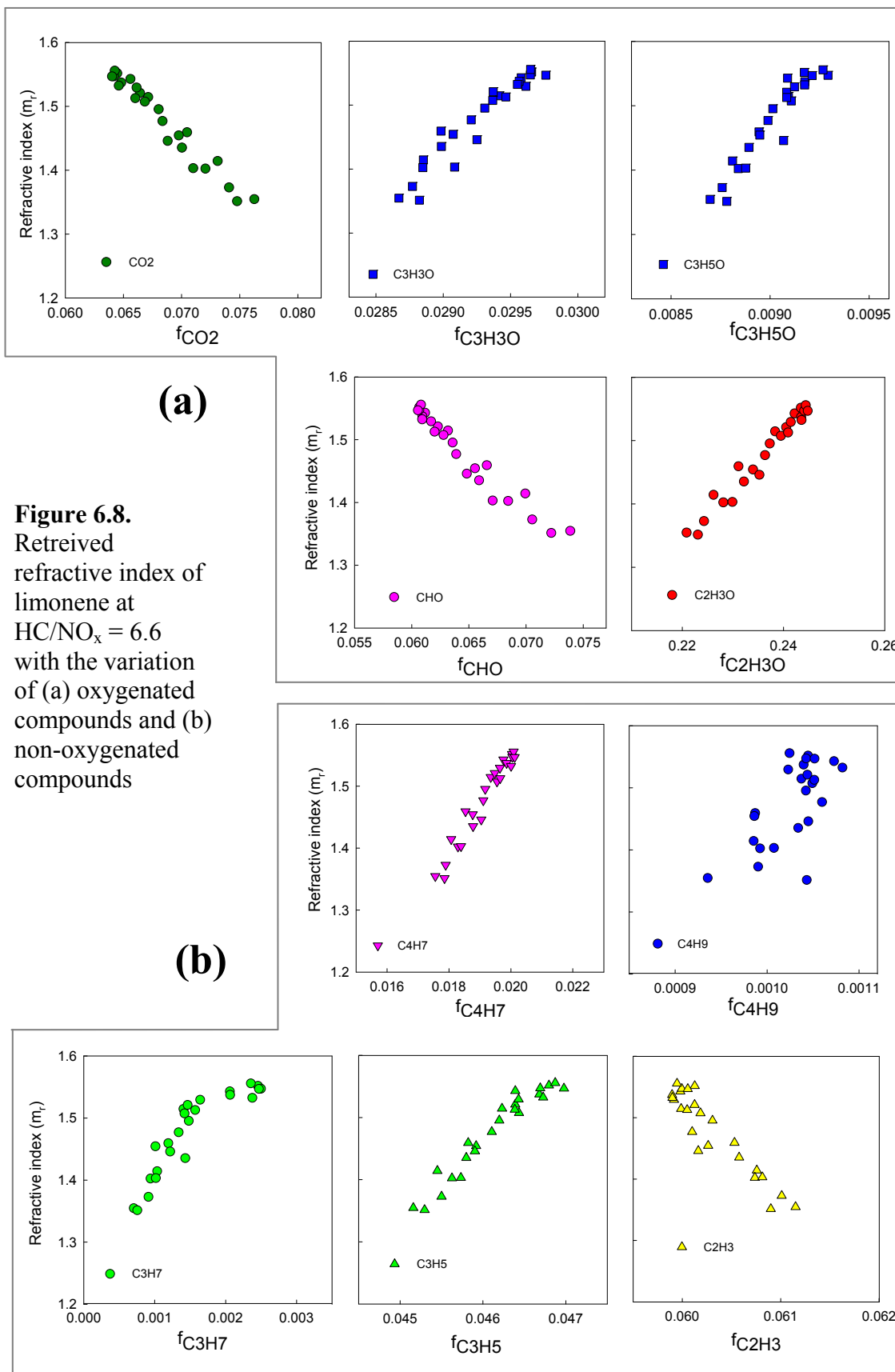
**Figure 6.4.** Change of  $f_{44}$  as a function of organic loading in the chamber over the course of (a) ozonolysis of  $\alpha$ -pinene with and without scavenger (b) photooxidation of  $\alpha$ -pinene (c) photooxidation of limonene at different HC/ $\text{NO}_x$  ratio.



**Figure 6.5.** Retrieved refractive index of ozonolysis of  $\alpha$ -pinene with and without scavenger and photooxidation of  $\alpha$ -pinene and limonene at different HC/ $\text{NO}_x$  ratio with the variation of (a) O:C (b) H:C (c)  $f_{44}$  (d)  $f_{43}$

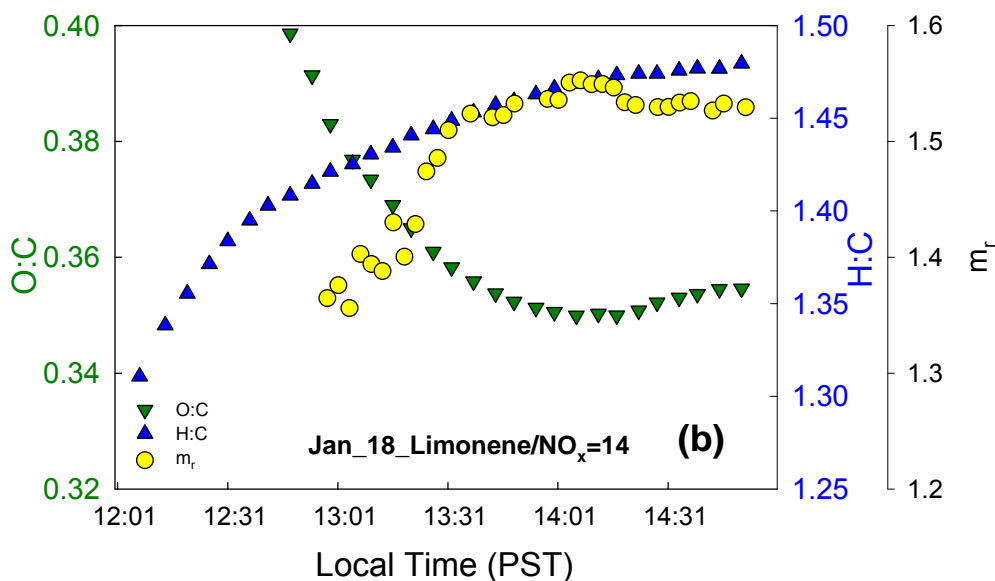
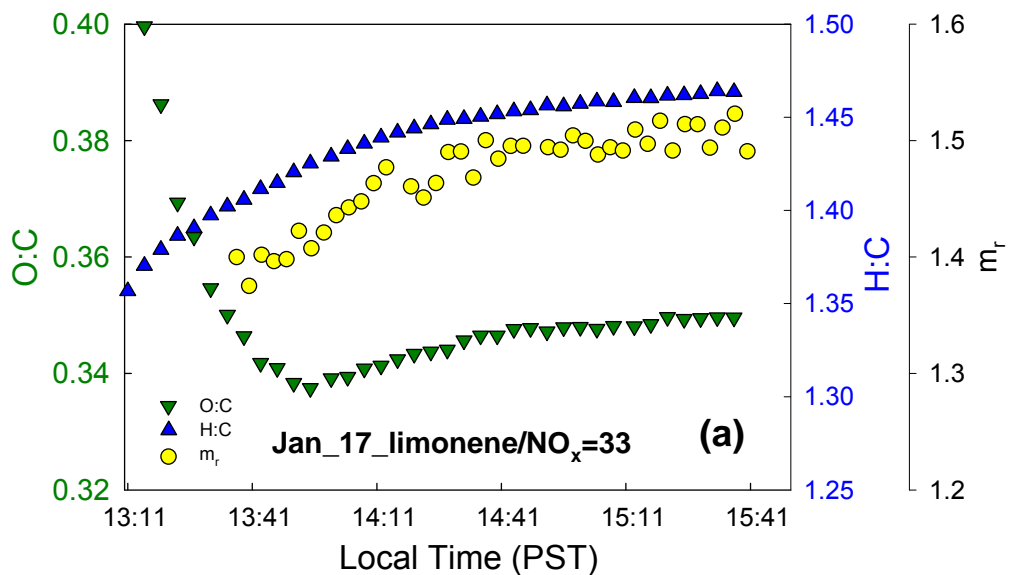


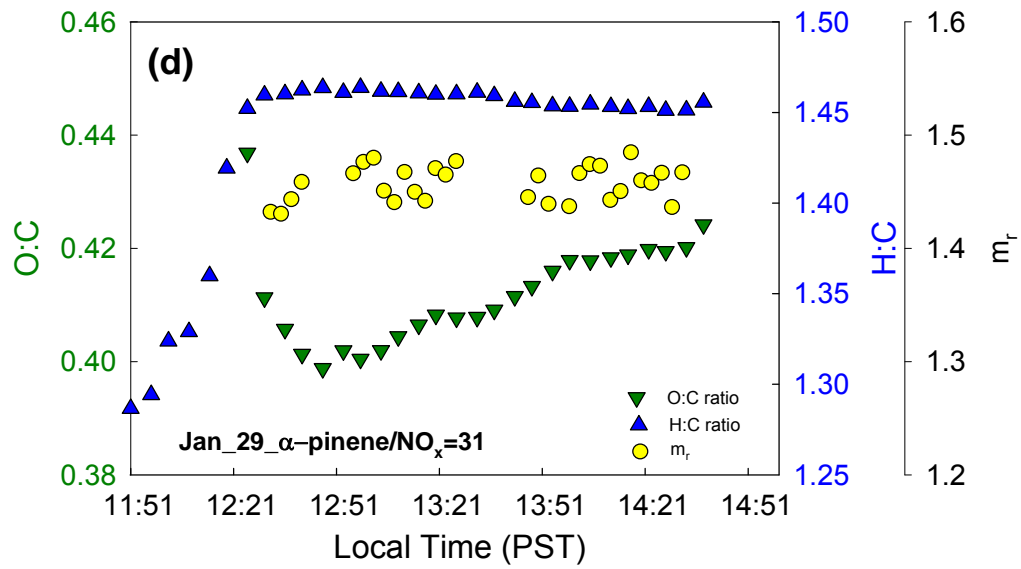
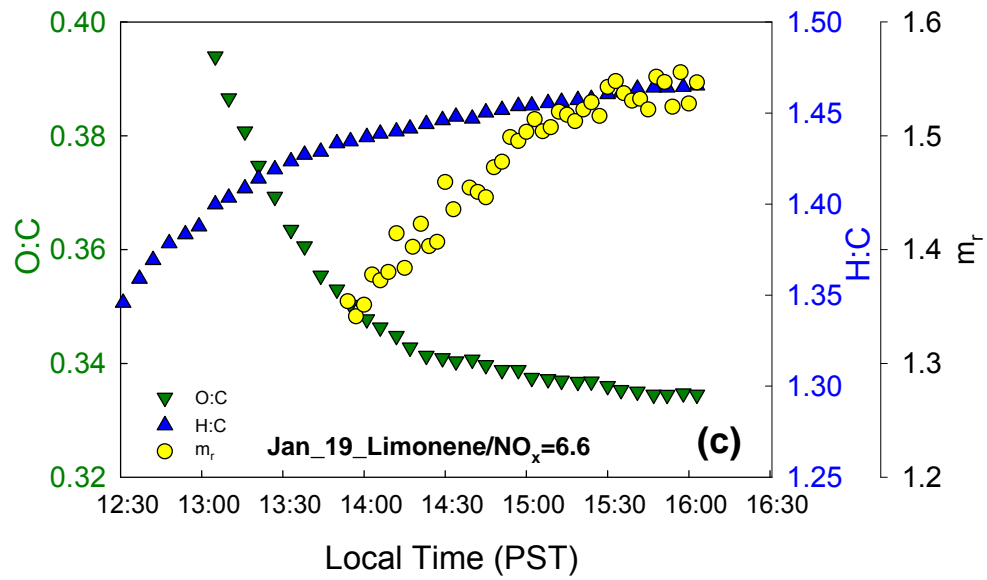




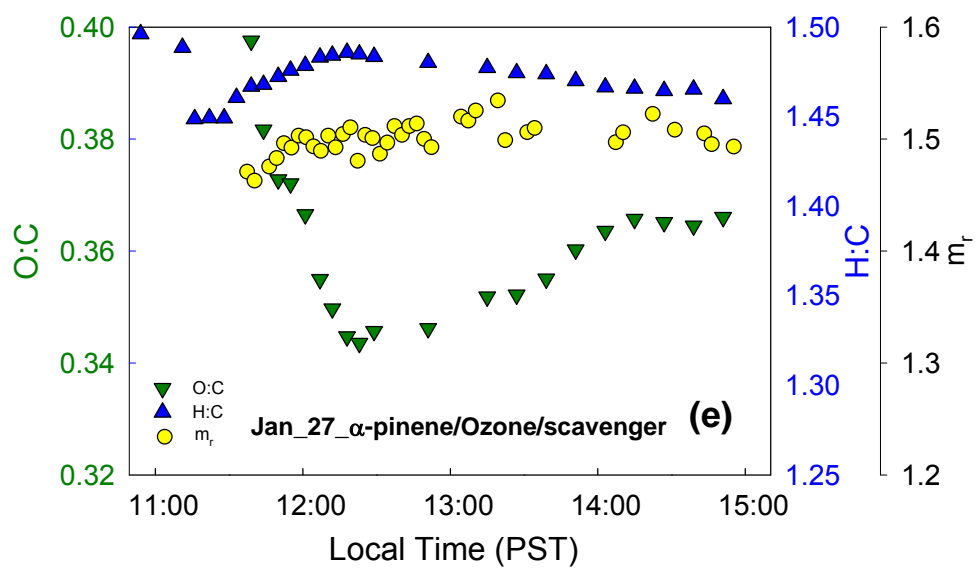
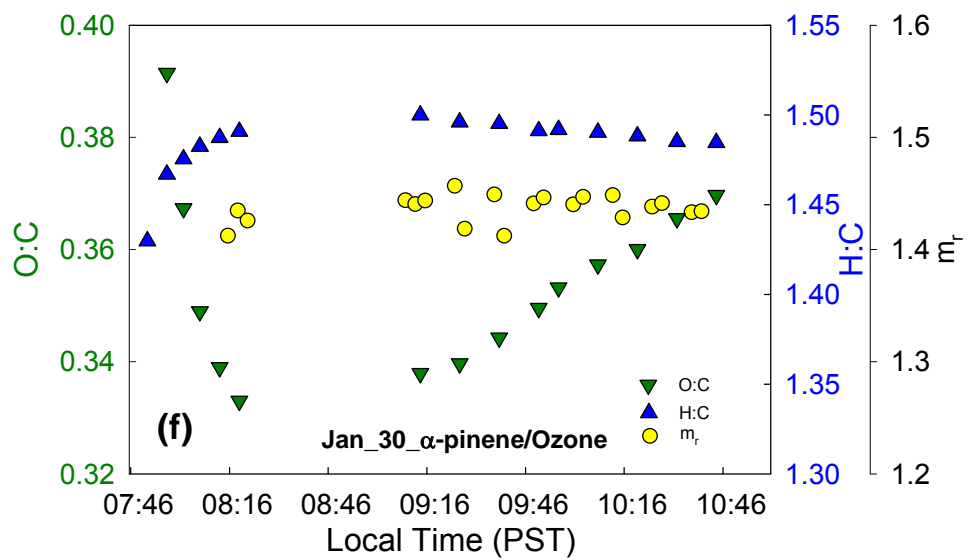
**Figure 6.9**

O:C and H:C ratio with retrieved refractive indices for each separate experiments (a,b,c) photochemically generated limonene SOA at different HC/NO<sub>x</sub> ratio, (d) photochemically generated  $\alpha$ -pinene SOA at high HC/NO<sub>x</sub> ratio (=31), (e) SOA generated from ozonolysis with scavenger and (f) without scavenger









## **Chapter 7**

### **FINAL CONCLUSIONS AND FUTURE WORKS**

## 7.1 Final conclusions and atmospheric implications.

This is the first study to investigate the refractive index of secondary organic aerosols (SOA) with sufficient resolutions to explore the relationship between this quantity with factors such as size, chemical composition and growth stage. The refractive index is the fundamental parameter controlling aerosol optical properties. Even though secondary organic aerosols constitute a large fraction of aerosols in the atmosphere, there are not well defined refractive indices that can be used to characterize SOA. This is due to the complexity of organic aerosols [Kanakidou *et al.*, 2005] but also results from the limited number of measurements available. Among SOA investigated, range of refractive indices is unexpectedly wide, ranging from 1.34 to 1.62. This range is much wider than the range of values for SOA currently assumed by radiative transfer modelers. [Kinne *et al.*, 2003; Pere *et al.*, 2011; Zaveri *et al.*, 2010].

At the beginning of the project, several questions were posed;

- 1) Current model approaches using single refractive index are enough for accurate estimation of radiative transfer?
- 2) If not, how various the refractive indices are for SOA?
- 3) What are the factors that control refractive indices?

In an effort to answer these questions, refractive index of various types of SOA was assessed, controlling chemical compositions under conditions as relevant to the atmosphere as possible. Chemical composition was altered using different hydrocarbons, oxidation chemistry, aerosol mass concentration and other factors such as temperature and aerosol aging.

Figure 7.1 shows the ranges of  $m_{p,s}$  determined from the set of chamber experiments evaluated in this thesis, compared with values used in models. Measured  $m_{p,s}$  are plotted separated by parent HC and oxidation chemistry separated into undenuded and thermodenuded.

The wide ranges for each experiment result from the changing chemical composition as the particles are growing or aging. It is clear that SOA  $m_r$ s are highly variable and dependent on a number of experimental parameters (e.g., different HC/NO<sub>x</sub> ratios, mass, size, aging and temperature) which determine the chemical composition of SOA.

In Chapter 3, for the first time, the importance of SOA generation chemistry, mass concentration, aging and parent hydrocarbon to aerosol refractive index is probed. This was made possible by the development of a polar nephelometer in our laboratory. It quickly becomes clear that SOA  $m_r$ s were surprisingly variable dependent on several of the above factors. However, these experiments were performed at unrealistically high mass concentrations, by updating polar nephelometer with a high power 1W 532 nm laser, investigating more atmospheric relevant SOA become possible. As described in Chapter 4, mass concentrations that were lower by a factor of 5-18 compared to the results described in Chapter 3, it was found that limonene and  $\alpha$ -pinene SOA refractive indices are closely related to particle size, which is in turn influenced mainly by the HC/NO<sub>x</sub> ratio (for summer conditions; winter results described in Chapter 6 showed less effect of HC/NO<sub>x</sub> ratio on diameter). The refractive index ranges from 1.34 to 1.56 for limonene and from 1.36 to 1.52 for  $\alpha$ -pinene, generally decreasing as the HC/NO<sub>x</sub> ratio increases from between 6.3- 8.1 and 33 ppbC/ppb. Existing hydrocarbon oxidation and aerosol formation models produce the prediction that refractive indices should fall in a narrow range similar to the values commonly assumed for radiative transfer models (Figure 7.1). Based on chemical kinetics simulation studies of limonene SOA, we hypothesize that observed high and low end  $m_r$  values are mostly due to oligomerization and uptake of water/small soluble molecules (e.g., glyoxal), respectively.

Chamber generated SOA contain species with a wide range of volatilities, because the degree of partitioning to the particle phase depends on mass loading; as the aerosol mass concentration increases, higher vapor pressure species condense on the particles. In order to investigate similar chemical composition SOA with ambient aerosols as possible and the relationships between refractive index and volatility, a laboratory built thermodenuder was used (Chapter 5). With this instrument, semivolatile species can be evaporated from chamber particles at various temperatures, leading to particles that appear to have similar chemical composition as ambient aerosol [Kostenuidou *et al.*, 2009; Lee *et al.*, 2011]. This study revealed the very different volatilities of anthropogenic and biogenic SOA; generally upon heating biogenic SOA, both diameter and  $m_r$  changed, whereas anthropogenic SOA were not affected by heating, indicating the much lower volatility of anthropogenic SOA compared to biogenic SOA. For biogenic SOA, after removing high volatility material,  $m_r$ s still spanned a relatively wide in range from 1.39 to 1.55.

In order to investigate to what extent variations in particle composition correspond to variations in refractive index, the chemical composition of SOA was monitored with HR-ToF-AMS in parallel with refractive index measurements (Chapter 6). This helps compare and apply chamber data to ambient aerosols. Using aerosol mass spectrometer, organic aerosol as well as specific SOA components such as  $m/z$  43 ( $C_2H_3O^+$ ,  $C_3H_7^+$ ),  $m/z$  44 ( $CO_2^+$ ) can be quantified which indicate semivolatile and low volatile, respectively. By presenting chemical composition data in the  $f_{43}$  vs.  $f_{44}$  space (triangle plot),  $m_r$  retrieved chamber SOA data fall outside of the ambient data residing at low  $f_{44}$  (low volatility) and high  $f_{43}$  (high volatility) and could not reach the degree of oxygenation of ambient low volatility species.

For photochemically generated SOA, the refractive index ranges from about 1.34 to 1.55 for limonene and from 1.44 to 1.47 for  $\alpha$ -pinene, generally increasing with diameter. Limonene SOA shows more variations in fraction of  $m/z$  43 ( $f_{43}$ ) and H:C than  $\alpha$ -pinene SOA.  $\alpha$ -Pinene SOA generated from ozonolysis also shows a narrow range of  $m_r$ s as 1.43-1.45 (19-22 °C) and 1.46-1.53 (23-29 °C) with small changes of  $f_{43}$  and H:C ratio. H:C ratio appears to be the best correlation with refractive index showing that increasing H:C ratio increase  $m_r$ s due to condensation of semivolatile species. However, from some points, at high H:C, refractive index starts to decrease suggesting that H:C ratio is not the only factor controlling the refractive index. Importantly, this result proves that shifting chemical composition due to condensation of semivolatile species is reflected to the values of  $m_r$ s.

Recently, *Ng et al.*, [2010] showed that ambient aerosols in the Northern hemisphere fall into a triangle plot with a range of  $f_{44}$  (0.01- 0.3) and  $f_{43}$  (0.02 - 0.17), which is wider range than the chamber result ( $f_{44}$  (0.13-0.26) and  $f_{43}$  (0.13-0.26)). Although more studies linking between optical properties and chemical composition with atmospherically relevant aerosol need to be done, the variations of refractive index (1.34 - 1.55) with narrower ranges of  $f_{44}$  (0.13-0.26) and  $f_{43}$  (0.13-0.26) max suggest that there would be more variations of  $m_r$ s of ambient aerosols.

We are the first to begin to understand what controls the variability of  $m_r$ . Examination of the all SOA data shows that within SOA measurements in this thesis, range of refractive indices is reasonably wide from 1.34 to 1.62; ranging from 1.37 to 1.53 for  $\alpha$ -pinene, from 1.37 to 1.53 for  $\beta$ -pinene, from 1.34 to 1.56 for limonene and 1.4-1.62 for toluene, reflecting all combined factors to control the chemical composition influence to the  $m_r$ s. Even after evaporating more volatile materials at the temperature range 60 – 110 °C, there is a range from 1.39 to 1.55 for biogenic SOA, from 1.34 to 1.62 for anthropogenic SOA. Ranges of  $m_r$ s for SOA studied here

would have a significant impact on radiative transfer calculations of SOA direct effects. There is more work to be done before we can say with confidence what the best numbers are to use in climate models, however a single value for SOA refractive index will not be sufficient to accurately model radiative transfer.

## 7.2 Future work

The full range of atmospheric conditions has not yet been performed in chamber studies, so SOA formation in the atmosphere could occur under regimes different from those performed in chamber studies so far. Possible cases for this difference between chamber and ambient SOA generation conditions are;

- 1) Different oxygenated status due to mass concentration
- 2) Aging
- 3) Additional SOA precursors

Each possibility will be the area more works are needed and is discussed below.

- 1) Different oxidation state.

AMS measurements indicate that most laboratory generated SOA is substantially less oxidized than ambient oxygenated organic aerosol. This may be due in part to the high aerosol loadings typically employed in chamber experiments; SOA at low mass concentration tends to be enriched in the least volatile and most oxygenated products [Bahreini *et al.*, 2005; Shilling *et al.*, 2009]. This underscores the need for laboratory experiments to be carried out under atmospherically relevant organic aerosol loading. In previously described study of Chapter 5, a thermodenuder was applied to generate more atmospheric relevant SOA. More such studies are needed.

- 2) As discussed before, chamber studies generally are not carried out for more than ~6h. Chamber generated SOA refractive index reflect the extent of SOA formation over the chamber experiments. In the atmosphere, oxidation reactions can precede as long as the organic aerosol is in atmosphere, thus, chamber studies cannot capture sustained, longer time (4-7 days) oxidation and its effects on chemical composition and associated optical properties. SOA aging studies have been performed primarily in flow-tube reactors with high OH radical concentrations ( $10^8 - 10^{10}$  molec/cm<sup>3</sup>) and short exposure times (less than 30 min). These studies focus on changes in chemical composition [Alfarra *et al.*, 2006; Robinson *et al.*, 2007; Sage *et al.*, 2008]. Recently, Cappa *et al.*, [2011] measured the evolution of organic aerosol optical properties and chemical composition oxidizing azelaic acid and squalene with OH radical concentrations ( $\sim 10^{11}$  molec/cm<sup>3</sup>). This study successfully showed the relationship between the O:C ratio and extinction coefficient; increasing extinction with increasing O:C ratio. This kind of study will be needed with SOA to investigate how much SOA can be aged and associate optical properties with aging.
- 3) The most abundant contributor to SOA is believed to be biogenic SOA which has been studied in many research groups so far, whereas anthropogenic SOA make only a minor contribution to SOA formation in global scale. However, ambient measurement in local scale showed the important contribution of anthropogenic SOA [Johnson *et al.*, 2006; Takegawa *et al.*, 2006; Volkamer *et al.*, 2006]. Laboratory AMS measurement of SOA from anthropogenic precursors are generally more similar to ambient chemical composition than those of biogenic precursors [Bahreini *et al.*, 2005; Sage *et al.*, 2008], as well as somewhat different mass spectra with biogenic SOA [Ng *et al.*, 2010]. Ng *et*



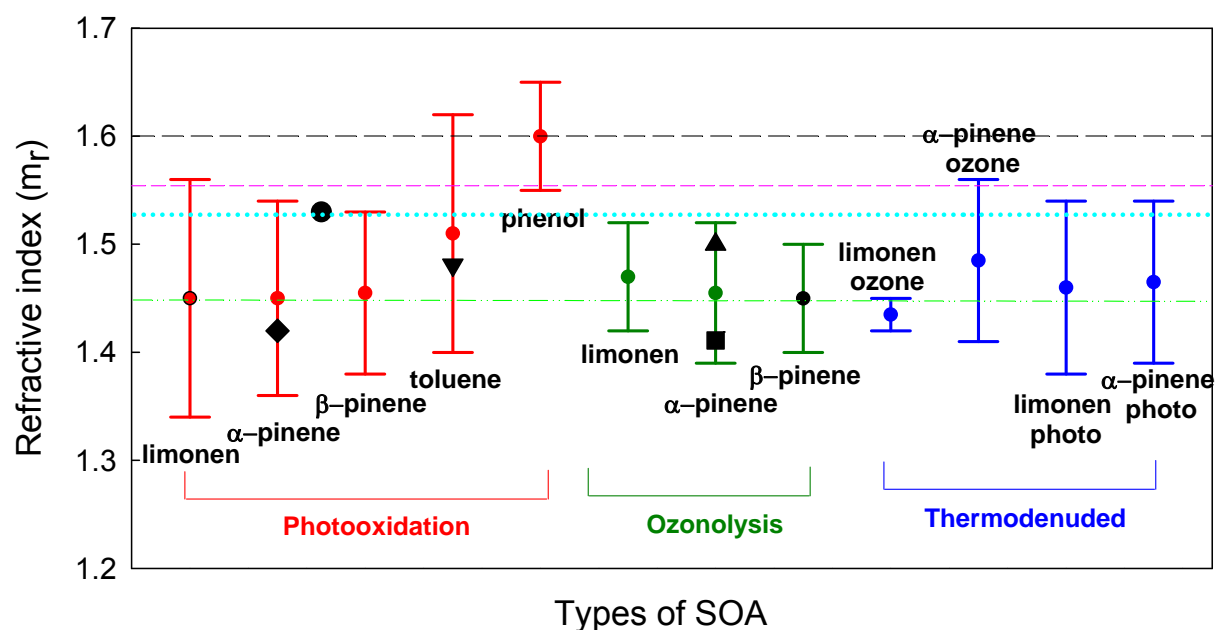
*al.*, [2010] showed quite different trend of  $f_{44}$  with organic loading;  $f_{44}$  start to increase (not decrease as observed for biogenic SOA) from the beginning of experiment and continuing over the experiment. In the study described in Chapter 6, we did not measure the chemical composition of SOA generated from aromatic compounds. However, our previous toluene  $m_r$  data indicate it is quite different from biogenic SOA, starting from somewhat higher  $m_r$ s and continuing to increase to higher values (1.62) [Kim *et al.*, 2010]. It seems the  $m_r$ s reflect the very low volatility and different chemical composition of anthropogenic SOA, but further studies are needed. Additionally, some literature and appendix A of this thesis show the evidence of absorption of aromatic SOA at short wavelengths ( $< 400\text{nm}$ ), a phenomenon not observed in biogenic SOA [Zhong and Jang, 2011; Nakayama *et al.*, 2010]. Aromatic and other anthropogenic SOA requires further studies on the measurement of optical properties for better estimation of radiative transfer.

### 7.3 References

- Alfarra, M. R., D. Paulsen, M. Gysel, A. A. Garforth, J. Dommen, A. S. H. Prevot, D. R. Worsnop, U. Baltensperger, and H. Coe (2006), A mass spectrometric study of secondary organic aerosols formed from the photooxidation of anthropogenic and biogenic precursors in a reaction chamber, *Atmospheric Chemistry and Physics*, 6, 5279-5293.
- Bahreini, R., M. D. Keywood, N. L. Ng, V. Varutbangkul, S. Gao, R. C. Flagan, J. H. Seinfeld, D. R. Worsnop, and J. L. Jimenez (2005), Measurements of secondary organic aerosol from oxidation of cycloalkenes, terpenes, and m-xylene using an Aerodyne aerosol mass spectrometer, *Environmental Science & Technology*, 39(15), 5674-5688.
- Cappa, C. D., D. L. Che, S. H. Kessler, J. H. Kroll, and K. R. Wilson (2011), Variations in organic aerosol optical and hygroscopic properties upon heterogeneous OH oxidation, *Journal of Geophysical Research*, 116, 12.
- Johnson, D., S. R. Utembe, and M. E. Jenkin (2006), Simulating the detailed chemical composition of secondary organic aerosol formed on a regional scale during the TORCH 2003 campaign in the southern UK, *Atmospheric Chemistry and Physics*, 6, 419-431.
- Kanakidou, M., J. H. Seinfeld, S. N. Pandis, I. Barnes, F. J. Dentener, M. C. Facchini, R. Van Dingenen, B. Ervens, A. Nenes, C. J. Nielsen, E. Swietlicki, J. P. Putaud, Y. Balkanski, S. Fuzzi, J. Horth, G. K. Moortgat, R. Winterhalter, C. E. L. Myhre, K. Tsigaridis, E. Vignati,

- E. G. Stephanou, and J. Wilson (2005), Organic aerosol and global climate modelling: a review, *Atmos. Chem. Phys.*, *5*, 1053-1123.
- Kim, H., B. Barkey, and S. E. Paulson (2010), Real refractive indices of alpha- and beta-pinene and toluene secondary organic aerosols generated from ozonolysis and photo-oxidation, *Journal of Geophysical Research-Atmospheres*, *115*, 10.
- Kinne, S., U. Lohmann, J. Feichter, M. Schulz, C. Timmreck, S. Ghan, R. Easter, M. Chin, P. Ginoux, T. Takemura, I. Tegen, D. Koch, M. Herzog, J. Penner, G. Pitari, B. Holben, T. Eck, A. Smirnov, O. Dubovik, I. Slutsker, D. Tanre, O. Torres, M. Mishchenko, I. Geogdzhayev, D. A. Chu, and Y. Kaufman (2003), Monthly averages of aerosol properties: a global comparison among models, satellite data, and AERONET ground data, *Journal of Geophysical Research*, *108*(D20).
- Kostenidou, E., B. H. Lee, G. J. Engelhart, J. R. Pierce, and S. N. Pandis (2009), Mass Spectra Deconvolution of Low, Medium, and High Volatility Biogenic Secondary Organic Aerosol, *Environmental Science & Technology*, *43*(13), 4884-4889.
- Lee, B. H., J. R. Pierce, G. J. Engelhart, and S. N. Pandis (2011), Volatility of secondary organic aerosol from the ozonolysis of monoterpenes, *Atmospheric Environment*, *45*(14), 2443-2452.
- Nakayama, T., Y. Matsumi, K. Sato, T. Imamura, A. Yamazaki, and A. Uchiyama (2010), Laboratory studies on optical properties of secondary organic aerosols generated during the photooxidation of toluene and the ozonolysis of alpha-pinene, *Journal of Geophysical Research-Atmospheres*, *115*, 11.
- Ng, N. L., M. R. Canagaratna, Q. Zhang, J. L. Jimenez, J. Tian, I. M. Ulbrich, J. H. Kroll, K. S. Docherty, P. S. Chhabra, R. Bahreini, S. M. Murphy, J. H. Seinfeld, L. Hildebrandt, N. M. Donahue, P. F. DeCarlo, V. A. Lanz, A. S. H. Prevot, E. Dinar, Y. Rudich, and D. R. Worsnop (2010), Organic aerosol components observed in Northern Hemispheric datasets from Aerosol Mass Spectrometry, *Atmospheric Chemistry and Physics*, *10*(10), 4625-4641.
- Pere, J. C., M. Mallet, V. Pont, and B. Bessagnet (2011), Impact of aerosol direct radiative forcing on the radiative budget, surface heat fluxes, and atmospheric dynamics during the heat wave of summer 2003 over western Europe: A modeling study, *Journal of Geophysical Research-Atmospheres*, *116*.
- Robinson, A. L., N. M. Donahue, M. K. Shrivastava, E. A. Weitkamp, A. M. Sage, A. P. Grieshop, T. E. Lane, J. R. Pierce, and S. N. Pandis (2007), Rethinking organic aerosols: Semivolatile emissions and photochemical aging, *Science*, *315*(5816), 1259-1262.
- Sage, A. M., E. A. Weitkamp, A. L. Robinson, and N. M. Donahue (2008), Evolving mass spectra of the oxidized component of organic aerosol: results from aerosol mass spectrometer analyses of aged diesel emissions, *Atmospheric Chemistry and Physics*, *8*(5), 1139-1152.
- Shilling, J. E., Q. Chen, S. M. King, T. Rosenoern, J. H. Kroll, D. R. Worsnop, P. F. DeCarlo, A. C. Aiken, D. Sueper, J. L. Jimenez, and S. T. Martin (2009), Loading-dependent elemental composition of alpha-pinene SOA particles, *Atmospheric Chemistry and Physics*, *9*(3), 771-782.
- Takegawa, N., T. Miyakawa, Y. Kondo, D. R. Blake, Y. Kanaya, M. Koike, M. Fukuda, Y. Komazaki, Y. Miyazaki, A. Shimono, and T. Takeuchi (2006), Evolution of submicron organic aerosol in polluted air exported from Tokyo, *Geophysical Research Letters*, *33*(15).
- Volkamer, R., J. L. Jimenez, F. S. Martini, K. Dzepina, Q. Zhang, D. Salcedo, L. T. Molina, D. R. Worsnop, and M. J. Molina (2006), Secondary organic aerosol formation from anthropogenic air pollution: rapid and higher than expected, *Geophysical Research Letters*, *33*(17), 4 pp.-4 pp.

- Zaveri, R. A., J. C. Barnard, R. C. Easter, N. Riemer, and M. West (2010), Particle-resolved simulation of aerosol size, composition, mixing state, and the associated optical and cloud condensation nuclei activation properties in an evolving urban plume, *Journal of Geophysical Research-Atmospheres*, 115.
- Zhong, M., and M. Jang (2011), Light absorption coefficient measurement of SOA using a UV-Visible spectrometer connected with an integrating sphere, *Atmospheric Environment*, 45(25), 4263-4271.



- · — ULAQ/Itay [Kinne et al., 2003]
- · · · · ECHAM4/ Max-planck-Inst., GOCART (Geogia tech., NASA Goddard), GISS/NASA-GISS, CCSR/Japan, Grantour/(U. of Michigan) [Kinne et al., 2003]
- · — PartMC-MOSAIC, CHEMERE [Pere et al., 2011; Zaveri et al., 2010]
- · — MIRAGE/PNNL [Kinne et al., 2003]
- ◆ Barkey et al., 2007
- ▲ Schnaiter et al., 2005
- Photooxidation of VOC from Holm Oak [Lang-Yona et al., 2010]
- Nakayama et al., 2010
- ▼ Nakayama et al., 2010

Figure 7.1. Refractive indices of various types of SOA studied in this thesis. Ranges of refractive index for each SOA result from changing chemical composition as the particles are growing or ageing. Dashed lines represent the refractive index for SOA or organic aerosol that assumed by different current models. Black symbols represent literature values of SOA generated using same hydrocarbon and oxidation chemistries denoted in the figure.

## **Appendix A**

**Optical properties of absorbing Secondary Organic Aerosols  
generated from Photo-oxidation of toluene, phenol and limonene.**

## **Abstract**

Characterization of optical properties of secondary organic aerosols is important to help determine the aerosol direct effect on radiation forcing, however, the light absorption of secondary organic aerosols has not been investigated that much. Here, we studied the absorption coefficient of secondary organic aerosols (SOA) generated from the photooxidation of limonene, toluene and phenol at different HC/NO<sub>x</sub> ratios. Absorption coefficient were obtained from the measurement of attenuation of 370 and 880 nm light using aethalometer with measured mass concentrations of particles collected on quartz filters. The data suggests that for all investigated SOA, light absorption was observed at 370 nm and none of them shows the absorption at 880 nm. Limonene SOA shows weak absorption at 370 nm without color and increase with HC/NO<sub>x</sub> ratio. Aromatic SOA from toluene and phenol appears to have strong absorption at 370 nm with yellowish or brownish color showing opposite correlation of HC/NO<sub>x</sub> to limonene SOA; decreaseing absorption with HC/NO<sub>x</sub>. From these studies, it is found that depending on precursors, the compounds to contribute for the absorption are different; organic peroxide seems do important role for limonene SOA absorption whereas nitrate compounds have a role to enhance the absorption for aromatic SOA.

## **1. Introduction**

Atmospheric aerosols play an important role in determining the direct radiative transfer by scattering and absorbing solar radiation [*Intergovernmental Panel on Climate Change, 2007*] but the magnitude as well as the sign of the forcing effect is highly uncertain. Among aerosols, only black carbon (BC) is known to have a positive direct aerosol forcing, warming the atmosphere and most direct radiative forcing models consider that the light absorption of organic aerosols is negligible [*Forster et al., 2007*]. Organic compounds make up a substantial fraction of

atmospheric aerosols, accounting for 20 – 90 % of aerosol mass in the lower troposphere, of which roughly 70 % is secondary [Hallquist *et al.*, 2009]. However, the radiative properties of these ubiquitous SOA particles are poorly understood [Kanakidou *et al.*, 2005]. This is due to the chemical and physical complexity of the organic aerosols as well as the limited number of measurements available.

There have been several evidences of absorption of SOA [Bones *et al.*, 2010; Chang and Thompson, 2010; Jacobson, 1999; Jaoui *et al.*, 2008; Laskin *et al.*, 2010]. Jacobson, [1999] investigated the possible importance of the near-UV light absorption by nitrated and aromatic aerosol components on reductions in downward solar irradiance in the los angels. Some other studies showed the evidence of possible light absorption of nitrated and aromatic aerosols, generating colored SOA. Bones *et al.*, [2010] and Laskin *et al.*, [2010] showed the colored organic compounds generated by chemical aging of SOA produced by ozonolysis of limonene in the presence of ammonia. Chang and Thompson, [2010] generate colored organic aerosol from the irradiation of aqueous solutions containing H<sub>2</sub>O<sub>2</sub> and phenolic compounds and Jaoui *et al.*, [2008] showed the yellowish color of SOA generated from photooxidation of toluene with NO<sub>x</sub>.

Recently, some studies measured absorption coefficient at near-UV light. Zhong and Jang, [2011] reported a small absorption coefficient of 0.038 m<sup>2</sup>/g at 350 nm for limonene SOA generated by photooxidation (HC/NO<sub>x</sub> = 30). Nakayama *et al.*, [2010] measured absorption coefficient of SOA generated from toluene SOA at 355nm as 0.3 - 3 m<sup>2</sup>/g using cavity ring down method. However, absorption at wavelengths above 500 nm was measured to be very small, or zero for biogenic SOA [Lang-Yona *et al.*, 2010; Redmond and Thompson, 2011; Zhong and Jang, 2011; Nakayama *et al.*, 2010]. Kim *et al.*, [2012] also showed that there is no evidence of significant absorption at 532 and 670 nm for the particles generated from  $\alpha$ -pinene and limonene,

showing GA retrievals (which can provide only a rough estimate of absorption) return imaginary components of order  $10^{-5}$ , and particles are colorless when collected on filters. These evidences showed that further studies on the measurement of absorption of secondary organic aerosols is necessary for better radiative transfer model.

Here we study absorbing SOA generated from limonene as biogenic sources and toluene and phenol as anthropogenic sources at different HC/NO<sub>x</sub> ratios, in an effort to probe the effect of RO<sub>2</sub> + NO vs. RO<sub>2</sub> + HO<sub>2</sub> and RO<sub>2</sub> + RO<sub>2</sub> on SOA optical properties. Limonene is the second highest monoterpenes emitted in the atmosphere following by  $\alpha$ -pinene, accounting for approximately 16 % of global monoterpene emissions [Kanakidou *et al.*, 2005]. However, limonene has much higher SOA yields presumably because it is doubly unsaturated. Aromatic hydrocarbons comprise 20% of nonmethane hydrocarbons in the urban area and considered to be one of the major precursors to urban SOA [Calvert *et al.*, 2002], through multigenerational reactions [Ng *et al.*, 2007; Sato *et al.*, 2007]. Phenolic compounds are one of the major first generation products of OH reaction with aromatic hydrocarbons [Calvert *et al.*, 2002] and toluene is typically the most abundant aromatic compound [Kanakidou *et al.*, 2005]. In this study, we measure the absorption coefficient using aethalometer at 370 and 880 nm of light for photochemically generated limonene, toluene and phenol SOA collected on quartz filters. Our results are the first to explore the influence of HC/NO<sub>x</sub> ratio on absorption coefficient.

## **2. Experimental**

### **2.1 Secondary organic aerosol generation**

Experiments were performed in a 24 m<sup>3</sup> Teflon chamber constructed on the roof of the Math Sciences Building at UCLA. The chamber is described in detail in Chung *et al.*, [2008]. Air is supplied to the chamber by two 33 gallon oil-free portable air compressors (Craftsman)



purified with a series of packed bed scrubbers filled with Purafil Triple Blend (Purafil Inc.), activated charcoal, and HEPA capsule filters (Gelman). The scrubbed air has typically < 5 and NO<sub>x</sub> (Thermo Electron model 14B/E), O<sub>3</sub> (Dasibi 1001-RS), and organics (GC, HP 5890-II) levels below the 1 ppb detection limits. Access to the inside of the chamber is provided by custom Teflon sampling ports. Teflon (gasses) and copper (particles) sampling lines extend 20 cm into the chamber and pull samples at 0.6 (NO<sub>x</sub>), 2 (O<sub>3</sub> and organics), and 1 (particles) LPM. Between experiments, a vent is opened and the chamber is flushed with clean air for 10 hours in full sun in preparation for the next experiment. Table 1 shows initial conditions and summary statistics for 18 experiments. Initially, the chamber, covered with a black tarpaulin (supported on a frame above the chamber), was half filled with purified air. At this point NO (Scott Specialty Gases) and propene (Aldrich, as a photochemical initiator for toluene and phenol) were added. Next, the SOA precursor hydrocarbon liquid was evaporated into the air stream filling the chamber. Limonene (Aldrich, 99.8 %)  $\alpha$ -pinene (Fluka, 98.5 %), toluene (Aldrich, 99.8 %) and phenol (Aldrich, 99%) were used as received. The chamber contents were then allowed to mix for about 40 min. Once the gas chromatograph returned two SOA precursor hydrocarbon measurements within 2% of one another, the tarps were removed and photochemistry initiated. The overall oxidation time for three precursors was 4 – 6 h depending on the HC/NO<sub>x</sub> ratio.

Aerosols were characterized with an aethalometer (OT21, MAGEE Scientific, Berkeley, California), integrating nephelometer (Ecotech M9003), a scanning mobility particle sizer (SMPS, TSI model 3080), and by gravimetric mass ( $\pm 1 \mu\text{g}$ , Sartorius). The primary purpose of the integrating nephelometer is to provide checks for the SMPS and also provides temperature and relative humidity in the chamber. Light absorption of aerosols was measured by an aethalometer (OT21, MAGEE Scientific, Berkeley, California), a filter-based optical

transmissometer at 370 nm and 880 nm, respectively. Aerosols were collected on pre-baked (24h at 550 °C) 25 mm quartz fiber filters (Pall Life Sciences) for 10-15 min at 20 LPM once SOA mass growth had stabilized at the end of the experiment. Mass concentration was measured using SMPS every 3 minutes while particles were collecting, then we averaged the mass concentration and calculated the mass of SOA on the filters. Gravimetric mass of particles was also determined weighting them on a microbalance (Sartorius,  $\pm 1 \mu\text{g}$ ) in a temperature and relative humidity controlled room. Blank calibration was done for each measurement, and attenuation of both 370 nm and 880 nm wavelength were measured. For each SOA collected filter, 10 measurements were done and averaged their attenuation results. Empty pre-baked quartz fiber filter was used as blank reference filter.

### **3. Results and Discussion**

Absorption coefficient was measured for most of SOA investigated in *Kim et al.*, [2010; 2012]. Among those experiments, photochemically generated limonene, toluene SOA generated at three different conditions ; low  $\text{NO}_x$  (initial  $\text{HC}/\text{NO}_x = 30 - 33$ ), intermediate  $\text{NO}_x$  ( $\text{HC}/\text{NO}_x = 10-15$ ) and high  $\text{NO}_x$  ( $\text{HC}/\text{NO}_x = 6-9$ ) showed the absorption at short wavelength (370nm). In order to investigate the absorption of aromatic compound further, two experiments with phenol were performed: photooxidation at low  $\text{NO}_x$  (initial  $\text{HC}/\text{NO}_x = 35$  and 41). Detailed experimental conditions of absorbing SOA including phenol SOA and calculated absorption coefficients are shown in Table 1. For SOA not showing absorption both at 370 nm and 880 nm are not listed in the Table 1.

#### **3.1 Calculation of UV absorption of SOA**

Biogenic SOA,  $\alpha$ - and  $\beta$ -pinene and limonene SOA are colorless, while filter samples of aromatic SOA from toluene and phenol has a slight or deep yellowish tint. The absorption cross

section ( $\sigma_{\text{abs}}$ , in units of  $\text{m}^2/\text{g}$ ) was calculated using attenuation (equ.1) measured from the aethalometer and SOA mass (g) collected on the quartz fiber filters. Gravimetric mass concentration was used for this calculation. SMPS measured masses are also compared with gravimetric mass, showing  $17 \pm 7\%$  lower than that of gravimetric mass measurements.

$$ATTENUATION = \ln\left(\frac{\text{blank\_filter\_light\_transmission}}{\text{SOA\_collected\_filter\_light\_transmission}}\right) \quad (1)$$

The SOA is collected on only a  $3.5 \text{ cm}^2$  portion of the 2.5 cm radius filter. The filter collection area is calculated from the area that the SOA is collected on the 2.5 cm (radius) quartz filter because some area of the filter is not available to collect the particles.

The absorption cross section ( $\sigma_{\text{abs}}$ , in units of  $\text{m}^2/\text{g}$ ) was calculated by;

$$\sigma (\text{m}^2/\text{g}) = \frac{\text{Attenuation}}{M(\text{g}/\text{m}^2)} \quad (2)$$

where attenuation is the value measured from the aethalometer and M is the aerosol mass concentration collected on the filter ( $\text{g}/\text{m}^2$ ).

### 3.2 UV absorption of SOA

#### 3.2.1 Aromatic SOA

None of the chamber generated SOA shows the absorption at 880 nm. The  $\alpha$ - and  $\beta$ -pinene SOA from both  $\text{O}_3$  and  $\text{NO}_x$  based oxidation systems have absorption values at 370 nm that are barely differentiable from zero and range from 0 to  $0.04 \text{ m}^2/\text{g}$ .

Most significant absorption was observed with aromatic SOA generated from toluene and phenol. The toluene and phenol SOA collected filters show yellowish or brownish tint which is close in appearance to filters shown at *Jaoui et al.*, [2008]. We measured their absorption

coefficient with aethalometer and both toluene and phenol SOA absorb strongly at 370 nm as shown in Figure 1. The absorption of toluene and phenol SOA appears to be related to the HC/NO<sub>x</sub> ratio, decreasing from 4.67 – 20.6 to 3.86 m<sup>2</sup>/g when HC/NO<sub>x</sub> ratio increase from 7.7-9 to 32 for toluene and decreasing from 17.6 to 9.4 m<sup>2</sup>/g with increasing HC/NO<sub>x</sub> from 35 to 41 for phenol.

Both SOA show that increasing NO<sub>x</sub> concentration, the absorption coefficient increase, indicating nitrated aerosols seem to contribute for absorption. Many of previous studies show the evidence of absorption of aromatic SOA but none of them studies the NO<sub>x</sub> concentration effect. *Jacobson*, [1999] showed that some compounds including nitrated aromatics, phenols and nitrated inorganics absorb light at UV or near UV wavelengths. Nitrated aromatics exhibit strong absorption because the nitro substituent on the aromatic ring enhances absorption as well as shift the absorption to longer wavelengths (>350 nm). For example, *Jacobson*, [1999] showed that 4-nitro-o-cresol, one of the major components of the toluene SOAs [*Sato et al.*, 2007] has a strong absorption with a maximum absorption cross section of  $3.44 \times 10^{-17}$  cm<sup>2</sup> molecule<sup>-1</sup> and imaginary part of the refractive index of 0.54 at 319 nm, while non nitrated compounds such as o-cresol (2-methylphenol) has a weak absorption with a maximum absorption cross section of  $1.65 \times 10^{-17}$  cm<sup>2</sup> molecule<sup>-1</sup> and small imaginary refractive index of 0.096 at 273 nm. Also *Jang and Kamens*, [2001] showed that 4,6-dinitro-o-cresol is one of the major toluene SOA products which can show a yellow color corresponding with the visible absorption spectrum beyond 400 nm [*Howard*, 1991]. Being consistent with previous studies, current our results showed that NO<sub>x</sub> concentration do an important role for the formation of absorbing materials in aromatic SOA.

But for the case of toluene SOA, for lowest HC/NO<sub>x</sub> ratio (7.7-9), the ranges of absorption coefficient are various from 4.67 to 20.6. m<sup>2</sup>/g At this point, it is not yet clear the

variants (none of temperature, humidity effect can explain this) and possibly due to some instrumentation errors or contamination of filters.

### 3.2.2. Biogenic SOA

On the other hand, biogenic SOA from  $\alpha$ - and  $\beta$ -pinene and limonene shows distinct differences. Most of biogenic SOA show no absorption. As mentioned earlier (section 3.1) none of SOA from  $\alpha$ - and  $\beta$ -pinene did not show the absorption and they are colorless on the filters. However, some of studies showed that limonene can generate absorbing SOA and our study also show the consistent result. Limonene SOA is also colorless when it was collected on the filters but little amount of absorption was investigated, but higher than  $\alpha$ - and  $\beta$ -pinene as 0.86-2.06 m<sup>2</sup>/g. Several studies show the evidence of absorption of limonene SOA [*Bones et al.*, 2010; *Zhong and Jang*, 2011]. It appears that the absorption coefficient depend on HC/NO<sub>x</sub> ratios but apposite direction with aromatic SOA as shown at Figure 1; increasing HC/NO<sub>x</sub> ratios from 6 to 33, the absorption coefficient increases from 0.86 to 2.06 m<sup>2</sup>/g. It seems than rather than the products from RO<sub>2</sub> + NO, the products from RO<sub>2</sub> + HO<sub>2</sub> and RO<sub>2</sub> + RO<sub>2</sub> contribute to the absorption. *Walser et al.*, [2007] suggested that the primary absorbers in limonene SOA particles are organic peroxides, from the studies of UV wavelength dependent photolysis product yield. *Zhong and Jang*, [2011] also showed the absorption of limonene SOA generated with ozone at 428 nm and the absorption was increased during the experiment from the formation of conjugated products through particle phase reaction. These studies showed that for limonene, nitrate compounds are not necessary for the absorption. Rather, some other conjugated products mainly do a role for absorption. There are some other studies emphasizing the importance of nitrate for limonene SOA; *Bones et al.*, [2010] and *Laskin et al.*, [2010] showed the colored limonene SOA generated from aging in the presence of ammonia. These studies show stronger absorption due to colored

materials whereas *Walser et al.*, [2007], *Zhong and Jang*, [2011] and our SOA has weak absorption without color. It seems that nitrate compounds can enhance the absorption as the case of aromatic SOA, however, in case of limonene, even without the nitrate compounds; there are products that show weak absorption at short wavelength.

## 5.0 Atmospheric implications

Absorption measurement at 370 nm shows the weak absorption for limonene SOA and significant absorption for toluene and phenol SOA have showing a yellowish tint. Biogenic SOA including limonene SOA are colorless on the filters. Overall data shows that HC/NO<sub>x</sub> affect to the absorption of SOA but with different ways depending on precursors; aromatic SOA, NO<sub>x</sub> concentration increase the absorption whereas limonene SOA absorption shows the opposite trend, indicating primary absorbers for each SOA are different. Overall our data showed here has higher absorption coefficient value than literature reported value.; 1.11-2.06 m<sup>2</sup>/g vs 0.038 m<sup>2</sup>/g [*Zhong and Jang*, 2011] for limonene SOA generated by photooxidation at HC/NO<sub>x</sub> = 30-33 and 3.86 (at HC/NO<sub>x</sub> = 32) vs. 0.3 - 3 m<sup>2</sup>/g (at HC/NO<sub>x</sub> = ~ 64) [*Nakayama et al.*, 2010] for toluene. It is possibly because aethalometer is not enough for using weaker absorbing aerosols than black carbon. Or as previously reported in some studies [*Cappa et al.*, 2008; *Lack et al.*, 2008], the method we used, filter based method cause uncertainties of measurement. As *Cappa et al.*, [2008] and *Lack et al.*, [2008] reported, there are bias in filter based absorption measurement and require various corrections, which are unique to each measurement technique (e.g., particle soot absorption photometer, aethalometer and multi-angle absorption photometer) and also they suggest to consider changes in the filter properties upon loading with aerosols. Empirical corrections (e.g. 20-30% for PSAP, [*Bond et al.*, 1999]) are suggested and they limit the overall accuracy of. In order to compare with previously reported data, using similar ways such as using

uv vis spectrometer or non filter based method will be preferable. While further detailed work is needed to completely quantify the absorption coefficient, our report shows that SOA also shows the fairly enough amount of absorption and should not be ignored for radiative transfer model.

## Acknowledgements

H.K. gratefully acknowledges the support of a UCLA dissertation year fellowship. The authors appreciate assistance with experiments from Ms. Leila Lackey and Ms. Michelle Kuang.

## References

- Bond, T. C., T. L. Anderson, and D. Campbell (1999), Calibration and intercomparison of filter-based measurements of visible light absorption by aerosols, *Aerosol Science and Technology*, 30(6), 582-600.
- Bones, D. L., D. K. Henricksen, S. A. Mang, M. Gonsior, A. P. Bateman, T. B. Nguyen, W. J. Cooper, and S. A. Nizkorodov (2010), Appearance of strong absorbers and fluorophores in limonene-O(3) secondary organic aerosol due to NH<sub>4</sub>(+)-mediated chemical aging over long time scales, *Journal of Geophysical Research-Atmospheres*, 115.
- Calvert, J. G., R. Atkinson, K. H. Becker, R. M. Kamens, J. H. Seinfeld, T. J. Wallington, and G. Yarwood (2002), The mechanism of atmospheric oxidation of aromatics hydrocarbons, *Oxford University Press*.
- Cappa, C. D., D. A. Lack, J. B. Burkholder, and A. R. Ravishankara (2008), Bias in filter-based aerosol light absorption measurements due to organic aerosol loading: Evidence from laboratory measurements, *Aerosol Science and Technology*, 42(12), 1022-1032.
- Chang, J. L., and J. E. Thompson (2010), Characterization of colored products formed during irradiation of aqueous solutions containing H<sub>2</sub>O<sub>2</sub> and phenolic compounds, *Atmospheric Environment*, 44(4), 541-551.
- Chung, A., A. A. Lall, and S. E. Paulson (2008), Particulate emissions by a small non-road diesel engine: Biodiesel and diesel characterization and mass measurements using the extended idealized aggregates theory, *Atmospheric Environment*, 42(9), 2129-2140.
- Forster, P., V. Ramaswamy, P. Artaxo, T. Berntsen, R. Betts, D. W. Fahey, J. Haywood, J. Lean, D. C. Lowe, G. Myhre, J. Nganga, R. Prinn, G. Raga, M. Schulz, and R. V. Dorland (2007), Changes in Atmospheric Constituents and in Radiative Forcing. In: *Climate Change 2007: The Physical Science Basis. Contribution of Working Group I to the Fourth Assessment Report of the Intergovernmental Panel on Climate Change* [Solomon, S., D. Qin, M. Manning, Z. Chen, M. Marquis, K.B. Averyt, M. Tignor and H.L. Miller (eds.)], *Cambridge University Press, Cambridge, United Kingdom and New York, NY, USA*.
- Hallquist, M., J. C. Wenger, U. Baltensperger, Y. Rudich, D. Simpson, M. Claeys, J. Dommen, N. M. Donahue, C. George, A. H. Goldstein, J. F. Hamilton, H. Herrmann, T. Hoffmann, Y. Iinuma, M. Jang, M. E. Jenkin, J. L. Jimenez, A. Kiendler-Scharr, W. Maenhaut, G. McFiggans, T. F. Mentel, A. Monod, A. S. H. Prevot, J. H. Seinfeld, J. D. Surratt, R.

- Szmigielski, and J. Wildt (2009), The formation, properties and impact of secondary organic aerosol: current and emerging issues, *Atmos. Chem. Phys.*, 9(14), 5155-5236.
- Howard (1991), Handbook of Environmental Fate and Exposure Data for Organic Chemicals. Pesticides, *Lewis Publishers, chelsea, MI*.
- Jacobson, M. Z. (1999), Isolating nitrated and aromatic aerosols and nitrated aromatic gases as sources of ultraviolet light absorption, *Journal of Geophysical Research-Atmospheres*, 104(D3), 3527-3542.
- Jang, M. S., and R. M. Kamens (2001), Characterization of secondary aerosol from the photooxidation of toluene in the presence of NO<sub>x</sub> and 1-propene, *Environmental Science & Technology*, 35(18), 3626-3639.
- Jaoui, M., E. O. Edney, T. E. Kleindienst, M. Lewandowski, J. H. Offenberg, J. D. Surratt, and J. H. Seinfeld (2008), Formation of secondary organic aerosol from irradiated alpha-pinene/toluene/NO(x) mixtures and the effect of isoprene and sulfur dioxide, *Journal of Geophysical Research-Atmospheres*, 113(D9).
- Kanakidou, M., J. H. Seinfeld, S. N. Pandis, I. Barnes, F. J. Dentener, M. C. Facchini, R. Van Dingenen, B. Ervens, A. Nenes, C. J. Nielsen, E. Swietlicki, J. P. Putaud, Y. Balkanski, S. Fuzzi, J. Horth, G. K. Moortgat, R. Winterhalter, C. E. L. Myhre, K. Tsigaridis, E. Vignati, E. G. Stephanou, and J. Wilson (2005), Organic aerosol and global climate modelling: a review, *Atmos. Chem. Phys.*, 5, 1053-1123.
- Kim, H., B. Barkey, and S. E. Paulson (2010), Real refractive indices of alpha- and beta-pinene and toluene secondary organic aerosols generated from ozonolysis and photo-oxidation, *Journal of Geophysical Research-Atmospheres*, 115, 10.
- Kim, H., B. Barkey, and S. E. Paulson (2012), Real refractive indices and formation yields of secondary organic aerosol generated from photooxidation of limonene and  $\alpha$ -pinene: the effect of the HC/NO<sub>x</sub> Ratio, *The Journal of Physical Chemistry A*, *accepted*.
- Lack, D. A., C. D. Cappa, D. S. Covert, T. Baynard, P. Massoli, B. Sierau, T. S. Bates, P. K. Quinn, E. R. Lovejoy, and A. R. Ravishankara (2008), Bias in filter-based aerosol light absorption measurements due to organic aerosol loading: Evidence from ambient measurements, *Aerosol Science and Technology*, 42(12), 1033-1041.
- Lang-Yona, N., Y. Rudich, T. F. Mentel, A. Buchholz, A. Kiendler-Scharr, E. Kleist, C. Spindler, R. Tillmann, and J. Wildt (2010), The chemical and microphysical properties of secondary organic aerosols from Holm Oak emissions, *Atmos. Chem. Phys.*, 10(2), 4753-4788.
- Laskin, J., A. Laskin, P. J. Roach, G. W. Slysz, G. A. Anderson, S. A. Nizkorodov, D. L. Bones, and L. Q. Nguyen (2010), High-Resolution Desorption Electrospray Ionization Mass Spectrometry for Chemical Characterization of Organic Aerosols, *Analytical Chemistry*, 82(5), 2048-2058.
- Nakayama, T., Y. Matsumi, K. Sato, T. Imamura, A. Yamazaki, and A. Uchiyama (2010), Laboratory studies on optical properties of secondary organic aerosols generated during the photooxidation of toluene and the ozonolysis of alpha-pinene, *Journal of Geophysical Research-Atmospheres*, 115, 11.
- Ng, N. L., P. S. Chhabra, A. W. H. Chan, J. D. Surratt, J. H. Kroll, A. J. Kwan, D. C. McCabe, P. O. Wennberg, A. Sorooshian, S. M. Murphy, N. F. Dalleska, R. C. Flagan, and J. H. Seinfeld (2007), Effect of NO<sub>x</sub> level on secondary organic aerosol (SOA) formation from the photooxidation of terpenes, *Atmospheric Chemistry and Physics*, 7(19), 5159-5174.



- Redmond, H., and J. E. Thompson (2011), Evaluation of a quantitative structure-property relationship (QSPR) for predicting mid-visible refractive index of secondary organic aerosol (SOA), *Phys. Chem. Chem. Phys.*, *13*(15), 6872-6882.
- Sato, K., S. Hatakeyama, and T. Imamura (2007), Secondary organic aerosol formation during the photooxidation of toluene: NO<sub>x</sub> dependence of chemical composition, *Journal of Physical Chemistry A*, *111*(39), 9796-9808.
- Walser, M. L., J. Park, A. L. Gomez, A. R. Russell, and S. A. Nizkorodov (2007), Photochemical aging of secondary organic aerosol particles generated from the oxidation of d-limonene, *Journal of Physical Chemistry A*, *111*(10), 1907-1913.
- Zhong, M., and M. Jang (2011), Light absorption coefficient measurement of SOA using a UV-Visible spectrometer connected with an integrating sphere, *Atmospheric Environment*, *45*(25), 4263-4271.

**Table 1. Initial conditions, temperatures, relative humidities and results of the experiments**

Expt.	Initial Conditions				Results						
	Hydrocarbon	HC (ppb)	NO <sub>x</sub> (ppb)	HC/NO <sub>x</sub> (ppbC/ppb)	Temp (°C) <sup>1</sup>	RH (%) <sup>1</sup>	ΔHC (ppb)	# density (#/cm <sup>3</sup> ) <sup>2</sup>	Size mode (nm) <sup>2</sup>	σ <sub>λ=380nm</sub> (m <sup>2</sup> /g) <sup>3</sup>	Yield <sup>4</sup> (%)
<b>16-Aug-11</b>	Limonene	130	39	33	35-39-34	22-18-24	132	2150	372	1.44	33
<b>26-Aug-10</b>	Limonene	60	20	30	37-39-35	18-16-20	60	3720	217	2.06	27
<b>17-Sep-10</b>	Limonene	65	20	33	31-34-33	17-15-16	64	5640	217	1.11	38
<b>8-Oct-10</b>	Limonene	77	40	19	35-31	19-25	77	7250	217	0.99	33
<b>30-Aug-10</b>	Limonene	75	56	13	31-32-28	21-20-25	74	4560	260	1.27	40
<b>15-Sep-10</b>	Limonene	73	78	9.3	39-36	14-16	71	2070	334	0.86	30
<b>5-Nov-10</b>	Limonene	72	120	6.3	39-35	14-17	72	3530	334	0.95	35
<b>15-Nov-10</b>	Limonene	90	150	6.0	32-25	15-22	83	2750	400	0.37	38
<b>16-Aug</b>	Limonene	130	39	33	35-39-34	22-18-24	130	2795	372	1.44	47
<b>29-Aug-11</b>	Toluene	2760	1350	15	42-35	18-26	990	5460	445	3.16	4.0
<b>24-Aug-11</b>	Toluene	2770	620	32	39-35	20-24	820	3090	429	3.86	11
<b>7-Sep-11</b>	Toluene	3100	2800	8.2	48-42	17-23	820	11400	250	13.8	4.1
<b>9-Sep-11</b>	Toluene	3400	3230	7.7	38-35	18-20	810	17700	260	14.8	4.9
<b>14-Sep-11</b>	Toluene	3000	2800	7.9	35-31	24-35	480	11800	136	20.6	0.8
<b>19-Sep-11</b>	Toluene	3100	2650	8.7	34-33	29-33	540	7360	175	12.6	1
<b>12-Oct-11</b>	Toluene	3400	2750	9	47-49-44	15-14-20	820	4520	279	4.67	1.6
<b>14-Oct-11</b>	Phenol	800	143	41	38-42-38	16-14-17	344	1620	461	11.4	9.4
<b>26-Oct-11</b>	Phenol	1068	210	35	31-27	27-35	506	1800	661	13.5	17.6

<sup>1</sup>Initial and final temperature and relative humidity

<sup>2</sup>Final aerosol number concentration and size mode. These values have not been adjusted for wall losses.

<sup>3</sup>Absorption coefficient calculated using equation 1 and 2.

<sup>4</sup>Calculated from peak measured aerosol mass corrected for wall losses and the corresponding quantity of reacted hydrocarbon. Because of the uncertainties in the measurement from GC (± 3 %) and measurement of SMPS (± 10 %) yields are uncertain to ± 10 %.

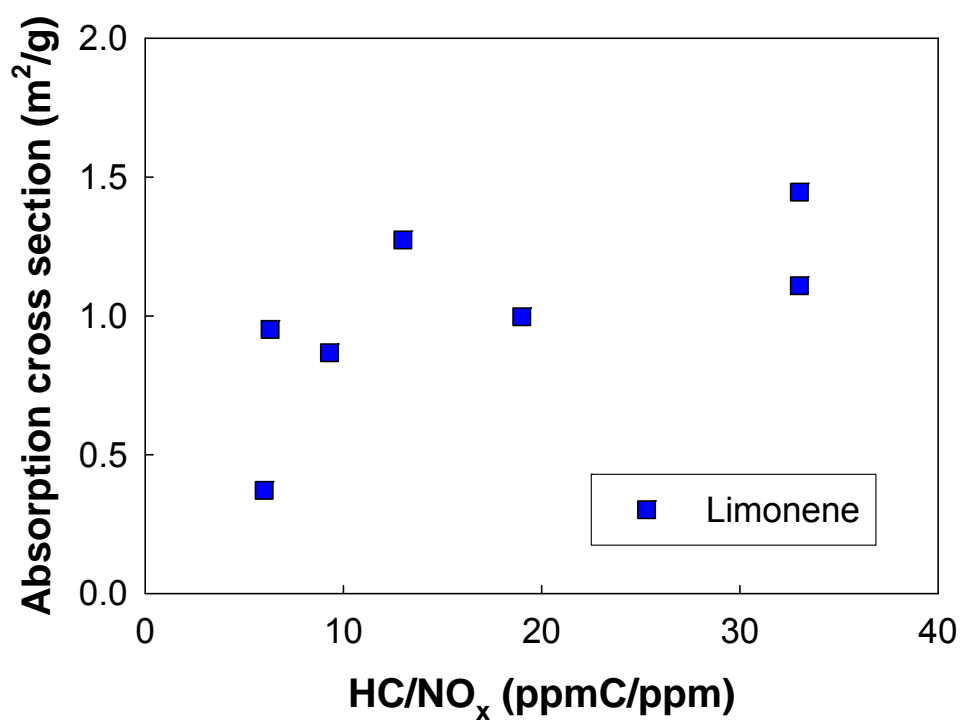


Figure 1. Absorption cross section at 370 nm for photochemically generated limonene SOA at different HC/NO<sub>x</sub> ratios.

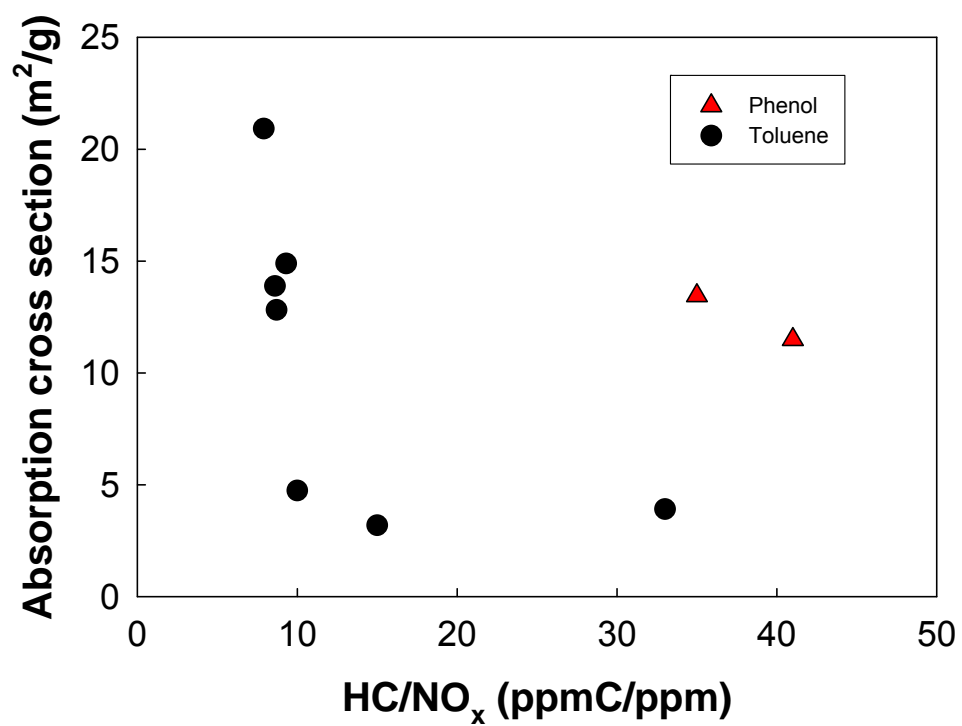


Figure 2. Absorption cross section at 370 nm for photochemically generated toluene SOA and phenol SOA at different HC/NO<sub>x</sub> ratios.

## **Appendix B**

### **Aerosol partitioning of condensing species.**

We calculated the gas-aerosol partitioning of the limonene oxidation products using the equilibrium absorptive partitioning equation *Pankow*, 1994;

$$K_p = \frac{F/TSP}{A} = \frac{760 RT f_{om}}{10^6 MW \gamma_i P_{L,i}^0} \quad (1)$$

Where F and A are the total aerosol phase and gaseous concentrations of the compound of interest, respectively, and TSP is the concentration of total suspended particulate matter. The right hand side of the expression shows the equilibrium constant in terms of thermodynamic properties; R is the universal gas constant ( $8.206 \times 10^{-5} \text{ atm m}^3 \text{ K}^{-1} \text{ mol}^{-1}$ ), T is temperature (K),  $f_{om}$  is the weight fraction of organic matter in the total aerosol (assumed to be 1),  $\gamma$  is the activity coefficient (assumed to be 1), *MW* is the averaged molecular weight of the absorbing organic aerosol phase (assumed to be 120 g/mol [*Kamens and Jaoui*, 2001]) and  $P_{L,i}^0$  is the vapor pressure of the compound of interest (atm). This gives the partitioning coefficient,  $K_p$  in units of  $\text{m}^3 \mu\text{g}^{-1}$ .

We calculate values in the  $10^{-12}$  to  $10^{-4}$  atm range for the equilibrium gas/aerosol partitioning of 282 condensable semivolatile species containing alcohol (-OH), ketone (-C(=O)), aldehyde (-CHO), hydroperoxide (-OOH), peracids (-C(=O)OOH), nitrates (-ONO<sub>2</sub>) and peroxy acetyl nitrates (-C(=O)OONO<sub>2</sub>), “PAN”) groups. These functional groups have been identified in particle phase of SOA by several experimental studies [*Jaoui et al.*, 2006; *Larsen et al.*, 2001; *Leungsakul et al.*, 2005]. Because there are no measurements of vapor pressures for most limonene products, structure activity relationships (SARs) were used to estimate  $P_{L,i}^0$ . Several SAR approaches for estimating  $P_{L,i}^0$  are available in the literature [*Moller et al.*, 2008; *Myrdal and Yalkowsky*, 1997; *Nannoolal et al.*, 2008]. The differences in the  $P_{L,i}^0$  estimated based on determined SARs can reach many orders of magnitude for species in the  $P_{L,i}^0$  range of  $10^{-13}$  and

$10^{-5}$  atm [Compernelle *et al.*, 2010]. Further, a major drawback of the above methods is the absence of parameterizations for group contribution by several chemical species believed to play an important role in SOA formation. These include hydroperoxides (-OOH), peracids (-C(=O)OOH), nitrates (-ONO<sub>2</sub>) and peroxy acetyl nitrates (-C(=O)OONO<sub>2</sub>, “PAN”) [Leungsakul *et al.*, 2005; Reinnig *et al.*, 2009; Rollins *et al.*, 2010]. In this study, we use the Myrdal and Yalkowsky, [1997]’s method modified by Camredon *et al.*, [2007] because of its relative simplicity and reliability.

To initiate SOA formation within the model (the experiments did not have seed particles), a small amount of “seed aerosol” is allowed to create the surface on which semivolatile species can partition. Seed aerosol is composed of species with estimated vapor pressures as low as  $10^{-18}$  atm [Kamens *et al.*, 1999]. In this model, seed species arise from reactions between Criegee intermediates and carbonyls such as limonene aldehyde and limononic acid. Partitioning is implemented by determining the gas phase fractions of each species at each time step, assuming partitioning is effectively instantaneous. The measured mass concentration of SOA from the SMPS was compared with the model result and, as reported in previous studies [Fry *et al.*, 2009; Kamens and Jaoui, 2001], the predicted vapor pressures underestimate the mass of aerosol produced. The modeled SOA mass concentrations were fit to the measured masses by applying a factor (17 – 40) to the estimated partitioning coefficients of all considered condensing species, greatly improving measurement/model agreement. The large discrepancy underscores the uncertainties in the SOA composition calculated in this way. While it might be possible to improve the situation somewhat, the goal here is to compare measured and calculated refractive indices (below). Because the majority of condensing species have estimated refractive indices that fall in a range that is much narrower than the measurements, without major changes

affecting particle chemical composition, incremental improvements to the model or partitioning will not likely improve agreement of measured and modeled refractive indices much.

#### References

- Camredon, M., B. Aumont, J. Lee-Taylor, and S. Madronich (2007), The SOA/VOC/NO<sub>x</sub> system: an explicit model of secondary organic aerosol formation, *Atmospheric Chemistry and Physics*, 7(21), 5599-5610.
- Compernelle, S., K. Ceulemans, and J. F. Muller (2010), Technical Note: Vapor pressure estimation methods applied to secondary organic aerosol constituents from alpha-pinene oxidation: an intercomparison study, *Atmospheric Chemistry and Physics*, 10(13), 6271-6282.
- Fry, J. L., A. Kiendler-Scharr, A. W. Rollins, P. J. Wooldridge, S. S. Brown, H. Fuchs, W. Dube, A. Mensah, M. dal Maso, R. Tillmann, H. P. Dorn, T. Brauers, and R. C. Cohen (2009), Organic nitrate and secondary organic aerosol yield from NO<sub>3</sub> oxidation of beta-pinene evaluated using a gas-phase kinetics/aerosol partitioning model, *Atmospheric Chemistry and Physics*, 9(4), 1431-1449.
- Jaoui, M., E. Corse, T. E. Kleindienst, J. H. Offenberg, M. Lewandowski, and E. O. Edney (2006), Analysis of secondary organic aerosol compounds from the photooxidation of d-limonene in the presence of NO<sub>x</sub> and their detection in ambient PM<sub>2.5</sub>, *Environmental Science & Technology*, 40(12), 3819-3828.
- Kamens, R., M. Jang, C. J. Chien, and K. Leach (1999), Aerosol formation from the reaction of alpha-pinene and ozone using a gas-phase kinetics aerosol partitioning model, *Environmental Science & Technology*, 33(9), 1430-1438.
- Kamens, R. M., and M. Jaoui (2001), Modeling aerosol formation from alpha-pinene plus NO<sub>x</sub> in the presence of natural sunlight using gas-phase kinetics and gas-particle partitioning theory, *Environmental Science & Technology*, 35(7), 1394-1405.
- Larsen, B. R., D. Di Bella, M. Glasius, R. Winterhalter, N. R. Jensen, and J. Hjorth (2001), Gas-phase OH oxidation of monoterpenes: Gaseous and particulate products, *Journal of Atmospheric Chemistry*, 38(3), 231-276.
- Leungsakul, S., H. E. Jeffries, and R. M. Kamens (2005), A kinetic mechanism for predicting secondary aerosol formation from the reactions of d-limonene in the presence of oxides of nitrogen and natural sunlight, *Atmospheric Environment*, 39(37), 7063-7082.
- Moller, B., J. Rarey, and D. Ramjugernath (2008), Estimation of the vapour pressure of non-electrolyte organic compounds via group contributions and group interactions, *Journal of Molecular Liquids*, 143(1), 52-63.
- Myrdal, P. B., and S. H. Yalkowsky (1997), Estimating pure component vapor pressures of complex organic molecules, *Industrial & Engineering Chemistry Research*, 36(6), 2494-2499.
- Nannoolal, Y., J. Rarey, and D. Ramjugernath (2008), Estimation of pure component properties - Part 3. Estimation of the vapor pressure of non-electrolyte organic compounds via group contributions and group interactions, *Fluid Phase Equilibria*, 269(1-2), 117-133.
- Pankow, J. F. (1994), An absorption model of the gas aerosol partitioning involved in the formation of secondary organic aerosol, *Atmospheric Environment*, 28(2), 189-193.
- Reinigg, M. C., J. Warnke, and T. Hoffmann (2009), Identification of organic hydroperoxides and hydroperoxy acids in secondary organic aerosol formed during the ozonolysis of different monoterpenes and sesquiterpenes by on-line analysis using atmospheric pressure chemical



ionization ion trap mass spectrometry, *Rapid Communications in Mass Spectrometry*, 23(11), 1735-1741.

Rollins, A. W., J. D. Smith, K. R. Wilson, and R. C. Cohen (2010), Real Time In Situ Detection of Organic Nitrates in Atmospheric Aerosols, *Environmental Science & Technology*, 44(14), 5540-5545.

## **Appendix C**

**Tables of initial conditions, temperatures, relative humidities and results of the experiments not described in main chapters.**

**Table C.1;** Tables of initial conditions, temperatures, relative humidities and results of the Photooxidation experiments with myrcene,  $\alpha$ -humulene, isoprene, phenol and dodecane

Expt.	Initial Conditions						Results				
	HC	HC (ppb)	NO <sub>x</sub> (ppb)	HC/NO <sub>x</sub> (ppbC/ppb)	Temp (°C) <sup>1</sup>	RH (%) <sup>1</sup>	$\Delta$ HC (ppb)	# density <sup>2</sup> (#/cm <sup>3</sup> )	Size mode <sup>2</sup> (nm)	Mass <sup>3</sup> ( $\mu$ g/m <sup>3</sup> )	Yield <sup>4</sup> (%)
<b>1-Jul-10</b>	myrcene	226	200	11	28-37	22-14	226	20900	311	816	65
<b>24-Jun-10</b>	$\alpha$ -Humulene	231	420	8	28-34-25	24-15-26	231	163000	122/532	3487	181
<b>29-Oct-10</b>	isoprene	560	50	56	23-34	18-11	418	17400	69	9.7	N/A
<b>17-Nov-10</b>	isoprene	416	153	14	24-31-28	21-15-17	384	71700	62	37(4.5)	N/A
<b>1-Dec-10</b>	isoprene	564	165	17	23-29-24	14-11-13	495	47300	51	15.3(14.5)	N/A
<b>3-Dec-10</b>	isoprene	479	135	18	22-27-24	22-16-20	361	77700	69	43	N/A
<b>7-Dec-10</b>	isoprene	638	175	18	21-32-28	23-15	638	8510	118	15	N/A
<b>14-Oct-11</b>	phenol	800	143	41	38-42-38	16-14-17	344	1620	461	93	9.4
<b>26-Oct-11</b>	phenol	1068	210	35	31-27	27-35	506	1800	661	263	17.6
<b>31-Oct-11</b>	phenol	2100	970	14	32-26	16-18	102	1830	242.1	18.3	5.0
<b>28-Oct-11</b>	dodecane	1230	370	43	34-37-33	14-12-14	30	N/A	N/A	N/A	N/A

All data shown here is not corrected with wall loss

<sup>1</sup>Initial and final temperature and relative humidity

<sup>2</sup>Final aerosol number concentration and size mode. These values have not been adjusted for wall losses. Except for isoprene experiments

<sup>3</sup>Mass concentration in the chamber was determined from the maximum SMPS measured size distribution in the chamber over the period for which meaningful PN measurements

<sup>4</sup>Calculated from peak measured aerosol mass and the corresponding quantity of reacted hydrocarbon. Because of the uncertainties in the measurement from GC ( $\pm 3\%$ ) and measurement of SMPS ( $\pm 10\%$ ) yields are uncertain to  $\pm 10\%$ .

Isoprene data; seed aerosol ((sulfuric acid ,0.015M + ammonium sulfate (0.015M)) was used.

Size mode, mass and number density shown here is the value of seed aerosol when tarp was removed.

Since SOA was not formed well, SOA data is not shown. Value in parenthesis of mass is from the SOA part (increased mass due to SOA - minimum mass right before increasing mass)

**Table C.2;** Tables of initial conditions, temperatures, relative humidities and results of the Ozonolysis experiments with myrcene,  $\alpha$ -humulene.

Initial conditions						Results				
Run	HC	HC (ppb)	Ozone (ppb)	Temp (°C)	RH (%)	$\Delta$ HC (ppb)	# density <sup>1</sup> (#/cm <sup>3</sup> )	Size mode <sup>1</sup> (nm)	Mass <sup>2</sup> ( $\mu$ g/m <sup>3</sup> )	Yield <sup>3</sup> (%)
<b>21-Jun-10</b>	myrcene	400	250	21-24	26-24	329	49800	250	945.85	52
<b>23-Jul-10</b>	myrcene	157	250	22-25	26-21	155	28500	163	192	22
<b>26-Jul-10</b>	$\alpha$ -Humulene	190	250	23-25-22	23-21-26	106	55600	225	832	94

Data shown here is not corrected with wall loss

<sup>1</sup> Final aerosol number concentration and size mode. These values have not been adjusted for wall losses.

<sup>2</sup> Particle density was assumed as 1.2 g/cm<sup>3</sup> for  $\alpha$ -pinene, myrcene, humulene and 1.25 g/cm<sup>3</sup> for limonene. Measured particle number concentrations were corrected for wall losses and mass concentration was calculated.

<sup>3</sup> Calculated from peak measured aerosol mass not corrected for wall losses and the corresponding quantity of reacted hydrocarbon. Because of the uncertainty in measurement of GC ( $\pm 3\%$ ) and measurement of SMPS ( $\pm 10\%$ ) yields are uncertain to  $\pm 10\%$ .

<sup>4</sup> Cyclohexane was added in 50 fold excess compared to the hydrocarbon to suppress OH formation.

**Table C.3;** Tables of initial conditions, temperatures, relative humidities and results of the experiments

Expt.							Results				
	HC	HC (ppb)	NO <sub>x</sub> (ppb)	HC/NO <sub>x</sub> (ppbC/ppb)	Temp (°C)	RH (%)	ΔHC (ppb)	# density <sup>1</sup> (#/cm <sup>3</sup> )	Size mode <sup>1</sup> (nm)	Mass <sup>2</sup> (μg/m <sup>3</sup> )	Yield <sup>3</sup> (%)
13-Oct-10	limonene	62	50	12.4	39-35	15-18	61.0	2340	241	50	15
10-Nov-10	limonene	104	72	14.4	23-30-23	26-17-26	104.0	7460	334	358	62
11-Oct-10	limonene	48	60	8.0	39-35	15-18	48.0	1230	217	13	4.9
15-Nov-10	limonene	90	150	6.0	32-25	15-22	83	2750	400	176	38
18-Jun-10	limonene	300	330	9.1	33-35-29	15-14-17	300	7390	533	2037 <sup>a</sup>	122
14-Jun-10	limonene	402	170	24	29-36	21-15	402	18300	414	2587 <sup>a</sup>	116
28-Jul-10	limonene	126	111	11	31-33	18-16	113	3960	385	329 <sup>a</sup>	52
16-Jul-10	limonene	104	38	27	36-43-36	16-12-15	94	7590	269	326 <sup>a</sup>	62
2-Aug-10	limonene	48	44	11	34-31	20-21	46	205	311	5 <sup>a</sup>	2
19-Jul-10	limonene	59	24	25	35-37	16-15	53	6180	195	73 <sup>a</sup>	25
14-Nov-11	limonene	160	110	15	24-23	29-33	159	3640	303	120	14
29-Nov-11	limonene	271	365	7.4	29-31	31-32	137	N/A	N/A	N/A	N/A
21-Nov-11	α-pinene	181	260	7.0	24-18	33-48	101	6400	195	33	5.9
8-Nov-11	α-pinene	118	91	13	26-27	30-33	110	6310	241.4	107	18
6-Jan-12	α-pinene	170	125	14	29-26	15-19	170	1950	429	196	28
9-Jan-12	α-pinene	147	45	33	27-30	25-30	147	1080	429	139	17
20-Aug-10	α-pinene	75	24	31	38-43-37	15-13-16	73	2900	225	50	12
23-Aug-10	α-pinene	95	105	9.0	44-45-37	14-13-18	95	1110	300	35	6.6
7-Sep-11	toluene	3100	2800	8.2	48-42	17-23	820	11400	250	127	4.1
9-Sep-11	toluene	3400	3230	7.7	38-35	18-20	810	17700	260	221	4.9
14-Sep-11	toluene	3000	2800	7.9	35-31	24-35	480	11800	136	22	0.8
19-Sep-11	toluene	3100	2650	8.7	34-33	29-33	540	7360	175	30	1
12-Oct-11	toluene	3400	2750	9	47-49-44	15-14-20	820	4520	279	74	1.6

<sup>1</sup>Final aerosol number concentration and size mode. These values have not been adjusted for wall losses.

<sup>2</sup>Max mass concentration. Measured particle number concentrations were corrected for wall losses and mass concentration was calculated. Particle density was assumed as 1.2 g/cm<sup>3</sup> for α-pinene, 1.25 g/cm<sup>3</sup> for limonene and 1.24 g/cm<sup>3</sup> for toluene.

<sup>3</sup>Calculated from peak measured aerosol mass corrected for wall losses and the corresponding quantity of reacted hydrocarbon. Because of the uncertainty in measurement of GC (± 3 %) and measurement of SMPS (± 10 %) yields are uncertain to ± 10 %.

<sup>a</sup> Wall loss is not corrected

**Table C.4;** Tables of initial conditions, temperatures, relative humidities and results of the experiments

Initial conditions						Results					
Run	Hydrocarbon	HC (ppb)	Ozone (ppb)	Temp (°C)	RH (%)	$\Delta$ HC (ppb)	# density <sup>1</sup> (#/cm <sup>3</sup> )	Size (nm)	mode <sup>1</sup>	Mass <sup>2</sup> ( $\mu$ g/m <sup>3</sup> )	Yield <sup>3</sup> (%)
<b>16-Jun-10</b>	limonene	500	250	23-25-21	24-22-26	181	31100	269		1360 <sup>a</sup>	135
<b>28-Jun-10</b>	limonene	381	250	17-25-21	28-19-23	181	48500	250		1441.59 <sup>a</sup>	143
<b>12-Jul-10</b>	limonene	152	250	23-25	26-24	117	48700	241		892 <sup>a</sup>	137
<b>21-Jul-10</b>	limonene <sup>4</sup>	168	250	22-26-24	26-21-24	157	21500	241		560 <sup>a</sup>	64
<b>27-Oct-10</b>	limonene	59	250	26-30	20-16	59	3810	169		215	66
<b>1-Oct-10</b>	limonene	65	250	29-28	23-25	65	14900	188		218	60
<b>16-Sep-11</b>	$\beta$ -pinene <sup>4</sup>	201	500	21-23	38-34	166	4270	300		100 <sup>a</sup>	11
<b>26-Sep-11</b>	$\beta$ -pinene	220	500	22-26	42-33	220	10800	209		130 <sup>a</sup>	11

Final aerosol number concentration and size mode. These values have not been adjusted for wall losses.

<sup>1</sup>Max mass concentration. Particle density was assumed as 1.2 g/cm<sup>3</sup> for  $\beta$ -pinene and 1.25 g/cm<sup>3</sup> for limonene. Measured particle number concentrations were corrected for wall losses and mass concentration was calculated.

<sup>2</sup>Calculated from peak measured aerosol mass corrected for wall losses and the corresponding quantity of reacted hydrocarbon. Because of the uncertainty in measurement of GC ( $\pm 3\%$ ) and measurement of SMPS ( $\pm 10\%$ ) yields are uncertain to  $\pm 10\%$ .

<sup>3</sup>Cyclohexane was added in 50 fold excess compared to the hydrocarbon to suppress OH formation.

<sup>4</sup>Wall loss is not corrected

## **Appendix D**

**Bi-modal size distribution of SOA generated from photooxidation of  $\alpha$ -humulene/ $\text{NO}_x$  experiment (HC/ $\text{NO}_x=8.3$ )**

$\alpha$ -Humulene/NO<sub>x</sub>(3.47 ppmc/0.42 ppm=8.3)

